Development of a vibration-based non-destructive testing method for in-service utility poles

A Thesis for Doctoral Research in the Faculty of Engineering and Applied Science

By

Mohammad Hadi Jalali

Supervisory Committee

Dr. Geoff Rideout (Supervisor)

Dr. Lorenzo Moro

Dr. Mohammad Al Janaideh

Faculty of Engineering and Applied Science,

Memorial University of Newfoundland

St. John’s, Canada

March 2021

Abstract

Wooden utility poles for electric networks are widely used, with approximately two million poles in North America. A reliable and cost-effective non-destructive testing (NDT) method is necessary for strength evaluation during the life span of the poles. To improve an emerging modal testing-based NDT method, this thesis develops a novel method to measure natural frequencies and damping ratios of poles even though they are connected to conductors. This thesis makes contributions to the wood pole NDT state of the art in two major areas – analytical and numerical modeling of pole-cable systems, and frequency-domain decoupling methods to identify pole properties despite their connection to cables.

Improved analytical models of the “cable-beam” system were developed in order to understand the coupled vibration behavior of the system. Bending stiffness and sag of the cable were considered in the modeling and the effects of them on vibration behavior of the system was studied. Two-dimensional and three-dimensional dynamic models using bond graph method were developed for vibration of stranded cables and vibration of the cable-beam system. The models were verified by experiments in free and forced vibration.

The second contribution area is the development of substructure decoupling-related methods to decouple the beam frequency response function (FRF) from the assembled cable-beam system. The FRF of the beam was obtained as an independent substructure after decoupling analysis and the FRF was compared to the directly measured FRF from modal testing of the beam substructure. A good agreement showed that the substructure decoupling method can be used to filter out the effects of cables from the assembled system in cabled structures, assuming that all points in the system are accessible for measurement.

An FRF-based finite element model updating was then developed to overcome the practical limitation of accessing some measurement points in the field. The FRFs of accessible points were

used as a basis for updating the FE model and then the FRFs of inaccessible points were obtained from the updated (optimized) FE model.

A substructural damage detection was also developed for the systems that consist of a few substructures but only the main (target) substructure is susceptible to damage. In the developed method, FRF of the main substructure is first obtained using the substructure decoupling method and then FRF-based finite element model updating is used for damage detection, localization and quantification. The method was successfully able to identify location and magnitude of damage, which was modeled as a localized reduced stiffness due to material degradation or cracking.

Finally, in support of the larger ongoing NDT research project, full-scale pole modal testing was done in the field. In-ground pole FRF's with and without cables were generated, for future use in model validation. In-ground poles without cables were subjected to modal testing, and then brought to the lab for modal and destructive testing. The differences in the resulting FRF's allow future simulation-based prediction of the foundation properties, and the destructive tests have added to the research group's database for correlation of modal properties and pole strength.

Letter of Transmittal

I, Mohammad Hadi Jalali, certify that my PhD thesis is prepared in accordance with the Faculty of Engineering and Applied Science guidelines for thesis proposals and I am fully responsible for its contents.

I am ready to proceed to have my thesis evaluated by my supervisor committee.

Mr. Mohammad Hadi Jalali

Date: March 2021

Acknowledgment

I would like to express profound gratitude to my supervisor, Dr. Geoff Rideout, for his expert guidance, encouragement and academic and non-academic supports throughout my PhD. I gratefully acknowledge his technical expertise, as well as his immense patience, which enabled me to complete my Ph.D. successfully. I believe that, besides academic and technical expertise, he is a nice and genuine person.

I would also like to thank NL Hydro Company, the National Sciences and Engineering Research Council (NSERC) and Memorial University Graduate School for their financial support during this PhD thesis. I would like to thank Matthew Curtis, technician at Memorial university structure lab, for destructive testing of the utility poles and Andrew Marshall, transmission line engineer at NL Hydro, for in-kind support for transmission of the utility poles to the lab.

Last but not least, I am forever indebted to my mother and father for their encouragement and kindness, to whom I owe much of what I have become. My exceptional gratitude goes out to my wife, Jessica, for her patience, emotional support and encouragement during these years. I thank them for their love, support and kindness throughout my life. This dissertation would not have been possible without their warm love, continued patience, and endless support.

And I would like to dedicate this thesis to my daughter Ellie, who is just six months old now, but I would give anything away in my life for her smile.

Table of Contents

List of Figures

List of Tables

Chapter 1

1 Introduction

1.1 Background

Wooden utility poles are widely used by utility companies to support transmission lines. In Newfoundland and Labrador alone there are approximately 26000 wooden poles of varying ages [1]. Wood has many advantages over steel and concrete. They are abundant and relatively inexpensive, have great ratio of strength to weight, and present excellent dielectric characteristics [2]. However, during its life span, wooden poles are subjected to environmental conditions that cause degradation of the material. Insect infestation, animal perforations, plant and fungi growth, weather variations, etc., all contribute to the deterioration of the wooden pole [3]. With time, these factors compromise the network reliability, the safety of the population and the operators of the electrical system. Pole strength degradation is a serious issue, causing the industry to invest considerable amounts of money in maintenance programs and research. Figure 1.1 shows an electricity pole failure and this catastrophic incident happens quite often around the world. Therefore, a reliable and cost-effective Non-destructive testing (NDT) method is necessary for strength evaluation during the life span of the poles.

Figure 1.1: Electricity pole failure [4]

Various non-destructive test methods have been used for utility poles. Most NDT methods use some forms of energy propagation through or around a material to infer some important characteristics about the specimen being examined [5]. All these methods are used locally but localized damage detection may require a large number of tests and damage closer to the pole tip may go undetected. In the field, the tests can only be conducted near the ground line, unless personnel are raised with a hoist.

1.2 Problem Statement

NL Hydro presents online reports which show that in 2017, investments of 3.8 million Canadian dollars will be expended on pole maintenance and upgrades [6]. A Wood Pole Line Management Program (WPLM) was initiated by Haldar [1] in Newfoundland and Labrador Hydro (NLH) to systematically collect and analyze data, and to perform reliability analysis for wooden utility transmission lines. To generate data for the Reliability Centered Maintenance (RCM) program, which aims to extend pole life while preventing pole failure; and to verify the effectiveness of non-destructive testing (NDE) equipment, full-scale destructive pole tests were carried out in the Structures Laboratory at Memorial University in the previous stages of the program [7,8]. The ultrasonic “POLETEST” NDT equipment manufactured by a company called Engineering Data Management (EDM international) [9] did not show acceptable correlation with full-scale test data in predicting strength. NL Hydro has concerns about the efficacy of current NDT methods for predicting pole strength; and thus for predicting whether or not to remove poles from service based on the prediction intervals reported in the literature and the strength cut-off limit in the POLETEST manual. According to NLH, correlation was higher between destructive and NDT values for new poles, and unacceptably low for older poles, with old pole strength typically overpredicted. The low correlation for older poles was of primary concern given that removing a pole from service prematurely creates needless cost to NLH, and failing to remove an unacceptably weak pole from service creates a safety hazard for inspectors and possible power outages. It is essential to detect “danger poles” early to avoid safety hazards, and to maximize the opportunity to apply corrective actions such as preservative treatment or additional support to extend pole life [1].

This research is a continuation of work initiated by NL Hydro and Memorial University with the aim of development of a new NDT method for wooden utility poles using modal tests. In this vibration-based NDT method, the overall strength of the pole could be achieved and localized damaged detection that is the basis of other NDT methods would not be needed.

In the three previous phases of the project, modal impact and destructive static tests were performed on a number of utility poles [10]. From the data collected, a method has been developed to predict the ground line stress at which failure will occur for full scale poles. The method predicts a correlation between the maximum stress and the measured damping ratios obtained through modal impact testing. Predictions made from modal damping ratios are more accurate than predictions made with POLETEST ultrasonic NDT equipment currently used in the lab. Recent investigations by the previous researchers in the project have been shown that the modal test quality decreases in the field compared to lab, presumably due to foundation damping and compliance, cables, or a combination of both effects [7,11,12] since lab modal tests have been carried out with the lab-scale clamp fixture and without cables connected to the pole. Figure 1.2 shows the frequency response functions (FRFs) of two sample utility poles obtained in the field modal testing in a transmission line in Goose Bay, Labrador. The modal test was performed on the utility pole in both the conditions, the cables connected and disconnected to the pole. As can be seen, FRF of the pole with and without connected conductors differ and conductors have significant effect on frequency response of the utility pole. Figure 1.3 shows the modal testing of the pole using modal hammer and accelerometers. The details of the modal test procedure is discussed in Appendix.

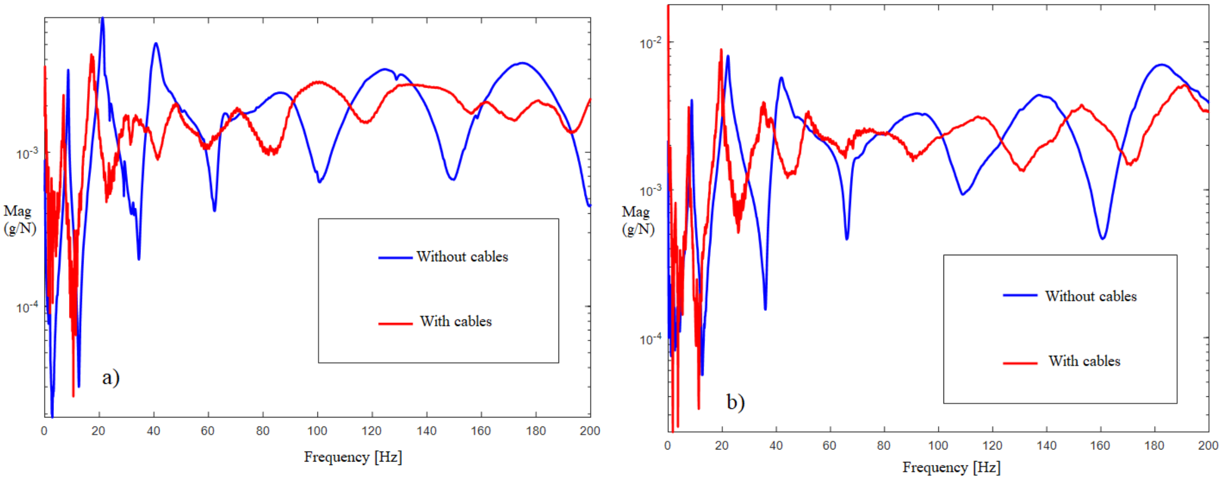

Figure 1.2 : FRF of two different utility poles with and without cable –Field Modal test

Figure 1.3: Field modal test in Goose bay, Labrador

Figure 1.4 shows the difference in modal data obtained from lab modal test and field modal test of the pole without cables. The poles are the same poles, removed from the field and then tested in the lab. As can be observed, modal test quality decrease from lab to the field. The two points circled in the right figure were new poles, replaced within the 10 years prior to the testing. Those two poles clearly ended up much closer to the trend line when tested in the lab.

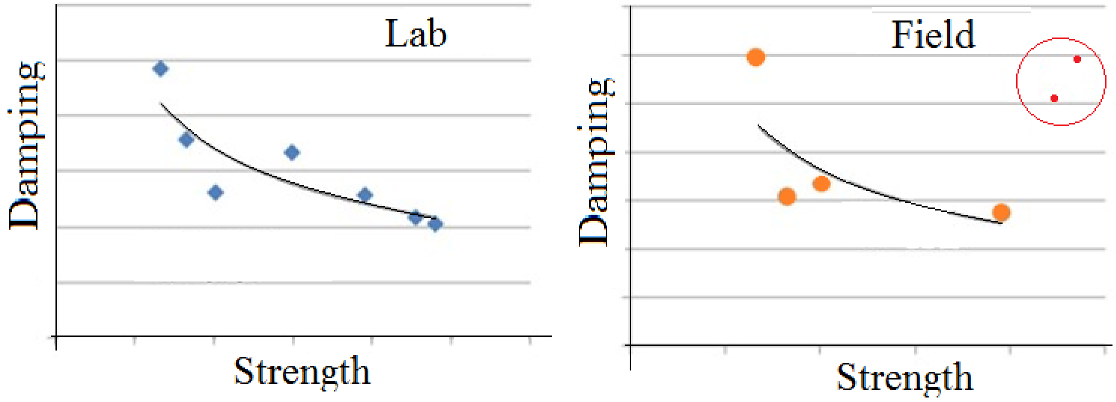

Figure 1.4: Damping-strength correlation in the lab and in the field

1.3 Thesis Statement

The aim of this PhD thesis is to investigate the effect of conductors on vibration properties of utility poles and to filter out the effect of cables/foundation from frequency response of the poles obtained in modal testing. In order to achieve these two main goals, analytical and numerical modeling, lab-scale and field modal testing were carried out.

This thesis consists of three main contribution areas:

a) Analytical and Numerical Simulation

To help better understand the coupled vibration behavior of cable-beam systems, new analytical and numerical models have been developed. These models can be generalized to cable-beam systems beyond the utility poles that are the application of immediate interest. An analytical model is developed and experimentally validated for a cable-beam system considering bending stiffness and sag of the cable and the natural frequencies, mode shapes and FRF of the system obtained from the model is compared to the experimental results. From this study, the following contributions were achieved:

1. It is concluded that bending stiffness of the cable has significant effect on vibration behavior of cable-beam systems, an important parameter that has been neglected in all the available published studies.
2. Experimental cable stiffness parametrization was performed. An apparatus was developed for bending stiffness measurement in different tensions and it was concluded that bending stiffness of the stranded cables increase with the increase in tension, as expected. Another apparatus was developed for axial stiffness and damping measurement of a cable. Axial stiffness and damping values were measured and the measured values were used for modeling.
3. It was concluded that by adding cable to the beam, vibration modes of the system are cable dominated modes, beam dominated modes or hybrid (coupled) modes, as expected.

In another study in this part, three-dimensional bond graph models for a cable and cable-beam system are developed and validated in order to investigate the free and forced vibration of the system in three dimensions and to simulate the modal testing in in-plane and out-of-plane conditions. The following contributions were achieved in this study:

4. The cable-only model predicts the in-plane and out-of-plane natural frequencies and free and forced vibration response. The bond graph model could be easily used to model any cable by simply changing the geometrical properties.
5. The cable-beam model allows prediction of in-plane and out-of-plane natural frequencies and free and forced vibration response of the cable-beam system. The model can be used to simulate modal testing and free vibration.
6. The bond graph models could be easily expanded to the real utility pole-cable system model by changing the geometrical properties and adding any number of cables.

b) Substructure decoupling analysis

The second part is the investigation of applying substructure decoupling method to the cable-beam systems. Substructure decoupling or inverse substructuring method [13,14] is a known method to decouple a substructure from the rest of the structure using FRF matrices. The novelty of this thesis is the application and experimental validation of substructuring for utility pole non-destructiuve testing. Substructure decoupling method is applied here to the cable-beam system in the lab and the beam FRFs are obtained completely decoupled from the rest of the structure. The following contributions were achieved in this part:

7. The decoupled beam FRFs were compared to the directly measured FRFs and good accuracy was obtained. It is concluded that this method is a reliable and sufficiently accurate method for filtering out effects of cable from an assembled cable-beam system.
8. An FRF-based finite element model updating technique was proposed to overcome the practical limitation of accessing some measurement points. The measured FRFs (from accessible points) were used as a basis for updating the FE model and FRFs of inaccessible points were obtained from the updated FE model. It is concluded that this FRF-based FE updating method can be used to obtain the FRFs corresponding to inaccessible points in the field. A combination of numerical and experimental FRFs were used to obtain the decoupled FRFs.
9. A substructural damage detection method was developed for detecting damage of structures that consist of a few substructures but only one of the substructures (the main or target substructure) is susceptible to damage. Using this method, damage detection of the global structure would not be needed and only the main substrucuture can be analyzed for damage detection. By substructure decoupling, the main substructure FRFs are first obtained and then FE updating (using only the main substructure FE model) is used for damage localization and quantification in the main substructure.

c) Full-scale pole testing

The third part is field and lab modal testing and destructive testing of the utility poles. The modal test is carried out on 30 utility poles in the field in two separate test batches (each batch, 20 poles). The first batch of poles (in Goose bay, Labrador) were modally tested in two different conditions of with and without the connected cables and the purpose of this test was to study the effects of cables on the FRFs of the pole in the field. The second batch (in Paradise, Newfoundland) was tested only without the connected cables. This batch was then transmitted to the lab and was modally tested. The purpose of test of the second batch was to compare the FRFs obtained from the in-ground poles and in the lab-fixture poles. Destructive testing of the second batch was also performed based on ASTMD1036 to increase our database for the correlation between damping ratios and strength.

In section 1.4, the organization of this thesis is presented, and different chapters are briefly explained.

1.4 Thesis Organization

This thesis is organized as below:

Chapter 1 (the current chapter) includes the research background and motivation, the statement of the problem, thesis statement and the organization of the thesis.

Chapter 2 focuses on reviewing the literature of the following topics: the other existing NDT methods for utility poles, analytical modeling of cable-beam systems and application of dynamic substructuring in different engineering applications.

Chapter 3 is a full manuscript of a journal paper published in Journal of Vibration and Control [15]. This chapter presents the analytical modeling of a cable-beam system considering cable bending stiffness and sag and the verification of the model by experiments. The partial differential equations of a system consisted of a cantilever beam connected to a stranded cable is derived and solved and effects of cable sag and bending stiffness on the natural frequencies is investigated. Bending stiffness of the stranded cable in different tensions is measured using the designed apparatus and it is concluded that the cable bending stiffness has significant effect on the vibration behavior even though this parameter has been neglected in the literature. It is also concluded that mode shapes of the coupled system are cable dominated, beam dominated or hybrid modes.

Chapter 4 is a manuscript of a conference paper presented in Canadian Society of mechanical engineer's conference, CSME2018 [16]. This chapter presents a 2D bond graph model for a power line and the verification of the model by experiments. Free and forced vibration simulation is performed using the model and the results are verified in the lab. The cable bond graph model can be easily added to a beam bond graph model to model a cable-beam system. It is concluded that more studies on damping modeling for the cable is needed.

Chapter 5 is a full manuscript of a conference paper presented in ASME2019 [17]. This chapter is an expansion of Chapter 4 to provide a three-dimensional bond graph model for stranded cable. This chapter presents the model that allows prediction of in-plane an out-of-plane natural frequencies of the cable and a good understating of out-of-plane vibration is achieved even though the out-of-plane vibration is normally neglected in the literature.

Chapter 6 is a full manuscript of a journal paper published in Mathematical and Computer Modeling of Dynamical Systems Journal [18]. This chapter presents the three-dimensional bond graph model of a cable-beam system. The natural frequencies of the coupled system are obtained in in-plane and out-of-plane directions and are compared to the results obtained from modal test. A complete experimental cable parametrization is carried out for axial and bending stiffness of the cable. The developed model can be easily expanded to the real utility pole-power line system or any other cable structure.

Chapter 7 is a full manuscript of a journal paper which is published in Journal of Vibration and Control [19]. This chapter studies the application of substructure decoupling method in cable-beam systems for the first time in the literature. The frequency response function of a cantilever beam in a single-beam-cable system and in a multi-beam-cable system is obtained, completely decoupled from the rest of the structure and it is compared to the directly measured beam FRF. It is concluded that substructure decoupling method is a reliable and sufficiently accurate method to extract the FRF of the beam with the effects of cable, filtered out. An FRF-based finite element model updating method is also proposed to overcome the practical limitation of accessing some measurement points (in the field). The FRFs of measurable points are used as a basis for updating the FE model and FRFs of inaccessible points are obtained from the "updated" model.

Chapter 8 is a full manuscript of a conference paper presented in EURODYN2020 [20]. This chapter presents the results of decoupling analysis for a cable-beam system but using the measured FRFs from the assembled system and the numerically obtained FRF (Finite element) from the cable subsystem. It is concluded that experimental-numerical decoupling can be used when some FRFs should be obtained from numerical models due to difficulty in accessing the measurement points.

Chapter 9 is a full manuscript of a journal paper that is under review in Mechanical and Signal Processing Journal. In this chapter, a substructural damage detection method is developed for systems consisted of some substructures but only the main or the target substructure is susceptible to damage. Unlike other substructural damage detection methods in the literature, dynamics (FRF matrix) of the main subsystem is obtained as a "standalone" component without the need of interface virtual support or identifying interface forces. The target substructure FRFs are first obtained using decoupling method and then the damage in the target substructure is located and quantified using FRF-based finite element model updating.

Chapter 10 presents the concluding remarks of the thesis and describes the future work.

Appendix A discusses the destructive tests of the full-scale poles that were performed in this thesis and Appendix B discusses the modal tests of the full-scale poles in the lab ad in the field.

Chapter 2

2 Literature Review

2.1 Non-destructive Testing Methods

Over a few decades, many NDT techniques for assessing in-service utility poles have been studied and developed [21]. However, until now most, if not all, of the techniques have not been widely accepted for practical use in the industry [5]. Undoubtedly, an effective and reliable NDT technique plays a key role in asset management of utility poles. The technique should be capable of correctly identifying any pole that is likely to fail due to inadequate strength caused by decay or insect attack, so that the pole could be condemned reasonably. However, utility poles are a kind of widely distributed structures, and hence very complex indeed. A single pole may be considered as a simple structure, but a transmission line usually consists of hundreds of poles, distributed over a very long distance, and maybe over different terrains. Therefore, the use of NDE techniques for utility poles must be considered in a broad context of asset management [5]. The current NDT techniques for utility poles either lack sufficient sensitivity to the pole's deterioration, or are too expensive, or use too large and complex equipment to make in-service inspections practical [5]. Based on their form of energy propagation, all the current and older NDT techniques in general can be classified into five types [5]:

I) Visualizing methods: Such as visual inspection and those utilizing chemical techniques [22] to visualize defects or other characteristics on surface of wood. These methods are very subjective to technician experience and only give qualitative assessment of the pole but can be combined to the other NDT methods to give some results. They're also limited to the surface damage detection of the pole. Recently, drones have also been used for recording video of the poles close to power line to be used for visualizing methods [23–25].

II) Semi-non-destructive methods: In these methods, some small parts of the structure that have negligible effect on the performance of the object are actually damaged [26]. The common semi-destructive testing methods for wooden structures are resistance drilling (resistograph) [26–29] and core drilling [30]. However, these methods are only useful for very local points on the pole and cannot give overall strength prediction of the pole. A good understanding of these methods can be found in [31]. The other available method is POLUX [32] that uses the energy needed to penetrate on the pole to evaluate the strength.

III) Electrical Methods: Including electrical resistance measurement [33] to determine moisture content or to detect decay in wood.

IV) Methods using mechanical waves: These methods are very common in NDT of wooden utility poles [34] and include stress wave method [35], ultrasonic method [36–38] and acoustic emission [39–41]. The most common method of NDT of utility poles currently being used in the industry is ultrasonic. Ultrasonic and acoustic emission techniques are also local techniques and a damage closer to the pole tip may go undetected because of the limitations in wave propagation in the material.

V) Methods using electromagnetic waves: These methods use electromagnetic waves and include X-ray radiography and X-ray computed tomography (CT) [42,43]. Single X-ray information can give information about a cross section of the pole (2D image) and by X-ray CT method, three dimensional information can be achieved by doing the test in various locations along the pole [42]. This method is very expensive and detect localized damages very exactly but needs too many tests when overall strength prediction of the whole pole is needed.

With the existing NDT techniques, the tests can only be conducted near the ground line in the field, unless personnel are raised with a hoist. Localized damage detection may require a large number of tests, and damage closer to the pole tip may go undetected [44]. A research project started at

2008 in NL Hydro with collaboration with Memorial University, with the aim of development of a new NDT technique based on modal testing. Modal parameters are influenced not only by global changes in wood fiber strength, but also by localized damage such as from rot or woodpeckers. Modal parameters are insensitive to the location at which the impact occurs and can be extracted with a single hammer hit and accelerometer response signal.

Basics of all vibration-based NDT's can be explained as follows. For any structure, it can be taken as a dynamic system with stiffness, mass and damping [45]. Once some damages emerge in the structure, the structural parameters will change, and the frequency-response function and modal parameters of the structural system will also change. Thus, the change of the structural modal parameters can be taken as the signal of early damage occurrence in the structural system [45,46][47][48].

In the previous phases of this project, modal impact test and destructive bending test based on ASTM standard [49] were performed on a large number of utility poles in the lab and a correlation between modal damping ratios and strength of the pole was found. Strength predictions made from modal damping ratios were more accurate than predictions made with ultrasonic NDT equipment currently used in line management in NL Hydro. However, modal test quality decreased in the field compared to lab, presumably due to foundation effect, conductors, or a combination of both effects [11][7]. The purpose of this PhD thesis is to filter out effect of cables and foundation on the dynamics of poles in order to make the proposed modal test NDT method practical because the cables are connected to the pole and the foundation is different from lab clamp fixture, during the real operation of poles.

2.2 Cable-Beam System Modeling

Vibration analysis of conductors used in cable structures have been studied by many researchers for different applications and models of cable vary in their treatment of bending stiffness and cable sag due to self-weight. Papailiou [50] developed a well-known model for stranded cables, typically used in transmission lines, that took into account the interlayer friction and the interlayer slip in the conductor. He developed theoretical formula for bending stiffness of the conductors depending on the curvature and tension and validated his theory by experiments.

Ricciardi et. al. [51] and Kang et. al. [52] developed continuous models for vibration analysis of cables with sag considering the bending stiffness and observed the significance of sag and bending stiffness on linear and nonlinear vibration of cable-only systems. Sousa et. al. [53] analyzed the effect of considering bending stiffness, shear stiffness and rotational inertia on the natural frequencies of the overhead transmission line conductors. They found the error from neglecting shear and rotational inertia to be very small compared to the error from neglecting the bending and geometric stiffness of the cable. Gattulli et. al. [54] studied the linear and nonlinear dynamic behavior of cable-stayed beam structures. Bending stiffness of the cable was ignored in solving the equations of in-plane and out-of-plane motion of the coupled system. Linear analysis revealed the existence of global (beam dominated), local (cable dominated) and hybrid modes.

Lie et. al. [55] presented a simplified 3D computational model of a transmission tower-line system due to seismic excitations. The transmission cables and their supporting towers were modeled as a lumped mass system. Pinto et. al. [56] developed a bond graph model for pole with a cable attached to the free end. In their paper, the cable was modeled as a series of point masses connected by translational springs and the pole was represented by a modal expansion based on separation of variables. They obtained the modal parameters of the cable and pole-cable systems numerically and experimentally. From the literature review of cable vibration, it is concluded that bending stiffness and sag of the cable has significant effect on vibration of the cable but is often not considered in cable-beam system modeling in the literature. In this thesis, an analytical model for a beam with two connected cables considering bending stiffness and sag is presented for investigation of the cable-beam dynamics that can be extended to the real electricity pole and can be used for understanding the effects of cable on the pole modal properties. The analytical model and results are presented in Chapter 3.

2.3 Dynamic Substructuring Methods

Dynamic substructuring (DS) techniques have been well established over the past decades. These techniques consist of constructing the structural dynamic model of a large and complex system by assembling the dynamic models of its simpler components (also called subsystems or substructures) [13]. However, sometimes one has to consider the reverse problem, namely how a substructure model can be found from the assembled system. This problem arises when substructures cannot be measured separately but only when coupled to neighboring substructures, a situation regularly encountered in practice [57]. The substructure decoupling method, reverse of dynamic substructuring (coupling) method can be used when dynamics of a substructure of the global system should be obtained from dynamic analysis of the coupled system and another substructure has known dynamics. Practical applications of substructure decoupling can be imagined in structural monitoring and vibration control techniques, where monitoring and controlling of individual (critical) components in an assembly can be very valuable [13]. In a general framework, dynamic substructuring is analyzed in three distinct domains: the physical domain, modal and frequency domains [14] as can be seen in Figure 2.1. In the physical domain, the structure is characterized by its mass, stiffness, and damping distributions, which are given by the corresponding stiffness, mass, and damping matrices for a discretized linearized model. A structure in the frequency domain is seen through its frequency response functions. In the modal domain, the dynamic behavior of a structure is interpreted as a combination of modal responses [14]. From a theoretical perspective, the same information is contained in all different representations.

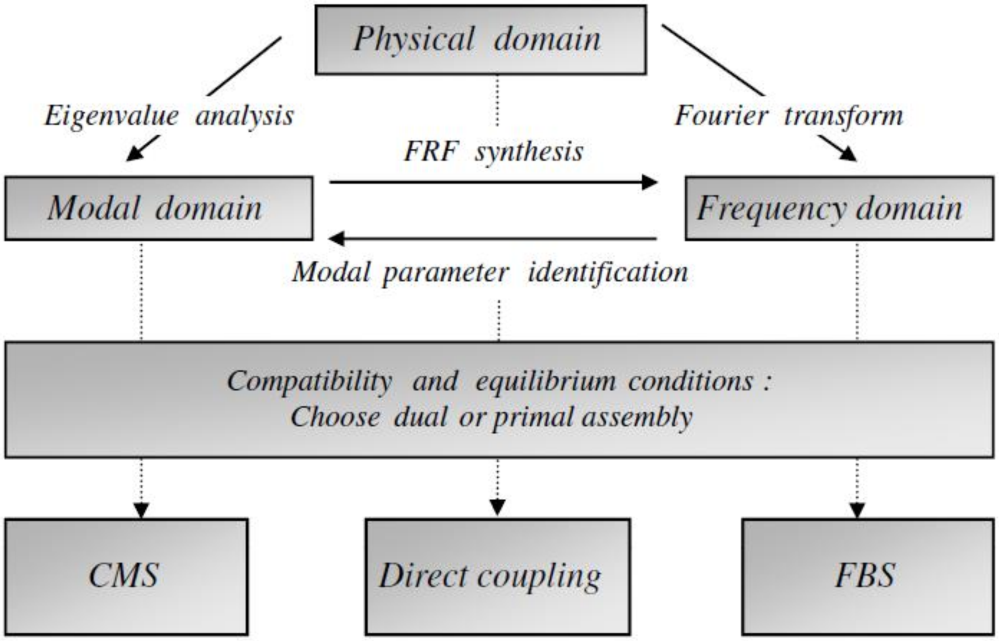

Figure 2.1: Representation of system dynamics in three domains [14]

To illustrate the problem at hand, consider the subsystems A and B shown in Figure 2.2 when assembled they form system AB. In this case, it is assumed that the dynamic models of the assembled system AB and the substructure A are known (e.g. from measurements or numerical analyses). Based on this information, the aim is to find the dynamics of subsystem B as a "standalone" component that is completely decoupled from subsystem A.

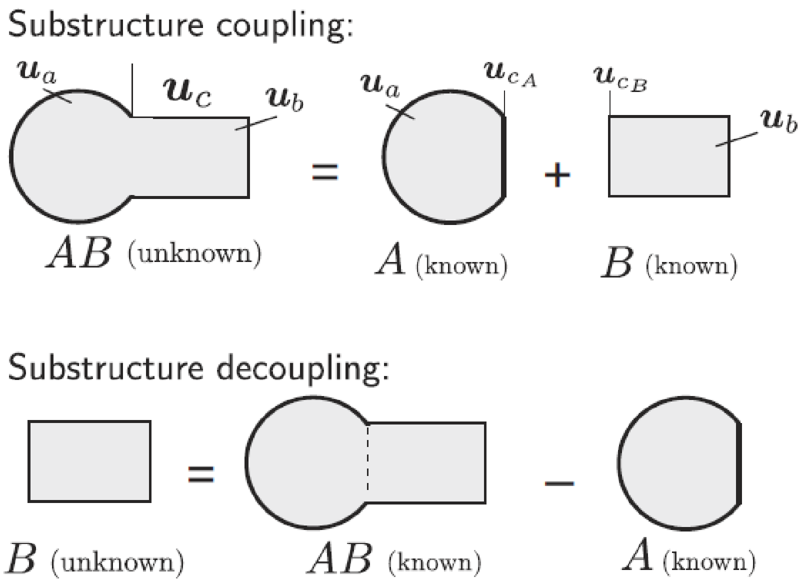

Figure 2.2: Substructure coupling (dynamic substructuring) and substructure decoupling schematic [13]

Researches on dynamic substructuring (decoupling) contains many published papers but here I review the literature briefly. The first steps toward frequency based (de)coupling and using frequency response function (FRF) in coupling and decoupling problems was taken by Crowley et. al [58] and Jetmundsen et. al. [59] with introducing the dual from of substructuring. In 2006, Klerk. et. al. [60] presented a dual domain decomposition method called Lagrange multiplier frequency based susbstructuring (LM FBS) method. The advantage of LM FBS method is the that the formulation is simpler than the FBS method from Jetmundsen et. al. [59]. There are many papers published in the literature to modify substructuring methods and reduce the effect of measurement errors on substructuring results as one of the problems in this method is the sensitivity of the final results to small errors [61]. I do not focus on literature review of these works here but some of the papers published in this area are [62–64].

Generally, substructure decoupling can be used as Experimental substructure decoupling or Experimental-Numerical substructure decoupling. Experimental decoupling can be used when measurements can be performed on both the coupled system and the substructure(s) that should be decoupled (residual substructure) and Experimental-Numerical decoupling can be used when either dynamics of the coupled system or the residual substructure cannot be measured and numerical (mostly Finite element) modeling is needed to have dynamics of one of them.

Various researches have been done in experimental decoupling in practical applications. For example, Law et. al. [65] applied the substructuring method for obtaining the dynamics of a mobile machine tool prior to moving the machine to new part/location. They used FRF based decoupling first to obtain the dynamics of a machine base by decoupling from the coupled base-part system and then used FRF based coupling to obtain dynamics of another part-base system with the same base dynamics that they obtained. Tol et. al. [66] proposed an experimental identification method based on FRF decoupling and optimization algorithm for modeling structural joints. They obtained bolted joint dynamic properties by measurement of FRFs of the two substructures joined together and FRF decoupling method. Seijs [67] in his PhD thesis, comprehensively studied experimental dynamic substructuring and transfer path analysis (TPA) to analyze the vibrations of the electric power-assisted steering (EPS) system in a vehicle. Mehrpouya et. al. [68] investigated dynamics of joint in a machine tool using FRF based decoupling using experimental and finite element investigations. D’Ambrogio et. al. [69] in another application, applied the experimental dynamic decoupling method to obtain the dynamics of free-free solar panel by measuring the FRF’s of solar panel with support structure and decoupling the support structure from the coupled (panel with support) system. As can be seen in this literature review of experimental substructure decoupling, many complicated structures were solved using substructure decoupling method.

In the case of Experimental-Numerical decoupling, a substructure can be modelled numerically, and dynamics of other substructure(s) can be obtained experimentally, and decoupling can be performed using both the numerical and experimental models. Eliasdottir et. al. [70] developed the dual form of experimental-numerical substructuring and applied the method to the three-bladed-hub assembly of a wind turbine test bed. Giagopulos et. al. [71] applied hybrid (Experimental-

Numerical) method in the frequency and time domains and obtained and validated their study with some practical case studies. The concept of transmission simulator (TM) has been studied by various researchers for connecting the experimental and numerical models [72–74].

In this thesis, substructure decoupling method is used to decouple the cable dynamics from the assembled cable-beam system. The discussion of theory of substructure decoupling and the results obtained in this thesis are presented in Chapters 7-9.

Chapter 3

3 Analytical and Experimental Investigation of Cable–Beam System Dynamics

[a] Mohammad Hadi Jalali, [a] Geoff Rideout

[a] Faculty of Engineering and Applied Science, Memorial University, St. John’s, Canada

This chapter was published as a full paper in Journal of Vibration and Control, 2019, Vol. 25(19–20) 2678–2691. In this chapter, an analytical model for a cable-beam system considering cable sag and bending stiffness is developed and validated through experiments. The co-authorship statement for this chapter follows:

The declaration applies to the following article	
Title of Chapter	Chapter 3: Analytical and Experimental Investigation of Cable–Beam System Dynamics
Article status: Published	
The PhD student analyzed the literature, performed the experiments, collected the data, developed the codes and prepared the manuscript. The experimental setup was designed by the co-op student. The supervisor edited, helped organize the manuscript, and provided training and advice on the experimental apparatus.	

Abstract

Interactions between cables and structures affect the design and non-destructive testing of electricity transmission lines, guyed towers, and bridges. An analytical model for an electricity pole beam-cable system is presented, which can be extended to other applications. A cantilever beam is connected to two stranded cables. The cables are modeled as tensioned Euler-Bernoulli beams, considering the sag due to self-weight. The pole is also modeled as a cantilever Euler-Bernoulli beam and the equations of motion are derived using Hamilton’s Principle. The model was validated with a reduced-scale system in the laboratory and a set-up was designed to measure the bending stiffness of the stranded cable under tension. It is concluded that the bending stiffness and sag of the cable have a significant effect on the dynamics of beam-cable structures. By adding the cable to the pole structure, some hybrid modes emerge in the eigenvalue solution of the system. Modes with anti-symmetric cable motion are sag-independent and the modes with symmetric cable motion are dependent on the cable sag. The effect of sag on the natural frequencies is more significant when the bending stiffness of the cables is higher.

Keywords: Beam-Cable System Dynamics, Stranded Cable, Bending Stiffness, Modal Testing, Structural Dynamics

3.1 Introduction and Literature Review

There exist many application areas for which product design, analysis or inspection are enhanced by vibration modeling of cables and cable-beam structures. Predicting power line “galloping”, developing vibration-based non-destructive evaluation methods for poles and predicting bridge response to vehicle loading would all be facilitated by dynamic models and computer simulations of coupled cable-beam response. Models of cables in the literature are reviewed, followed by models of cable-beam systems.

Models of cables typically treat the cable as a string or a beam or as a series of beam-like segments. Models vary in their treatment of bending stiffness and cable sag due to self-weight. Barry et. al. [75] presented an analytical model for vibrations of a single transmission line conductor with an attached Stockbridge damper and investigated the effect of damper parameters on the vibration of conductor. Ricciardi and Saitta [51] and Kang t. al. [52] developed continuous models for vibration analysis of cables with sag considering the bending stiffness and observed the significance of sag and bending stiffness on linear and nonlinear vibration of cable-only system. Sousa et. al. [53] analyzed the effect of considering bending stiffness, shear stiffness and rotational inertia on the natural frequencies of the overhead transmission line conductors. They found the error from neglecting shear and rotational inertia to be very small compared to the error from neglecting the bending and geometric stiffness of the cable. Ni et. al. [76] formulated a three-node finite element for dynamic analysis of large diameter sagged cables, concluding that ignoring bending stiffness gives rise to unacceptable errors in predicting higher order natural frequencies. The literature review of vibration analysis of cables-only shows that considering the bending stiffness and sag of the cable has significant and non-negligible effect on vibration response and should be considered in modeling and simulation.

Gattulli et. al. [54] studied the linear and nonlinear dynamic behavior of cable-stayed beam structures. Bending stiffness of the cable was ignored in solving the equations of in-plane and out-of-plane motion of the coupled system. Linear analysis revealed the existence of global (beam dominated), local (cable dominated) and hybrid modes. Gattulli et. al. [77] presented an analytical model for dynamic investigation of a beam-cable-beam coupled system as a model for masonry walls connected with a stranded cable.

Parl et. al. [78] presented a Rayleigh-Ritz analytical model for obtaining the principal natural frequency of a wind turbine tower-cable coupled system composed of a turbine tower and four guy cables, modeling the cables as rods, without sag.. Nonlinear internal modal interactions of the local and global modes in the cable-beam structures were studied in [79–81]. The models developed in this paper are motivated by ongoing development of a non-destructive evaluation (NDE) method for utility poles. Extensive work has been done during the past few decades regarding the use of non-destructive testing (NDT) methods for utility poles such as ultrasound, x-ray, electrical conductivity and resistograph [5]. The authors are developing an NDT method based on vibration response and modal testing [7,8] that requires extraction of modal properties. Since conductors are attached to the poles, vibrations of the conductors affect the modal properties of the system. Removing the effect of the conductors to reveal pole properties requires a system model that captures the complex interactions between the cables and the pole.

Lie et. al. [55] presented a simplified 3D computational model of a transmission tower-line system due to seismic excitations. The transmission cables and their supporting towers were modeled as a lumped mass system. Pinto and Rideout [56] developed and validated a bond graph model for pole with a point mass lumped-segment cable attached to the free end. Jalali and Rideout [16] developed and validated a bond graph model for vibration analysis of conductors based on rigid body lumped segments. They obtained the bending stiffness of cables without tension, experimentally.

In this paper, a new parametric analytical model for a cable-beam system, representing a portion of an electricity transmission line, is presented. The cables are modeled as Euler-Bernoulli beams with bending stiffness, under tension and self-weight. The beam is also a cantilevered Euler-Bernoulli beam. The linearized equations of motion of in-plane transverse vibration of the coupled system were obtained and the Eigen problem was analytically solved. A wide parametric analysis has been carried out to investigate the effect of cable bending stiffness and sag on the modal properties of the system. Experimental bending tests were performed to accurately measure the bending stiffness of the conductor with different tensions, and experimental modal impact testing was carried out to validate the analytical model. The results of this paper show that the bending stiffness and sag of the cables has significant effect on the natural frequencies of the beam and should be considered in the dynamic analysis of cable-beam structures. Also, by mode shape analysis, the existence of coupled and global (beam dominated) modes is revealed.

3.2 Analytical Model

The model is composed of two horizontal suspended cables attached to the tip of a cantilever beam. The cables have a small sag d to length l_c ratio (namely ${d}/{l_c} < \frac{1}{8}$) based on Irvine's model [82] and the cable static configuration under self-weight can be described by the function:

$$y(x_c) = 4d\left(\frac{x_c}{l_c} - \left(\frac{x_c}{l_c}\right)^2\right) \tag{3.1}$$

Figure 3.1 shows the system model in the deformed static (self-weight) (C_I) and dynamic (C_V) configurations, following the notation in [51].

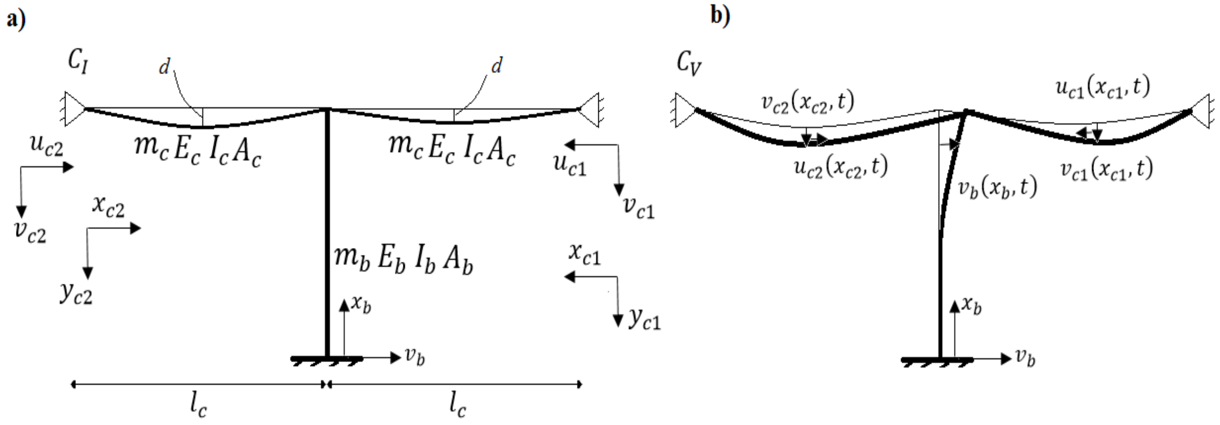

Figure 3.1: Analytical model of the structural cable-beam system a) static configuration b) dynamic deformed configuration

If u_{ci} $(u_{c1} = u_c, u_{c2} = v_c\ , u_{c3} = w_c)$ are the dynamic cable displacements with respect to the static deformed shape C_I and a Cartesian system ox_i $(i = 1,2,3)$ is used to describe the positions for the static shape ${x_i}^I$ and the dynamic shape ${x_i}^V$ of the suspended cables, the dynamic component of an arbitrary point on the cables can be expressed [51].

$${x_i}^V(s^I, t) = u_i(s^I, t) + {x_i}^I(s^I) \qquad i = 1,2,3 \tag{3.2}$$

From Eq. (3.2), the expressions of Lagrangian strain in the configurations of C_I and C_V can be expressed as:

$$\varepsilon^V = \frac{1}{2}\left(\frac{\partial {x_i}^V}{\partial s^0}\frac{\partial {x_i}^V}{\partial s^0} - 1\right) \tag{3.3}$$

$$\varepsilon^I = \frac{1}{2}\left(\frac{\partial x_i{}^I}{\partial s^0}\frac{\partial x_i{}^I}{\partial s^0} - 1\right) \tag{3.4}$$

where s^0 is the curvilinear abscissa in the natural configuration of the cables. By substituting Eq. (3.2) into Eq. (3.3) and considering Eq. (3.4) and after some manipulations, the following equation can be obtained [51]:

$$\varepsilon^V = \varepsilon^I + \varepsilon \left({ds^I}/{ds^0}\right)^2 \tag{3.5}$$

where

$$\varepsilon = \frac{\partial u_i}{\partial s^I}\,\frac{\partial x_i}{\partial s^I} + \frac{1}{2}\frac{\partial u_i}{\partial s^I}\frac{\partial u_i}{\partial s^I} \tag{3.6}$$

According to previous studies [51,52,83] , we assume $ds^V \approx ds^I \approx ds^0 \approx dx_c$ and thus, Eq. (3.6), the nonlinear strain contribution can be expressed in planar motion without index notation as:

$$\varepsilon = \frac{\partial u_c}{\partial x_c} + \frac{\partial v_c}{\partial x_c}\frac{\partial y_c}{\partial x_c} + \frac{1}{2}\left[\left(\frac{\partial u_c}{\partial x_c}\right)^2 + \left(\frac{\partial v_c}{\partial x_c}\right)^2\right] \tag{3.7}$$

By considering the above equation and neglecting *V* and *I* superscripts for brevity and considering every motion with respect to the static configuration, the potential energy of the two cables U_c and the beam U_b can be expressed as:

$$U_c = \int_0^{l_{c1}} \left[H\varepsilon_1 + \frac{1}{2}E_{c1}A_{c1}\varepsilon_1{}^2\right] dx_{c1} + \int_0^{l_{c2}} \left[H\varepsilon_2 + \frac{1}{2}E_{c2}A_{c2}\varepsilon_2{}^2\right] dx_{c2} +$$

$$\frac{1}{2}\int_0^{l_{c1}} E_{c1}\, I_{c1} \left(\frac{\partial^2 v_{c1}}{\partial x^2{}_{c1}}\right)^2 dx_{c1} + \frac{1}{2}\int_0^{l_{c2}} E_{c2}\, I_{c2} \left(\frac{\partial^2 v_{c2}}{\partial x^2{}_{c2}}\right)^2 dx_{c2} \tag{3.8}$$

$$U_b = \frac{1}{2}\int_0^{l_b} E_b\, I_b \left(\frac{\partial^2 v_b}{\partial x^2{}_b}\right)^2 dx_b$$

where H is the horizontal component of cable tension, and $E_{c1}A_{c1}$ and $E_{c2}A_{c2}$ are the axial stiffnesses of the cables 1 and 2, respectively. $E_{c1}I_{c1}$, $E_{c2}I_{c2}$ and E_bI_b are bending stiffnesses of cables 1 and 2 and the beam, respectively. Span lengths of the cables are l_{c1} and l_{c2}, while v_{c1}, v_{c2} and v_b are the bending displacements of the cables 1 and 2 and the beam, respectively. The potential energy of the cable consists of three terms: the work done by initial tension force (*H*), the work done by dynamic axial forces and the work done by bending moments . The nonlinear strain contribution expressions of the cables 1 and 2 are:

$$\varepsilon_1 = \frac{\partial u_{c1}}{\partial x_{c1}} + \frac{\partial v_{c1}}{\partial x_{c1}}\frac{\partial y_c}{\partial x_{c1}} + \frac{1}{2}\left[\left(\frac{\partial u_{c1}}{\partial x_{c1}}\right)^2 + \left(\frac{\partial v_{c1}}{\partial x_{c1}}\right)^2\right] \tag{3.9}$$

$$\varepsilon_2 = \frac{\partial u_{c2}}{\partial x_{c2}} + \frac{\partial v_{c2}}{\partial x_{c2}}\frac{\partial y_c}{\partial x_{c2}} + \frac{1}{2}\left[\left(\frac{\partial u_{c2}}{\partial x_{c2}}\right)^2 + \left(\frac{\partial v_{c2}}{\partial x_{c2}}\right)^2\right] \tag{3.10}$$

The kinetic energy of the cables T_c and beam T_b and the work done by the dead loads W_c are:

$$T_c = \frac{1}{2}\int_0^{l_{c1}} m_c \left(\frac{\partial v_{c1}}{\partial t}\right)^2 dx_{c1} + \frac{1}{2}\int_0^{l_{c2}} m_c \left(\frac{\partial v_{c2}}{\partial t}\right)^2 dx_{c2} \tag{3.11}$$

$$T_b = \frac{1}{2}\int_0^{l_b} m_b \left(\frac{\partial v_b}{\partial t}\right)^2 dx_b \tag{3.12}$$

$$W_c = \int_0^{l_{c1}} m_c g\, v_{c1} dx_{c1} + \int_0^{l_{c2}} m_c g\, v_{c2} dx_{c2} \tag{3.13}$$

where m_c and m_b are the mass per unit length of the cable and beam, respectively. By considering the same material properties and span length for the two cables and deriving the energies for the whole coupled system, ($U = U_c + U_b, T = T_c + T_b, W = W_c$) and using Hamilton's Principle, the in-plane linear equations of motion of the coupled system can be obtained, after linearization. The longitudinal inertial forces are normally neglected [83] and the dynamic elongation of the cables can be obtained independent of spatial coordinates:

$$\tilde{e}_1 = \frac{u_{c1}(l_c,t) - u_{c1}(0,t)}{l_c} + \frac{1}{l_c}\int_0^{l_c} y'_c v'_{c1} d_{xc1} \tag{3.14}$$

$$\tilde{e}_2 = \frac{u_{c2}(l_c,t) - u_{c2}(0,t)}{l_c} + \frac{1}{l_c}\int_0^{l_c} y'_c v'_{c2} d_{xc2} \tag{3.15}$$

Therefore, the in-plane transverse equations of motion of the coupled cable-beam system can be written as:

$$m_c\ddot{v}_{c1} - H{v''}_{c1} - E_cA_c{y''}_c\tilde{e}_1 + E_cI_c{v''''}_{c1} = 0 \tag{3.16}$$

$$m_c\ddot{v}_{c2} - H{v''}_{c2} - E_cA_c{y''}_c\tilde{e}_2 + E_cI_c{v''''}_{c2} = 0 \tag{3.17}$$

$$m_b\ddot{v}_b + EI_b{v''''}_b = 0 \tag{3.18}$$

where $\tilde{e}_1$ and $\tilde{e}_2$ are presented in Eq. (3.14)-(3.15). The PDE Eq'ns. (3.16)-(3.18) are completed by the boundary conditions. The cable is considered as pinned-pinned and the beam is considered as clamped in one end and free in the other end but affected by the axial force caused by the cable ends in the shear direction of the beam. The connection point of the cables and beam is also considered as a pin support, thus there is no moment transfer from the cables to the beam in the beam tip end. The deflection angle and curvature of the two cables are equal to each other in the connection point because only one continuous cable is actually used.

The following equations present the boundary conditions of the coupled system.

$$v_{c1}(0,t) = 0, v_{c2}(0,t) = 0,\ \ {v''}_{c1}(0,t) = 0,\ {v''}_{c2}(0,t) = 0,\ v_{c1}(l_c,t) = 0,\ v_{c2}(l_c,t) = 0 \tag{3.19}$$

$${v'}_{c1}(l_c,t) = {v'}_{c2}(l_c,t),\ {v''}_{c1}(l_c,t) = {v''}_{c2}(l_c,t)$$

$$v_b(0,t) = 0, {v'}_b(0,t) = 0,\ EI_b{v''}_b(l_b,t) = 0,\ E_bI_b{v'''}_b(l_b,t) = E_cA_c(\tilde{e}_1 - \tilde{e}_2) \tag{3.20}$$

A non-dimensional form of the problem can be obtained by introducing the following parameters.

$$\eta = \Omega_1 t\ \ , \bar{x}_{c1} = \frac{x_{c1}}{l_c}, \bar{x}_{c2} = \frac{x_{c2}}{l_c}, \bar{x}_b = \frac{x_b}{l_b}, \bar{v}_b = \frac{v_b}{l_c}, \bar{v}_{c1} = \frac{v_{c1}}{l_c}, \bar{v}_{c2} = \frac{v_{c2}}{l_c}, \omega = \frac{\Omega}{\Omega_1} \tag{3.21}$$

$$\alpha = \frac{l_b}{l_c}, \rho = \frac{m_c}{m_b}, \chi = \frac{E_bI_b}{{l_b}^2E_cA_c}, \nu = \frac{d}{l_c}, \mu = \frac{E_cA_c}{H}, \lambda^2 = 64\mu\nu^2, \bar{y}_c = \frac{y_c}{d}, \tau = \frac{E_cI_c}{{l_c}^2H} \tag{3.22}$$

where Ω_1 is the first dimensional natural frequency of the system, ω is the dimensionless natural frequency of the system, α describes the system aspect ratio, ρ stands for the beam-to-cable mass ratio, χ is the beam-to-cable (flexural-to-axial) stiffness ratio and λ^2 is the well-known Irvine parameter. Finally τ is the non-dimensional bending stiffness for the cables. By applying the non-dimensionalization process and omitting the bar for brevity, the following dimensionless equations of motion result:

$$\beta_c{}^2\ddot{v}_{c1} - \omega^2 v''{}_{c1} + 8\nu\mu\omega^2 e_1 + \tau\omega^2 v^{(4)}{}_{c1} = 0 \tag{3.23a}$$

$$\beta_c{}^2\ddot{v}_{c2} - \omega^2 v''{}_{c2} + 8\nu\mu\omega^2 e_2 + \tau\omega^2 v^{(4)}{}_{c2} = 0 \tag{3.23b}$$

$$\beta_b{}^4\ddot{v}_b + \omega^2 v^{(4)}{}_b = 0 \tag{3.23c}$$

Non-dimensional spatial frequencies have been introduced:

$$\beta_c{}^2 = \omega^2 \frac{m_c l_c{}^2}{H} \Omega_1{}^2, \beta_b{}^4 = \omega^2 \frac{m_b l_b{}^4}{E_b I_b} \Omega_1{}^2 \tag{3.24}$$

These frequencies cannot be independent of each other, since they are required to depend on the same frequency ω, with the following equation:

$$\beta_c = \frac{\beta_b{}^2}{\alpha}\sqrt{\mu\rho\chi} \tag{3.25}$$

The equations of motions (3.23a) are accompanied by dimensionless boundary conditions:

$$v_{c1}(0,t) = 0, v_{c2}(0,t) = 0,\ v''{}_{c1}(0,t) = 0,\ v''{}_{c2}(0,t) = 0, v_{c1}(1,t) = 0, v_{c2}(1,t) = 0 \tag{3.26}$$

$$v'{}_{c1}(1,t) = v'{}_{c2}(1,t),\ v''{}_{c1}(1,t) = v''{}_{c2}(1,t)$$

$$v_b(0,t) = 0,\ \ v'{}_b(0,t) = 0,\ \ \ v''{}_b(1,t) = 0,\ \chi v'''{}_b(1,t) = e_1 - e_2 \tag{3.27}$$

where dynamic elongations e_1 and e_2 are expressed as:

$$e_1(\eta) = v_{c1}(1,\eta) + 8\upsilon \int_0^1 v_{c1} dx_{c1} \tag{3.28a}$$

$$e_2(\eta) = v_{c2}(1,\eta) + 8\upsilon \int_0^1 v_{c2} dx_{c2} \tag{3.28b}$$

where the integration by parts has been used, together with the static profile function Eq. (3.1).

Employing the separation of variables method, $\left(v_{cj} = \phi_{cj}\left(x_{cj}\right)e^{i\omega\eta}\ (j = 1{,}2), v_b = \phi_b(x_b)e^{i\omega\eta}\right)$, in Eq'ns (3.23a)-(3.27) :

$$\beta_c{}^2\phi_{c1} + \phi''{}_{c1} - 8\nu\mu e_1 - \tau\phi^{(4)}{}_{c1} = 0 \tag{3.29a}$$

$$\beta_c{}^2\phi_{c2} + \phi''{}_{c2} - 8\nu\mu e_2 - \tau\phi^{(4)}{}_{c2} = 0 \tag{3.29b}$$

$$\phi^{(4)}{}_b - \beta_b{}^4\phi_b = 0 \tag{3.29c}$$

where

$$e_1 = \phi_{c1}(1) + 8\upsilon\int_0^1 \phi_{c1}dx_{c1} \tag{3.30a}$$

$$e_2 = \phi_{c2}(1) + 8\upsilon\int_0^1 \phi_{c2}dx_{c2} \tag{3.30b}$$

where the dimensionless natural frequencies of the system should be obtained by imposing the boundary conditions. It should be mentioned that one of the β_c or β_b can be considered as the principal unknown (no matter which one) and the other one can be obtained by Eq. (3.25):

$$\begin{aligned} &\phi_{c1}(0) = 0, \phi_{c2}(0) = 0,\ \phi''{}_{c1}(0) = 0, \phi''{}_{c2}(0) = 0,\ \phi_{c1}(1) = 0,\ \phi_{c2}(1) = 0 \\ &\phi'{}_{c1}(1) = -\phi'{}_{c2}(1),\ \phi''{}_{c1}(1) = \phi'{}'{}_{c2}(1) \end{aligned} \tag{3.31}$$

$$\phi_b(0) = 0,\ \phi'{}_b(0) = 0\ ,\ \phi''{}_b(1) = 0,\ \chi\phi'''{}_b(1) = e_1 - e_2 \tag{3.32}$$

The solutions of Eq. (3.29a) are:

$$\phi_{c1}(x_{c1}) = A_1cos(px_{c1}) + A_2sin(px_{c1}) + A_3cosh(qx_{c1}) + A_4sinh(qx_{c1}) + \frac{8\mu ve_1}{\beta_c{}^2} \tag{3.33a}$$

$$\phi_{c2}(x_{c2}) = A_5cos(px_{c2}) + A_6sin(px_{c2}) + A_7cosh(qx_{c2}) + A_8sinh(qx_{c2}) + \frac{8\mu ve_2}{\beta_c{}^2} \tag{3.33b}$$

$$\phi_b(x_b) = A_9sin(\beta_bx_b) + A_{10}cos(\beta_bx_b) + A_{11}sinh(\beta_bx_b) + A_{12}cosh(\beta_bx_b) \tag{3.33c}$$

where p and q are given in Appendix A. Substituting Eq. (3.33a) into Eq'ns. (3.31)-(3.32) and considering Eq. (3.30a) yields the following matrix equation:

$$\boldsymbol{F}(\beta_b)\boldsymbol{\Phi} = \boldsymbol{0} \tag{3.34}$$

where $\boldsymbol{\Phi} = \begin{Bmatrix} \boldsymbol{\phi_{c1}} \\ \hline \boldsymbol{\phi_{c2}} \\ \hline \boldsymbol{\varphi_b} \end{Bmatrix}$ is the mode shape vector for the coupled system and the entries of the matrix $\boldsymbol{F}(\beta_b)\ \epsilon R^{12\times 12}$ are given in Appendix A. In order to have a non-trivial solution, the determinant of matrix $\boldsymbol{F}(\beta_b)$ should be equal to zero. The equation developed from equating the determinant of $\boldsymbol{F}(\beta_b)$ to zero is solved using Newton-Raphson method and the corresponding dimensioned natural frequencies of the coupled system are obtained using Eq. (3.24) after calculating the values of β_b from the characteristic equation. In order to obtain an FRF of the system analytically, the equation of motion of the beam under concentrated harmonic forced vibration is used:

$$m_b\ddot{v}_b + EI_b v''''_b = F\delta(x - x_f)sin(\omega_{ex}t) \tag{3.35}$$

where ω_{ex} is the excitation frequency, F is the magnitude of the force, and $\delta(x - x_f)$ is the Dirac delta function. By using expansion theorem [84], vibration response of the above equation, $v_b(x,t) = \sum_{n=1}^{\infty}\phi_{bn}(x_b)q_n(t)$ is considered. By substitution of the response into Eq. (3.35) and using the orthogonality condition [85], the displacement and acceleration time-history responses for forced vibration can be obtained.

$$v_b(x,t) = \sum_{n=1}^{\infty}\frac{\phi_{bn}(x_b)\phi_{bn}(x_f)F}{\Omega^2-\omega_{ex}{}^2}sin(\omega_{ex}t) \tag{3.36}$$

Where Ω is dimensioned natural frequency of the beam. Therefore, the displacement frequency function can be obtained:

$$H(\omega) = \sum_{n=1}^{\infty}\frac{\phi_{bn}(x_b)\phi_{bn}(x_f)}{\Omega^2-\omega_{ex}{}^2} \tag{3.37}$$

3.3 Experimental Investigations

3.3.1 Experimental Modal Testing

In order to verify the analytical model, experimental tests were carried out. Figure 3.2 presents the schematic of the modal tests. Two rigid frames were secured to the floor on the right and left sides. The natural frequencies of the frames were verified to be far away from the natural frequencies of the system. The right end of the cable was attached to a threaded rod to adjust the tension of the cable and an in-line load cell at the left end of the cable measured the longitudinal tension of the cable.

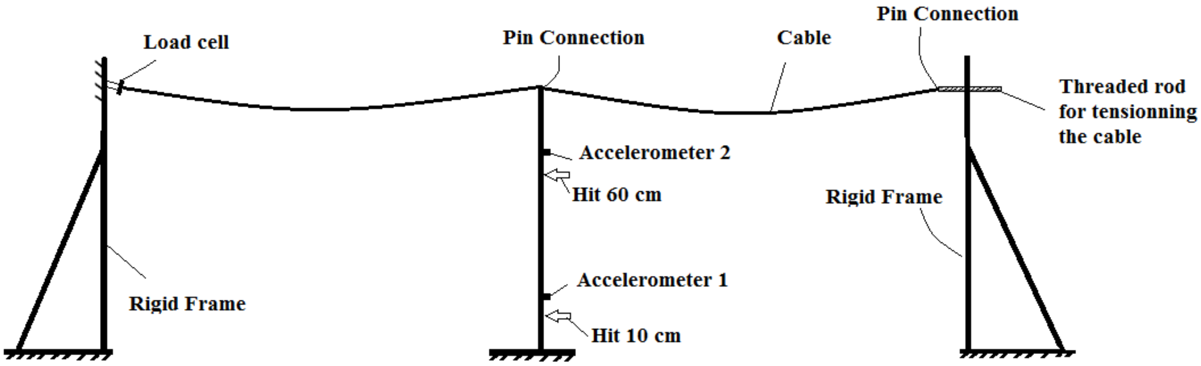

Figure 3.2. Schematic of experimental vibration testing of cable-beam system

Figure 3.3 shows the setup used for impact modal testing and the material properties are presented in Table 3.1. The cable (7*19 stranded cable) was supported with a pin connection at both ends and at the connection point with the beam. Two U-bolts were used in the connection point of the beam and cable to simulate the pin connection. The length of the cantilever beam was 75 cm. Two accelerometers positioned 0.1m and 0.65 m from the clamped end were used and hammer impacts were made 0.1 m and 0.6 m (Figure 3.2) to ensure the first several modes were excited. The experiments were performed with five different tensions 10 N, 25 N, 100 N, 200 N and 300 N in the cable. The amount of sag of the cable changes depending on the tension in the cable.

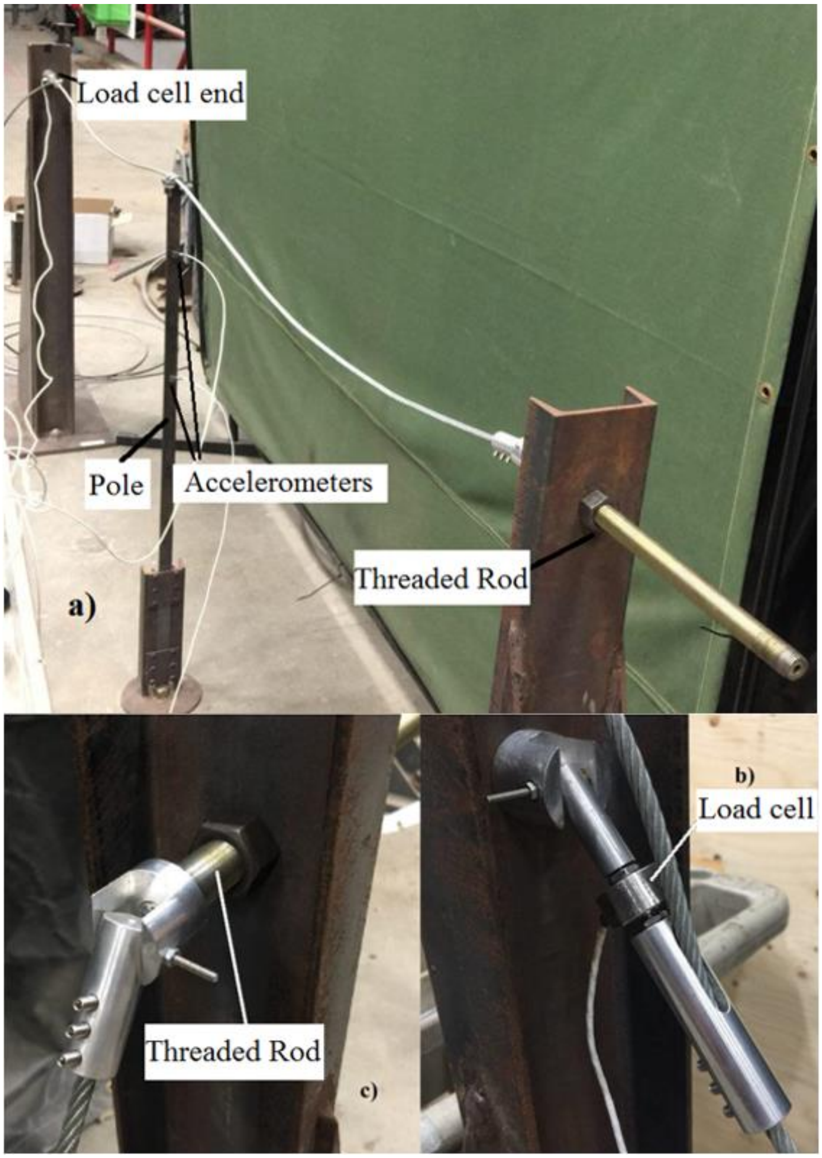

Figure 3.3: Experimental setup for modal testing of the beam-cable system a) The beam-cable system b) The load cell end of the cable and pin support c) Threaded rod and pin support

Table 3.1. Material properties of the cable and beam in experimental analysis

Cable properties	$E_c(GPa)$	$A_c(mm^2)$	$m_c\left({kg}/{m}\right)$	$l_c(m)$
	190	31.66	0.166	1.21
Beam properties	$E_b(GPa)$	$A_b(mm^2)$	$m_b\left({kg}/{m}\right)$	$l_b(m)$
	190	46.67	0.367	0.75

3.3.2 Bending Stiffness Tests

Figure 3.4 shows the test apparatus for measuring the bending stiffness of the cable. A hydraulic cylinder is secured to the frame at the top of the setup to apply the load at the middle of the cable, and an LDVT is attached to the cylinder to measure the deflection of the cable at midspan at the same time. The inline load cell was used to measure cable tension, which was adjusted with a threaded rod. An S-type load cell was also attached to the cylinder to measure the applied load. The cable was secured with clamped-clamped end conditions and the theoretical procedure used to measure the bending stiffness follows [86]. The bending stiffness of the stranded cables increased with tension in previous studies [86,87] and the results obtained in the present study confirm this trend. The bending tests were performed at the same five tensions as in the modal testing.

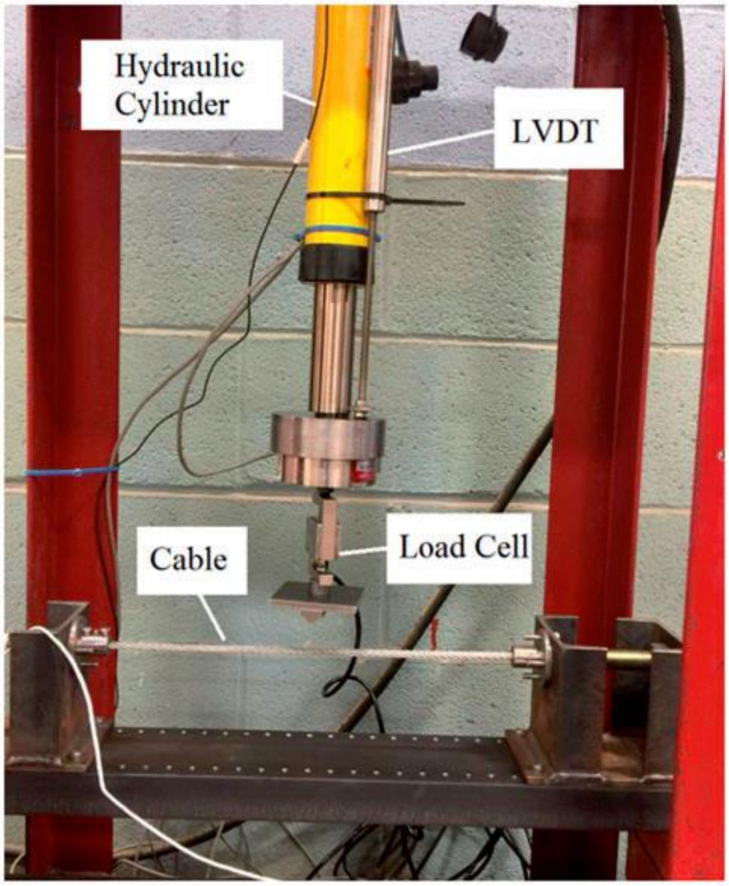

Figure 3.4: Experimental set up for bending stiffness measurement

The bending stiffness of stranded cables is bounded by two extreme flexural stiffness's EI_{max} and EI_{min}. The maximum bending stiffness EI_{max} corresponds to a solid cross section with no slippage of the strands and wires on top of each other and the minimum bending stiffness EI_{min} corresponds to all the stands of the cable slipping past each other as static friction between the strands is overcome [50,87].

The bending stiffness values that are measured in the present study are in this range for all the tensions and they are all close the minimum bending stiffness limit. The measured bending stiffness values are presented in Table 3.2 and the theoretical limits of bending stiffness are $EI_{min} = 0.0306$ and $EI_{max} = 15.5632$, respectively. The most thorough treatment of bending stiffness of stranded cables considers the change of the bending stiffness with curvature, but that is not considered in this work. The amplitude of the deflection is low in the bending tests, meaning the bending stiffness behavior is linear and independent of the deflection amplitude.

Table 3.2. Bending stiffness of the conductor measured in bending tests

Tension (N)	10	25	100	200	300
EI (Nm^2)	0.2190	0.2549	0.4948	0.5972	0.8283

3.4 Verification

The natural frequencies of the beam with and without cables are obtained using the analytical model and by performing the experimental modal testing. There is a tip mass welded to the free end of the beam to hold the U-bolts, and this mass (17g) affects the natural frequencies of the beam. Table 3.3 compares the theoretical natural frequencies of the beam with the experimental results. The tip mass is not considered in the analytical model, introducing a small error, but it is less significant when the cables are connected. Table 3.4 presents a comparison of natural frequencies of the beam with connected cables having different tensions. As can be seen from this table, the analytical model gives accurate results compared to experiments and the discrepancies could be attributed to the difficulty in replicating the boundary conditions during the experiments and that the tip mass is not considered in the analytical model. Another source of error in the result is due to lack of damping in the analytical model.

Table 3.3. Natural frequencies comparison of beam without cable

Mode	Experimental [Hz]	Theoretical with tip mass [Hz]	Error (%)
1	2.24	2.36	5.35
2	14.7	15.23	3.60
3	41.57	43.45	4.53
4	84.22	86.38	2.56
5	138.2	144.32	4.43
6	215.22	217.39	1.01

Table 3.4. Natural frequency comparison: beam-cable system

Mode Number		**1**	**2**	**3**	**4**	**5**	**6**	**7**	**8**
10 N	**Test [Hz]**	2.652	3.935	4.977	6.651	8.801	12.144	14.944	16.586
	Analytical [Hz]	2.688	3.706	4.179	7.951	8.957	14.531	16.182	16.846
	Error (%)	1.360	5.819	16.025	19.547	1.777	19.658	8.281	1.567
25 N	**Test [Hz]**	2.619	5.299	6.730	11.660	12.958	14.897	19.105	22.201
	Analytical [Hz]	2.688	5.361	5.828	11.292	12.284	16.846	19.092	20.700
	Error (%)	2.637	1.173	13.408	3.155	5.198	13.083	0.066	6.762
100 N	**Test [Hz]**	-	8.610	12.670	16.890	21.850	24.320	-	-
	Analytical [Hz]	2.688	10.287	10.904	16.846	21.336	22.628	-	-

	Error (%)	-	19.473	13.942	0.261	2.351	6.956	-	-
200 N	**Test [Hz]**	-	13.490	14.537	16.069	26.111	32.404	39.604	-
	Analytical [Hz]	2.688	14.398	15.063	16.846	29.487	30.857	46.190	-
	Error (%)	-	6.728	3.616	4.835	12.929	4.775	16.629	-
300 N	**Test [Hz]**	-	14.043	15.263	18.524	36.715	40.654	44.576	50.129
	Analytical [Hz]	2.688	16.846	17.596	18.375	36.017	37.622	47.171	56.241
	Error (%)	-	19.959	15.282	0.805	1.901	7.457	5.821	12.192

3.5 Results and Discussion

3.5.1 Effect of Cables on the Frequency Response of Beam

The experimental and numerical analyses reveal that connecting cables to the beam introduces modes different from the modes of the beam without cables. When the cables are less tensioned and as a result have more sag, the number of hybrid modes between the consequent global modes increases. This can be observed in Table 3.4, the natural frequencies of 2.688 Hz and 16.846 Hz are the first and second global natural frequencies, and it can be seen that with less tension (more sag), more natural frequencies exist between these two beam-dominated modes. Figure 3.5 shows the experimental and analytical FRF of the system (Eq. (3.37)) with and without cables at tensions of 200 and 300 N. As can be seen, some new modes are added to the modes of the beam when the cable is connected, and this effect is more visible in the analytical results because of the difficulties in obtaining the hybrid modes in experimental testing.

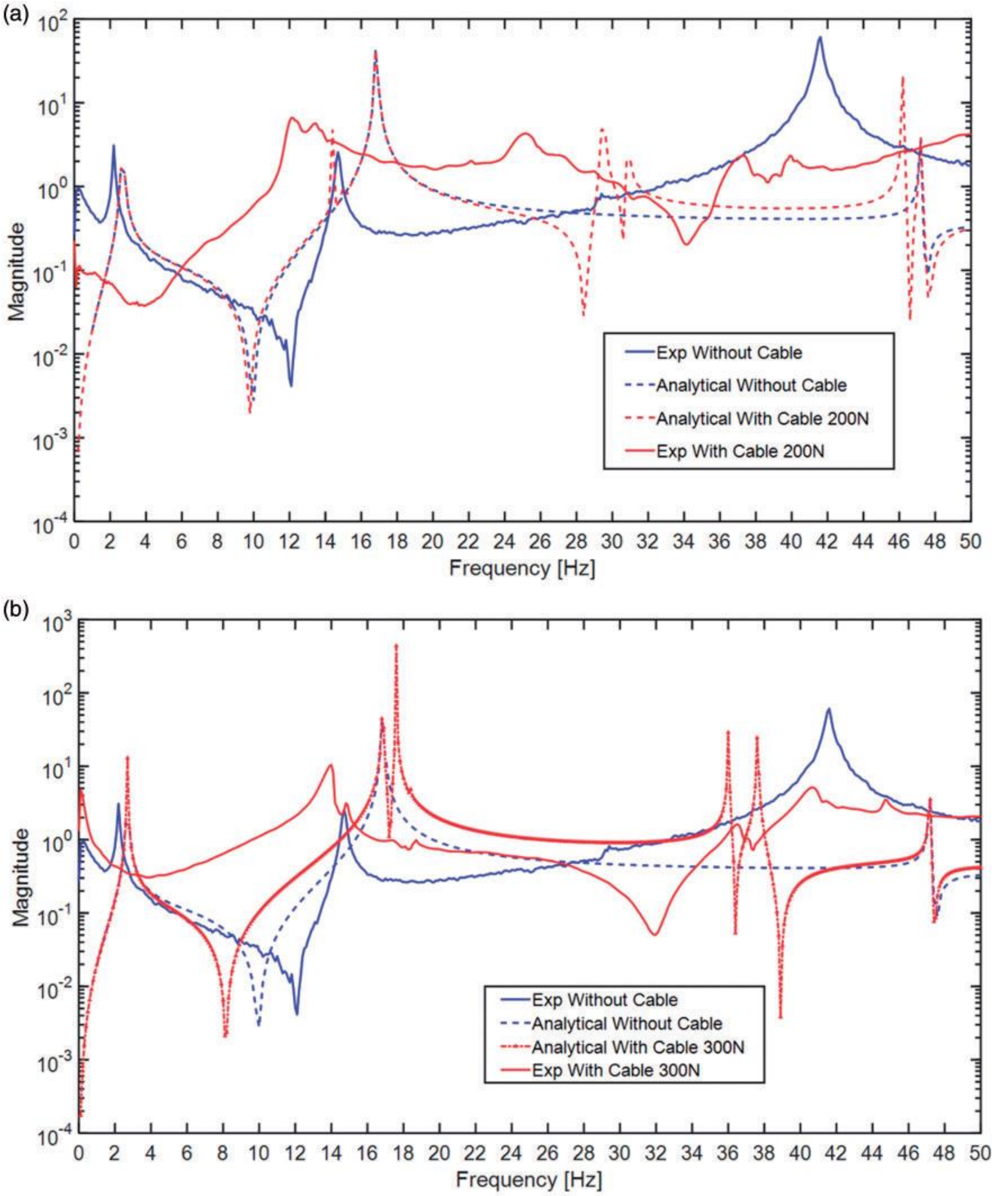

Figure 3.5: Experimental and analytical FRF of the beam without and with cable with a) 200 N tension b) 300 N tension

Due to lack of damping in the analytical model, the amplitude of frequency response functions is difficult to compare, but analytical and experimental FRF's show the same change when cable is connected.

3.5.2 Parametric Studies

The effect of different parameters values on the modal properties of the coupled system is investigated in this section. The presence or absence of cable sag produces a substantial difference in the dynamics of the system. In the case of non-zero sag, the beam oscillation is never completely uncoupled from the cable transverse vibration [77]. Generally, there are global (beam dominated modes), local (cable dominated modes) and hybrid modes (both beam and cables dynamically involved) in the parameter space. In the global modes, the cantilever beam behaves as if it is tip-connected by an elastic linear spring with equivalent non-dimensional stiffness $^{\alpha}/_{\chi}$ [77]. Pure cable modes never occur when the cable has non-zero sag [54]. It should be mentioned that in some parameter ranges, not all types of modes might be seen. Therefore, the global modes are independent of beam-cable stiffness ratio and only the motion of beam actually can be seen in the mode shape. In Figure 3.6, the six first mode shapes of the coupled system are depicted.

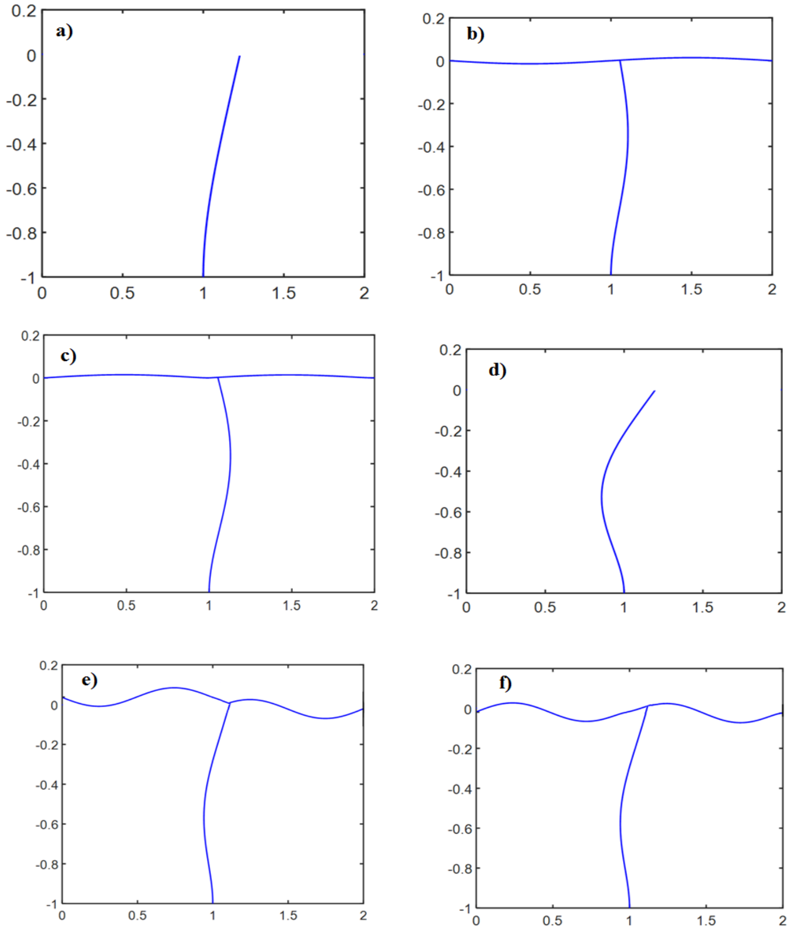

Figure 3.6: Modes of the system a) First Mode (1G): global b) 2nd Mode (1H): Hybrid c) 3rd Mode (2H): Hybrid d) 4th Mode (2G): Global e) 5th Mode (3H): Hybrid f) 6th Mode (4H): Hybrid

As can be seen from the figure, the first mode of the system (Figure 3.6-a) is the first global mode (1G) and the fourth mode (Figure 3.6-d) is the second global mode (2G) and only the beam has transverse vibration. The second and third modes (Figure 3.6 b-c) are the first (1H) and second (2H) hybrid modes and the fifth and sixth modes of the system (Figure 3.6 e-f) are the third (3H) and fourth (4H) hybrid modes. The elongations of the two cables are equal, with the same extension and compression magnitudes. The natural frequencies of these two pairs of modes are close to each other. In each pair, the cables have either opposite motion or the same motion on both sides of the pole. For example, Figure 3.6-b and e are the mode shapes in which cables motions are opposite on both sides. The second and third modes of the system contain the first symmetrically-shaped mode of the cables and the fifth and sixth modes contain the first antisymmetrically-shaped mode of the cables. According to previous studies [51,52] and the results in the present study, the anti-symmetric cable modes (even modes) are sag independent but the symmetric cable modes (odd modes) are influenced by the amount of sag of the cable.

Figure 3.7 shows the dimensionless natural frequency of a system with technically relevant parameters versus ratio of beam bending to cable axial stiffness. As can be seen, the global modes of the system (1G and 2G) are not affected by beam-cable stiffness ratio and the two pairs of coupled natural frequencies are decreased by the increase in stiffness ratio.

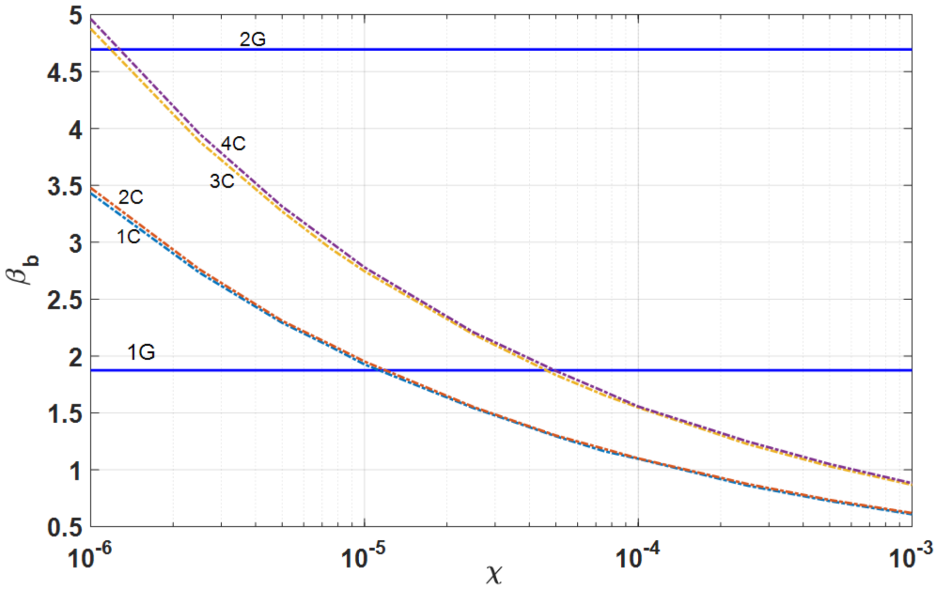

Figure 3.7: Eigen solution versus varying χ parameter

$\nu = 0.0024, \mu = 61754, \tau = 0.0014, \rho = 0.4538, \alpha = 0.6152$

The effect of sag on the natural frequencies of the coupled system can be seen in Figure 3.8 in which β_b is shown versus sag (ν) and bending stiffness (τ) dimensionless parameters. It is observed that the sag does not affect the modes of the coupled system with anti-symmetrically shape cable modes (Figure 3.6 e-f) but influences the natural frequencies of the modes with symmetrically shape cable modes (Figure 3.6 b-c).

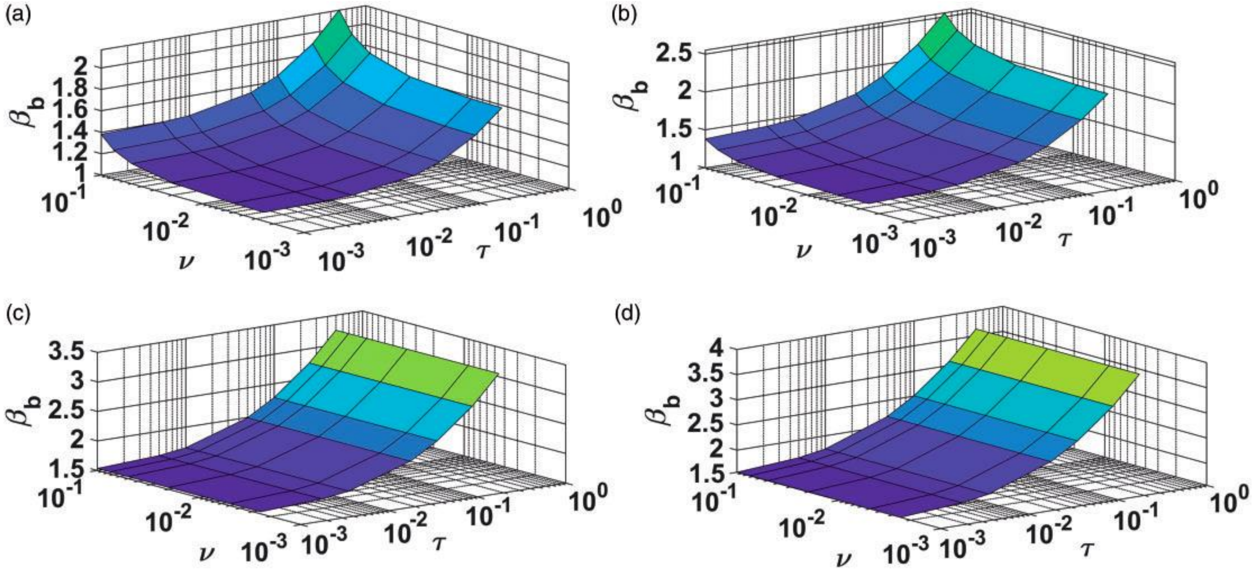

Figure 3.8: Non-dimensional coupled frequencies of the system versus sag and bending stiffness dimensionless parameter a) Mode 1H b) Mode 2H c) Mode 3H d) Mode 4H ($\mu = 61754, \rho = 0.4538, \alpha = 0.6152$)

In addition, the effect of sag on the natural frequencies are more significant when the bending stiffness of the cables has higher values. Finally, Figure 3.9 shows sections of plots of Figure 3.8 at selected values of τ. The hybrid modes with anti-symmetrically shape cable modes (3rd and 4th system modes) are not affected by sag but the hybrid modes with symmetrically shape cable modes are increased by the increase in sag with different values of bending stiffness parameters.

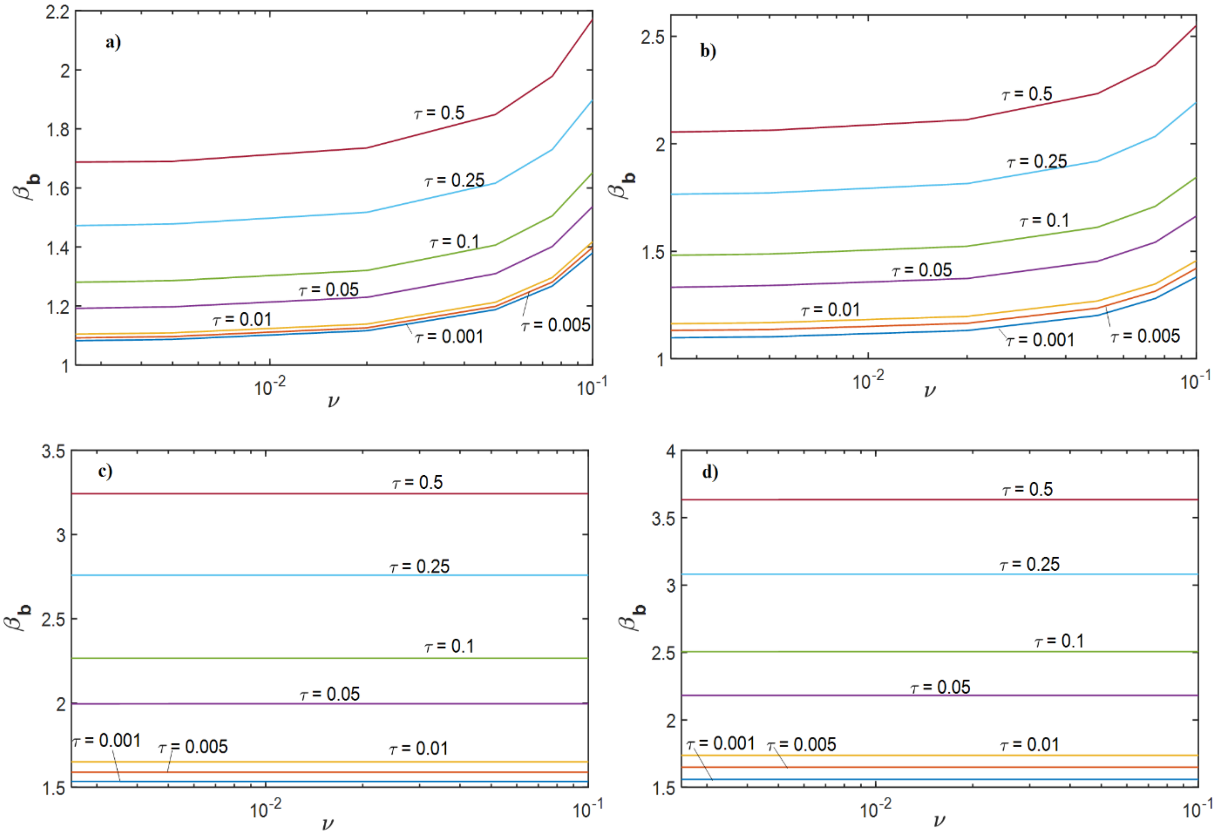

Figure 3.9: Dimensionless natural frequency versus sag with different bending stiffness parameters

$\tau = 0.001, 0.005, 0.01, 0.05, 0.1, 0.25, 0.5$ $(\mu = 61754, \chi = 1e-4, \rho = 0.4538, \alpha = 0.6152)$

a) Mode 1H b) Mode 2H c) Mode 3H d) Mode 4H

3.6 Conclusions

A novel analytical model was presented for the investigation of dynamics of a beam-cable system composed of a cantilever beam with two attached horizontal sagged cables. The linearized Eigen value problem describing the undamped free planar vibration of the system was solved analytically. The cables were considered as tensioned Euler-Bernoulli beams with bending stiffness and sag, and the cantilever beam was also modeled as an Euler-Bernoulli beam. Bending tests were performed to measure the bending stiffness of the conductor with different tensions, and the analytical model was validated with experimental modal testing. It is concluded that bending stiffness and sag of the cables have significant effect on the vibration of the beam in beam-cable structures and they should be considered in the vibration analysis of cable structures. It is concluded that by increasing the dimensionless bending stiffness of the cable, the natural frequencies of the system increase and this effect is more significant with more sag in the cable. The natural modes of the system that contain (anti) -symmetric cable modes are (in)dependent (of)on the amount of sag.

Declaration of Conflicting Interests

The Authors declare that there is no conflict of interest.

Appendix A

In Eq. (3.33a), p and q are:

$$p = \sqrt{\frac{\sqrt{4\tau{\beta_c}^2+1}-1}{2\tau}},\ q = \sqrt{\frac{\sqrt{4\tau{\beta_c}^2+1}+1}{2\tau}} \tag{A1}$$

And matrix F is a 12×12 matrix:

$$F = \begin{bmatrix} F_{cc} & F_{cb} \\ F_{bc} & F_{bb} \end{bmatrix}$$

$$F_{cc} = \begin{bmatrix} 1+fF_{1p} & fF_{2p} & 1+fF_{3q} & fF_{4q} & 0 & 0 & 0 & 0 \\ 0 & 0 & 0 & 0 & 1+fF_{1p} & fF_{2p} & 1+fF_{3q} & fF_{4q} \\ -p^2 & 0 & q^2 & 0 & 0 & 0 & 0 & 0 \\ 0 & 0 & 0 & 0 & -p^2 & 0 & q^2 & 0 \\ csp+fF_{1p} & sp+fF_{2p} & chq+fF_{3q} & shq+fF_{4q} & 0 & 0 & 0 & 0 \\ 0 & 0 & 0 & 0 & csp+fF_{1p} & sp+fF_{2p} & chq+fF_{3q} & shq+fF_{4q} \\ -psp & pcsp & qshq & qchq & -psp & pcsp & qshq & qchq \\ -p^2cp & -p^2sp & q^2chq & q^2shq & p^2cp & p^2sp & -q^2chq & -q^2shq \end{bmatrix} \tag{A2}$$

$$F_{cb} = \left[0_{8\times4}\right]$$

$$F_{bc} = \begin{bmatrix} \multicolumn{8}{c}{0_{3\times8}} \\ hF_{1p} & hF_{2p} & hF_{3q} & hF_{4q} & -hF_{1p} & -hF_{2p} & -hF_{3q} & -hF_{4q} \end{bmatrix}$$

$$F_{cc} = \begin{bmatrix} 0 & 1 & 0 & 1 \\ 1 & 0 & 1 & 0 \\ -{\beta_b}^2 \sin\beta_b & -{\beta_b}^2 \cos\beta_b & {\beta_b}^2 \sinh\beta_b & {\beta_b}^2 \cosh\beta_b \\ \chi{\beta_b}^3 \cos\beta_b & -\chi{\beta_b}^3 \sin\beta_b & -\chi{\beta_b}^3 \cosh\beta_b & -\chi{\beta_b}^3 \sinh\beta_b \end{bmatrix}$$

where

$$f = \frac{8\mu\nu}{{\beta_c}^2 - \lambda^2}\ , h = \frac{{\beta_c}^2}{{\beta_c}^2 - \lambda^2}\ ,$$

$$F_{1p} = cp + \frac{8\nu sp}{p}, F_{2p} = sp + 8\nu\frac{1 - cp}{p}, F_{3q} = chq + 8\nu\frac{shq}{q}, F_{4q} = shq + 8\nu\frac{chq - 1}{q} \tag{A3}$$

$$sp = \sin(p)\,, cp = \cos(p)\,, shq = \sinh(q)\,, chq = \cosh(q).$$

Chapter 4

4 Development and Validation of a Numerical Model for Vibration of a Power Lines

[a] Mohammad Hadi Jalali, [a] Geoff Rideout

[a] Faculty of Engineering and Applied Science, Memorial University, St. John's, Canada

This chapter was presented in Canadian Society of Mechanical engineers CSME2018. In this chapter, a lumped segment model for vibration of power lines is developed using bond graph formalism. The cable is modeled as number of lumped segments jointed with axial and torsional springs and dampers and the numerical results are validated with the experiments. The co-authorship statement for this chapter follows:

The declaration applies to the following article	
Title of Chapter	Chapter 4: Development and Validation of a Numerical Model for Vibration of a Power Lines
Article status: Published	
The PhD student analyzed the literature, performed the experiments, collected the data, developed the codes and prepared the manuscript. The supervisor edited, helped organize the manuscript, contributed to literature review, and provided training and advice on the bond graph formulation.	

Abstract

Modal testing is being investigated as a means of non-destructive evaluation of wooden utility pole strength. In order to understand the effects of conductors on the dynamics of the poles, a numerically efficient model based on lumped segments for the conductor has been developed and experimentally validated. The cable is modeled as a number of lumped segments jointed with axial and torsional springs and dampers representing the cable's compliance and damping. In order to validate the models, an experimental set up for vibration testing of the cable has been built. Time

response measurement and modal testing are performed and the comparison of the experimental results with the numerical results show that the lumped segment model has the fidelity to capture the dynamics of the cables efficiently and accurately.

Keywords: Cable dynamics; Lumped segment model; Modal testing; Bond graph model.

4.1 Introduction

Wooden utility poles are extensively used in North America for electrical power transmission and distribution. These wooden poles are subject to deterioration due to aging, rot, woodpecker damage, and fungal attack. Developing a non-destructive pole evaluation method based on modal testing requires numerical modeling of the poles and attached cables (conductors). Because cables are attached to the utility poles, vibrations of the cables affect the measurement of the modal properties of the poles. Therefore, a numerically efficient model should be developed to capture the dynamics of the cables.

Barry et. al. [75] investigated the vibrations of a single transmission line conductor with attached Stockbridge damper. They modeled the system as a double-beam system and derived the equations of motion of the system using Hamilton's principle. They validated the analytical results with experimental results and investigated the effect of damper location and characteristics on the conductor natural frequencies. Ricciardi et al. [51] developed a continuous model for vibration analysis of cables with sag considering the bending stiffness. They derived the vibration equation of motion of a sagged cable as an Euler-Bernoulli beam and solved the equation by an exact method. They performed a parametric study to investigate the effect of sag and bending stiffness on the cable natural frequencies and validated the results using finite element (FE) and finite difference methods. The exact method that they used could not be used when the cable is attached to a pole or moving support structure. Barbieri et. al. [88] used linear and nonlinear finite element models for analyzing the dynamic behavior of three different transmission line cables. They validated the numerical results by experimental tests and investigated the effect of inclusion of Stockbridge damper and linearity of the FE model on the natural frequencies. They concluded that linear finite element models provide good results for short cables only. Li et. al [55] and Wang et. al [89] presented a simplified computational model of a high-voltage transmission tower-line system under out-of-plane and in-plane vibrations due to seismic excitations. The transmission cables and their supporting towers were modeled as a lumped mass system. They did not consider the bending stiffness of conductors and their model was a simplified model for obtaining the response to seismic excitations. They obtained the mass and stiffness matrices of the coupled system and derived the linear equations of motion and validated the theoretical results with experiments. Papailiou [50] for the first time proposed a model for conductors that took into account the interlayer friction and the interlayer slip in the conductor during bending, obtaining a bending stiffness that changes with the bending displacement and the tension applied to the conductor. Spak et. al. [90] reviewed helical cable models with a focus on cable damping modeling. They described the work done in the literature on the inclusion of damping through frictional effects, variable bending stiffness, and internal friction. Spak et. al. [91,92] developed the distributed transfer function method to model cables and simple cabled structures. They included shear effects, tension, and hysteretic damping for modeling of helical stranded cables and investigated the effect of cables on the dynamics of cabled structures using the developed model and by experimental tests. Pinto et. al [56] developed a bond graph model for a wooden pole with a cable attached to the free end. In their paper, the cable was modeled as a series of point masses connected by translational springs and the pole was represented by a modal expansion based on separation of variables. They obtained the modal parameters of the cable and pole-cable systems numerically and experimentally. They concluded that their model should be expanded and improved from point masses to rigid bodies with rotational inertia, connected with bending stiffness and damping elements as well as axial ones.

The bond graph formalism, details of which can be found in [93] is chosen because of the ease with which it allows expansion of the model by adding segments in a modular way. Bond graphs, which use a small set of generalized elements to model multi-domain systems, facilitate connection of the cable model with other subsystem models such as poles, regardless of whether the poles are modeled using lumped segments or modal expansion.

This paper consists of two main sections. In Section 4.2, a bond graph lumped segment model of the cable is presented. In this model, the cable is modeled as number of segments that are attached to each other by springs and dampers representing the axial and bending compliances and damping of the cable, respectively. Section 4.3 describes the experimental set up and procedure that is used for performing time series measurement and modal testing of the stranded cable. The modeling assumptions and the results are explained in Section 4.4.

4.2 Lumped Segment Model

4.2.1 Theoretical development

In this paper, the cable is modeled as a pinned-pinned beam divided into number of segments. A numerical solution is obtained by a lumped segment approximation that captures axial and bending motions. For the purpose of modeling, two types of coordinate systems are used in the model. The first coordinate system is the inertial coordinate system. A body-fixed coordinate system is attached to each segment, the origin of which is located at the center of gravity and the local x axis of which is in the axial direction. The advantages of using body coordinate system are that axial springs between the segments can be modeled simply along the local coordinates, and that orientation angles and inertia properties are more easily handled if the model is expanded to three dimensions. Figure 4.1 shows representative segments of the cable, and local and global coordinate systems.

The cable is represented by a series of rigid cylinders of equal length and cross section; each rigid body has the same properties as the corresponding portion of the cable. As the number of segments approaches infinity, the behavior of the lumped segment model will converge to that of the continuous cable. The length of each segment is defined by the number of rigid bodies, *n*. For each segment, three points are defined: *B* in the left end of the segment, *A* in the right end and *G* in the center of mass. Point *A* of element *i* and point *B* of element *i*+1 are linked by one torsional and two linear springs. The torsional spring represents the bending compliance or flexural rigidity of the beam in the *x*-*y* plane, and the linear springs in *x* local direction represents the axial compliance. Each spring is complemented with a damper acting in parallel to it that acts as the cable material damping (dampers are not shown in the figure). Figure 4.1 shows the connection of each segment to the next and previous segments using torsional and linear springs, also illustrates the body-fixed coordinate system. For simplicity purposes, the dampers are not shown in the figure.

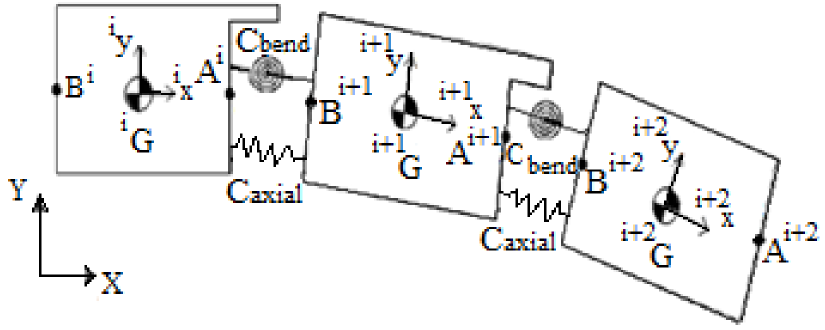

Figure 4.1: Multibody dynamic model

Cable Stiffness:

Equations (1)-(2) present the axial and bending stiffness of the cable, respectively [94].

$$C_{axial} = \frac{EA}{l} \tag{4.1}$$

$$C_{bend} = \frac{EI}{l} \tag{4.2}$$

where:

E = Young’s modulus of beam

A = Cross sectional area of the cable
l = Length of the cable segment
I = Area moment of inertia of the cross section

Cable Inertia:

The translational inertia of the lumped segments is equal to their mass. The rotational inertia of a cylinder about the axis perpendicular to the body-fixed coordinate plane, through the center of mass G, is as follows.

$$J_G = \frac{1}{12} m \left(\frac{3}{4} d^2 + l^2 \right) \tag{4.3}$$

Where m is mass of a segment, d is diameter of cable cross section, and l is segment length.

Cable Damping:

Damping in the cable is due to the material damping associated with the hysteresis energy losses in the material and interlayer wire slip. Because the stranded cable consists of a number of layers, the layers can slip on each other during vibration and this interlayer friction increases the damping in the stranded cables. In this paper, axial and bending dampers are placed in parallel with the springs in the model. The damper values are tuned to give decay of the response and natural frequencies close to experimental results. Further work should be done in the future to model the damping in the numerical model more accurately.

4.2.2 Kinematics of Rigid Bodies

In the bond graph model, we need to develop the velocity relations between points G and A and B in Figure 4.1. Eq'ns (4.4)-(4.5) represent the velocity of end points A and B in the local coordinate of the segment, respectively.

$${}^{i}\vec{V}_{A} = {}^{i}\begin{bmatrix} V_{Ax} \\ V_{Ay} \end{bmatrix} = {}^{i}\vec{V}_{G} + {}^{i}\vec{V}_{A/G} = {}^{i}\begin{bmatrix} V_{Gx} \\ V_{Gy} \end{bmatrix} + {}^{i}\begin{bmatrix} 0 \\ AG\omega \end{bmatrix} \tag{4.4}$$

$$ {}^{i}\vec{V}_{B} = {}^{i}\begin{bmatrix} V_{Bx} \\ V_{By} \end{bmatrix} = {}^{i}\vec{V}_{G} + {}^{i}\vec{V}_{B/G} = {}^{i}\begin{bmatrix} V_{Gx} \\ V_{Gy} \end{bmatrix} + {}^{i}\begin{bmatrix} 0 \\ -BG\omega \end{bmatrix} \tag{4.5} $$

where

${}^{i}\vec{V}_{A/G}$, ${}^{i}\vec{V}_{B/G}$ = relative velocity of points *A* and *B* with respect to *G*

$\omega =$ angular velocity of segment

Positive rotational speed of the segment is considered counterclockwise. Having defined the endpoint velocities, their relative motions are constrained by axial and bending springs and dampers. The velocity of center of mass (*G*) of each segment, while defined in the local coordinate system, must be transformed to the inertial coordinate system in order to apply gravity, and to allow system initialization through a static vertical displacement of a point on the cable, which is then released to create free vibration. The coordinate transformation for velocity of point G is as follows.

$$ {}^{I}\vec{V}_{G} = {}^{I}\begin{bmatrix} V_{Gx} \\ V_{Gy} \end{bmatrix} = \begin{bmatrix} \cos\theta & -\sin\theta \\ \sin\theta & \cos\theta \end{bmatrix} {}^{i}\vec{V}_{G} \tag{4.6} $$

where θ = angle of rotation of segment *i*.

Also, because the end point velocities of each segment need to be related, both end point velocities should be expressed in the same frame, in this case the local coordinate of the segment to the right. Eq. (4.7) represents the coordinate transformation relation between two connected sections.

$$ {}^{i+1}\begin{bmatrix} V_{Ax} \\ V_{Ay} \end{bmatrix} = \begin{bmatrix} \cos(\theta_{i+1}-\theta_i) & \sin(\theta_{i+1}-\theta_i) \\ -\sin(\theta_{i+1}-\theta_i) & \cos(\theta_{i+1}-\theta_i) \end{bmatrix} {}^{i}\begin{bmatrix} V_{Ax} \\ V_{Ay} \end{bmatrix} \tag{4.7} $$

Eq. (4.8) represents Newton’s Law for the segment in local coordinates.

$$ {}^{i}\sum\vec{F} = \frac{d}{dt}\,{}^{i}\vec{P} = {}^{i}\begin{bmatrix} m\dot{v}_x \\ m\dot{v}_y \end{bmatrix} + \vec{\omega}\times {}^{i}\begin{bmatrix} mv_x \\ mv_y \end{bmatrix} = {}^{i}\begin{bmatrix} m\dot{v}_x \\ m\dot{v}_y \end{bmatrix} + {}^{i}\begin{bmatrix} -m\omega v_y \\ m\omega v_x \end{bmatrix} \tag{4.8} $$

The first term on the right-hand side is modeled with generalized inertias in the bond graph, and the second term using modulated gyrators.

4.2.3 Bond Graph Model

The bond graph model of the cable consists of 30 segments, which is enough to produce the first few frequencies with reasonable accuracy. Each segment is connected to the next segment with a connection sub-model and each connection sub -model contains the compliance and damping bond graph elements. Figure 4.2 shows the bond graph model of a segment of the cable. A bond graph 1-junction represents a generalized Kirchoff loop law, with all bonded elements having the same flow, and efforts algebraically summing to zero. A bond graph 0-junction represents a generalized node law, with all bonded elements having the same effort. The 0-junction also sums velocities of bonded elements to zero, making it the element used to enforce velocity constraints. As can be seen from Figure 4.2, there are two modulated transformers (MTF), one for each row of Eq. (4.6), two MTF's for defining Eq'ns (4.4) and (4.5) and one modulated gyrator (MGY) for defining the Euler's Equations inner product terms of Eq. (4.8). The power bonds (with half-arrows) contain both force and velocity information. In Figure 4.2 sample junction equations are given. The 1-junction representing Newton's Law in the x direction sums forces, including constraint forces from adjoining elements that are on the same bonds that communicate velocity of points A and B to adjoining elements. Left superscripts indicate the local (i) or inertial (0) frame. Figure 4.3 shows the bond graph of one connection sub-model between two adjoining segments. As can be seen in Figure 4.3, there are four MTF's for defining coordinate transformation Eq. (4.7). The top row of the bond graph represents the velocities and elements in the x and y directions and the most bottom row represents the bending compliance.

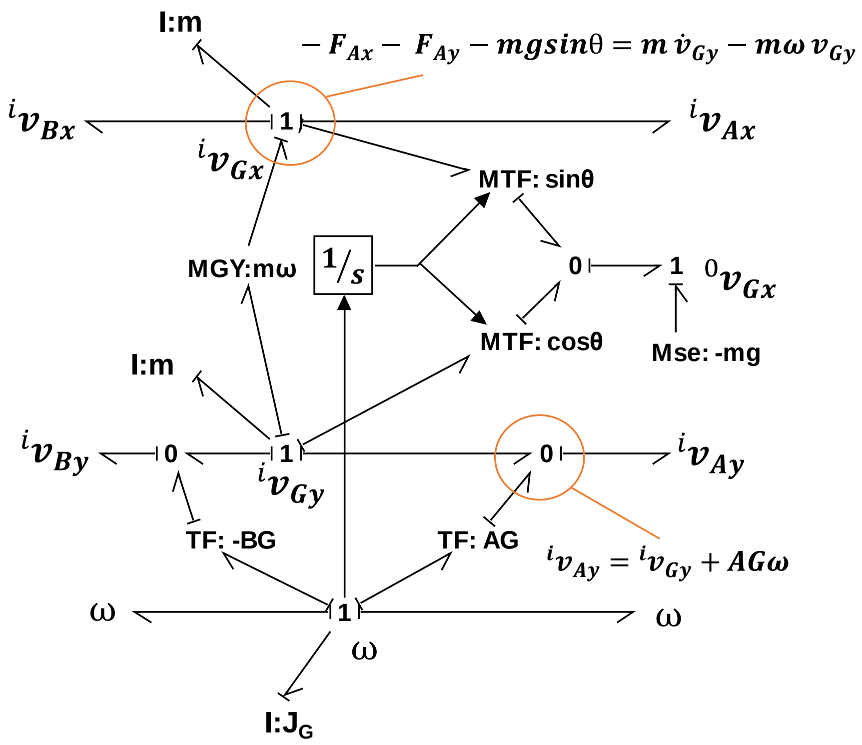

Figure 4.2: Bond Graph Model of a Segment of the Cable

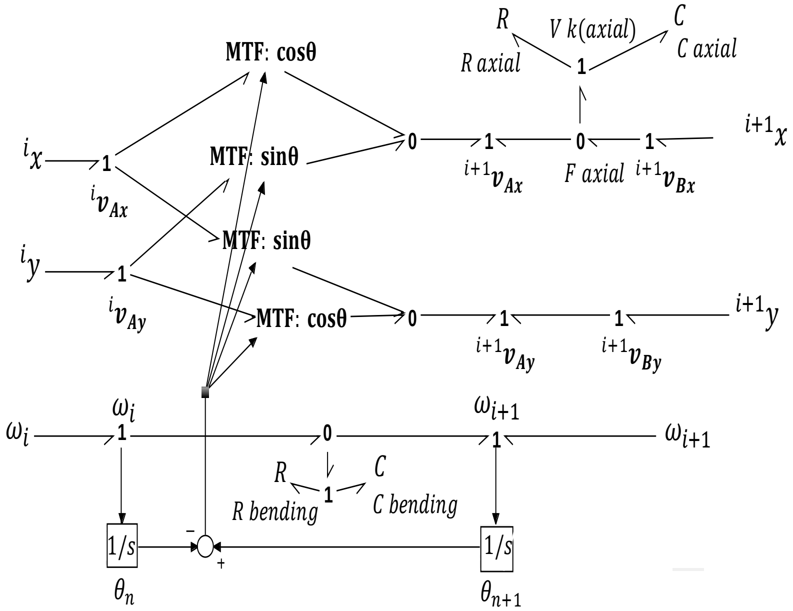

Figure 4.3: Bond graph model of complaint connection between consequent segments

In Figure 4.3, the 0-junction F_{axial} defines the velocity $v_{k(axial)}$ as the difference between v_{Bx} on segment i+1 and v_{Ax} on segment *i* defined in the *i*+1 coordinate system. The 1-junction equates the velocities of the parallel axial spring and damper. The bending spring/damper velocity is defined similarly. The block diagram elements define the relative angle between segments for the velocity transformation.

Point *B* of the left-most segment and Point *A* of the right-most segment are attached to the wall and therefore have zero velocity. Thus, two zero flow sources are used at each point in the x and y directions. In order to create the desired initial tension in the cable, the model is given zero initial conditions and then stretched until the desired tension is achieved. In this paper, four values of tension are considered for the analysis. For applying the stretching displacement to the right end of the cable in bond graph model, a flow source was temporarily applied to the 1-junction associated with the velocity of the right end of the cable in local x direction. After creating the desired tension, the zero-flow source was reinstated at the right end. The cable was then excited, with results of the bond graph model compared to experimental results.

4.3 Experimental Vibration Testing of the cable

4.3.1 Cable Bending Stiffness Measurement

The material properties of the conductor used for testing are tabulated in Table 4.1. The bending stiffness (*EI*) of the cable should be measured as it is stranded cable and its bending stiffness is not equal to the bending stiffness of solid cable with the same diameter [50]. Figure 4.4 shows the setup used for measuring the bending stiffness (*EI*) and consequently area moment of inertia (*I*) of the cable.

Table 4.1. Material properties of cable

Material	Length [m]	Density $\left({}^{kg}/_{m}\right)$	E [GPa]	Area [m^2]
Stainless Steel 7×7 wires	3.6	0.166	190	$2.78\text{x}10^{-5}$

Figure 4.4: Setup for Bending Stiffness Measurement

A section of the cable is clamped between two ends and a fixed-fixed configuration is made. Various weights are hung in the middle of the cable section and a LDVT is used to measure the deflection of the cable at midspan. By using standard force-deflection formulae for a fixed-fixed beam with force applied at midspan, the bending stiffness of the cable is obtained [95]. It should be noted that the value of measured *EI* from bending test is between theoretical minimum and maximum bending stiffness bounds for the stranded cables. $EI_{\min}$ corresponds to when all the layers of the cable slip on each other and $EI_{\max}$ is for all the wires are bonded and make a solid cable. The details of the theoretical bounds for bending stiffness can be found in [50]. Bending of the cable in a cantilever configuration was also performed with different lengths of the cable and the results were the same, which shows that the bending stiffness of the cable is not sensitive to length, over the range of segment lengths considered in this work. A measured constant value for *EI* is directly used in the bond graph model in numerical analyses. Table 4.2 presents the value of *EI* for three different lengths of cable sections and the average value is used in the model.

Table 4.2. Value of measured *EI* with different lengths

Length (mm)	$EI(Nm^2)$
205	0.555
364	0.444
400	0.547

4.3.2 Experimental Modal Testing

Figure 4.5 shows the set up used for modal impact testing of the cable.

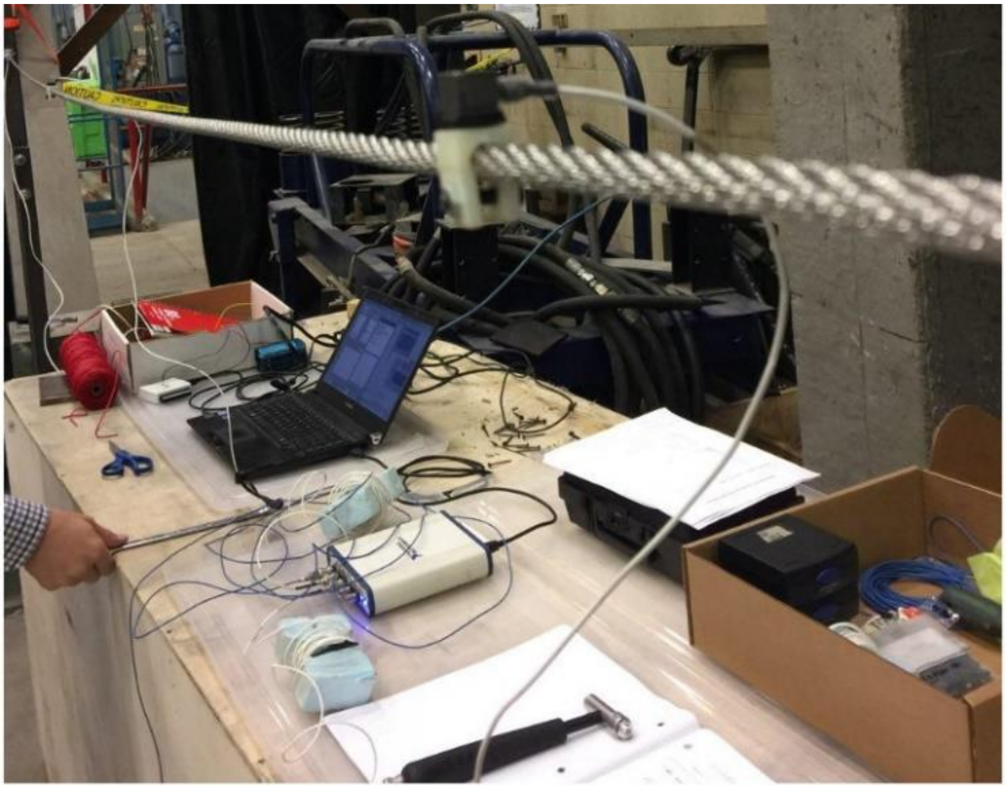

Figure 4.5: Cable Vibration Test Set up

Figure 4.6 presents a schematic illustrating two set-ups used for testing the cable. Two pin support structures hold the cable. The right end of the cable is attached to a threaded rod to adjust the static tension of the cable. A load cell is at the left end of the cable to measure the longitudinal tension of the cable. The load cell is directly inline with the cable to measure the longitudinal tension of the cable. The rectangular solid shapes and the black arrows represent respectively the position of the accelerometers and the hammer hits along the cable.

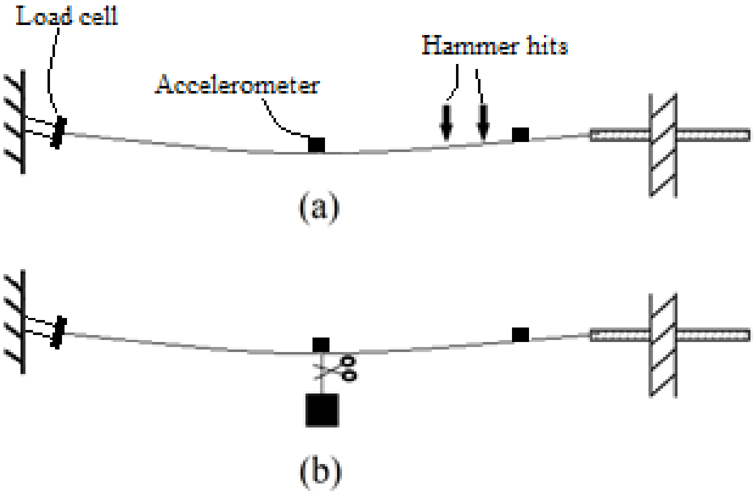

Figure 4.6: Schematic view of cable vibration testing

Modal tests are performed with a Bruel & Kjaer 8205-002 impact hammer, 4507 B 004 70-g accelerometers, and a National Instruments NI USB-4432 power supply and signal conditioner. Cable tension is measured with a load cell. Also, the software ModalView [95] is used to analyze the data. All modal tests averaged 5 hits.

Figure 4.6 (a) illustrates the setup used to perform hammer modal testing over the cable, experiment "A". With accelerometers positioned at 0.3 and 1.8 m from the right side, the measurements are taken hitting the hammer in two different positions, at 1/4 and 1/5 of the cable span. The modal test is performed with different tensions which are tabulated in the Results section. Another experiment, "B", is performed as illustrated by Figure 4.6 (b). The cable is supported the same way as before, however now there is a mass attached to the middle of the cable through a string. Cutting the string creates a force excitation that can be replicated in simulation.

4.4 Results and Discussion

The Frequency Domain Toolbox in the 20sim® bond graph simulation environment numerically generates a system transfer function from which eigenvalues are calculated. Table 4.3 presents the experimental and numerical results of the natural frequencies and damping ratios of the tensioned cable. In the simulation, an impulse force is applied at the quarter of the cable span which is in the 7th cable segment and the time response is obtained at the mid-span of the cable. The result of experiment (b) in Figure 4.6 and corresponding simulation results are illustrated in Figure 4.7 and Figure 4.8. The measured and simulated acceleration time response of the mid-span can be compared from these figures. Figure 4.7-4.8 show accelerations of similar magnitude. Discrepancies are primarily attributed to inaccurate high-frequency modes inherent in a lumped-segment representation.

Table 4.3. Cable modal data: simulation and experimental results

Tension (N)	Modal Testing		Simulation	
	Freq (Hz)	Damp (%)	Freq (Hz)	Damp (%)
91.4	2.37	4.025	2.41	1.612
	4.52	16.4	4.77	11.511
	6.88	3.880	-	-
140.6	4.53	0.645	4.21	5.672
	6.53	0.939	-	-
	10.15	1.18	13.03	2.014
230.8	4.96	1.074	5.19	4.223
	8.19	0.699	8.32	1.770
	12.39	0.900	13.31	54.881
300.7	5.14	0.913	5.11	32.85
	9.46	0.357	9.19	91.908
	14.22	0.436	14.8	2.741

350	5.35	0.878	5.02	1.918
	10.18	0.258	10.34	-
	15.27	0.343	-	-
400	5.58	0.807	5.07	17.997
	10.87	0.209	10.3	5.509
	16.27	0.487	15.23	0.778

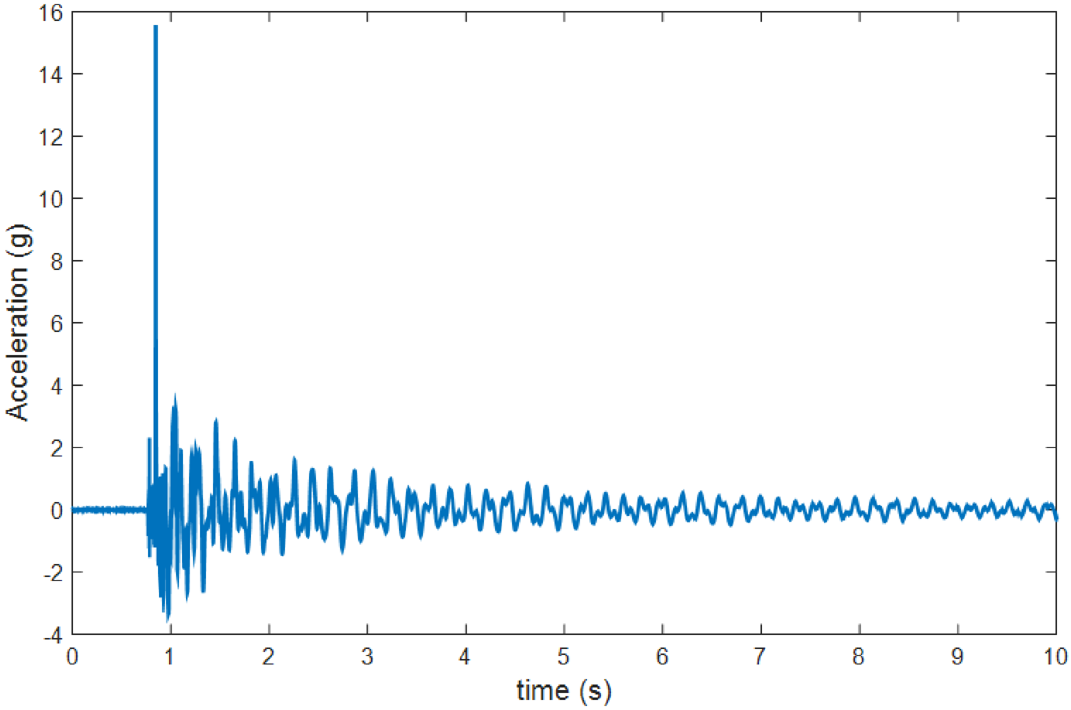

Figure 4.7: Acceleration time series of the midspan of the cable- Experimental result

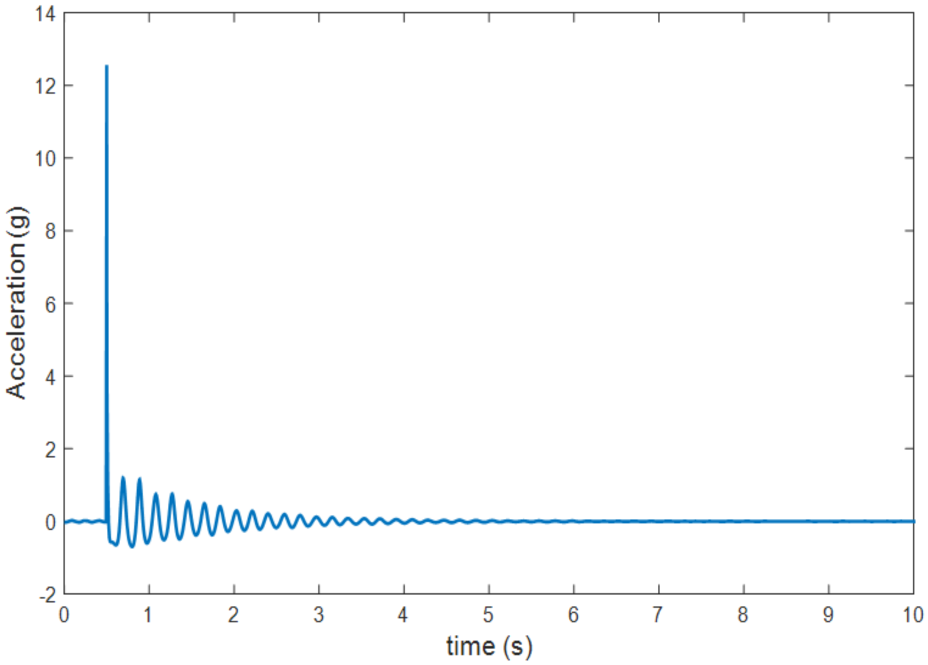

Figure 4.8: Acceleration time series of the midspan of the cable- Simulation result

4.5 Conclusion and Future work

A bond graph lumped segment model was developed to obtain the modal data of a conductor. The natural frequencies and damping ratios from modal testing of the physical setup were compared to those from simulation, along with time responses. The overall system frequencies were predicted with the simulation model for the range investigated. Discrepancies in damping ratios, and in time response, are attributed to the use of simple linear viscous damper elements. Developing and tuning a more accurate damping model remains an open research problem. In addition, as the overall goal of the research is to capture the effects of cable on dynamics of poles, cable numerical models should be combined with the pole models to investigate the effects of cables in a line of pole-cables in the future work.

Chapter 5

5 Three-dimensional Dynamic Model Development and Validation for Stranded Cables

[a] Mohammad Hadi Jalali, [a] Richard McKercher, [a] Geoff Rideout

[a] Faculty of Engineering and Applied Science, Memorial University, St. John's, Canada

This chapter presented in ASME2019 Conference in Salt Lake City, UT, USA as a conference paper. In this chapter, a three-dimensional bond graph model for stranded cables is developed and validated through experiments. In-plane and out-of-plane natural frequencies and free vibration response obtained from the model are validated with experimental free and forced vibration tests. The co-authorship statement for this chapter follows:

The declaration applies to the following article	
Title of Chapter	Chapter 5: Three-dimensional Dynamic Model Development and Validation for Stranded Cables
Article status: Published	
The PhD student analyzed the literature, performed the experiments, collected the data, developed the codes and prepared the manuscript. The experimental setup was designed by the co-op student. The supervisor edited, helped organize the manuscript, contributed to literature review, and provided training and advice on the bond graph formulation.	

Abstract

Interactions between cables and structures affect the design and non-destructive testing of electricity transmission lines, guyed towers, and bridges. In order to understand the effect of conductors on dynamics of utility poles, a three-dimensional dynamic model for stranded cables is presented based on the bond graph formalism and validated through experimentation. The cable is modeled considering the bending stiffness, tension and sag due to self-weight. The model consists of three-dimensional rigid segments, connected with translational and rotational springs and dampers. To validate the model, an instrumented set up for a stranded cable was tested in the laboratory and the model was validated in both the in-plane and out-of-plane directions in the frequency domain by measuring the cable response to hammer impacts in both directions. Time domain response obtained from simulation was also validated with experimental time response by performing a free vibration test. A set up was designed and built to accurately measure the bending stiffness of a stranded cable in different tensions and the measured values for bending stiffness were used in the numerical model. It was observed that the bending stiffness increased with the increase in tension. The modal properties of the cable were obtained numerically and experimentally for different tensions and consequently for different amounts of sag. The model is verified to have sufficient fidelity to predict the dynamics of cables undergoing both in-plane and out-of-plane motion, and can be used in a pole-cable system model to investigate the effect of cable on dynamics on poles or structures.

Keywords: Stranded Cable, Bond Graph Method, Modal Testing, Bending Stiffness, Numerical Model.

5.1 Introduction

Dynamic interaction between cables and the main structure in cabled structures has been a topic of interest for researchers in recent decades. Developing a nondestructive evaluation (NDE) method for utility poles based on modal testing requires numerical modeling of the poles and the attached cables (conductors) to understand the effect of cables on pole dynamics. A reliable and computationally efficient numerical model for the cable itself is a prerequisite. Models of cables typically treat the cable as a string or a beam or as a series of beam-like segments. Models vary in their treatment of bending stiffness and cable sag due to self-weight.

Ricciardi et. al [51] developed a continuous model for vibration analysis of cables with sag considering the bending stiffness. They considered the conductor as a tensioned Euler-Bernoulli beam under self-weight. They concluded that the bending stiffness and sag of the cable has significant effect on vibration properties of the cable and ignoring them can lead erroneous results. Sousa et. al. [53] analyzed the effect of considering bending stiffness, shear stiffness and rotational inertia on the natural frequencies of the overhead transmission line conductors. Using Euler-Bernoulli and Timoshenko beam theories, they found the error from neglecting shear and rotational inertia to be very small compared to the error from neglecting the bending and geometric stiffness of the cable. Papailiou [50] proposed a model for bending of stranded cables taking into account the slip and friction between the layers. They obtained a theoretical bending stiffness for the stranded cables dependent on curvature and tension and verified the bending stiffness model, experimentally. Ni et. al. [76] analyzed the vibration of large diameter sagged cables and developed a three-node finite element for dynamic analysis. A case study compared the measured and computed natural frequencies, with and without considering cable bending stiffness, of the main cables of the Tsing Ma Bridge. Ignoring the bending stiffness of sagged cables led to unacceptable errors in predicting the natural frequencies. Jalali et. al. [16] developed a 2D numerical model based on the bond graph method for vibration analysis of power lines. Their model consisted of lumped segments joined with axial and torsional springs and dampers representing the compliance and damping of the cable. Pinto et. al. [12,56] developed a bond graph model for a pole with a cable attached to the free end. The cable was modeled as a series of point masses connected by translational springs and the pole was represented by a modal expansion based on separation of variables. Modal parameters of the cable and pole-cable systems were obtained numerically and experimentally. They concluded that their model should be expanded and improved from point masses to rigid bodies with rotational inertia, connected with bending stiffness and damping elements as well as axial ones.

The bond graph method is a systematic method that several simple models can be combined to build a complex model and the dynamic equations of the system are obtained in a straightforward manner by investigating energy flow among the storage elements [96]. Bond graphs facilitate connection of the cable model with other subsystem models such as poles.

In this paper, a three-dimensional numerical model is developed for a stranded cable similar to the real conductors that are used in electrical transmission lines. The cable is modeled considering the bending stiffness and sag. The 3D rigid lumped segments are connected to each other with translational and rotational springs and dampers to model the compliance and damping of the cable and the numerical model is validated with experimental results. A setup was designed for measurement of bending stiffness of the stranded cable under different tensions and measured bending stiffness values were used in the BG model. The tuned numerical model can be used to simulate modal testing of power lines in in-plane and out-of-plane directions. The following Section describes the bond graph model and theoretical formulation, Section 5.3 presents the experimental vibration testing and cable bending stiffness measurement, and verifications and results are presented in Section 5.4.

5.2 Multibody bond graph model description

The cable is modeled with 3D rigid lumped segments connected with translational and rotational springs and dampers. In this model, 30 segments are used to model the cable. The lumped segments are joined with a translational spring/damper to model the axial compliance/damping and three rotational springs/dampers to model the torsional behavior and bending behavior in two directions. Figure 5.1 shows the segments of the cable connected with springs. The dampers are not shown for clarity. The translational spring corresponds to the axial compliance, $K_{axial_{cable}}$. The shear compliance of the cable is not considered in the analyses as it has negligible effect on the dynamics of the cable [53]. Rotary springs $K_{bend_{cable}}$ are the bending compliance of the cable about the local body-fixed *y* and *z* directions which are the same because of the axial symmetry of the cable and $K_{tor_{cable}}$ is the torsional compliance of the cable about the body-fixed *x* direction. In Figure 5.1, the bending rotary springs about the *z* direction are not shown for clarity and the springs are along the body-fixed coordinates of the body *i*+1.

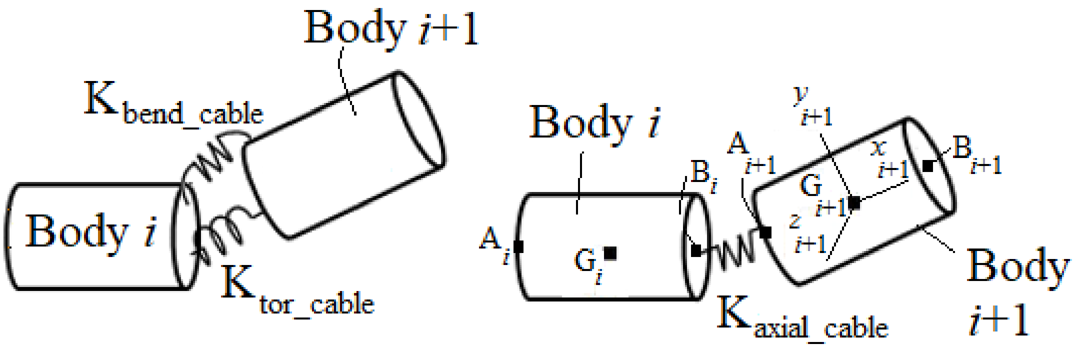

Figure 5.1: Successive multibody segments

Stiffness values are computed for a segment lengths of $l_c = \frac{L_c}{n_c}$, where $L_c$is the cable length and n_c is the number of segments, [93]:

$$K_{axial\_cable} = \frac{E_c A_c}{l_c} \tag{5.1}$$

$$K_{bend\_cable} = \frac{E_c I_c}{l_c} \tag{5.2}$$

$$K_{tor\_cable} = \frac{G_c J_c}{l_c} \tag{5.3}$$

where E_c is the cable elastic modulus, A_c is the cross section area, I_c is the cable moment of area, G_c is modulus of rigidity and J_c is the polar moment of area. The damper values are tuned in the model to give a close time response compared to experimental time responses and $E_c I_c$ of the cable was measured at various tensions () and the measured values were used in the model.

5.2.1 Bond Graph of Segments and Joints

In order to create the bond graph model of the system, dynamic equations of each segment and relative velocity of end points with respect to the center of gravity must be developed. The following equation relates velocity of end point *A* of body *i* to the velocity of center of gravity *G* of body *i*.

$$ {}^{i}\vec{V}_{Ai} = {}^{i}\vec{V}_{Gi} + {}^{i}\vec{V}_{\frac{Ai}{Gi}} \tag{5.4} $$

$$ {}^{i}\vec{V}_{\frac{Ai}{Gi}} = {}^{i}\vec{\omega}_{i} \times {}^{i}\vec{r}_{\frac{Ai}{Gi}} = {}^{i}\tilde{r}_{\frac{Ai}{Gi}}{}^{i}\vec{\omega}_{i} \tag{5.5} $$

where the left superscript i indicates that the vector is presented in a local body-fixed coordinate system, ${}^{i}\vec{V}_{Ai}$ is the absolute velocity of point *A* on body i in body-fixed coordinates, ${}^{i}\vec{\omega}_{i}$ is the rotational velocity vector, ${}^{i}\vec{r}_{\frac{Ai}{Gi}}$ is the position vector of point *A* with respect to *G* and ${}^{i}\tilde{r}_{\frac{Ai}{Gi}}$ is the skew-symmetric matrix containing the relative position vector components. The equations below describe Newton's law in three dimensions for the segment in local coordinates:

$$ \sum {}^{\mathrm{o}}\vec{\mathrm{F}} = \frac{\mathrm{d}}{\mathrm{dt}}\left(m\,{}^{\mathrm{o}}\vec{V}_{\mathrm{Gi}}\right) = m\,{}^{\mathrm{o}}\dot{\vec{V}}_{\mathrm{Gi}} \tag{5.6} $$

$$ \sum {}^{i}\vec{\tau} = \frac{d}{dt}{}^{i}\vec{H} = \vec{J}^{i}\dot{\vec{\omega}}_{i} + {}^{i}\vec{\omega}_{i} \times \vec{J}^{i}\vec{\omega}_{i} \tag{5.7} $$

where left superscript *o* indicates that the vector is defined in the inertial coordinate system. The first term in the right side of rotational Eq. (5.7) is the rotational inertia term and the second term is a gyrational term. To be able to add forces such as gravity and equate values in different reference frames, we need to be able to transform values from the body fixed frame to the inertial frame. This is accomplished with a rotation matrix. Rotation matrices are made for each of the three rotations θ, ψ, ϕ about *x*, *y* and *z* axes, respectively and are multiplied together to create the transformation matrix.

Vector bond graphs are used to represent the equations. Figure 5.2 shows the vector bond graph sub model representing the body segment *i*. In Figure 5.2, the 1-junctions are labeled with the corresponding translational or rotational velocities. Translational velocity Eq. (5.4) for defining the velocity of left end point *A* of the segment and the similar equation for the velocity of the right end point *B* of the segment with respect to center of mass gravity in the body-fixed coordinate are represented by two modulated transformer's (MTF) and two 0-junctions in Figure 5.2. A 0-junction is used to add ${}^{i}\vec{V}_{Gi}$ to ${}^{i}\tilde{r}_{\frac{Ai}{Gi}}{}^{i}\vec{\omega}_{i}$ to obtain ${}^{i}\vec{V}_{Ai}$ and a 0-junction is used to add ${}^{i}\vec{V}_{Gi}$ to ${}^{i}\tilde{r}_{\frac{Bi}{Gi}}{}^{i}\vec{\omega}_{i}$ to obtain ${}^{i}\vec{V}_{Bi}$. The two MTF's representing relative velocity cross products receive the relative position vector as an input signal. The coordinate transformation between body-fixed and inertial frames is represented by an MTF that multiplies ${}^{i}\vec{V}_{Gi}$ by the transformation matrix to obtain inertial center of gravity velocity ${}^{o}\vec{V}_{Gi}$. Translational force Eq. (5.6) is represented by a mass matrix multiport I element and the gravity effort source is connected to the ${}^{o}\vec{V}_{Gi}$ 1-junction (${}^{i}\vec{V}_{Gi}$ transformed to the inertial frame). The right hand side of Eq. (5.7) is represented by a rotational inertia I element, a modulated gyrator MGY, external moments from joints i and i-1 and moments from forces at end points A and B, connected to the ${}^{i}\vec{\omega}_{i}$ 1-junction. The MGY is used to represent the cross product of ${}^{i}\vec{\omega}_{i} \times \vec{J}\,{}^{i}\vec{\omega}_{i}$ with $\vec{J}\,{}^{i}\vec{\omega}_{i}$ as an input signal.

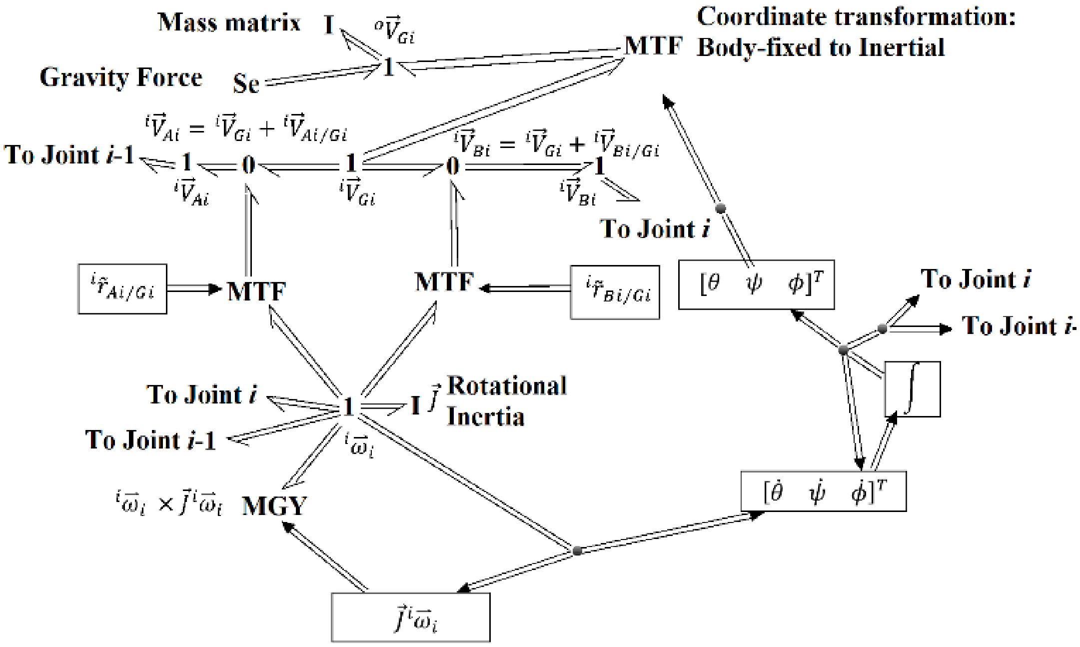

Figure 5.2: Body *i* bond graph

Figure 5.3 shows the bond graph sub model of joint *i* between successive segments. The 0-junctions represent the translational and angular velocity constraints that are caused by parallel spring/dampers between the left end point *A* of body *i*+1 and right end point *B* of body *i* (Figure 5.1). The velocity of *B* on body *i*, ${}^i\vec{V}_{Bi}$ and ${}^i\vec{\omega}_i$ are first transformed to the inertial coordinate system using a pair of MTF's and then transformed to the body *i*+1 local coordinate system using another pair of MTF's. The *C* multiport elements model the stiffness described in Eq's. (5.1)-(5.6) using a diagonal stiffness matrix. The *R* elements define the damping using a damping matrix. The damping values are tuned to give an accurate time response and natural frequencies compared to experimental results.

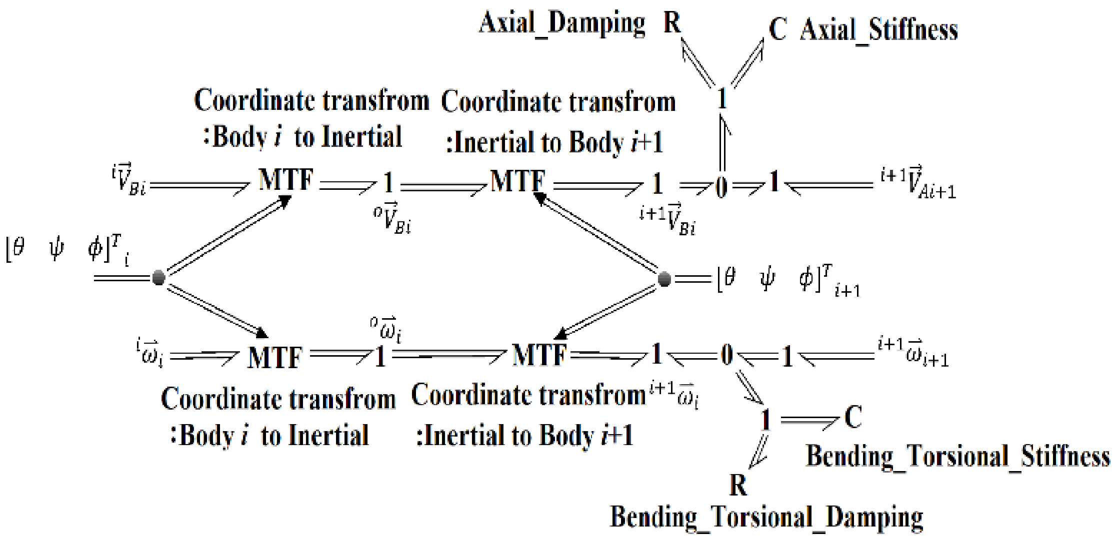

Figure 5.3: Joint *i* submodel bond graph

5.3 Experimental Methods

5.3.1 Experimental modal testing

In order to verify the numerical model, experimental vibration tests were carried out. Figure 5.2 presents the schematic of the vibration tests. Two rigid frames were secured to the floor on the right and left sides. The right end of the cable was attached to a threaded rod to adjust the tension of the cable and an in-line load cell at the left end of the cable measured the longitudinal tension of the cable. Tests were performed with a Bruel & Kjaer 8205-002 impact hammer, 4507 B 004 70-g accelerometers, and a National Instruments NI USB-4432 power supply and signal conditioner.

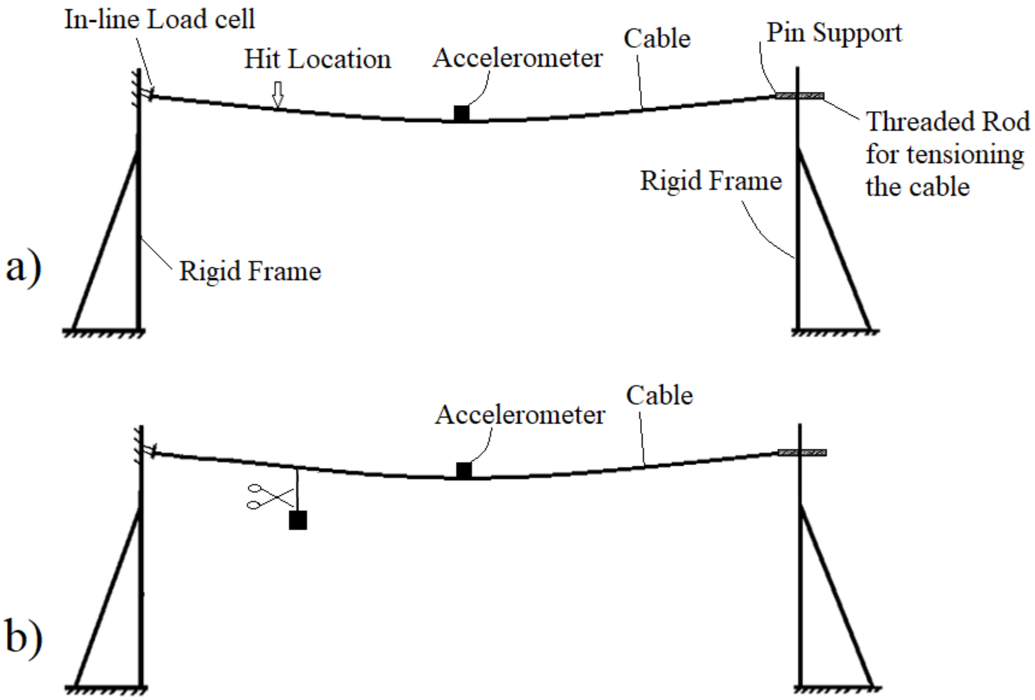

Figure 5.4: Schematic for experimental vibration testing a) Modal impact test b) Free vibration test

Two types of vibration tests were carried out. In Figure 5.4-a, the modal impact test is shown and Figure 5.4-b shows the free vibration test. The modal tests were carried out with five different tensions 25 N, 50 N, 100 N, 200 N and 300 N in the cable. The amount of sag of the cable changes depending on the tension in the cable. In place of the accelerometer in Figure 5.4, another accelerometer was used in the out-of-plane direction (perpendicular to the plane of Figure 5.4), to measure the out-of-plane vibration due to hammer impact load. The hammer hits were made at the quarter span length of the cable and the accelerometer was placed at mid span. Each test was performed five times and the average result was considered for the analysis. The RMS averaging method with exponential weighting was used to average the results and an exponential window was applied with duty cycle of 10 percent. In the free vibration test (Figure 5.4-b), a 1 kg weight was hung from the quarter span of the cable and by cutting the string attached to the weight, an initial displacement was created to cause free vibration of the cable. The in-plane vibration response at mid-span was measured by the accelerometer. Figure 5.5 shows the setup used and the material properties of the cable are presented in Table 5.1. The cable (7x19 stranded cable) was supported with a pin connection at both ends and the span length between the rigid frames was 2.4 m.

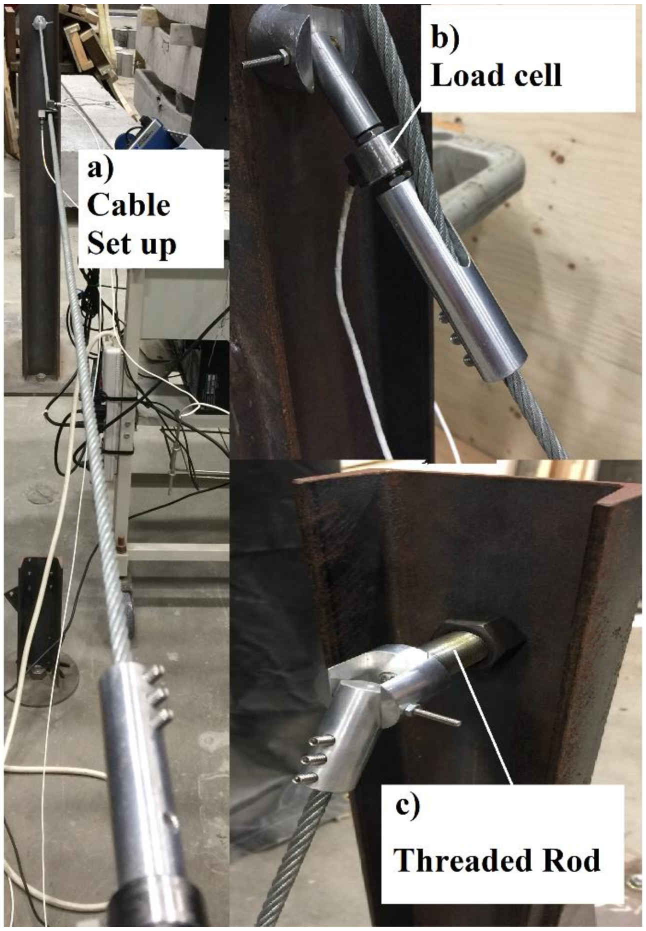

Figure 5.5: Cable vibration test a) test set up

B) in-line load cell end c) threaded rod

Table 5.1. Material properties of cable

$E_c(GPa)$	$A_c(mm^2)$	$m_c\left({}^{kg}/_{m}\right)$
190	31.66	0.166

5.3.2 Bending stiffness measurement

The bending stiffness of stranded cables is bounded by two extreme flexural stiffnesses EI_{max} and EI_{min} [87]. The maximum bending stiffness EI_{max} corresponds to a solid cross section with no slippage of the strands [15]:

$$EI_{max} = E\sum_{i=1}^{N_s}\left(\frac{\pi {d_{si}}^4}{64} + \frac{\pi {d_{si}}^2}{4}{y_{si}}^2\right) \approx E\frac{\pi {d_c}^4}{64} \tag{5.8}$$

where d_{si} is the diameter of the *ith* strand, y_{si} is the distance from the center of gravity of the *ith* strand to the center of gravity of the conductor, d_c is the diameter of the cable and N_s is the number of strands in the cable.

The minimum bending stiffness EI_{min} corresponds to all the strands of the cable slipping past each other as static friction between the strands is overcome. Therefore, the bending stiffness in this condition is the sum of bending stiffness of all the strands:

$$EI_{min} = E\sum_{i=1}^{N_s}\frac{\pi {d_{si}}^4}{64} \tag{5.9}$$

Figure 5.6 shows the test apparatus for measuring the bending stiffness of the cable. A hydraulic cylinder is secured to the frame at the top of the setup to apply the load at the middle of the cable, and an LDVT (Linear Variable Differential Transformer) is attached to the cylinder to measure the deflection of the cable at midspan at the same time. The inline load cell was used to measure cable tension, which was adjusted with a threaded rod. An S-type load cell was also attached to the cylinder to measure the applied load. The cable was secured with clamped-clamped end conditions and the theoretical procedure used to measure the bending stiffness follows [86]. The bending stiffness of the stranded cables increased with tension in [15,86] and the results obtained in the present study confirm this trend. The bending tests were performed at the same five tensions as in the modal testing. The measured bending stiffness values are presented in Table 5.2 and the theoretical limits of bending stiffness are $EI_{min} = 0.0306$ and $EI_{max} = 15.5632$, respectively.

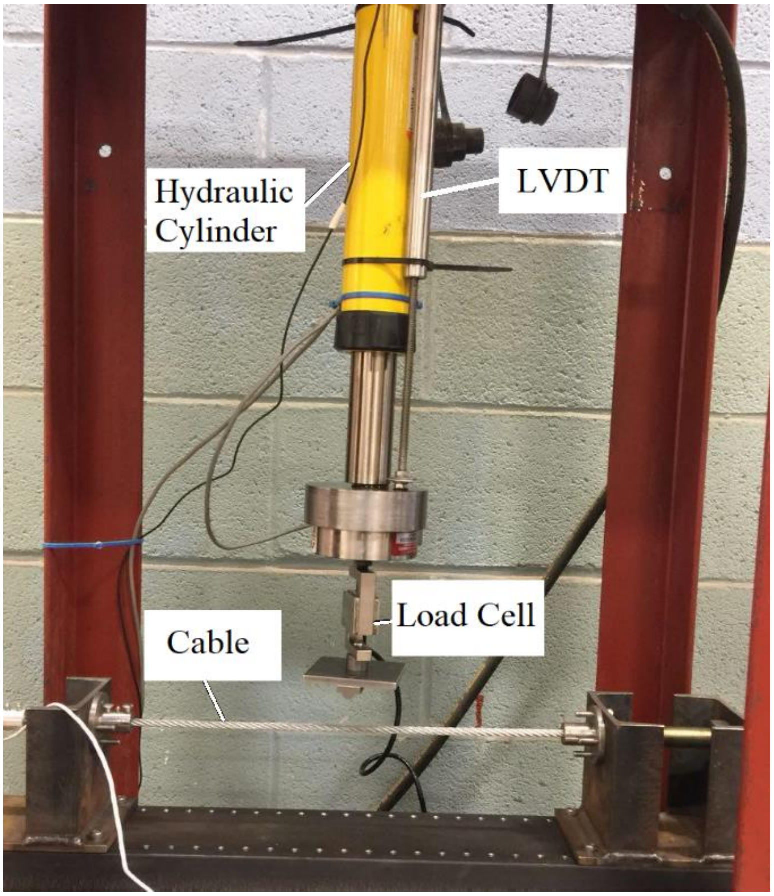

Figure 5.6: Experimental set up for cable bending stiffness measurement

Table 5.2. Measured bending stiffness of cable with different tensions

Tension (N)	25	50	100	200	300
$EI\ (Nm^2)$	0.2549	0.3420	0.4948	0.5972	0.8283

5.4 Results and Discussion

Two vibration tests (Figure 5.4-a and Figure 5.4-b) were simulated in 20sim® software using bond graph method. Modal impact testing (Figure 5.4-a) was simulated and the frequency domain toolbox in the software was used to generate transfer functions from which the eigenvalues can be extracted. In the simulation, an impulse force is applied at the quarter-span cable location and the time response is obtained at mid-span of the cable similar to the experimental test procedure (Figure 5.4). ModalView [95] software was used to analyze the experimental data and a stability diagram based on the frequency response functions was used to extract the natural frequencies with a sampling rate of 1024 Hz. Figure 5.7 shows an experimental FRF which was obtained from in-plane vibration of the cable with 300 N tension. Table 5.3 presents the comparison of in-plane natural frequencies of the cable with different tensions and Table 5.4 compares the out-of-plane natural frequencies of the cable. In order to excite and capture the in-plane modes, the hammer hit was performed in the plane of cable in Figure 5.4 and for out-of-plane modes, the cable was excited in the plane perpendicular to the plane of the cable. Some of the natural frequencies are missing in the tables and they were the modes that could not be captured numerically or experimentally. A convergence study was performed and increasing the number of segments did not significantly change the results.

Table 5.3. In-plane natural frequency comparison of the cable

Tension (N)	Modal Test [Hz]	Simulation [Hz]	Error (%)
25	5.26	6.23	18.44
	8.03	9.20	14.57
	13.19	13.43	1.82
50	7.63	7.85	2.88
	11.73	11.41	2.73
	16.17	16.50	2.04
	23.17	21.15	8.72
100	6.33	-	-
	11.29	11.02	2.36
	16.94	13.71	19.04
200	7.81	7.72	1.21
	--	9.37	--
	15.53	15.75	1.44
	23.06	23.96	3.94
300	9.08	9.68	6.61
	17.60	16.99	3.46
	25.91	26.00	0.35

Table 5.4: Out-of-plane natural frequency comparison of the cable

Tension (N)	Modal Test [Hz]	Simulation [Hz]	Error (%)
25	2.94	3.06	4.08
	5.97	6.28	5.19
	9.19	9.75	6.09
50	3.87	3.88	0.26
	7.92	7.90	0.25
	11.84	12.14	2.53
	18.57	16.65	10.34
100	4.51	5.27	16.84
	9.77	11.20	14.60
	13.90	11.22	19.27
200	6.82	6.86	0.53
	8.11	9.50	17.10
	14.22	14.06	1.14
300	8.64	8.32	3.71
	17.15	16.98	0.99
	24.62	24.85	1.34

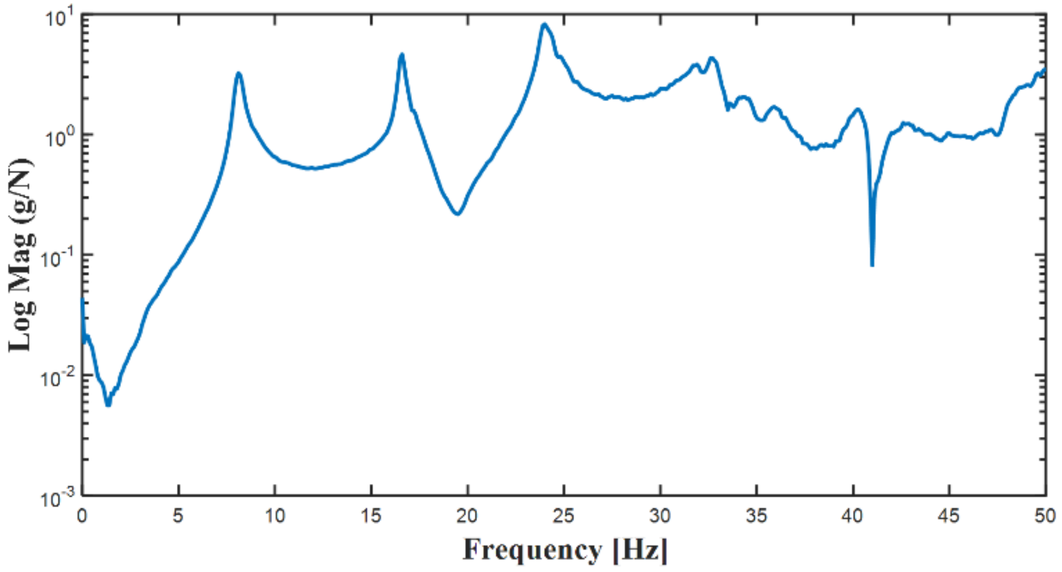

Figure 5.7: Experimental FRF: in-plane excitation with 300 N tension

As can be seen from Table 5.3 and Table 5.4, there is typically good agreement between the numerical bond graph frequency domain results (in-plane and out-of-plane) and the experimental results. The free vibration test (Figure 5.4-b) was also simulated in the numerical model and the acceleration in-plane time response at the mid-span obtained from experiment and simulation are compared in Figure 5.8. As can be seen, there is a good agreement between the numerical and experimental time responses and the numerical model is able to replicate the decay rate, vibration amplitude and frequency content of the experimental time response.

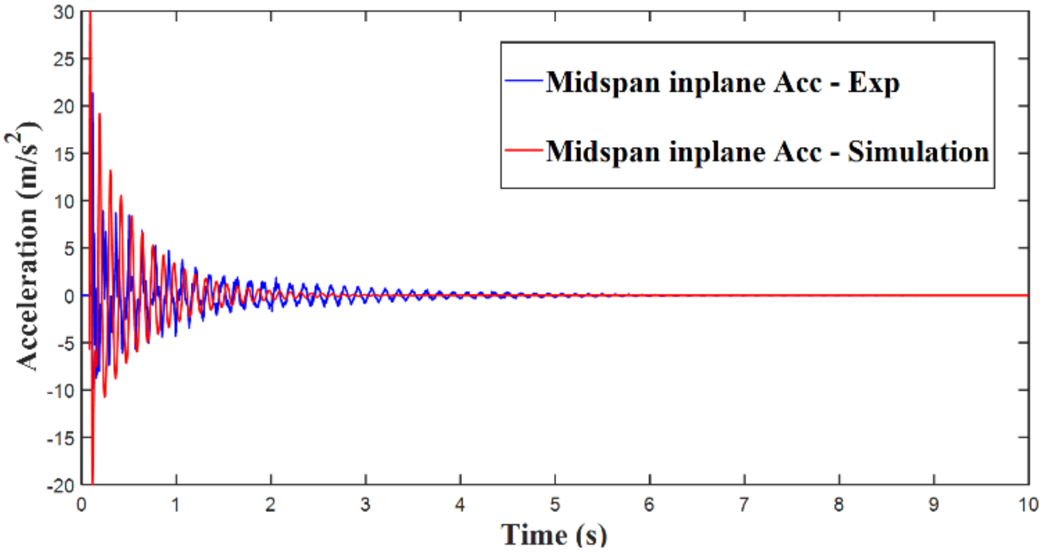

Figure 5.8: Time response comparison of simulation and experiment

The time domain and frequency domain verification of the numerical model shows that the developed model is an accurate and reliable model to capture dynamics of stranded cable and can be used in connection with the pole(s) model for cable-beam system dynamic investigations.

5.5 Conclusion

A three-dimensional dynamic model for a stranded cable was developed and validated with experiments. The lumped segment method was used to model the system and axial, bending and torsional behavior of cable was considered. In comparison to analytical methods or finite element analysis, the bond graph formalism is a very computationally efficient and straightforward method for connecting different sub models of cable and pole to each other. A set up was designed and used to accurately measure the bending stiffness of the stranded cable with different tensions and the measured stiffness values were used in the dynamic model. The bending stiffness was seen to increase with the increase in tension. The developed dynamic model is concluded to be a reliable and accurate model to be used for cable dynamic analysis in in-plane and out-of-plane directions.

Chapter 6

6 Three-Dimensional Dynamic Modeling and Validation for Vibration of a Beam-Cable System

[a] Mohammad Hadi Jalali, [a] Geoff Rideout

[a] Faculty of Engineering and Applied Science, Memorial University, St. John’s, Canada

This chapter is a manuscript of a full paper published in Mathematical and Computer Modeling of Dynamical Systems journal. In this chapter, a three-dimensional dynamical model for a cable-beam system is developed using bond graph formalism. The model is validated in free and forced vibration with the experiments. The co-authorship statement for this chapter follows:

The declaration applies to the following article	
Title of Chapter	Chapter 6: Three-Dimensional Dynamic Modelling and Validation for Vibration of a Beam-Cable System
Article status: Published	
The PhD student analyzed the literature, performed the experiments, collected the data, developed the codes and prepared the manuscript. The supervisor edited, helped organize the manuscript, contributed to literature review, and provided training and advice on the bond graph formulation.	

Abstract

In order to understand and to predict cable effects on structures, three-dimensional numerical models for a stranded cable and a beam-cable system consisting of a cantilever beam and two connected cables are presented. The multibond graph formalism is used to model the coupled cable-beam system, with the cable and beam substructures using 3D rigid lumped segments. The stranded cables are modeled considering the bending stiffness, tension and sag due to self-weight. While generally applicable, the cable-structure modeling approach in this paper is applied to vibration-based non-destructive evaluation of electrical utility poles and to simulate modal testing of the electrical pole-conductor system. Experimental parametrization of a stranded cable is carried out using specially-designed apparatus to accurately measure the bending stiffness at different tensions, and to measure the axial stiffness and axial damping. A reduced-scale lab setup is used and finite element models are developed for verification of the numerical models. Experimental free and forced vibration testing are performed on the individual cantilever beam and stranded cable subsystems, and on the coupled cable-beam system to verify the numerical models in the frequency and time domains. It is concluded that the 3D bond graph models can be used to understand the interaction between cable and the structure in cabled structures, to predict the in-plane and out-of-plane natural frequencies of the pole in a pole-line system and to predict the vibration time response. It is also concluded that by adding the cable to the pole structure, some modes emerge in the eigenvalue solution of the system which may be categorized as cable dominated modes, pole dominated or hybrid modes.

Keywords: Bond Graph Modeling, Cable-Beam System, Power Line, Stranded cable, Multibody dynamics.

6.1 Introduction

Dynamic interaction between cables and the main structure in cabled structures such as cable-stayed bridges, guyed towers, cable-stayed wind turbines, and power transmission lines has been a topic of interest of researchers for many years. Understanding the interaction of cables and the main structure would be facilitated by computer simulations of coupled cable-beam response. The application area that is the focus of this paper is single pole-transmission line modeling for simulated modal testing in order to develop a non-destructive evaluation (NDE) method for electrical transmission poles based on vibration response. This literature review consists of two parts: cable-only system modeling followed by cable-beam system analysis.

Models of cables typically treat the cable as a string or a beam or as a series of beam-like segments. Models vary in their treatment of bending stiffness and cable sag due to self-weight. Ricciardi *et. al*. [51] developed a continuous model for vibration analysis of cables with sag, considering the bending stiffness. The conductor was treated as a tensioned Euler-Bernoulli beam under self-weight, and Hamilton's principle was used to obtain the equations of motion. Natural frequencies and symmetric and anti-symmetric mode shapes were obtained and the results were validated by Finite Difference (FD) and Finite Element (FE) results. It was concluded that the bending stiffness and sag of the cable has significant effect on vibration properties of the cable and ignoring them can lead to erroneous results. Sousa *et. al*. [53] used Euler-Bernoulli and Timoshenko beam theories to investigate vibration of transmission line conductors. It was concluded that neglecting shear and rotational inertia cause a very small error compared to the error caused by neglecting the bending and geometric stiffness of the cable. Papailiou [50] proposed a model for bending of stranded cables taking into account the slip and friction between the layers, obtaining a theoretical bending stiffness model for stranded cables dependent on curvature and tension, and verifying the bending stiffness model experimentally. Ni *et. al*. [76] analyzed the vibration of large diameter sagged cables using a three-node finite element. A case study compared the measured and computed natural frequencies, with and without considering cable bending stiffness, of the main cables of the Tsing Ma Bridge. Ignoring the bending stiffness of sagged cables led to unacceptable errors in predicting the natural frequencies. Jalali *et. al*. [16] developed a 2D numerical model based on the bond graph method for vibration analysis of power lines. Lumped segments were joined with axial and torsional springs and dampers representing the compliance and damping of the cable. Bending stiffness of the cable, without tension, was measured experimentally. Analytical and finite element modeling of stranded cables and wire ropes has been performed by researchers in order to study axial, bending and torsional deformations [97–100]. In general, the literature shows that bending stiffness and cable sag have significant and non-negligible effects on vibration of cable structures and should be considered in the modeling to ensure reliable results. Dynamic analysis of cable-beam systems has been attempted by many researchers using various approaches. Gattulli *et. al*. [54] studied the linear and nonlinear dynamic behavior of cable-stayed beam structures, neglecting bending stiffness of the cable in solving the equations of in-plane and out-of-plane motion. The existence of global (beam dominated), local (cable dominated) and hybrid modes was revealed by linear analysis. Chen *et. al*. [101] reviewed analysis and modeling of transmission towers, transmission lines and transmission tower-line systems subjected to dynamic excitations due to wind, ice effects and seismic motion. The review suggested that future improvements in analytical models of tower-line systems are motivated and expected. Li *et. al*. [55] presented a simplified computational model of a high-voltage transmission tower-line system under out-of-plane and in-plane vibrations due to seismic excitations. The transmission cables and their supporting towers were modeled as a lumped mass system, validated with experiments. McClure *et. al*. [102] presented a modeling approach, using the specialized finite element software ADINA®, for dynamic investigation of a tower-line section subjected to conductor rupture shock loads in two- and three-dimensional space. A case study of a tower-line system failure during an ice storm was used to validate their model. Cables were modeled using two-node iso-parametric truss elements. Pinto *et. al*. [56] developed a two-dimensional bond graph model for a pole with a cable attached to the free end on one side of the pole. The cable was modeled as a series of point masses connected by translational springs and the pole was represented by a modal expansion based on separation of variables. Modal parameters of the cable and pole-cable system were obtained numerically and experimentally. The paper concluded that a more complex model is needed to get accurate time responses.

The models developed in this paper are motivated by ongoing development of a non-destructive evaluation (NDE) method for utility poles based on vibration testing. Existing NDT methods for poles, such as ultrasonic, x-ray and resistograph, are localized damage detection methods that evaluate the strength of the pole at one specific axial location [5]. The authors are developing an NDT method to detect damage at any location, based on vibration response from modal impact testing at a single arbitrary location [7,8,15,17]. Since power lines (conductors) are attached to the poles, vibrations of the conductors affect the modal properties of the system. Removing the effect of the conductors to reveal pole properties requires a system model that captures the complex interactions between the cables and the pole.

The bond graph method allows simple submodels to be easily combined into a complex model [93]. Bond graphs, based on explicit energy flow paths among storage, dissipative, and source elements, also facilitate derivation of the dynamic equations of the system [96]. The multibond graph formalism [103] is therefore used in this paper to model the coupled cable-beam system since it facilitates the connection of the cable model to the beam model and has a straightforward procedure for deriving simulation equations. Three-dimensional bond graph models are developed for the stranded cable and beam substructures individually, and then for a coupled system with one cantilever beam and cables on two sides. These models are easily extended to larger utility pole-lines by "cutting and pasting" pole-cable submodels. Since the bending stiffness of the cables has a significant effect on modal properties of the coupled system, the cable is modeled considering the bending stiffness and sag and the beam is modeled as a cantilevered beam. The 3D rigid lumped segments are connected to each other with translational and rotational springs and dampers to model the compliance and damping of the cable and beam. The modal properties of the cable, beam and the cable-beam system are obtained and time response analysis in in-plane and out-of-plane directions is carried out in free and forced vibration simulation. The numerical models are validated with finite element and experimental results in the frequency and time domains. A setup was used to measure the bending stiffness of the stranded cable under different tensions and an experimental test was performed to measure the axial stiffness/damping. The measured values were used in the bond graph and FE models. The following Section describes the bond graph model and theoretical formulation, Section 6.3 presents the finite element model; section 6.4 and 6.5 present the experimental cable parametrization and modal testing; an elementary verification of the cable and beam submodels is presented in Section 6.6 and the coupled system results are presented in Section 6.7.

6.2 Discrete Physical Modeling

The cable is assumed to have a small sag s to length l_c ratio (namely ${}^{s}\!/_{l_\mathrm{c}} < \frac{1}{8}$) based on Irvine's model [82] and is modeled as a tensioned Euler-Bernoulli beam with sag due to self-weight. The cable-beam system is composed of one horizontal suspended cable attached to the tip of a cantilevered beam and the cantilevered beam is considered as an Euler-Bernoulli beam. Figure 6.1 shows the schematic of the cable-beam system and the cable. The inertial coordinates X, Y, Z are used to describe the positions of cables and beam in the same coordinate system. X axis is in the beam in-plane direction and Z axis is in the beam out-of-plane direction. In Figure 6.1, the bending stiffness of the beam is EI_b and the bending stiffness of the cable is EI_c.

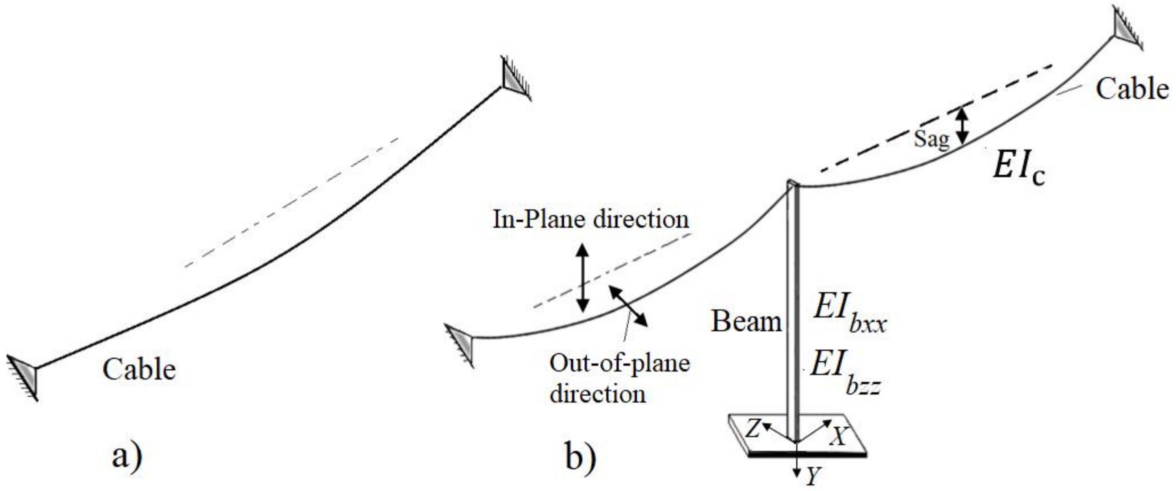

Figure 6.1. Cable and cable-beam system schematic a) 3D schematic of cable b) 3D schematic of cable-beam system

6.2.1 Bond Graphs

The bond graph method is used owing to the ease with which submodels of cables and beams can be connected to each other. In bond graphs, a small set of generalized elements is used to represent energy exchange with the environment, energy storage and dissipation, generalized loop and node laws, and power-conserving transformations and gyrator effects [104,105]. The connection of the cable bond graph submodels to the beam bond graph submodel is as simple as drawing a power bond between them.

6.2.1.1 3D Segment Submodel

The cables and beam are modeled with 3D rigid lumped segments connected with translational and rotational springs and dampers. The bond graph model with lumped segments has been used for different applications for modeling coupled system dynamics [104,106,107]. The greater the number of segments, the more accurate is the model. Excessive segments, beyond the number required for the numerical model results to converge to analytical results, increase simulation time. In this model, convergence studies in the time and frequency domains were performed and when increasing the number of segments above 30 for cable and beam, there was no significant improvement in the results. Thus 30 segments were used for modeling of the cable and 30 segments were used to model the cantilevered beam. The lumped segments of the cable and beam are joined with a translational spring and three rotational springs. Figure 6.2 shows beam and cable segments connected with springs. Dampers, not shown, are assumed to act in parallel with the springs. The translational springs correspond to the axial compliance of the beam and cable, $K_{\text{axial}_{\text{beam}}}$, $K_{\text{axial}_{\text{cable}}}$, respectively. The shear compliance of the beam and cables are not considered in the analyses as they have negligible effect on the dynamics of the cables and the coupled system [53] .Rotary springs $K_{\text{bend}_{\text{beamy}}}$, $K_{\text{bend}_{\text{beamz}}}$ are the bending compliance of the beam about the local *y* and *z* directions, respectively and $K_{\text{bend}_{\text{cable}}}$ is the bending compliance of the cable about the local body-fixed *y* and *z* directions. These stiffnesses are the same because of the axial symmetry of the cables. $K_{\text{tor}_{\text{beam}}}$ is the torsional compliance of the beam about body-fixed *x* coordinate and $K_{\text{tor}_{\text{cable}}}$ is the torsional compliance of the cable about body-fixed *x* direction. In Figure 6.2, the bending rotary springs about the *z* direction are not shown for clarity and the springs are along the body-fixed coordinates of the body *i*+1 in beam and cable segments. A similar description of the lumped segment model can also be found in [106] for different applications.

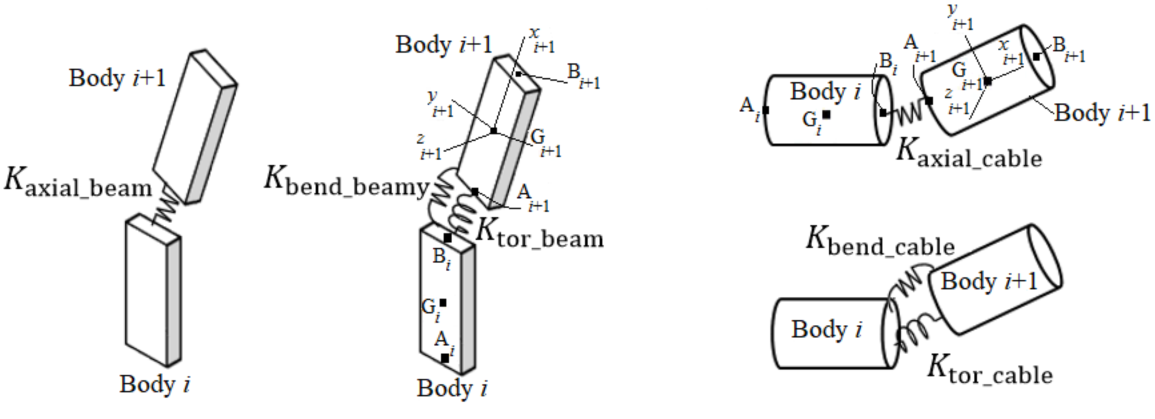

a)

b)

Figure 6.2: Successive multibody segments of a) beam b) cable

Stiffness values are computed for a segment lengths of $l_{\mathrm{b}} = \frac{L_{\mathrm{b}}}{n_{\mathrm{b}}}$ (beam of length $L_{\mathrm{b}}$with n_{b} segments) and $l_{\mathrm{c}} = \frac{L_{\mathrm{c}}}{n_{\mathrm{c}}}$ (cable of length L_{c} with n_{c} segments) [93,106]:

$$K_{\mathrm{axial}_{\mathrm{beam}}} = \frac{E_{\mathrm{b}} A_{\mathrm{b}}}{l_{\mathrm{b}}} \tag{6.1}$$

$$K_{\mathrm{axial}_{\mathrm{cable}}} = \frac{E_{\mathrm{c}} A_{\mathrm{c}}}{l_{\mathrm{c}}} \tag{6.2}$$

$$K_{\mathrm{bend}_{\mathrm{beamy}}} = \frac{E_{\mathrm{b}} I_{by}}{l_{\mathrm{b}}}, K_{\mathrm{bend}_{\mathrm{beamz}}} = \frac{E_{\mathrm{b}} I_{\mathrm{bz}}}{l_{\mathrm{b}}} \tag{6.3}$$

$$K_{\mathrm{bend}_{\mathrm{cable}}} = \frac{E_{\mathrm{c}} I_{\mathrm{c}}}{l_{\mathrm{c}}} \tag{6.4}$$

$$K_{\mathrm{tor}_{\mathrm{beam}}} = \frac{G_{\mathrm{b}} J_{\mathrm{b}}}{l_{\mathrm{b}}} \tag{6.5}$$

$$K_{\mathrm{tor}_{\mathrm{cable}}} = \frac{G_{\mathrm{c}} J_{c}}{l_{\mathrm{c}}} \tag{6.6}$$

where E_{b} and E_{c} are the elastic moduli of the beam and cable, respectively. A_{b} and A_{c} are the cross sectional areas of beam and cable, respectively. I_{by}, I_{bz} and I_{c} are the moments of area of the beam about local *y* and *z* axes, and cable moment of area, respectively. G_{b} and G_{c} are the modulus of rigidity of cable and beam, respectively and J_{b} and J_{c} are the polar moments of area. The cable axial damping values are measured experimentally (Section 6.4.2) and other damper values are tuned in the models to give a close time response compared to experimental time responses. The axial, $(E_{\mathrm{c}} A_{\mathrm{c}})$, and bending $(E_{\mathrm{c}} I_{\mathrm{c}})$, stiffnesses of the cable were measured (Section 6.4) and the resulting values were used in the models.

6.2.1.2 Bond Graph of Segments and Joints

Mechanics in bond graphs is done from a velocity standpoint, necessitating relative velocity equations between segment center of gravity and connection points. The following equation relates the velocity of end point A of body *i* to velocity of the center of gravity G of body *i* (Figure 6.2) [106]:

$$ {}^{i}\vec{V}_{\mathrm{A}i} = {}^{i}\vec{V}_{\mathrm{G}i} + {}^{i}\vec{V}_{\frac{\mathrm{A}i}{\mathrm{G}i}} \tag{6.7} $$

$$ {}^{i}\vec{V}_{\frac{\mathrm{A}i}{\mathrm{G}i}} = {}^{i}\vec{\omega}_{i} \times {}^{i}\vec{r}_{\frac{\mathrm{A}i}{\mathrm{G}i}} = {}^{i}\tilde{r}_{\frac{\mathrm{A}i}{\mathrm{G}i}}{}^{i}\vec{\omega}_{i} \tag{6.8} $$

where the left superscript i indicates that the vector is presented in a local body-fixed coordinate system (Figure 6.2), ${}^{i}\vec{V}_{\mathrm{A}i}$ is the absolute velocity of point A on body i resolved along body-fixed component directions, ${}^{i}\vec{\omega}_{i}$ is the angular velocity vector, ${}^{i}\vec{r}_{\frac{\mathrm{A}i}{\mathrm{G}i}}$ is the position vector of point A with respect to G and ${}^{i}\tilde{r}_{\frac{\mathrm{A}i}{\mathrm{G}i}}$ is the skew-symmetric matrix containing the relative position vector components. The relative position matrix ${}^{i}\tilde{r}_{\frac{\mathrm{A}i}{\mathrm{G}i}}$ is used here to express the equations in a matrix multiplication form which is common in multibond graphs [103] and is beneficial in programming the equations. The relative position vector ${}^{i}\vec{r}_{\frac{\mathrm{A}i}{\mathrm{G}i}}$ and relative position matrix ${}^{i}\tilde{r}_{\frac{\mathrm{A}i}{\mathrm{G}i}}$ are the following:

$$ {}^{i}\vec{r}_{\frac{Ai}{Gi}} = \left(\frac{-l_s}{2}\right)\hat{\imath} + (0)\hat{\jmath} + (0)\hat{k} \tag{6.9} $$

$$ {}^{i}\tilde{r}_{\frac{\mathrm{A}i}{\mathrm{G}i}} = \begin{bmatrix} 0 & 0 & 0 \\ 0 & 0 & \frac{-l_s}{2} \\ 0 & \frac{l_s}{2} & 0 \end{bmatrix} \tag{6.10} $$

where l_s is the segment length (can be l_b or l_c in Eq. (6.1)-(6.6)) and $\hat{\imath}$, $\hat{\jmath}$ and $\hat{k}$ are along the *x*, *y* and *z* body-fixed coordinates of segment *i*, respectively (Figure 6.2). All the other vectors (linear and rotational velocity, etc.) are also represented by column vectors of their components in the local coordinate system. The equations below describes Newton's law in three dimensions for the segment in local coordinates [106].

$$ \sum {}^{o}\vec{F} = \frac{d}{dt}\left(m{}^{o}\vec{V}_{Gi}\right) = m{}^{o}\dot{\vec{V}}_{Gi} \tag{6.11} $$

$$\sum {}^{i}\vec{\tau} = \frac{d}{dt}\,{}^{i}\vec{H} = J\,{}^{i}\dot{\vec{\omega}}_i + {}^{i}\vec{\omega}_i \times J\,{}^{i}\vec{\omega}_i \tag{6.12}$$

where left superscript *o* indicates that the vector is defined in the inertial coordinate system, *m* is the mass and *J* is the rotational inertia. The first term in the right side of rotational Eq. (6.12) is the rotational inertia term and the second term is a gyrational term. Including forces such as gravity and equating vectors in different reference frames requires coordinate transforms from the body fixed frame to the inertial frame. This is accomplished with a rotation matrix. Rotation matrices are made for each of the three rotations ψ, θ, ϕ about z, y and x axes, respectively. These matrices are multiplied together to create the transformation matrix. The final simplified rotation matrix is shown in the following equation that transforms coordinate frames from body fixed to inertial [93]:

$$\begin{bmatrix} X \\ Y \\ Z \end{bmatrix} = \begin{bmatrix} \cos\theta\cos\psi & -\cos\theta\sin\psi & \sin\theta \\ \cos\theta\sin\psi + \sin\phi\sin\theta\cos\psi & \cos\phi\cos\psi - \sin\phi\sin\theta\sin\psi & -\sin\phi\cos\theta \\ \sin\phi\sin\psi - \cos\phi\sin\theta\cos\psi & \sin\phi\cos\psi + \cos\phi\sin\theta\sin\psi & \cos\phi\cos\theta \end{bmatrix} \begin{bmatrix} x \\ y \\ z \end{bmatrix} \tag{6.13}$$

The following equation relates angular velocity components to the rates of change of orientation angles: [93]

$$\vec{\omega} = \begin{bmatrix} \omega_x \\ \omega_y \\ \omega_z \end{bmatrix} = R\vec{\Omega} = \begin{bmatrix} 1 & 0 & -\sin\theta \\ 0 & \cos\phi & \cos\theta\sin\phi \\ 0 & -\sin\phi & \cos\phi\sin\theta \end{bmatrix} \begin{bmatrix} \dot{\phi} \\ \dot{\theta} \\ \dot{\psi} \end{bmatrix} \tag{6.14}$$

Eq. (6.14) transforms the orientation angle rates into the body fixed angular velocity components. Taking the inverse of matrix *R* will allow us to transform in the other direction. The inverse transformation matrix is shown below.

$$R^{-1} = \begin{bmatrix} 1 & \sin\phi\tan\theta & \cos\phi\tan\theta \\ 0 & \cos\phi & -\sin\phi \\ 0 & \frac{\sin\phi}{\cos\theta} & \frac{\cos\phi}{\cos\theta} \end{bmatrix} \tag{6.15}$$

Figure 6.3 shows the symbols and constitutive laws of sources, storage and dissipative elements, and power-conserving elements in scalar form [108]. Figure 6.4 shows the vector bond graph submodel representing the body segment *i* of the cable and beam (developed in 20sim® software). The dynamic equations for the cable and beam segments are the same, thus, the bond graph formulation is the same for cable and beam. In Figure 6.4, the one-junctions are labeled with the corresponding translational or rotational velocities. Translational velocity Eq. (6.7) for defining the velocity of left end point A of the segment and the similar equation for the velocity of the right end point B of the segment with respect to center of mass in the body-fixed coordinates are represented by two modulated transformers (MTF) and two 0-junctions in Figure 6.4. A 0-junction is used to add ${}^{i}\vec{V}_{\mathrm{G}i}$ to ${}^{i}\tilde{r}_{\frac{\mathrm{A}i}{\mathrm{G}i}}{}^{i}\vec{\omega}_{i}$ to obtain ${}^{i}\vec{V}_{\mathrm{A}i}$ and a 0-junction is used to add ${}^{i}\vec{V}_{\mathrm{G}i}$ to ${}^{i}\tilde{r}_{\frac{\mathrm{B}i}{\mathrm{G}i}}{}^{i}\vec{\omega}_{i}$ to obtain ${}^{i}\vec{V}_{\mathrm{B}i}$. The two MTF's representing relative velocity cross products use the relative position vector as an input signal. The coordinate transformation between body-fixed and inertial frames is represented by an MTF that multiplies the transformation matrix and ${}^{i}\vec{V}_{\mathrm{G}i}$ to obtain inertial center of gravity velocity ${}^{\mathrm{o}}\vec{V}_{\mathrm{G}i}$. Translational force Eq. (6.11) is represented by a mass matrix multiport *I* element and the gravity effort source connected to the ${}^{\mathrm{o}}\vec{V}_{\mathrm{G}i}$ 1-junction. Orientation angle rates $[\dot{\theta} \quad \dot{\psi} \quad \dot{\phi}]^{T}$ are obtained by multiplication of the ${}^{i}\vec{\omega}_{i}$ body-fixed angular velocity by the matrix in Eq. (6.15), followed by integration to obtain the transformation angles $[\theta \quad \psi \quad \phi]^{T}$. The right hand side of Eq. (6.12) is represented by a rotational inertia *I* element and a modulated gyrator MGY. Other elements bonded to the ${}^{i}\vec{\omega}_{i}$ 1-junction create the external moments from joints *i* and *i*-1 and moments from forces at end points A and B. An MGY is used to represent the cross product ${}^{i}\vec{\omega}_{i} \times \vec{J}\,{}^{i}\vec{\omega}_{i}$.

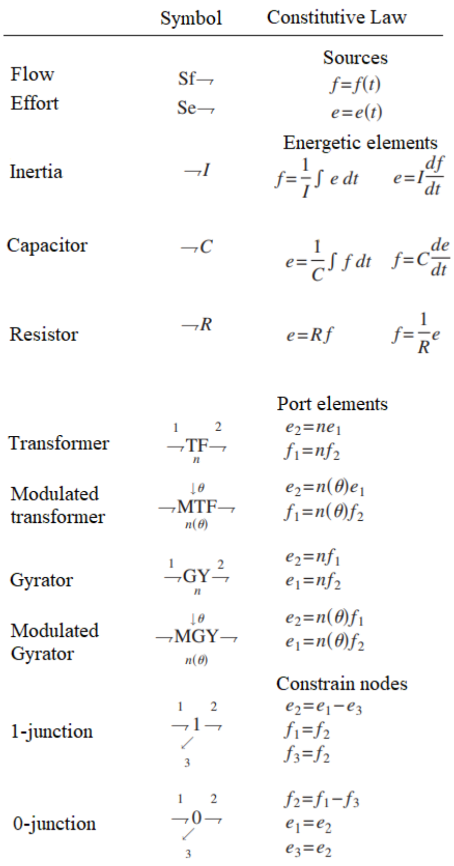

	Symbol	Constitutive Law
		Sources
Flow	$\mathrm{Sf}\rightharpoonup$	$f=f(t)$
Effort	$\mathrm{Se}\rightharpoonup$	$e=e(t)$
		Energetic elements
Inertia	$\rightharpoonup I$	$f=\frac{1}{I}\int e\,dt$ $e=I\frac{df}{dt}$
Capacitor	$\rightharpoonup C$	$e=\frac{1}{C}\int f\,dt$ $f=C\frac{de}{dt}$
Resistor	$\rightharpoonup R$	$e=Rf$ $f=\frac{1}{R}e$
		Port elements
Transformer	$\overset{1}{\rightharpoonup}\underset{n}{\mathrm{TF}}\overset{2}{\rightharpoonup}$	$e_2=ne_1$ $f_1=nf_2$
Modulated transformer	$\rightharpoonup\overset{\downarrow\theta}{\underset{n(\theta)}{\mathrm{MTF}}}\rightharpoonup$	$e_2=n(\theta)e_1$ $f_1=n(\theta)f_2$
Gyrator	$\overset{1}{\rightharpoonup}\underset{n}{\mathrm{GY}}\overset{2}{\rightharpoonup}$	$e_2=nf_1$ $e_1=nf_2$
Modulated Gyrator	$\rightharpoonup\overset{\downarrow\theta}{\underset{n(\theta)}{\mathrm{MGY}}}\rightharpoonup$	$e_2=n(\theta)f_1$ $e_1=n(\theta)f_2$
		Constrain nodes
1-junction	$\overset{1}{\rightharpoonup}\underset{\swarrow 3}{1}\overset{2}{\rightharpoonup}$	$e_2=e_1-e_3$ $f_1=f_2$ $f_3=f_2$
0-junction	$\overset{1}{\rightharpoonup}\underset{\swarrow 3}{0}\overset{2}{\rightharpoonup}$	$f_2=f_1-f_3$ $e_1=e_2$ $e_3=e_2$

Figure 6.3: Bond graph elements [108]

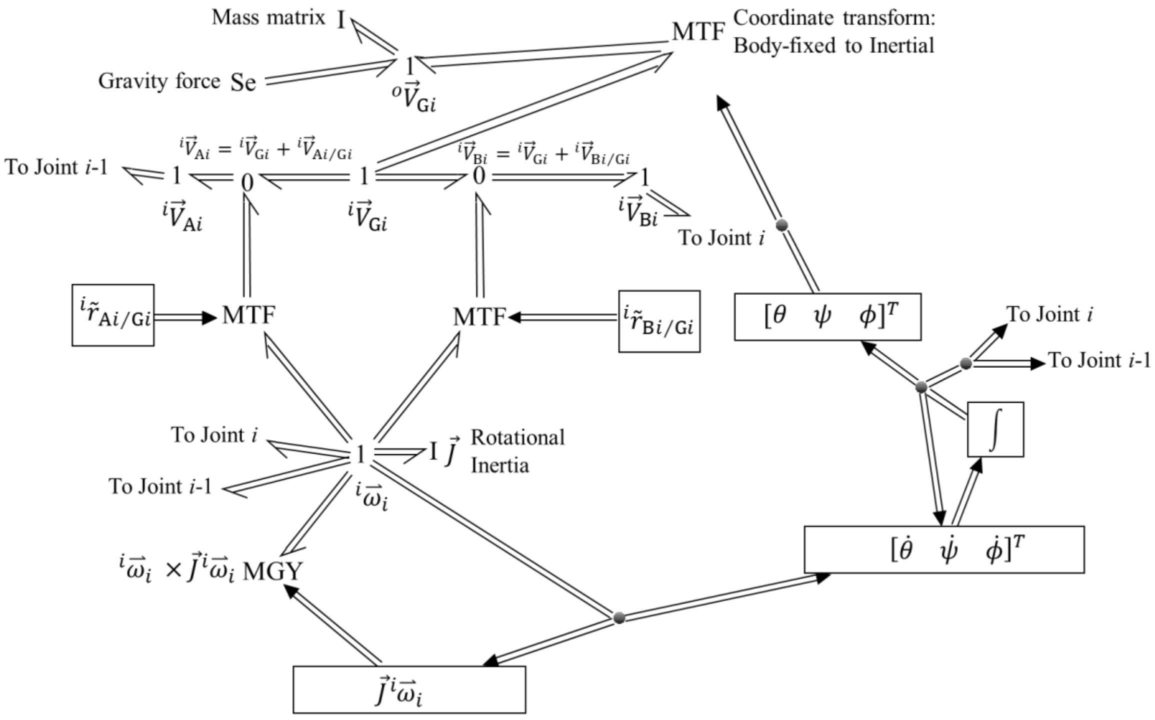

Figure 6.4: Body i bond graph

Figure 6.5 shows the bond graph submodel of joint *i* between successive segments (developed in 20sim® software). The 0-junctions represent the translational and angular velocity constraints that are caused by parallel spring/dampers between the left end point A of body *i*+1 and right end point B of body *i* (Figure 6.2). The velocity of B on body i, ${}^{i}\vec{V}_{\mathrm{B}i}$, and angular velocity ${}^{i}\vec{\omega}_{i}$ are first transformed to the inertial coordinate system using a pair of MTF's and then transformed to the body *i*+1 local coordinate system using another pair of MTF's. The *C* multiport elements model the stiffness described in Eq's. (6.1)-(6.6) using a diagonal stiffness matrix. The *R* elements define the damping using a damping matrix. The cable axial damping is measured and the other damping values are tuned to reduce discrepancies between numerical and experimental time response and natural frequencies.

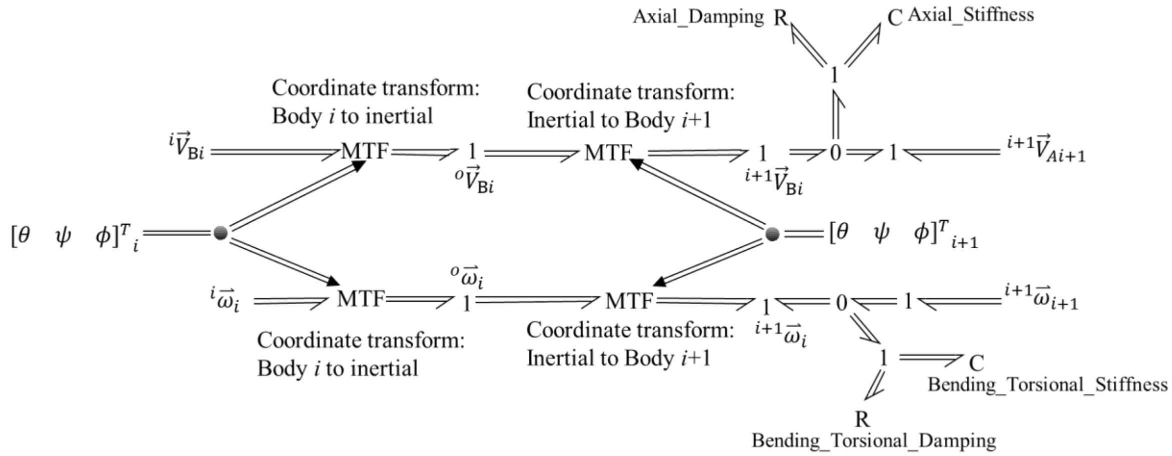

Figure 6.5: Joint i submodel bond graph

6.2.2 Cable-Beam Connection Bond Graph

Figure 6.6 illustrates the segments of the beam and cable at the connection point. The connection of the cable to the tip of the beam is realized by bonding the 1-junctions associated with the beam tip velocities and the cable endpoint velocities. Figure 6.7 shows the bond graph model at the connection point of beam tip and the cable. The angles that are calculated in the n_{c}-th joint submodel of the left cable are input as a signal to the beam tip segment and then the calculated angles in the beam tip segment are input signal for the first joint of the right cable attached to the beam. Beam tip velocity at point A (Figure 6.2), ${}^{n_\mathrm{b}}\vec{V}_{\mathrm{A}n_\mathrm{b}}$ is connected to the lower joint submodel of beam (joint n_b in Figure 6.7). Velocity of point B of the highest beam segment, ${}^{n_\mathrm{b}}\vec{V}_{\mathrm{B}n_\mathrm{b}}$ is connected to the joint n_c of left cable and the first joint of right cable in the beam n_b-th coordinate system. Rotational velocity 1-junctions are also bonded in the cable endpoints and the beam tip.

$$
{}^{n_\mathrm{b}}\vec{V}_{\mathrm{B}n_\mathrm{c}} = {}^{n_\mathrm{b}}\vec{V}_{\mathrm{B}n_\mathrm{b}} = {}^{n_\mathrm{b}}\vec{V}_{\mathrm{A}1}
$$

$$
{}^{n_\mathrm{b}}\vec{\omega}_{n_\mathrm{c}} = {}^{n_\mathrm{b}}\vec{\omega}_{n_\mathrm{b}} = {}^{n_\mathrm{b}}\vec{\omega}_{1}
$$

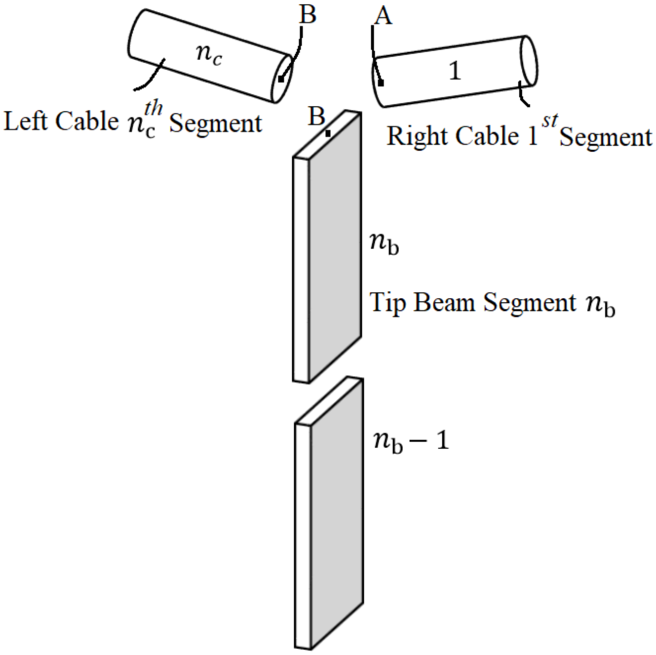

Figure 6.6: Connection point segments

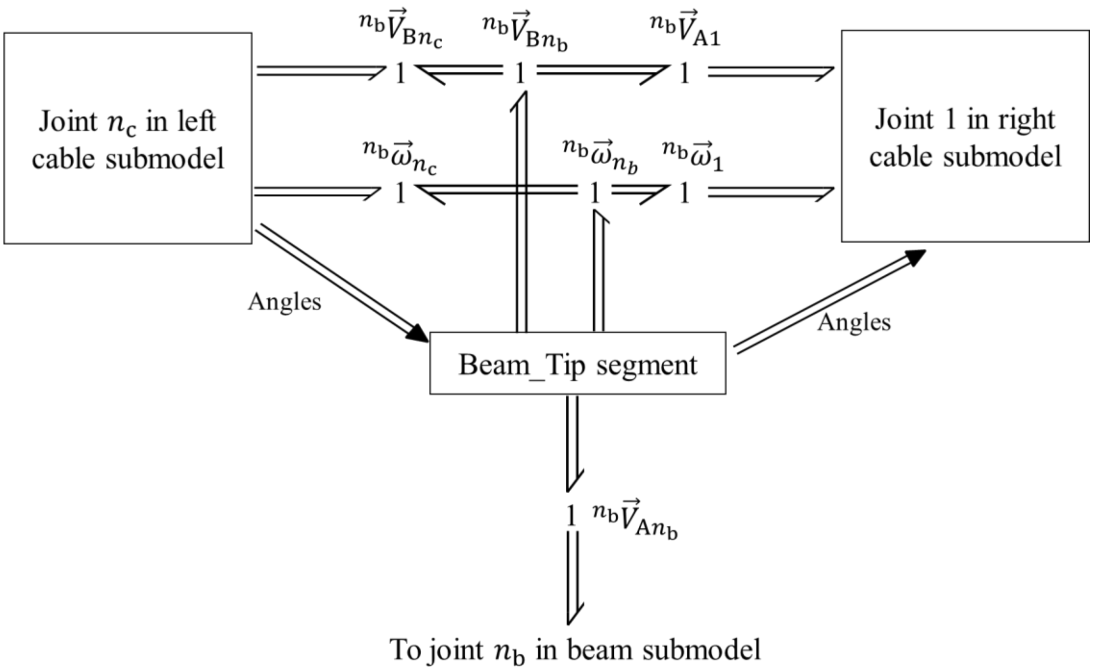

Figure 6.7: Cable and beam connection bond graph (developed in 20sim® software)

Two end points of the right and left cables are pinned to the wall and therefore have zero translational velocity. Thus, zero flow source is used at each end point to define the pin connection. The fixed boundary condition of the beam is applied by zero flow sources for translational and rotational velocities at the bottom-most point of the beam. In order to create the desired tension in the cable, the model is first given zero initial displacement and then stretched until the desired tension is achieved. Five values of tension are considered for the analysis. For applying the stretching displacement to the cable in the bond graph model, a flow source was temporarily applied to the 1-junction associated with the velocities of the end points of the left and right cables in the local *x* direction. After creating the desired tension, the zero flow source was reinstated at the right end.

6.3 Finite Element Model

The three-dimensional finite element model of the beam-cable system and the cable were developed in Ansys® software using solid elements. The model consists of around 36000 solid linear elements with each element having 48 degrees of freedom and 16 nodes. The displacement of the free end of the beam is defined to be equal to the displacements of one end cross section of each of the left and right cables with “bonded connection” boundary condition in Ansys®. The cables are pinned at the other end points and the beam is cantilever. A pre-tension is first applied to the cable and then Eigen Value analysis is performed and the natural frequencies and mode shapes of the system are obtained in a pre-stressed modal analysis. A convergence study was also performed and the results did not change significantly after having a finer mesh. The cables are modeled as cylinders but the geometric and mechanical properties of the cables are defined such that they match the measured bending stiffness and axial stiffness (Section 6.4) and mass of the cable at each value of tension. In order to have a cable model that matches the measured values of bending stiffness and axial stiffness and has the correct mass, the values of Young’s modulus, volumetric density and diameter of the cylinder model are adjusted at each value of tension so that the following equations are enforced:

$$
\begin{aligned}
&E_\mathrm{c} I_\mathrm{c} = a \Rightarrow E_\mathrm{c} \frac{\pi {d_\mathrm{c}}^4}{64} = a \\
&E_\mathrm{c} A_\mathrm{c} = b \Rightarrow E_\mathrm{c} \frac{\pi {d_\mathrm{c}}^2}{4} = b \qquad (6.16) \\
&\rho_\mathrm{c} A_\mathrm{c} = c \Rightarrow \rho_\mathrm{c} \frac{\pi {d_\mathrm{c}}^2}{4} = c
\end{aligned}
$$

where a, b are the measured bending stiffness and axial stiffness of the cable (Section 6.4) and c is the linear density of the cable, known from the cable manufacturer catalogue. Eq. (6.16) has three unknowns that can be solved using linear algebra so that the values of E_c, d_c and ρ_c can be calculated for each tension. The measured bending stiffness is different in each cable tension but the axial stiffness and linear density are the same, thus; all the three values of E_c, d_c and ρ_c are different in each tension.

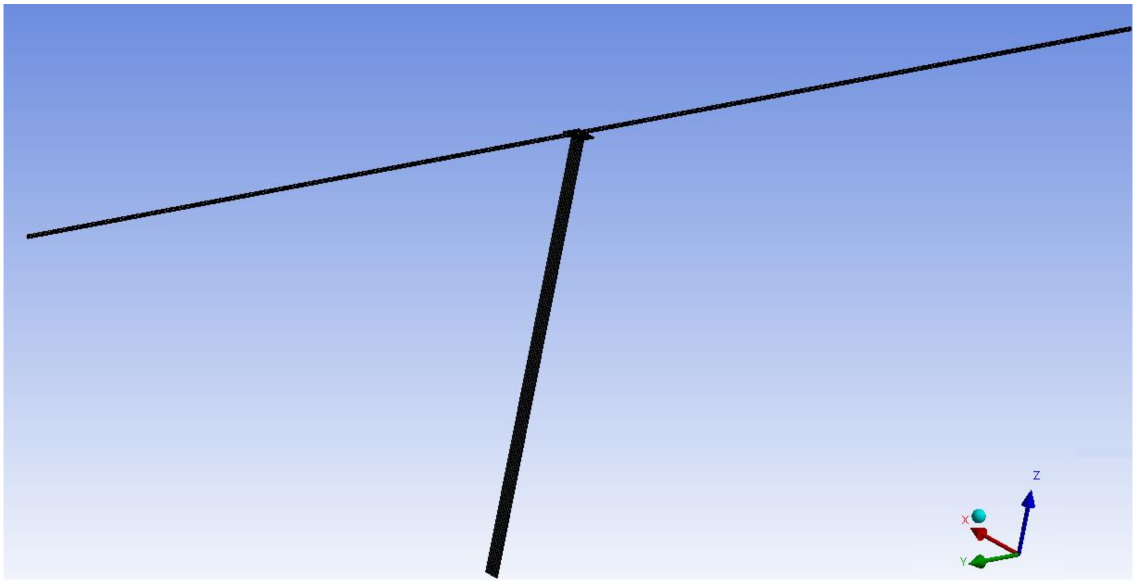

Figure 6.8: Finite element model of the cable-beam system

6.4 Experimental Cable Parameterization and Vibration Testing

In order to have a reliable numerical model for the stranded cable, the cable mechanical properties must be measured accurately. The stranded cable used in this study is a steel 7×19 cable with a nominal diameter of a quarter inch and the linear density of 0.16667 kg/m. An apparatus was designed to measure the bending stiffness $(E_c I_c)$ of the cable under different tensions, and a second apparatus was designed to measure the axial stiffness $(E_c A_c)$ and axial damping ratio (ξ). In Section 6.4.1, the bending stiffness measurement is described, the axial stiffness test is explained in section 6.4.2 and the experimental vibration tests on the cable and cable-beam system are detailed in Section 6.5.

6.4.1 Bending Stiffness Measurement

6.4.1.1 Theory

Figure 6.9 shows the schematic of the test set up used to measure bending stiffness of the cable under different tensions. The load Q is applied at the midpoint of the span length l of the cable causing the deflection δ at the mid-span and the cable is under tension P.

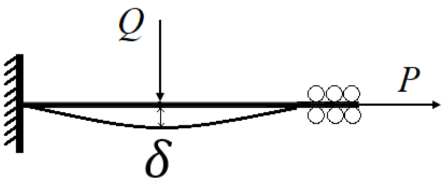

Figure 6.9. Schematic of bending stiffness tests

By solving the partial differential equation for the static deflection of an Euler beam under tension, deflection of the mid-span of the beam is [86]:

$$\delta = \frac{Ql^3}{48EI_\mathrm{c}}\left[\frac{3\lambda\sinh\lambda+6(1-\cosh\lambda)}{\lambda^3\sinh\lambda}\right] \tag{6.17}$$

where l is the span length, EI_c is bending stiffness of the cable and λ is the following:

$$\lambda = \sqrt{\frac{Pl^2}{4EI_\mathrm{c}}} \tag{6.18}$$

Eq. (6.17) can be rewritten as [86]:

$$\frac{4P\delta}{Ql} = 1 + \frac{2(1-\cosh\lambda)}{\lambda\sinh\lambda} \tag{6.19}$$

In order to obtain the bending stiffness EI of the cable, the ratio of $\frac{4P\delta}{Ql}$ was calculated for each value of tension P since the deflection-force diagram for the deflection range was considered linear. Eq. (6.19) was then solved numerically for each value of P to solve for λ and then EI_c was calculated using Eq. (6.18). The bending stiffness of stranded cables is bounded by two flexural stiffnesses EI_max and EI_min [15]. The former corresponds to a solid cross section with no slippage of the strands and wires relative to each other, and the latter corresponds to unrestricted wires and strand slip [15]:

$$EI_\mathrm{max} = E\sum_{i=1}^{N_s}\left(\frac{\pi {d_{si}}^4}{64} + \frac{\pi {d_{si}}^2}{4}{y_{si}}^2\right) \approx E\frac{\pi {d_\mathrm{c}}^4}{64} \tag{6.20}$$

$$EI_\mathrm{min} = E\sum_{i=1}^{N_s}\frac{\pi {d_{si}}^4}{64} \tag{6.21}$$

where d_{si} is the diameter of the i^{th} strand, y_{si} is the distance from the center of gravity of the i^{th} strand to the center of gravity of the conductor, d_c is the dimeter of the cable and N_s is the number of strands in the cable. The bending stiffness values that were measured in the present study fall within this range for all tensions, and are closer to the minimum bending stiffness limit.

6.4.1.2 Experimental Set up for Bending Stiffness Measurement

Figure 6.10 shows the setup for bending stiffness measurement. A hydraulic cylinder was used to apply the load Q at the middle of the cable and a high accuracy linear variable displacement transducer OMEGA LD621-150 (LVDT) was attached to the cylinder to measure the deflection of the cable at mid-span (δ). A threaded rod was used to adjust the tension in the cable and an inline tension/compression load cell STI 1608966 was used to measure cable tension P. An S-type load cell INTERFACE SSMF was attached to the cylinder to measure the applied load.

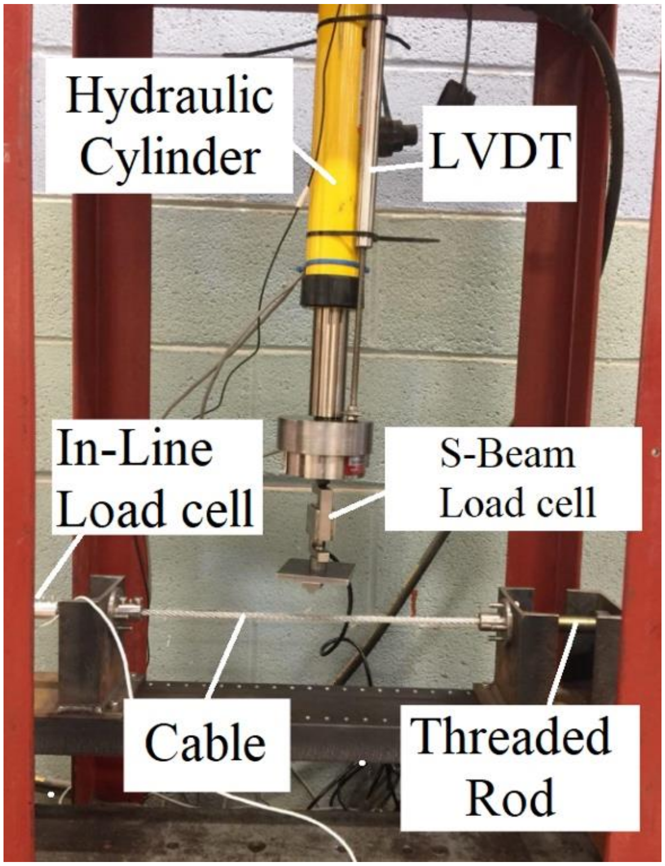

Figure 6.10: Experimental set up for measuring the bending stiffness of the cable

The bending tests were carried out with cable tension values of 25 N, 100 N, 200 N and 300 N. Table 6.1 presents the measured bending stiffness values. The theoretical limits of bending stiffness using Eq'ns. (6.20) and (6.21) are $EI_{\text{max}} = 15.5632$ and $EI_{\text{min}} = 0.0306$, respectively. As can be seen from Table 6.1, the bending stiffness values increase with tension.

Table 6.1. Measured bending stiffness in different tensions

Tension (N)	EI (Nm^2)
25	0.2549
100	0.4948
200	0.5972
300	0.8283

6.4.2 Axial Stiffness-Damping Measurement

6.4.2.1 Theory

Experimental characterization was carried out to measure the axial stiffness and damping of the cable. Axial stiffness of the cable is $\frac{E_\text{c}A_\text{c}}{l_\text{c}}$ (Eq. (6.2)) is assumed be to in the linear elastic range governed by Hooke's Law [109]:

$$F = kx \tag{6.22}$$

where F is the applied tension, k is the spring constant of the cable and x is the elongation caused by the tension F. For a homogeneous solid cylinder, the spring constant can be calculated using the Young's modulus of the material and the geometrical properties. However, the $E_\text{c}A_\text{c}$ value for a stranded cable cannot be calculated because of the complicated axial deformation behavior arising from the multiple wires and strands [29]. Previous attempts to obtain analytical axial and/or torsional stiffness theories for wire ropes and stranded cables can be found in [99][109][111][112] , but alternatively the spring constant of the cable can be measured using single degree of freedom (SDOF) mass-spring-damper oscillator theory. By initiating free vibration of a known mass hanging from the cable, the stiffness and damping properties can be identified [113]. Figure 6.11 shows the schematic of a SDOF system with cable as the spring.

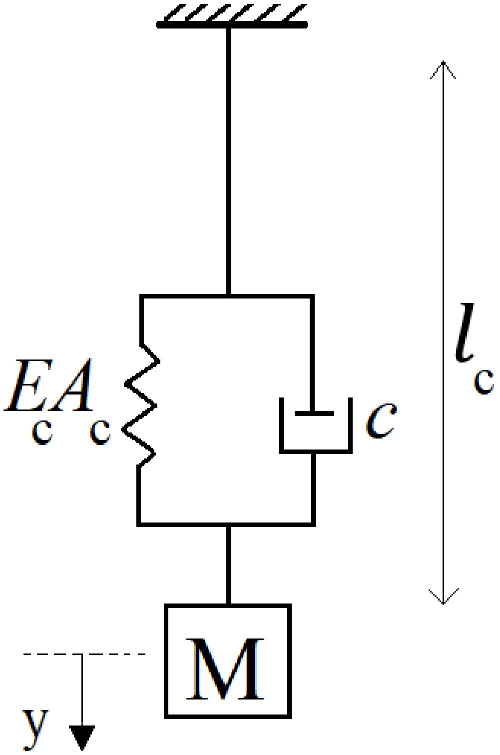

Figure 6.11: Cable and mass as SDOF oscillator

The damped frequency $\omega_d = \frac{2\pi}{\tau_d}$ can be calculated by measuring the time period of the oscillation (τ_d) and, after measuring damping ratio using logarithmic decrement, the following equation can be used to determine stiffness:

$$\sqrt{\frac{k}{M+\frac{m_c}{3}}}\sqrt{1-\xi^2} = \omega_d \tag{6.23}$$

where M is the hung mass (Figure 6.11) and m_c is the mass of the cable. The equivalent damping constant c can be calculated using the damping ratio:

$$\xi = \frac{c}{2\sqrt{kM}} \tag{6.24}$$

The calculated E_cA_c value and the damping constant were used in bond graph model for axial stiffness and damping, respectively.

6.4.2.2 Experimental Setup

Figure 6.12 shows the schematic of axial stiffness-damping measurement set up.

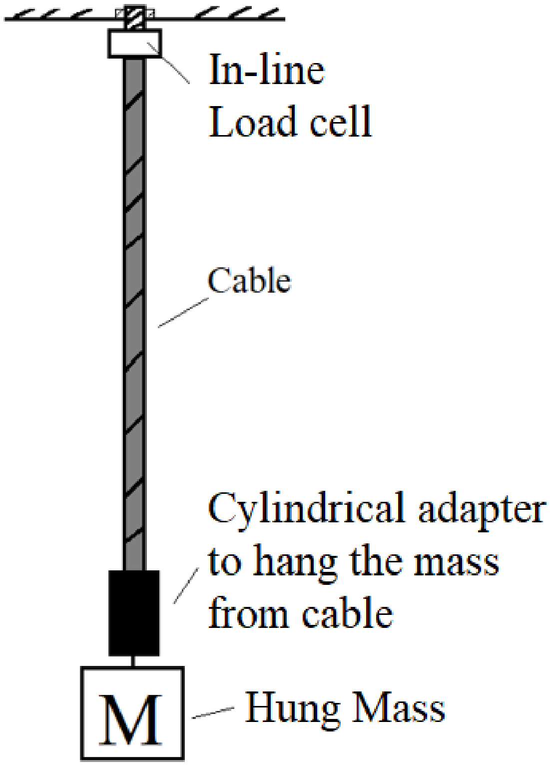

Figure 6.12: Axial stiffness-damping measurement schematic

A known mass (2.2 kg) was suspended from a measured length of the cable and an in-line load cell (Figure 6.12) was used to monitor the tension during the oscillation. In order to hang the mass from the end of the cable, a cylindrical adapter was used. Three sample lengths of 70 cm, 1 m and 1.3 m were used, and for each sample length, five impulses were applied to the sprung mass. Figure 6.13 shows the set up used for measurement. The tension was recorded with 500 Hz sampling frequency.

Figure 6.13: Axial stiffness and damping measurement set up

The difference of the results obtained from the three different sample lengths were negligible and the average results obtained from three sample lengths were considered for the final result. Figure 6.14 shows a recorded tension obtained from a 1 m sample length after curve fitting. Tension time response in Figure 6.14 was used to obtain the parameters.

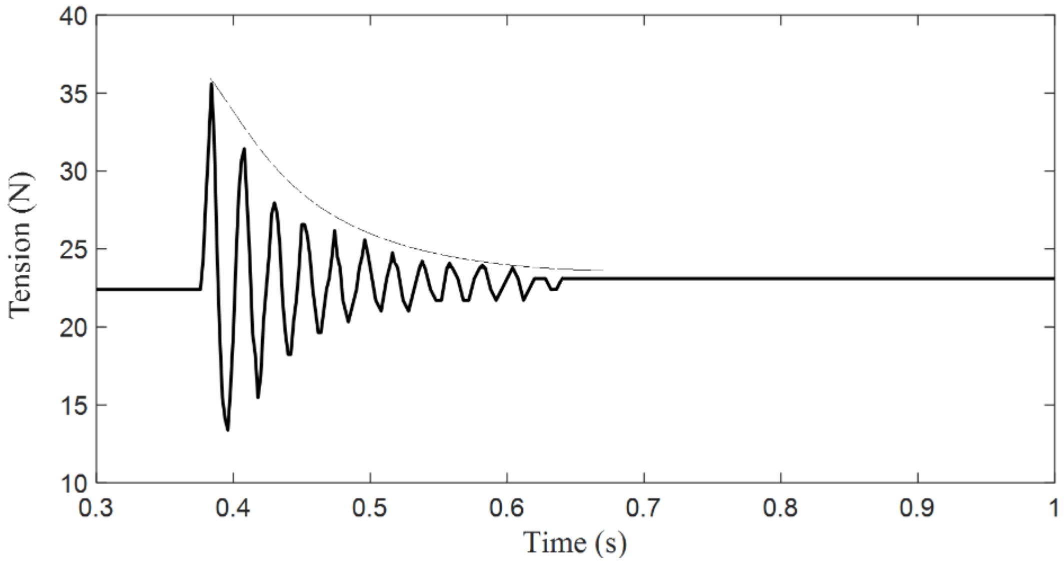

Figure 6.14: Tension record for the mass-spring-damper system using 1 m sample length

The axial stiffness of the cylindrical adapter used for hanging the cable had a small but non-negligible effect that was accounted for by treating it as a spring in series with the cable.

$$\frac{1}{k_{\mathrm{c}}} = \frac{1}{k} - \frac{1}{k_{\mathrm{m}}} \tag{6.25}$$

where k_m is the cylindrical adapter axial stiffness $\frac{E_{\mathrm{m}}A_{\mathrm{m}}}{l_{\mathrm{m}}}$ that can be simply calculated from material and geometric properties, k is the calculated spring constant from Eq. (6.23) and k_{c} is the cable spring constant. The value of $k_{\mathrm{c}}l_{\mathrm{c}}$ is a constant for a given cable and independent of cable length. The measured values for axial stiffness and damping ratio are $(E_{\mathrm{c}}A_{\mathrm{c}}) = 221.78$ kN and $\xi = 0.017$.

6.5 Vibration Testing

In order to validate the numerical models for cable, beam and cable-beam system, free and forced vibration tests were performed and the modal properties and time responses were obtained. The following sections present the procedure for vibration testing on the cable and cable-beam system. Modal test was also carried out on the cantilever beam but not explained here for brevity and only it’s results are presented in Section 6.6.1.

6.5.1 Cable Vibration Tests

Figure 6.15 presents the schematic of the vibration tests on the cable. Two rigid frames were secured to the floor. The right end of the cable was attached to a threaded rod to adjust the tension. An in-line load cell was used at the left end of the cable to measure the longitudinal tension. The test set up, in-line load cell and the threaded rod are shown in Figure 6.16. Two types of vibration tests were performed on the cable: Experiment *A* and Experiment *B*. Experiment *A* (Figure 6.15-a) is the modal testing for obtaining the natural frequencies of the cable in in-plane and out-of-plane directions. The modal tests were carried out with 25 N, 100 N, 200 N and 300 N cable tensions. The hammer hits were applied one quarter of the way along the cable in in-plane and out-of-plane directions in two separate tests and the accelerometers were placed at the mid-span. In addition to the in-plane accelerometer shown in Figure 6.15-a, another accelerometer that is not shown in the figure was also used (perpendicular to the plane of Figure 6.15) to measure the out-of-plane vibration due to a hammer impact load in that direction. Each test was performed five times and the average result was considered for the analysis. The cable was supported with a pin connection at both ends and the span length between the rigid frames was 2.4 m.

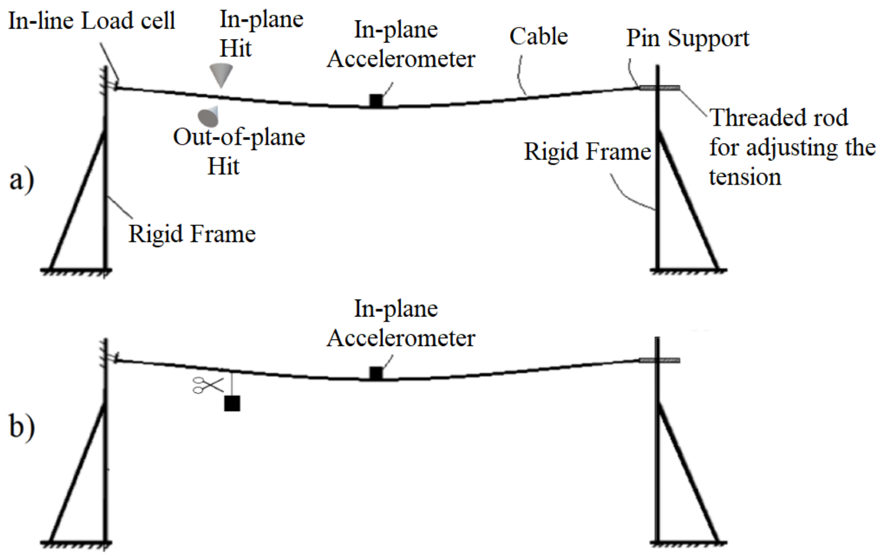

Figure 6.15: Schematic of vibration testing of the stranded cable a) Experiment A b) Experiment B

Experiment *B* was a free vibration test (Figure 6.15-b). In this test, a 1 kg weight was hung from the quarter span of the cable and by cutting the string attached to the weight, an initial displacement was created to cause free vibration of the cable. The in-plane vibration response at the mid-span was measured by the in-plane accelerometer.

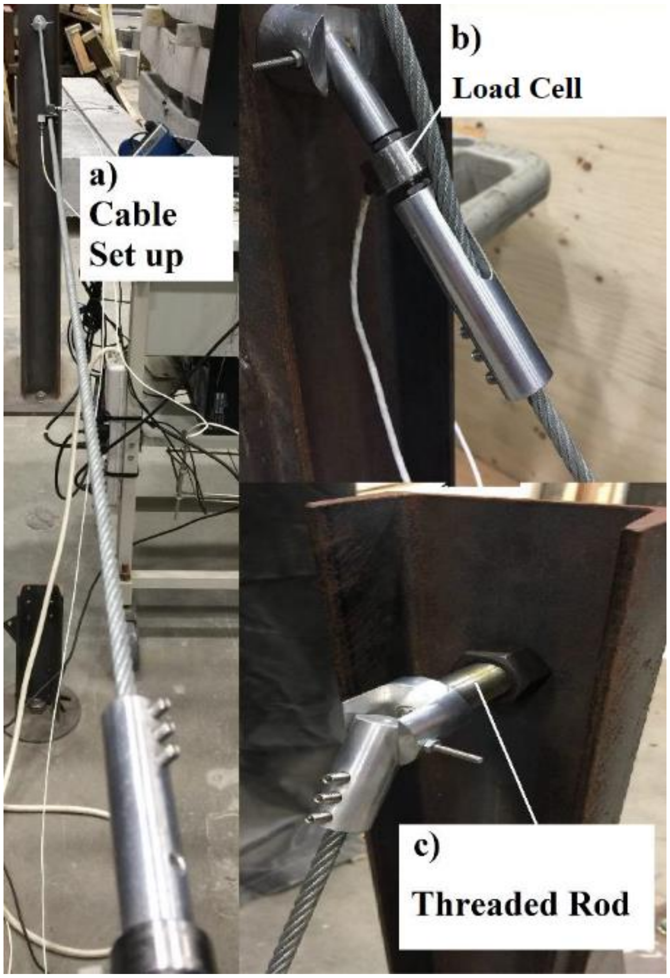

Figure 6.16: Cable vibration test set up a) Test set up b) In-line load cell c) Threaded rod

6.5.2 Pole-Line Vibration Tests

In order to validate the developed numerical model for the cable-beam system, an experimental lab-scale pole-line set up was built in the lab. Figure 6.17 shows the schematic of experimental tests on the cable-beam set up. Two U-bolts were used in the connection point of the cable and beam. The pole-line and U-bolts are shown in Figure 6.18. Similar to tests for cable only system, two types of vibration tests were performed: Experiment *A* and Experiment *B*. Experiment *A* is shown in the top part of Figure 6.17. Experiment *A* was impact testing (forced vibration). Two accelerometers positioned 0.45 m and 0.65 m from the clamped end of the beam and one accelerometer positioned at mid-span of the left cable were used to measure the response. The position of accelerometers was kept fixed and hammer impact was made at four different locations. Hit location 1 is 60 cm from the clamped end of beam, hit location 2 is at the quarter span length of the right cable, hit location 3 is at the mid-span of the right cable and hit location 4 is at the quarter span length of the left cable.

An out-of-plane impulse (perpendicular to the plane of Figure 6.17) was also applied to excite the beam and an out-of-plane accelerometer in place of Accelerometer 2 was used to measure the response.

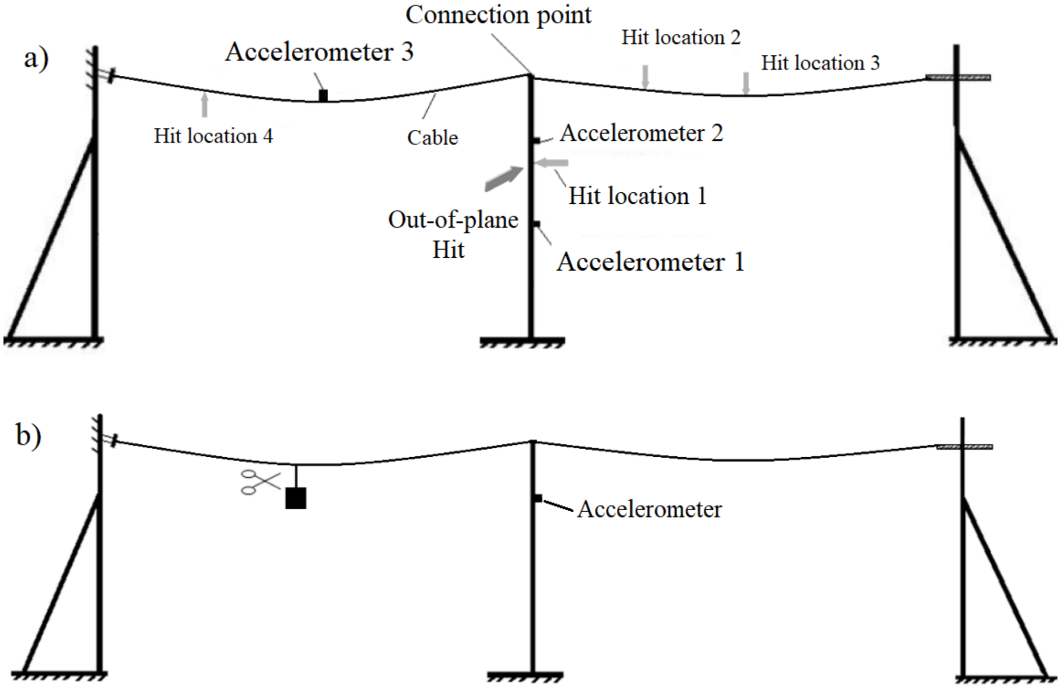

Figure 6.17: Schematic of experimental vibration testing of the beam-cable system a) Experiment *A* b) Experiment *B*

In Experiment *B* (Figure 6.17-b), a mass (200 g) was hung at mid-span of the left section of the cable through a string to cause a free vibration (Similar to Experiment B for cable-only test) An accelerometer positioned 0.6 m from the clamped end was used to measure the time response. Tests were performed with a Bruel & Kjaer 8205-002 impact hammer, 4507 B 004 70-g accelerometers, and a National Instruments NI USB-4432 power supply and signal conditioner. The software ModalView [95] was used to analyze the data.

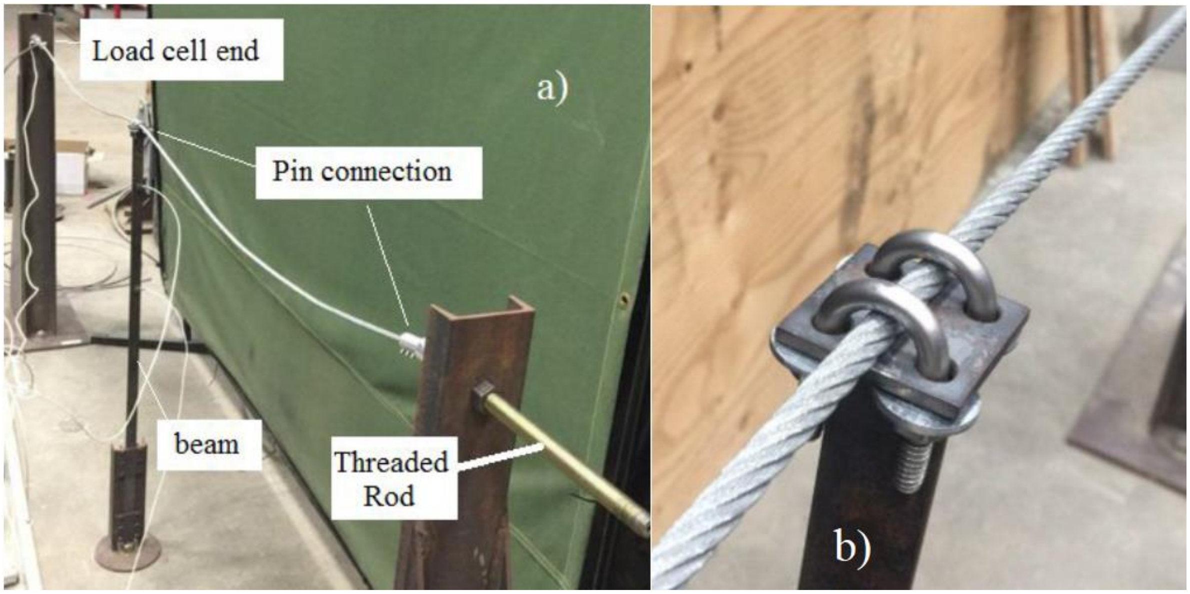

Figure 6.18: Experimental set up for vibration testing of the beam-cable system a) The beam-cable system b) Connection point

6.6 Elementary Verification

Simulation models of cable, beam and the coupled cable-beam system are verified with experiment and finite element results in the frequency and time domains. The 20sim® software was used to implement the bond graph models. In addition to a bond graph graphical user interface, the software has a frequency domain toolbox to numerically generate transfer functions and eigenvalues.

6.6.1 Beam Only Verification

The hammer impulse was simulated in the 20th segment of the beam bond graph model corresponding to 50 cm from the clamped end and the vibration response was obtained in the 25-th segment corresponding to 62.5 cm from the clamp end. Hammer impulse was simulated by applying a pulse signal using a modulated effort source, MSe, to the center of gravity velocity (in inertial coordinate) 1-junction,${}^{o}\vec{V}_{Gi}$ (Figure 6.4). Natural frequencies of the cantilever beam were obtained using the frequency toolbox and the results are compared with finite element and experiments in Table 6.2.

Table 6.2. Natural frequency comparison between numerical and experimental results: beam only

Mode Number	1	2	3	4	5
Exp [Hz]	2.24	14.70	41.57	84.22	138.2
BG [Hz]	2.34	15.79	45.40	90.56	151.65
FE {Hz]	2.41	15.38	43.57	86.14	143.36

6.6.2 Cable Only Verification

The cable model was implemented before connecting to the beam model, and modal impact testing was simulated, in the 20sim® software environment. In the simulation, an impulse force was applied at the quarter-span location, and the time response was obtained at mid-span as in the experimental test procedure (Figure 6.15). The Vode-Adams explicit integrator [114] is used for integration and simulation time is around 15 seconds for 10 seconds of time response simulation. Table 6.3 presents the comparison of in-plane natural frequencies of the cable with different tensions and Table 6.4 compares the out-of-plane natural frequencies of the cable.

Table 6.3. In-plane natural frequency comparison of the cable

Tension (N)	Sim [Hz]	FE [Hz]	Modal Test [Hz]
25	5.55	5.33	5.26
	8.08	8.23	8.03
	12.85	11.38	13.19
100	6.08	5.07	6.33
	11.30	10.16	11.29
	17.27	15.27	16.94
200	7.91	7.15	7.81
	15.85	14.32	15.53

	23.72	21.51	23.06
300	9.53	8.74	9.08
	19.38	17.55	17.6
	29.51	26.35	25.91

Table 6.4. Out-of-plane natural frequency comparison of the cable

Tension (N)	Sim [Hz]	FE [Hz]	Modal Test [Hz]
25	2.85	2.55	2.94
	5.87	5.11	5.97
	9.10	7.70	9.19
100	5.50	4.87	4.73
	6.08	6.32	6.08
	11.29	10.58	9.3
200	7.77	7.06	6.82
	7.88	8.20	8.11
	15.87	14.09	14.22
300	8.32	8.77	8.64
	16.98	17.47	17.15
	24.85	26.11	24.62

A free vibration test of the cable (Figure 6.15-b) was simulated in the cable numerical model. The experiment and simulation results for mid-span in-plane acceleration time response are compared in Figure 6.19 for a cable with 200 N tension. As can be seen, there is a good agreement between the numerical and experimental time responses and the cable numerical model is able to replicate the decay rate, vibration amplitude and frequency content of the experimental time response. There is a discrepancy in decay rate which could be due to the nature of lumped segment modeling of damping in bond graph model and difficulty in simulating the applied initial displacement caused by cutting the hung mass.

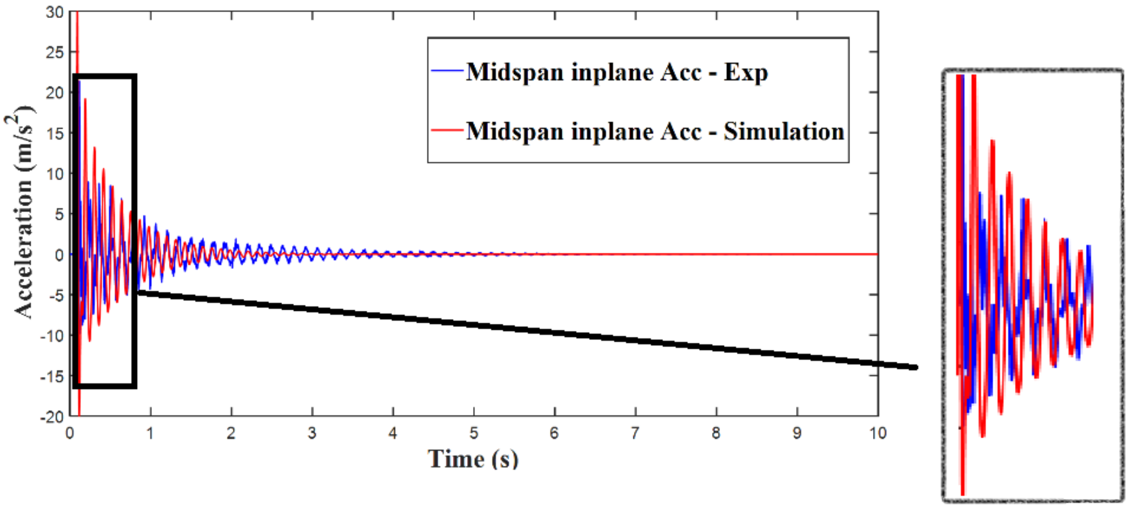

Figure 6.19: Cable time response comparison of simulation and experiment: 200N tension

6.7 Coupled System Simulation Results and Validation

The numerical (FE and bond graph) and experimental results for the coupled cable-beam system are presented in this section in three different sections. In Section 6.7.1, the natural frequency results from different methods are presented and compared with each other, Section 6.7.2 presents the mode shapes of the coupled system obtained from FEM and section 6.7.3 is the time domain response analysis.

6.7.1 Frequency Analysis

Table 6.5 presents the comparison of bond graph, finite element and experimental natural frequencies of the beam-cable system. There is a good overall agreement between the numerical and experimental results, suggesting that the bond graph model has enough accuracy to capture the dominant beam-cable system dynamics. Some of the lower modes were not revealed in the bond graph software’s numerical calculation of natural frequencies. Some discrepancy in the frequency values is attributed to the difficulty in exactly replicating the boundary conditions during the experiments.

Table 6.5. Natural frequency comparison between numerical and experimental results: beam-cable system

Mode Number		1	2	3	4	5	6
25 N	Test [Hz]	5.299	6.730	11.660	12.958	14.897	--
	BG [Hz]	6.199	6.430	10.159	--	14.092	--
	FE [Hz]	5.622	6.202	11.652	13.030	14.185	--
100 N	Test [Hz]	8.610	12.670	16.890	21.850	24.320	36.087
	BG [Hz]	6.299	12.190	15.124	--	24.932	37.884
	FE [Hz]	10.521	11.439	14.283	22.651	24.171	35.542
200 N	Test [Hz]	13.490	14.537	16.069	26.111	32.404	39.604
	BG [Hz]	--	15.788	16.740	27.410	33.887	41.185
	FE [Hz]	13.730	15.417	16.136	30.561	32.362	41.347
300 N	Test [Hz]	14.043	15.263	18.524	36.715	40.654	44.576
	BG [Hz]	--	17.094	20.705	37.719	40.825	47.188
	FE [Hz]	14.765	18.395	19.260	36.716	39.172	43.260

6.7.2 Mode Shapes

The mode shapes of the coupled cable-beam system are obtained from the FE model. Figure 6.20 shows the first eight in-plane mode shapes of the coupled cable-beam system with 200 N tension in the cable. As can be seen, some of the modes are beam dominated modes (BD), some are cable dominated modes (CD) and some are hybrid (H) modes (both beam and cable dynamically involved).

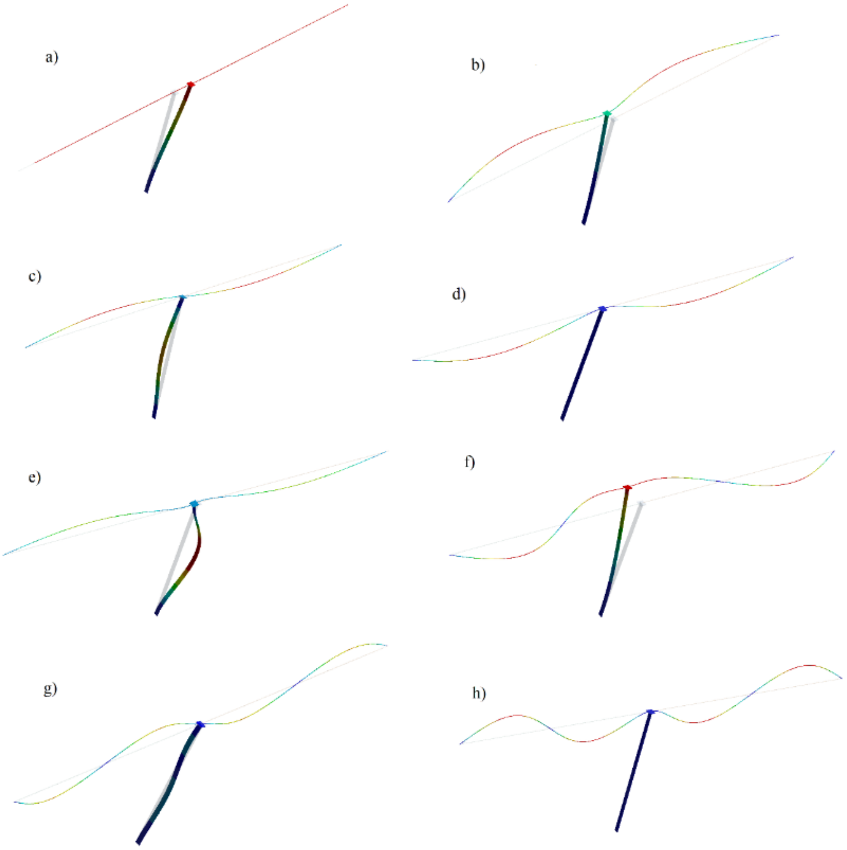

Figure 6.20: First eight in-plane mode shapes of the coupled cable-beam system a) Mode 1 (BD) b) Mode 2 (H) c) Mode 3 (H) d) Mode 4 (CD) e) Mode 5 (H) f) Mode 6 (H) g) Mode 7 (H) h) Mode 8 (CD)

6.7.3 Time Domain Analysis

In Experiment *A* and *B* of the cable-beam system experiments (Figure 6.17), time response of the beam was measured using accelerometers in forced and free vibration, respectively. To simulate a hammer strike (Experiment *A*), an impulse signal was applied to a modulated effort source (*MSe*) element in one segment of the beam model, to represent a hammer strike. The amplitude and period of the impulse was chosen to match the energy of the modal testing hammer impact. This value was determined by estimating the area under the force versus time plot from the impact hammer load cell. Experiment *B* was replicated by applying a step input force equal to the hanging mass weight at mid-span of the left cable. Removing the force simulated cutting the cable. Figure 6.21 and Figure 6.22 present the acceleration time response of the beam due to impact load, obtained from simulation and test, when the cable has 300 N tension and 200 N tension, respectively. The beginning of the time responses is zoomed to better show the two curves during the initial decay transient. As can be seen, numerical and experimental time responses are in good agreement with each other and show the same frequency content and amplitude and decay rate. Some discrepancies in frequency content are attributed to the difficulty of precisely simulating the hammer strike time series, the difficulty of modeling the same boundary condition in simulation and test and unmodeled dynamics in the laboratory support structure and load cell connection joint.

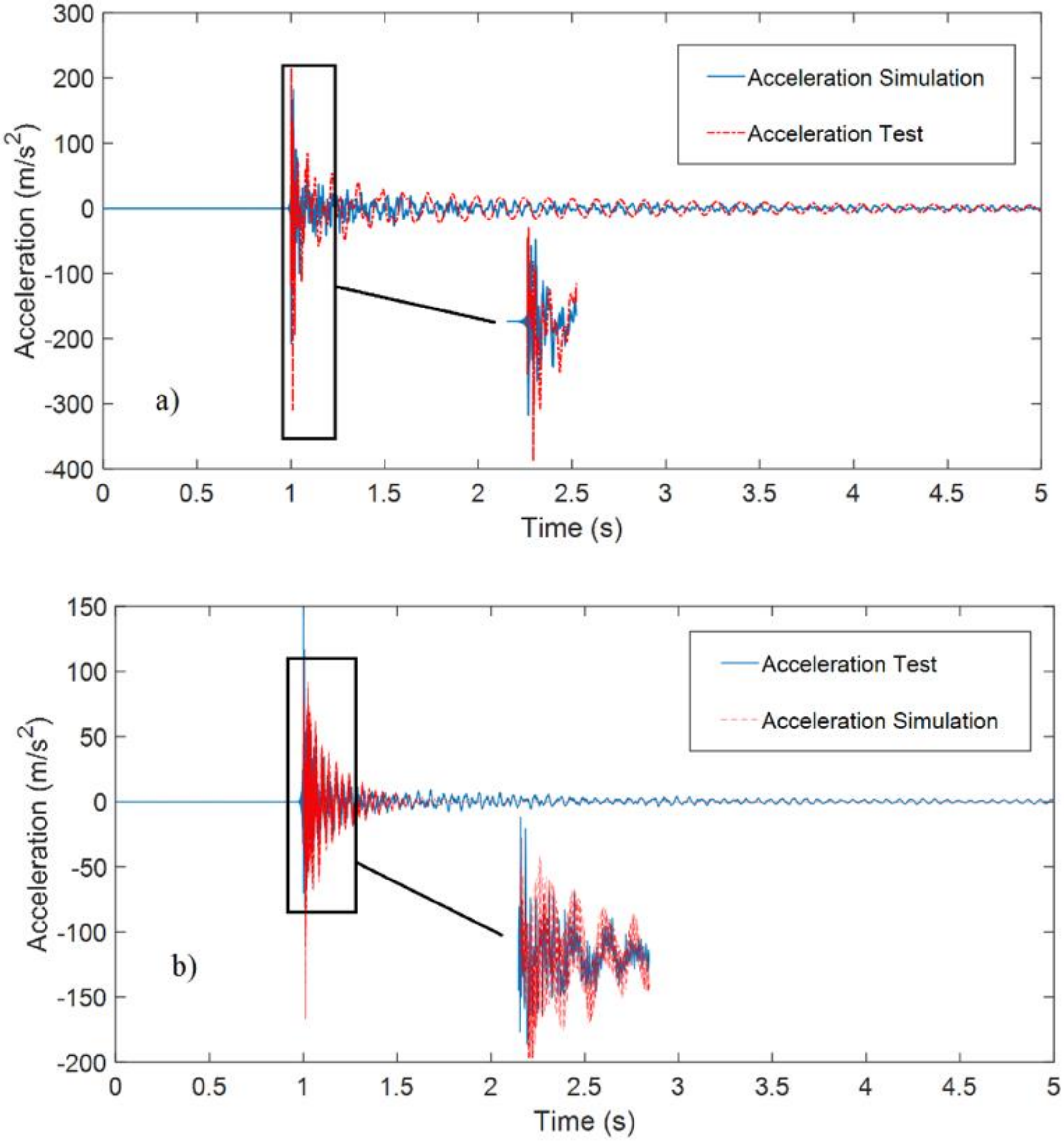

Figure 6.21: Acceleration time response due to impact with 300 N tension- Simulation and Test a) in-plane b) out-of-plane

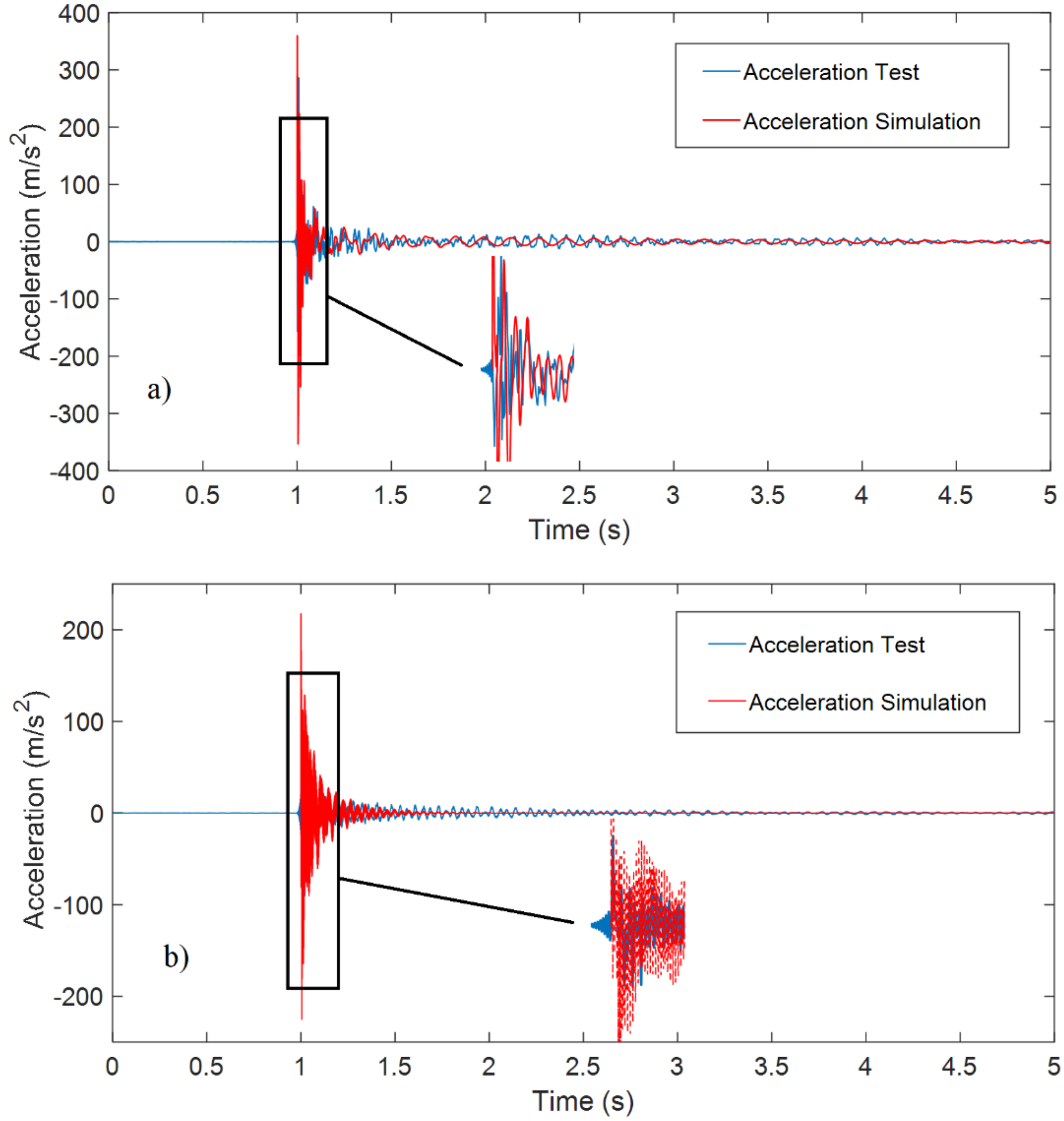

Figure 6.22: Acceleration time response due to impact with 200 N tension- Simulation and Test a) in-plane b) out-of-plane

Experiment *B* in Figure 6.17 is also simulated using the bond graph model and the time responses are presented in Figure 6.23. The results show that the numerical model can give accurate time responses under free and forced vibration. In Figure 6.23, in-plane acceleration response obtained from simulation and test are shown with the tension of 100 N and 200 N in the cable.

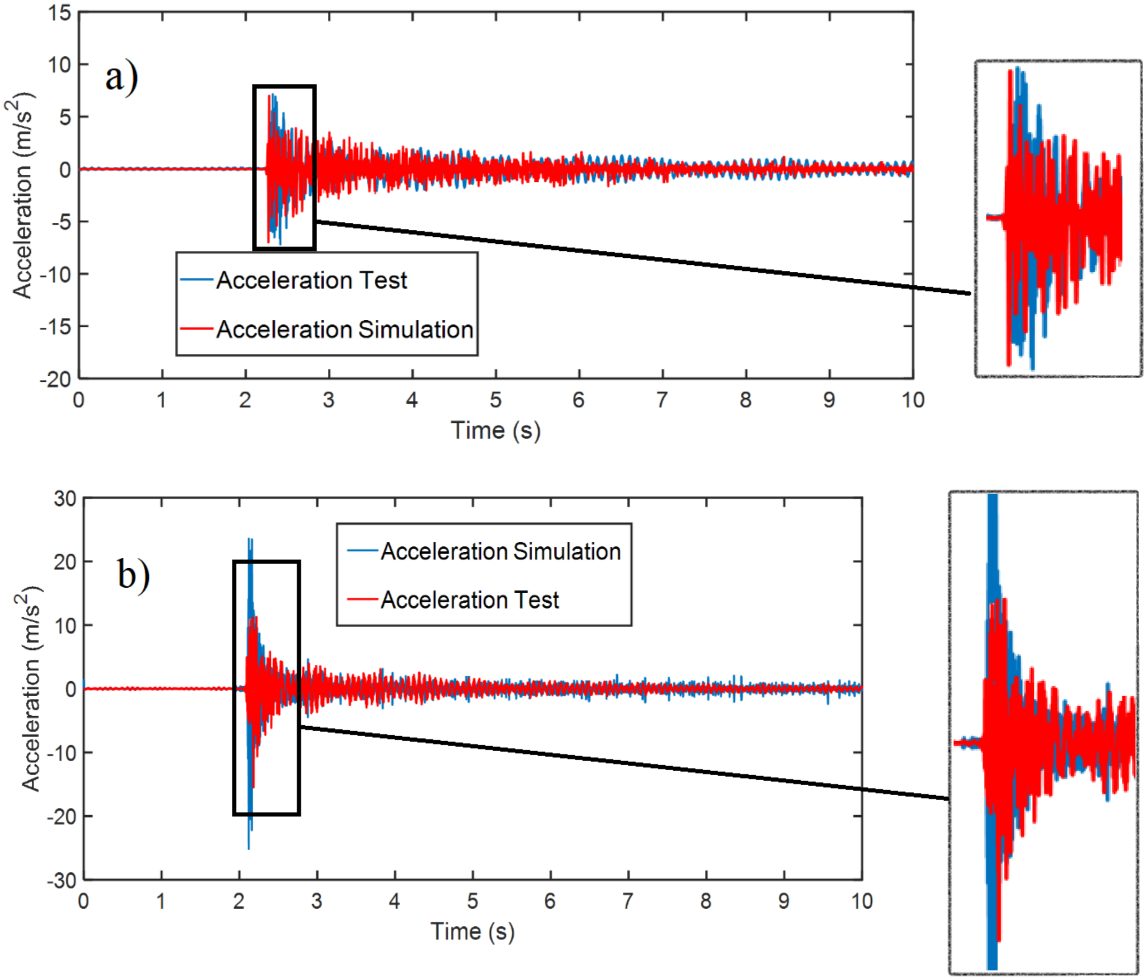

Figure 6.23: In-plane acceleration free vibration response - Simulation and Test a) 100 N b) 200N

6.8 Conclusions

A three-dimensional numerical model based on the bond graph method was developed for vibration analysis of a coupled cable-beam system, which can be extended to a utility pole-conductor system. The cables were modeled considering the bending stiffness and sag due to self-weight, and the beam was modeled as a cantilevered beam. Experimental parametrization for a stranded cable was carried out, measuring the bending stiffness under different tensions and the axial stiffness and damping using newly designed apparatus. The bending stiffness was concluded to increase with an increase in tension. Experimental free and forced vibration tests were performed on the substructures of cable and beam and on the lab-scale cable-beam coupled system. The tests were simulated in the numerical models and comparison of the results showed a good agreement. The natural frequencies of the system were obtained and the bond graph results were validated by experimental and finite element results. It is also concluded that by connecting the cable to the beam in a cable-beam system, some new modes called cable dominated modes and hybrid modes emerge in vibration modes of the system. It is concluded that the numerical models can be used to simulate the modal testing of any simple structure connected to cables. The authors will apply the modeling method to electricity transmission line systems to facilitate research into non-destructive evaluation of wood poles.

Funding

The authors would like to thank Newfoundland and Labrador Hydro for their financial and in-kind support, and the Natural Sciences and Engineering Research Council of Canada (NSERC) for their support under the Collaborative Research and Development (CRD) program.

Chapter 7

7 Frequency Based Decoupling and Finite Element Model Updating in Vibration of Cable-beam Systems

[a*]Mohammad Hadi Jalali, [a] Geoff Rideout

[a] Faculty of Engineering and Applied Science, Memorial University, St. John’s, Canada

This chapter is a manuscript of a full paper that is published in Journal of Vibration and Control. The substructure decoupling method is used in this chapter to obtain the FRF of a beam, decoupled from the rest of the cable-beam coupled structure. An FRF-based finite element model updating is also proposed to overcome the practical limitation of accessing some points in the structure for measurement. The co-authorship statement for this chapter follows:

The declaration applies to the following article	
Title of Chapter	Chapter 7: Frequency Based Decoupling and Finite Element Model Updating in Vibration of Cable-beam Systems
Article status: Published	
The PhD student analyzed the literature, performed the experiments, collected the data, developed the codes and prepared the manuscript. The supervisor edited, helped organize the manuscript, and contributed to the choice of case studies.	

Abstract

Interactions between cable and structure affect the modal properties of cabled structures such as overhead electricity transmission and distribution line systems. Modal properties of a single in-service pole are difficult to determine. A frequency response function (FRF) of a pole impacted with a modal hammer will contain information about not only the pole, but also the conductors and adjacent poles connected thereby. This paper presents a generally applicable method to extract modal properties of a single structural element, within an interacting system of cables and structures, with particular application to electricity poles. A scalable experimental lab-scale pole-line consisting of a cantilever beam and stranded cable, and a more complex system consisting of three cantilever beams and a stranded cable, are used to validate the method. The FRF of a cantilever (“pole”) is predicted by sub-structural decoupling of measured cable dynamics (known FRF matrix) from the measured response of the assembled cable-beam system (known FRF matrix). Various amounts of sag can be present in the cable. Comparison of the estimated and directly-obtained pole FRF’s show good agreement, demonstrating that the method can be used in cabled structures to obtain modal properties of an individual structural element with the effects of cables and adjacent structural elements filtered out. An FRF-based finite element model updating is then proposed to overcome the practical limitation of accessing some components of the real-world system for mounting sensors. FRFs corresponding to inaccessible points are generated based on the measured FRFs corresponding to accessible points. The results verify that FRF-based finite element model updating can be used for substructural decoupling of systems in which some essential points, such as coupling points, are inaccessible for direct FRF measurement.

Keywords: Cable-Beam System, FRF-Based Decoupling, Finite Element Model Updating.

7.1 Introduction

Dynamic interaction between cables and structural elements has been a topic of interest of researchers for many years. Modal properties of structures can give insight into the condition of the structure. Any cables attached to the structure will make it difficult to extract the modal properties of the structure itself. This paper proposes a method for removing the cable effect and accurately predicting structural natural frequencies and damping ratios, even for systems where some of the desired measurement points are not practically accessible. Specifically, the authors are engaged in ongoing development of a non-destructive evaluation (NDE) method for utility poles based on vibration testing [7,8,15,16,56] Existing NDT methods for poles, such as ultrasonic, X-ray and resistograph, are localized damage detection methods that evaluate the strength of the pole at one specific axial location [5]. The authors are currently exploring modal properties of the entire pole as an alternative. Since power lines (conductors) are attached to the poles, vibrations of the conductors affect the modal properties of the pole. Removing the effect of the conductors to reveal pole properties requires a structural dynamic method to decouple the cable from the assembled cable-pole system.

There are many studies of the interaction between cables and structures. (Li *al.*, 2005) presented a simplified computational model for a high-voltage transmission tower-line system to study the coupling behavior of adjacent tower spans and cables due to seismic excitations. The computational model was validated with experiments performed on a lab-scale tower-line system on a shaking table. [15] developed an analytical model to study the effect of cable sag and bending stiffness on coupled vibration behavior of a cable-beam system. It was concluded that cable bending stiffness and sag have significant effect on dynamics of a cable-beam system. The analytical results were verified by experiments on a lab-scale system. [115] studied the in-plane free vibration of a multi-cable-stayed beam using a transfer matrix method (TMM). Parametric analyses were carried out to investigate the effect of different parameters on modal properties, and numerical results were verified by finite element analysis. [101] reviewed analysis and modeling of transmission towers, transmission lines and transmission tower-line systems subjected to dynamic excitations due to wind, ice effects and seismic motion. The review suggested that future improvements in analytical models of tower-line systems are motivated and expected. [116] studied the coupled dynamics of a cable-harnessed structure by analytical modeling, verifying the FRF’s through experiments. [117] studied the cable and beam nonlinear interaction in a beam-cable-beam system. Their model consisted of two vertical cantilever beams connected with a suspended cable. The local, global and hybrid modes of the coupled structure were studied in linear and nonlinear analyses. [118] formulated a parametric section model to synthetically describe the geometrically nonlinear dynamics of cable-stayed and suspended bridges through a planar elastic multibody system. Reviewing the literature in cable-beam system dynamic analysis reveals that most prior work has focused on predicting responses of interacting cables and beams, with no research dealing with extracting dynamic properties of the beam as an independent substructure, through filtering out the effects of cables and adjacent beams.

Dynamic substructuring methods are well established and involve constructing the structural dynamic model of a complex system by assembling models of its simpler components. Some applications require the reverse problem, called "inverse dynamic substructuring" or "substructure decoupling", which is extracting a substructure dynamic model from the assembled system. This is a relevant issue for subsystems that cannot be measured separately, but only when coupled to their neighboring substructure(s) [13]. (Inverse) dynamic substructuring techniques have been used in many applications in recent years. Dynamic analysis of a coupled system of wind turbine hub and blades has been carried out using experimental substructuring [119]. [65] applied experimental substructure coupling to couple the dynamics of a mobile machine tool with measured dynamics of its base to predict the assembled system dynamics, and used experimental substructure decoupling to extract unsupported free–free response of the machine tool. [120] used inverse substructuring to obtain a substructure-level FRF in a three-component coupled packaging system.

In many applications of (inverse) dynamic substructuring, some points (often coupling points) are very difficult to access for mounting sensors, yet the FRFs corresponding to these points are necessary. In response to this challenge, the transmission simulator (TS) method has been developed [72]. In the TS method, an experimental substructure (TS substructure) is added to the structure at the coupling points (or any inaccessible point) and a finite element model for the TS is also developed. After coupling of the subsystems, the experimental and finite element TS models are subtracted from the system. By adding the TS substructure to the system, more accessible points are available for measurement and many problems can be solved [72]. The drawback of TS method is that another substructure should be added to the system and this is not possible in many applications. In this paper, an FRF-based finite element model updating is proposed to overcome this problem. The proposed FE updating technique uses numerical sensitivities instead of analytical sensitivities.

In this paper, frequency-based or FRF-based decoupling techniques (as opposed to time domain or modal domain techniques) are used due to compatibility with experimental data. An experimental reduced-scale cable-beam setup of one cantilever beam connected to a stranded cable, and a multi-beam cable setup consisting of three cantilever beams connected to a stranded cable, are used to obtain the FRF of the beams via the decoupling process. All points are assumed to be accessible. Then, an FRF-based finite element model updating for the single-beam-cable system is performed. The finite element model is updated (optimized) based on the measured FRFs of the points that would be accessible in the field. The optimized FE model is then used to generate FRFs corresponding to the inaccessible points. The decoupling process is repeated, this time using a combination of numerical (obtained from FE updating) and experimental FRFs (from the accessible points) to predict the beam FRFs. The results show that frequency-based decoupling can be used in dynamic analysis of complicated cable structures to extract the structure(s) dynamics with effects of cables and adjacent structures filtered out. Section 7.2 describes the theory and basics of the decoupling method and Section 7.3 describes FRF-based finite element model updating. Section 7.4 gives the details of the cable-beam systems and shows decoupling results. Section 7.5 presents the FE updating of single-beam-cable system and the decoupling results obtained from experimental-numerical decoupling.

7.2 Substructure Decoupling

In a cable-beam system, the cable and the beam are “substructures” of the assembled system and the purpose of substructure decoupling is to find the dynamics of the beam subsystem (B) as a “standalone” component that is completely decoupled from the cable subsystem (C). See Figure 7.1.

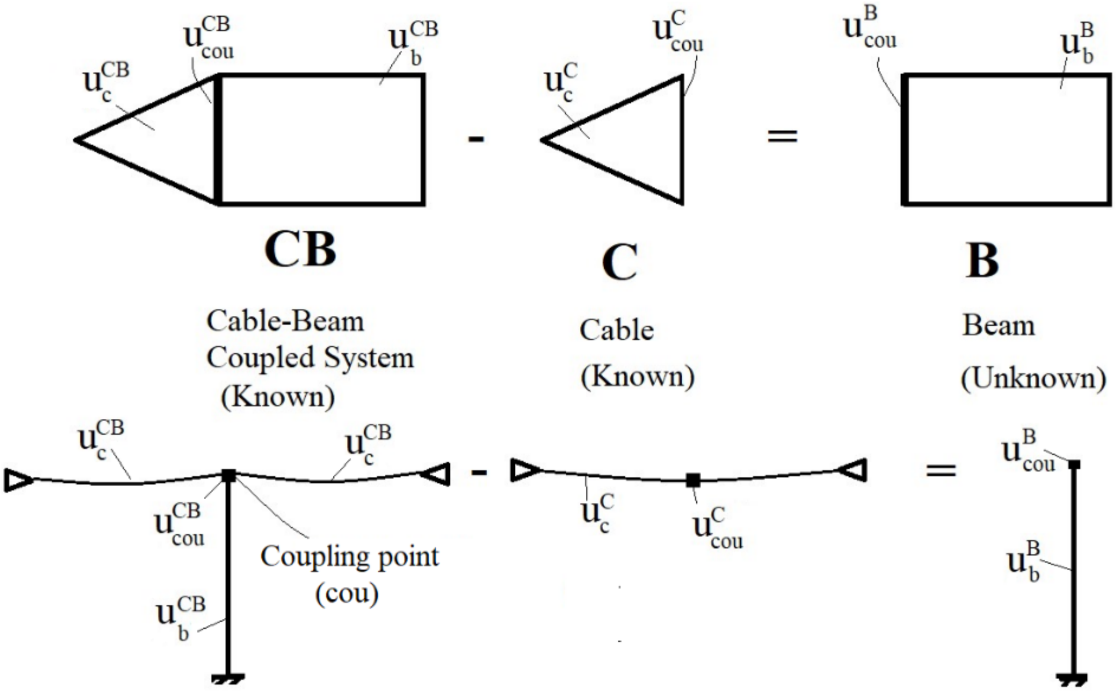

Figure 7.1: Substructure decoupling schematic

In Figure 7.1, system *CB* consists of degrees of freedom “internal to substructure *C* ”, $\boldsymbol{u}_c{}^{CB}$, “internal to substructure *B*”, $\boldsymbol{u}_b{}^{CB}$ and the coupling DOF, $\boldsymbol{u}_{cou}{}^{CB}$. The subsystems *C* and *B* also have their internal DOFs, $\boldsymbol{u}_c{}^{C}$and $\boldsymbol{u}_b{}^{B}$, respectively and the coupling DOFs, $\boldsymbol{u}_{cou}{}^{C}$and $\boldsymbol{u}_{cou}{}^{B}$, respectively. Assuming the dynamics of system *CB* and *C* are known (measured), a dynamic stiffness representation of the assembled system *CB* in compact form is [13]:

$$\boldsymbol{Z}^{CB}\boldsymbol{u}^{CB} = \boldsymbol{f}^{CB} + \boldsymbol{g}^{CB} \tag{7.1}$$

$$\begin{bmatrix} \boldsymbol{Z}_{c,c}^{CB} & \boldsymbol{Z}_{c,cou}^{CB} & \boldsymbol{0} \\ \boldsymbol{Z}_{cou,c}^{CB} & \boldsymbol{Z}_{cou,cou}^{CB} & \boldsymbol{Z}_{cou,b}^{CB} \\ \boldsymbol{0} & \boldsymbol{Z}_{b,cou}^{CB} & \boldsymbol{Z}_{b,b}^{CB} \end{bmatrix} \begin{bmatrix} \boldsymbol{u}_c \\ \boldsymbol{u}_{cou} \\ \boldsymbol{u}_b \end{bmatrix} = \begin{bmatrix} \boldsymbol{f}_c \\ \boldsymbol{f}_{cou} \\ \boldsymbol{f}_b \end{bmatrix} + \begin{bmatrix} \boldsymbol{0} \\ \boldsymbol{g}_{cou} \\ \boldsymbol{0} \end{bmatrix}$$

And subsystem *C*:

$$\boldsymbol{Z}^C \boldsymbol{u}^C = \boldsymbol{f}^C - \boldsymbol{g}^C \tag{7.2}$$

$$\begin{bmatrix} \boldsymbol{Z}_{cc}^{C} & \boldsymbol{Z}_{c,cou}^{C} \\ \boldsymbol{Z}_{cou,c}^{C} & \boldsymbol{Z}_{cou,cou}^{C} \end{bmatrix} \begin{bmatrix} \boldsymbol{u}_c^C \\ \boldsymbol{u}_{cou}^C \end{bmatrix} = \begin{bmatrix} \boldsymbol{f}_c \\ \boldsymbol{f}_{cou} \end{bmatrix} - \begin{bmatrix} \boldsymbol{0} \\ \boldsymbol{g}_{cou}^C \end{bmatrix}$$

Where $\boldsymbol{u}^{CB} = \begin{bmatrix} \boldsymbol{u}_c \\ \boldsymbol{u}_{cou} \\ \boldsymbol{u}_b \end{bmatrix}$ is the vector of DOF of system *CB* (Figure 7.1) (the superscripts are omitted for brevity), $\boldsymbol{u}^C = \begin{bmatrix} \boldsymbol{u}_c^C \\ \boldsymbol{u}_{cou}^C \end{bmatrix}$ is the vector of DOF of substructure *C*, $\boldsymbol{Z}^{CB}$ and $\boldsymbol{Z}^C$ are the stiffness matrices of system *CB* and *C*, respectively. Vectors $\boldsymbol{f}^*$ are the external force vectors and vectors $\boldsymbol{g}^*$ represent the additional disconnection forces (with non-zero entries only at the interface DOF) felt from the decoupling of the neighboring components [13].

The displacement compatibility condition, Eq. (7.3) and force equilibrium condition, Eq. (7.4), between the two (sub)structures are as follows:

$$\boldsymbol{u}_{cou}^C = \boldsymbol{u}_{cou} \tag{7.3}$$

$$\boldsymbol{g}_{cou} + \boldsymbol{g}_{cou}^C = \boldsymbol{0} \tag{7.4}$$

A more systematic description of the problem can be written by introducing the Boolean matrices $\boldsymbol{B}$ and $\boldsymbol{L}$:[13]

$$\boldsymbol{B}\boldsymbol{u} = \begin{bmatrix} \boldsymbol{B}^{CB} & \boldsymbol{B}^C \end{bmatrix} \begin{bmatrix} \boldsymbol{u}^{CB} \\ \boldsymbol{u}^C \end{bmatrix} = \boldsymbol{u}_{cou}^C - \boldsymbol{u}_{cou} = \boldsymbol{0} \tag{7.5}$$

$$\boldsymbol{L^T g} = [\boldsymbol{L}^{CB^T} \quad \boldsymbol{L}^{C^T}] \begin{bmatrix} \boldsymbol{g}^{CB} \\ \boldsymbol{g}^{C} \end{bmatrix} = \begin{bmatrix} \mathbf{0} \\ \mathbf{0} \\ \mathbf{0} \\ \boldsymbol{g}_{cou} + \boldsymbol{g}_{cou}^{C} \end{bmatrix} = \mathbf{0} \tag{7.6}$$

Eq. (7.5) presents the compatibility equation and Eq. (7.6) presents the equilibrium equation, with matrices $\boldsymbol{B}$ and $\boldsymbol{L}$ defined as:

$$\boldsymbol{B} = [\boldsymbol{B}^{CB} \quad \boldsymbol{B}^{C}] = [\mathbf{0} \quad \boldsymbol{I} \quad \mathbf{0} \ \ \| \ \ \mathbf{0} \quad -\boldsymbol{I}] \tag{7.7}$$

$$\boldsymbol{L^T} = [\boldsymbol{L}^{CB^T} \quad \boldsymbol{L}^{C^T}] = \left[\begin{array}{ccc|c|cc} \boldsymbol{I} & \mathbf{0} & \mathbf{0} & & \mathbf{0} & \mathbf{0} \\ \mathbf{0} & \mathbf{0} & \boldsymbol{I} & & \mathbf{0} & \mathbf{0} \\ \mathbf{0} & \mathbf{0} & \mathbf{0} & & \boldsymbol{I} & \mathbf{0} \\ \mathbf{0} & \boldsymbol{I} & \mathbf{0} & & \mathbf{0} & \boldsymbol{I} \end{array}\right] \tag{7.8}$$

Therefore, the decoupling problem can be described in the following equations:

$$\begin{aligned} &\begin{bmatrix} \boldsymbol{Z}^{CB} & \mathbf{0} \\ \mathbf{0} & \boldsymbol{Z}^{C} \end{bmatrix} \begin{bmatrix} \boldsymbol{u}^{CB} \\ \boldsymbol{u}^{C} \end{bmatrix} = \begin{bmatrix} \boldsymbol{f}^{CB} \\ \boldsymbol{f}^{C} \end{bmatrix} + \begin{bmatrix} \boldsymbol{g}^{CB} \\ -\boldsymbol{g}^{C} \end{bmatrix} \\ &[\boldsymbol{B}^{CB} \quad \boldsymbol{B}^{C}] \begin{bmatrix} \boldsymbol{u}^{CB} \\ \boldsymbol{u}^{C} \end{bmatrix} = \mathbf{0} \\ &[\boldsymbol{L}^{CB^T} \quad \boldsymbol{L}^{C^T}] \begin{bmatrix} \boldsymbol{g}^{CB} \\ \boldsymbol{g}^{C} \end{bmatrix} = \mathbf{0} \end{aligned} \tag{7.9}$$

Employing the dual formulation for decoupling [60], the interface forces are satisfied a priori by choosing interface forces of the form:

$$\boldsymbol{g} = -\boldsymbol{B}^{T}\boldsymbol{\lambda} \tag{7.10}$$

where $\boldsymbol{\lambda}$ are Lagrange multipliers, corresponding physically to the interface force intensities. The equilibrium condition in Eq. (7.6) thus becomes:

$$\boldsymbol{L^T g} = -\boldsymbol{L^T B^T \lambda} = \mathbf{0} \tag{7.11}$$

This condition is always satisfied [14]. The decoupling problem can therefore be formulated in a dual way as:

$$\begin{bmatrix} \boldsymbol{Z}^{CB} & \boldsymbol{0} & \boldsymbol{B}^{CB^T} \\ \boldsymbol{0} & -\boldsymbol{Z}^{C} & \boldsymbol{B}^{C^T} \\ \boldsymbol{B}^{CB} & \boldsymbol{B}^{C} & \boldsymbol{0} \end{bmatrix} \begin{bmatrix} \boldsymbol{u}^{CB} \\ \boldsymbol{u}^{C} \\ \boldsymbol{\lambda} \end{bmatrix} = \begin{bmatrix} \boldsymbol{f}^{CB} \\ \boldsymbol{0} \\ \boldsymbol{0} \end{bmatrix} \tag{7.12}$$

In a more general form, different Boolean matrices for the compatibility and equilibrium conditions can be taken [13]:

$$\begin{bmatrix} \boldsymbol{Z}^{CB} & \boldsymbol{0} & \boldsymbol{E}^{CB^T} \\ \boldsymbol{0} & -\boldsymbol{Z}^{C} & \boldsymbol{E}^{C^T} \\ \boldsymbol{C}^{CB} & \boldsymbol{C}^{C} & \boldsymbol{0} \end{bmatrix} \begin{bmatrix} \boldsymbol{u}^{CB} \\ \boldsymbol{u}^{C} \\ \boldsymbol{\lambda} \end{bmatrix} = \begin{bmatrix} \boldsymbol{f}^{CB} \\ \boldsymbol{0} \\ \boldsymbol{0} \end{bmatrix} \tag{7.13}$$

where $\boldsymbol{E}^{*}$ are the Boolean matrices defining the location of the uncoupling forces while $\boldsymbol{C}^{*}$ are the matrices enforcing compatibility. In order to eliminate Lagrange multipliers $\boldsymbol{\lambda}$, Eq. (7.13) can be written:

$$\begin{bmatrix} \boldsymbol{Z} & \boldsymbol{E}^{T} \\ \boldsymbol{C} & \boldsymbol{0} \end{bmatrix} \begin{Bmatrix} \boldsymbol{u} \\ \boldsymbol{\lambda} \end{Bmatrix} = \begin{Bmatrix} \boldsymbol{f} \\ \boldsymbol{0} \end{Bmatrix} \tag{7.14}$$

where $\boldsymbol{Z} = \begin{bmatrix} \boldsymbol{Z}^{CB} & \boldsymbol{0} \\ \boldsymbol{0} & -\boldsymbol{Z}^{C} \end{bmatrix}$ $\boldsymbol{u} = \begin{bmatrix} \boldsymbol{u}^{CB} \\ \boldsymbol{u}^{C} \end{bmatrix}$, $\boldsymbol{f} = \begin{bmatrix} \boldsymbol{f}^{CB} \\ \boldsymbol{0} \end{bmatrix}$, $\boldsymbol{E}^{T} = \begin{bmatrix} \boldsymbol{E}^{CB^T} \\ \boldsymbol{E}^{C^T} \end{bmatrix}$ and $\boldsymbol{C} = [\boldsymbol{C}^{CB} \quad \boldsymbol{C}^{C}]$. Therefore, the system of equations is:

$$\begin{aligned} &\boldsymbol{Z}\boldsymbol{u} + \boldsymbol{E}^{T}\boldsymbol{\lambda} = \boldsymbol{f} \\ &\boldsymbol{C}\boldsymbol{u} = \boldsymbol{0} \end{aligned} \tag{7.15}$$

From the first of Eqs. (7.15):

$$\boldsymbol{u} = \boldsymbol{Z}^{-\boldsymbol{1}}\boldsymbol{f} - \boldsymbol{Z}^{-\boldsymbol{1}}\boldsymbol{E}^{T}\boldsymbol{\lambda} \tag{7.16}$$

By substituting Eq. (7.16) in the second of Eqs. (7.15):

$$\boldsymbol{C}\boldsymbol{Z}^{-\boldsymbol{1}}\boldsymbol{f} - \boldsymbol{C}\boldsymbol{Z}^{-\boldsymbol{1}}\boldsymbol{E}^{T}\boldsymbol{\lambda} = \boldsymbol{0} \;\Rightarrow\; \boldsymbol{\lambda} = (\boldsymbol{C}\boldsymbol{Z}^{-\boldsymbol{1}}\boldsymbol{E}^{T})^{+}\boldsymbol{C}\boldsymbol{Z}^{-\boldsymbol{1}}\boldsymbol{f} \tag{7.17}$$

where $^{+}$ denotes the (Moore–Penrose) pseudo-inverse since the matrix in the parenthesis is not necessarily an square matrix. By back-substitution of $\boldsymbol{\lambda}$ in the first of Eqs. (7.15) and considering $= \boldsymbol{Z}^{-1}$:

$$\boldsymbol{Z}\boldsymbol{u} + \boldsymbol{E}^{T}[(\boldsymbol{C}\boldsymbol{Z}^{-1}\boldsymbol{E}^{T})^{+}\boldsymbol{C}\boldsymbol{Z}^{-1}\boldsymbol{f}] = \boldsymbol{f} \;\Rightarrow\; \boldsymbol{u} = [\boldsymbol{H} - \boldsymbol{H}\boldsymbol{E}^{T}(\boldsymbol{C}\boldsymbol{H}\boldsymbol{E}^{T})^{+}\boldsymbol{C}\boldsymbol{H}]\boldsymbol{f} \tag{7.18}$$

Eq. (7.18) can be expanded and written:

$$\begin{aligned}\begin{bmatrix}\boldsymbol{u}^{CB}\\ \boldsymbol{u}^{C}\end{bmatrix} = \Bigg(&\begin{bmatrix}\boldsymbol{H}^{CB} & \boldsymbol{0}\\ \boldsymbol{0} & -\boldsymbol{H}^{C}\end{bmatrix} - \\ &\begin{bmatrix}\boldsymbol{H}^{CB} & \boldsymbol{0}\\ \boldsymbol{0} & -\boldsymbol{H}^{C}\end{bmatrix}\begin{bmatrix}\boldsymbol{E}^{CB^{T}}\\ \boldsymbol{E}^{C^{T}}\end{bmatrix}\left([\boldsymbol{C}^{CB} \quad \boldsymbol{C}^{C}]\begin{bmatrix}\boldsymbol{H}^{CB} & \boldsymbol{0}\\ \boldsymbol{0} & -\boldsymbol{H}^{C}\end{bmatrix}\begin{bmatrix}\boldsymbol{E}^{CB^{T}}\\ \boldsymbol{E}^{C^{T}}\end{bmatrix}\right)^{+}[\boldsymbol{C}^{CB} \quad \boldsymbol{C}^{C}]\begin{bmatrix}\boldsymbol{H}^{CB} & \boldsymbol{0}\\ \boldsymbol{0} & -\boldsymbol{H}^{C}\end{bmatrix}\Bigg)\boldsymbol{f}\end{aligned} \tag{7.19}$$

Eq. (7.19) is of the form $\boldsymbol{u} = \boldsymbol{H}\boldsymbol{f}$. Therefore, the decoupled FRF matrix in a general form can be found:

$$\begin{aligned}\boldsymbol{H}^{B} = &\begin{bmatrix}\boldsymbol{H}^{CB} & \boldsymbol{0}\\ \boldsymbol{0} & -\boldsymbol{H}^{C}\end{bmatrix} - \\ &\begin{bmatrix}\boldsymbol{H}^{CB} & \boldsymbol{0}\\ \boldsymbol{0} & -\boldsymbol{H}^{C}\end{bmatrix}\begin{bmatrix}\boldsymbol{E}^{CB^{T}}\\ \boldsymbol{E}^{C^{T}}\end{bmatrix}\left([\boldsymbol{C}^{CB} \quad \boldsymbol{C}^{C}]\begin{bmatrix}\boldsymbol{H}^{CB} & \boldsymbol{0}\\ \boldsymbol{0} & -\boldsymbol{H}^{C}\end{bmatrix}\begin{bmatrix}\boldsymbol{E}^{CB^{T}}\\ \boldsymbol{E}^{C^{T}}\end{bmatrix}\right)^{+}[\boldsymbol{C}^{CB} \quad \boldsymbol{C}^{C}]\begin{bmatrix}\boldsymbol{H}^{CB} & \boldsymbol{0}\\ \boldsymbol{0} & -\boldsymbol{H}^{C}\end{bmatrix}\end{aligned} \tag{7.20}$$

Matrix $\boldsymbol{H}^{B}$ in Eq. (7.20) is called the decoupled FRF matrix of substructure *B* but also contains extra rows and columns corresponding to subsystem *C*. Also, those rows and the columns of $\boldsymbol{H}^{B}$ corresponding to compatibility and equilibrium DoFs appear twice, both in the rows and columns in $-\boldsymbol{H}^{C}$ and $\boldsymbol{H}^{CB}$ [121]. Therefore, only the rows and columns corresponding to the subsystem *B* are extracted from matrix $\boldsymbol{H}^{B}$ and are considered decoupled FRFs of subsystem *B*. Based on choosing different DOFs for compatibility ($\boldsymbol{C}$) and equilibrium ($\boldsymbol{E}$), various collocated and non-collocated decoupling approaches can be used [13]. Eq. (7.20) is used in this paper for obtaining the decoupled FRF of substructure *B* in multiple ways, and the best results are presented in Section 7.4.

7.3 FRF-Based Finite Element Model Updating

The accelerance FRF $H_{a,b}(\omega)$ is the acceleration response at node a, $A_a(\omega)$, divided by the force at node b, $F_b(\omega)$, both in the frequency domain [122]:

$$H_{a,b}(\omega) = \frac{A_a(\omega)}{F_b(\omega)} \cong \sum_{i=1}^{m} \frac{-\omega^2 \hat{\phi}_{ai} \hat{\phi}_{bi}}{-\omega^2 + 2i\omega\Omega_i\xi_i + {\Omega^2}_i} \tag{7.21}$$

where m is the number of modes used for constructing the FRF, ω is frequency, Ω_i is i^{th} natural frequency of the system, ξ_i is i^{th} damping ratio corresponding to i^{th} mode and $\hat{\phi}_{ai}$ and $\hat{\phi}_{bi}$ are the scalar values of mode shape i at response node a and excitation node b, respectively. The form of FRF used for model updating is as follows, with the values of the FRF magnitude in dB:

$$\bar{H}_{a,b}(\omega) = 20\log_{10}\left(\left|H_{a,b}(\omega)\right|\right) \tag{7.22}$$

The goal of the FE model updating is to change the properties of a FEM such that the response of the model matches measured data. After developing the FE model, Eq. (7.21) and Eq. (7.22) are used to obtain the FRF at the response and excitation nodes corresponding to the response and excitation locations considered in the experiment. Then the difference between analytical and measured FRFs, the error or residual, is found and a scalar objective error function value is calculated [123]. With the scalar objective error function value, numerical optimization techniques are used to minimize the difference between the analytical and measured FRFs by modifying the parameters of the FEM [123]. Any combination of stiffness, mass, and damping parameter updating may be performed. Substituting Eq. (7.21) and Eq. (7.22) and using modal responses as functions of the unknown updating parameters p results in Eq. (7.23) [123]:

$$\bar{H}_{a,b}(\omega, p) = 20\log_{10}\left(\left|\sum_{i=1}^{m} \frac{-\omega^2 \hat{\phi}_{ai}(p) \hat{\phi}_{bi}(p)}{-\omega^2 + 2i\omega\Omega_i(p)\xi_i(p) + {\Omega^2}_i(p)}\right|\right) \tag{7.23}$$

The error function, or residual e, is defined as:

$$e(\omega,p) = \bar{H}^{a}{}_{a,b}(\omega,p) - \bar{H}^{m}{}_{a,b}(\omega,p) \quad (7.24)$$

where $\bar{H}^{a}{}_{a,b}(\omega,p)$ and $\bar{H}^{m}{}_{a,b}(\omega,p)$ are analytical and measured FRFs, respectively. Then, a scalar objective error function J is created and minimized through bounded numerical optimization:

$$J(p) = e^{T}(\omega,p)e(\omega,p) \quad (7.25)$$

The purpose of optimization is to minimize $J(\omega,p)$ by considering the upper and lower bounds for p [123]. The scalar objective error function is normalized by the initial value of the scalar objective error function $J(p)_1$ so that the optimization starts at a value of 1 and the perfect match would be a value of 0.

$$J(p)_i = \frac{J(p)_i}{J(p)_1} \quad (7.26)$$

The parameter p is a unitless modifier that modifies any structural parameter. This optimization process is used in Section 7.5 to update the numerically-obtained FRFs corresponding to inaccessible points in the real system. The updated FRFs are then used to provide the required FRFs in decoupling analysis.

7.4 Experimental Decoupling Results and Discussion

The decoupling analysis is performed on two cable-beam systems, the first consisting of one vertical cantilever beam connected to a cable on both sides and the second system consisting of three vertical cantilever beams connected to a cable throughout the line.

7.4.1 Single-Beam-Cable System

The schematic of the assembled single-beam-cable system (*CB*) and the cable substructure (*C*) is shown in Figure 7.2. The cantilever is a steel rectangular beam with cross section area of 46.67 mm^2 and the cable is a 7 × 19 steel stranded cable with a nominal diameter of 1/4 inch and linear density of 0.16667 kg/m. Six measurement points (accelerometer points) are considered for experimental decoupling. In Figure 7.2-a, points 1, 2, 3 are cable substructure internal DOFs ($\boldsymbol{u}_c^{CB}$ in Figure 7.1), point 4 is a coupling DOF ($\boldsymbol{u}_{cou}^{CB}$ in Figure 7.1) and points 5 and 6 are the beam internal DOFs ($\boldsymbol{u}_b^{CB}$ in Figure 7.1) within the assembled system. In Figure 7.2-b (same cable tension), the cable internal DOFs ($\boldsymbol{u}_c^{C}$ in Figure 7.1) and the coupling point 4 ($\boldsymbol{u}_{cou}^{C}$ in Figure 7.1) are shown. All the DOFs are along the *z* direction.

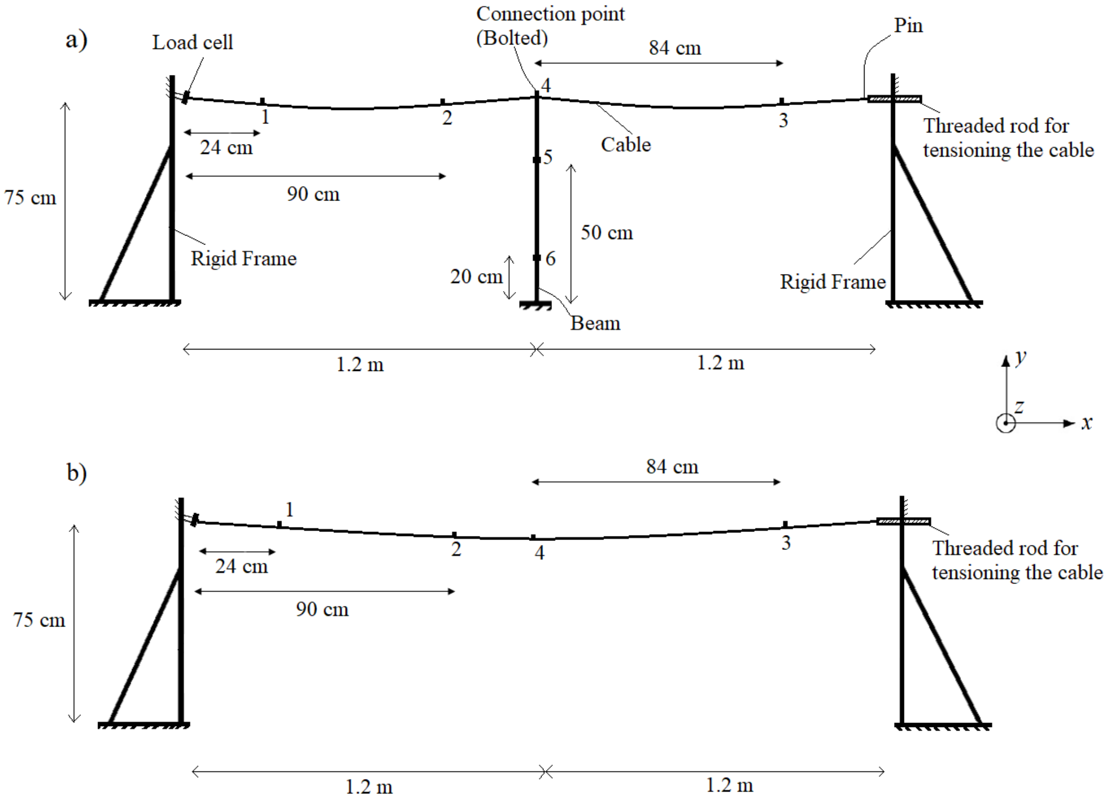

Figure 7.2: Schematic of a) Assembled single-beam-cable system (CB) b) Cable substructure (C)

The main steps in the decoupling process are presented in Figure 7.3. The arrays of FRF matrices are obtained and the reciprocity check is performed.

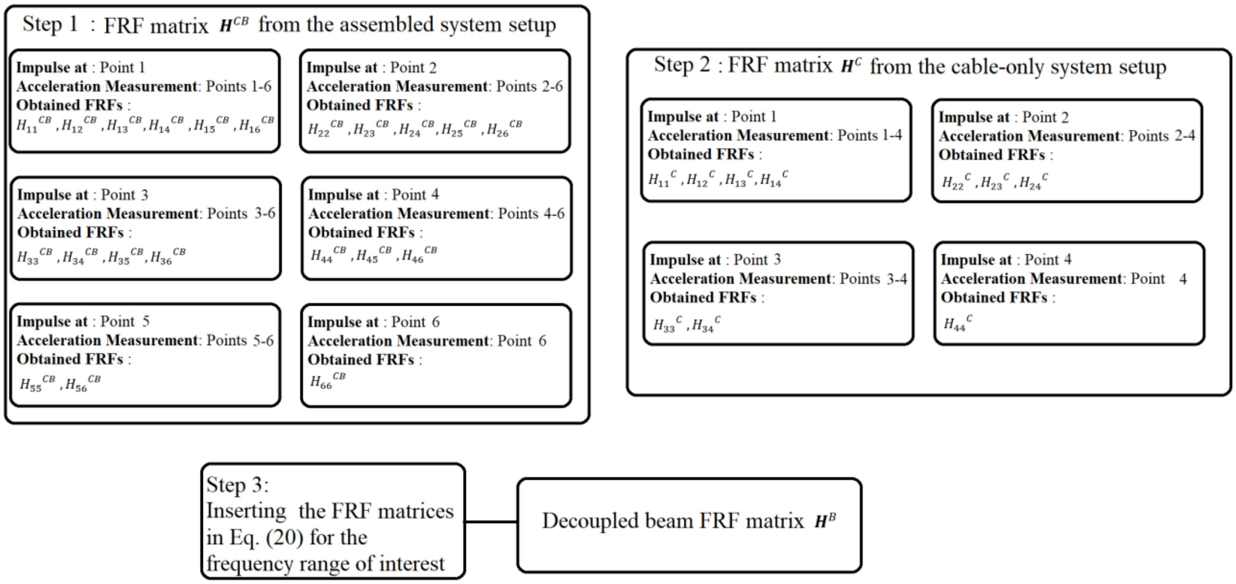

Figure 7.3: Steps in experimental decoupling of the single-beam-cable system

The cable sag has a significant effect on the vibration of a cable-beam system [15]. Therefore, three different amounts of cable sag were considered to demonstrate the robustness of the proposed method. The setup for assembled system (*CB*), and the cable-only substructure (*C*), both with 50 N tension, are shown in Figure 7.4. The right end of the cable was attached to a threaded rod to adjust the tension and an in-line load cell at the left end measured the tension. Two U-bolts were used in the connection point of the cable and beam and they are shown in Figure 7.4-b. Points 1-6 (Figure 7.2) were used in the experiments. Three Bruel & Kjaer 4507 B 004 70-g accelerometers and three PCB 352C33 accelerometers were used at the six locations.

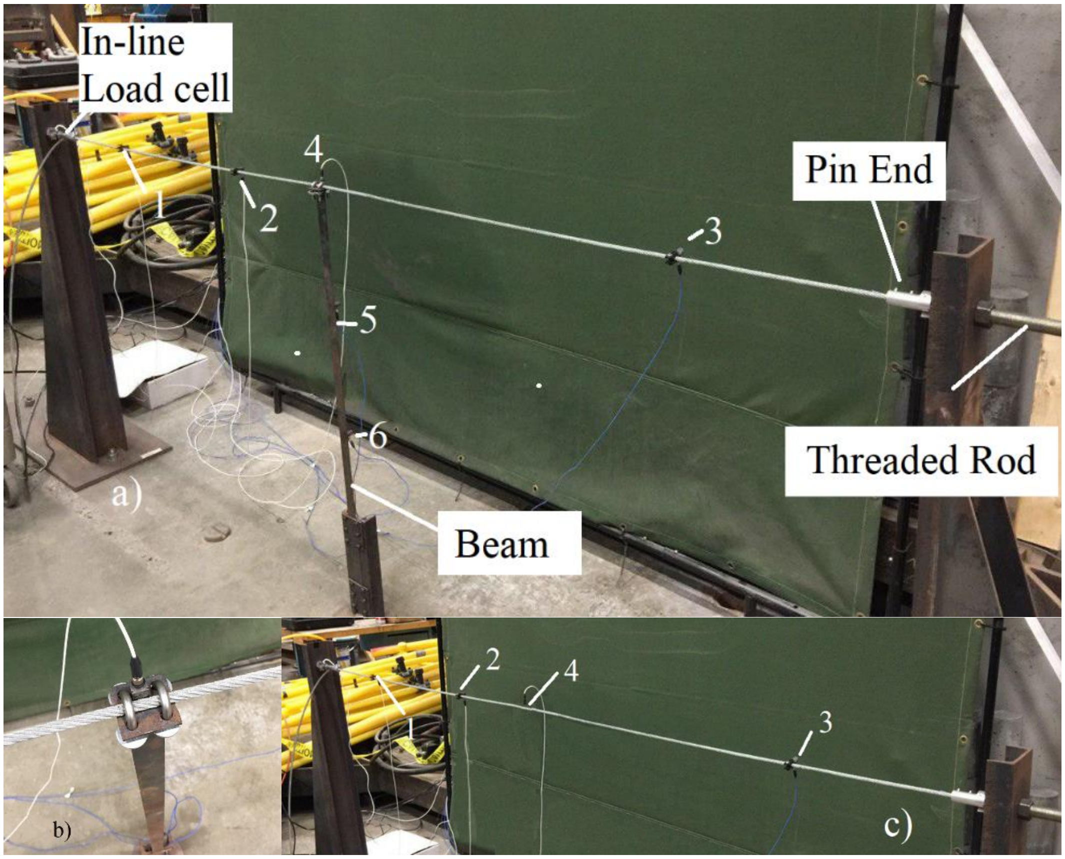

Figure 7.4: a) Experimental setup of single-beam-cable system and measurement points b) Connection point and accelerometer c) Cable substructure setup

FRFs were obtained using a B&K 8205-002 impact hammer, a National Instruments c-DAQ 9172 chassis and the software ModalView [95]. Separate analyses were conducted at the three cable tensions 10N, 50N and 150 N. In each tension, the experimental FRFs of structure CB (assembled structure) and C (cable) were obtained at six locations on the assembled structure and four locations on the cable. A 6×6 matrix $\boldsymbol{H}^{CB}$ and a 4×4 matrix $\boldsymbol{H}^{C}$ were measured in a 0-300 Hz frequency range. The measured FRFs are used in Eq. (7.20) and various decoupling approaches were used to predict the decoupled FRF. Figure 7.5 shows the predicted FRFs ${H_{66}}^{B}$ and ${H_{56}}^{B}$ after applying decoupling on the systems with 10N, 50N and 150 N cable tension. Decoupled FRFs show a good agreement with the measured FRFs in each tension, but the accuracy is lower in the high frequency range due to the measurement errors and difficulty in exciting and measuring the high frequency vibration. There is a spurious peak around 140 Hz that could be due to numerical singularity that is common in dynamic substructuring [124]. There might also be interactions with the environment at high frequencies. The FRFs used for obtaining Figure 7.5 were the raw measured FRFs except for the 150 N system (Figure 7.5-c and Figure 7.5-f) that used modally fitted (synthesized) FRFs of the assembled system and cable. The decoupling result from fitted FRFs for 10 N and 50 N tensions were not significantly different from the result obtained from raw FRFs, therefore; they are not presented here.

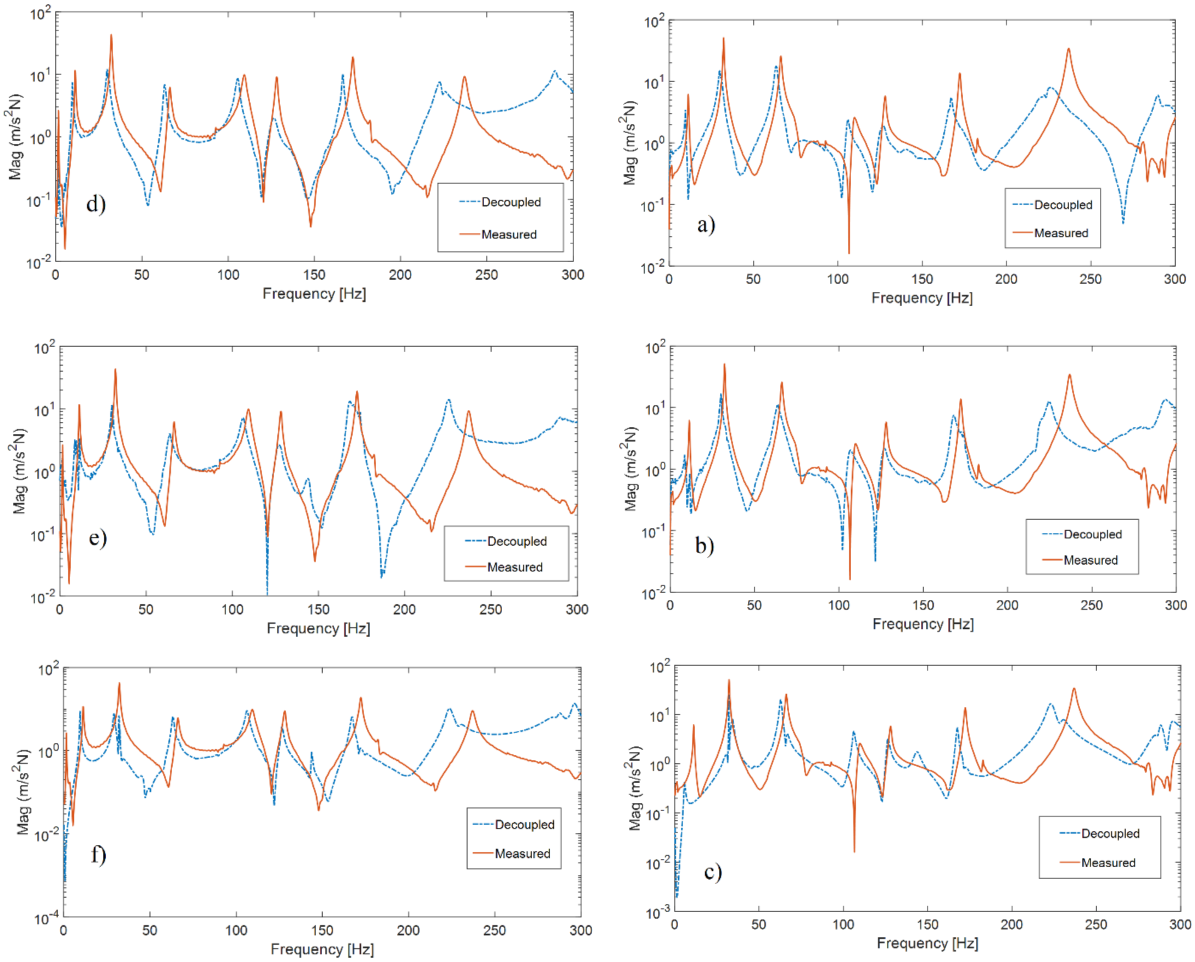

Figure 7.5: Comparison of decoupled and measured beam FRFs in single-beam-cable system

a) $H_{66}{}^{B}$ 10N b) $H_{66}{}^{B}$ 50N c) $H_{66}{}^{B}$ 150N d) $H_{56}{}^{B}$ 10N e) $H_{56}{}^{B}$ 50N f) $H_{56}{}^{B}$150N

Natural frequencies and damping ratios of the beam extracted from the predicted FRFs (using different cable tensions) and measured FRFs are compared Table 7.1. The 3db method [94] was used to extract the damping ratios from the FRF peaks. The agreement between the modal properties of the beam extracted from the measured and predicted FRFs for different cable tensions shows that frequency-based decoupling is effective and appears to be independent of cable sag. In some modes, the predicted and measured damping ratios differ, which could be attributed to measurement uncertainty and difficulty in exciting the coupling point in the assembled and isolated substructure at exactly the same location. Damping ratio of the first mode was predicted very well using 10 N tension but the first mode damping ratio error was very high at 50 N and 150 N systems and is not presented in the table. The reason for this error could be the measurement noise in the low frequency range and as a result the peak is not clear enough to extract the damping ratio.

Table 7.1. Natural frequencies (Hz) and damping ratios (%) of beam: predicted (decoupled) using different tensions and measured

Mode	1		2		3		4		5		6		7		8	
	Hz	%	Hz	%	Hz	%	Hz	%	Hz	%	Hz	%	Hz	%	Hz	%
Measured	1.6	2.03	11.2	1.42	32.2	0.52	66.2	0.52	92.8	0.19	109.4	0.68	128	0.35	172.4	0.23
Decoupled 10N	1.8	2.00	9.8	1.60	29.8	0.88	63.2	0.64	92.4	0.26	105.4	0.62	126.4	0.98	166.6	0.18
Decoupled 50N	1.4	-	11.4	0.88	30.6	0.42	63.6	0.94	92.6	0.25	106	0.80	127	0.94	174.2	0.20
Decoupled 150N	1.4	-	9.6	1.37	32	0.37	63.2	0.59	--	--	106.2	0.57	126.4	0.31	167.6	0.21

7.4.1.1 Effect of Number of Measurement Points on Decoupling Results

Minimizing the number of measurement points is desirable if the method is to be used in the field. Figure 7.6 shows the comparison of predicted beam FRFs using only measurement points 4, 5 and 6, and using all 6 points, for 10 N cable tension. A similar result is obtained for the other two tensions. The agreement suggests that use of three measurement points gives sufficient accuracy in the frequency range 0-100 Hz that is relevant to the authors’ application.

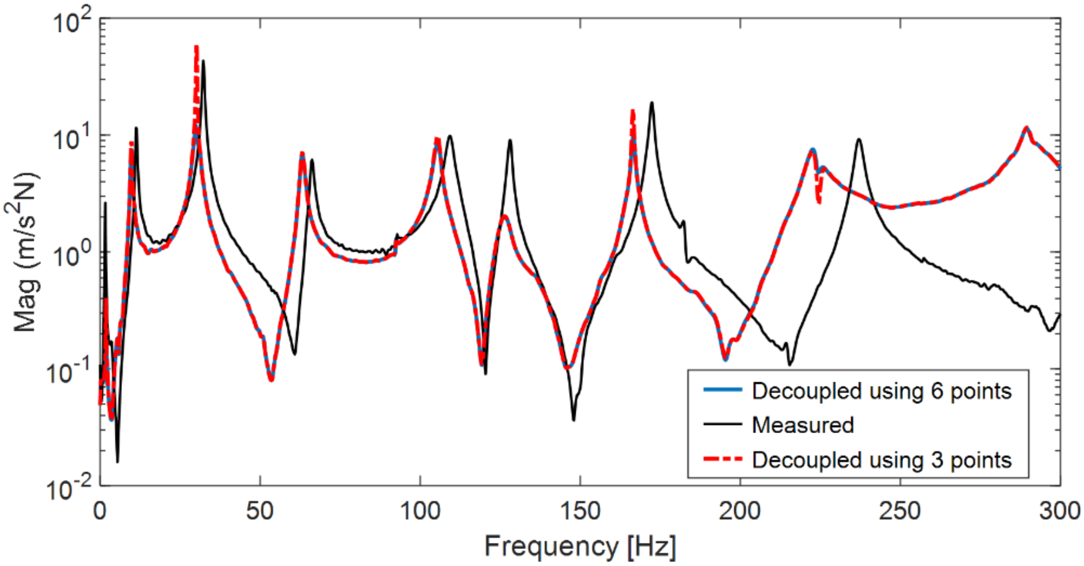

Figure 7.6: Comparison of measured and decoupled beam FRF H_{56}^{B} using three and six measurement points

7.4.2 Multi-Beam-Cable System

In the multi-beam-cable system, three beams (B1, B2 and B3) are bolted to a 4.8 m stranded cable and two different cable tensions (10N and 100N) were considered. The decoupling analysis was carried out for all three beams. As for the single-beam-cable analysis, six points (DOF) were chosen for the decoupling analysis as shown in Figure 7.7, and the steps are the same as in Figure 7.3. In each analysis, point 5 is the coupling DOF located at the connection point of the desired beam, point 6 is the beam internal DOF and points 3 and 4 are at the connection points of the adjacent beams to capture the impact of adjacent beam vibration on the vibration of the desired beam.

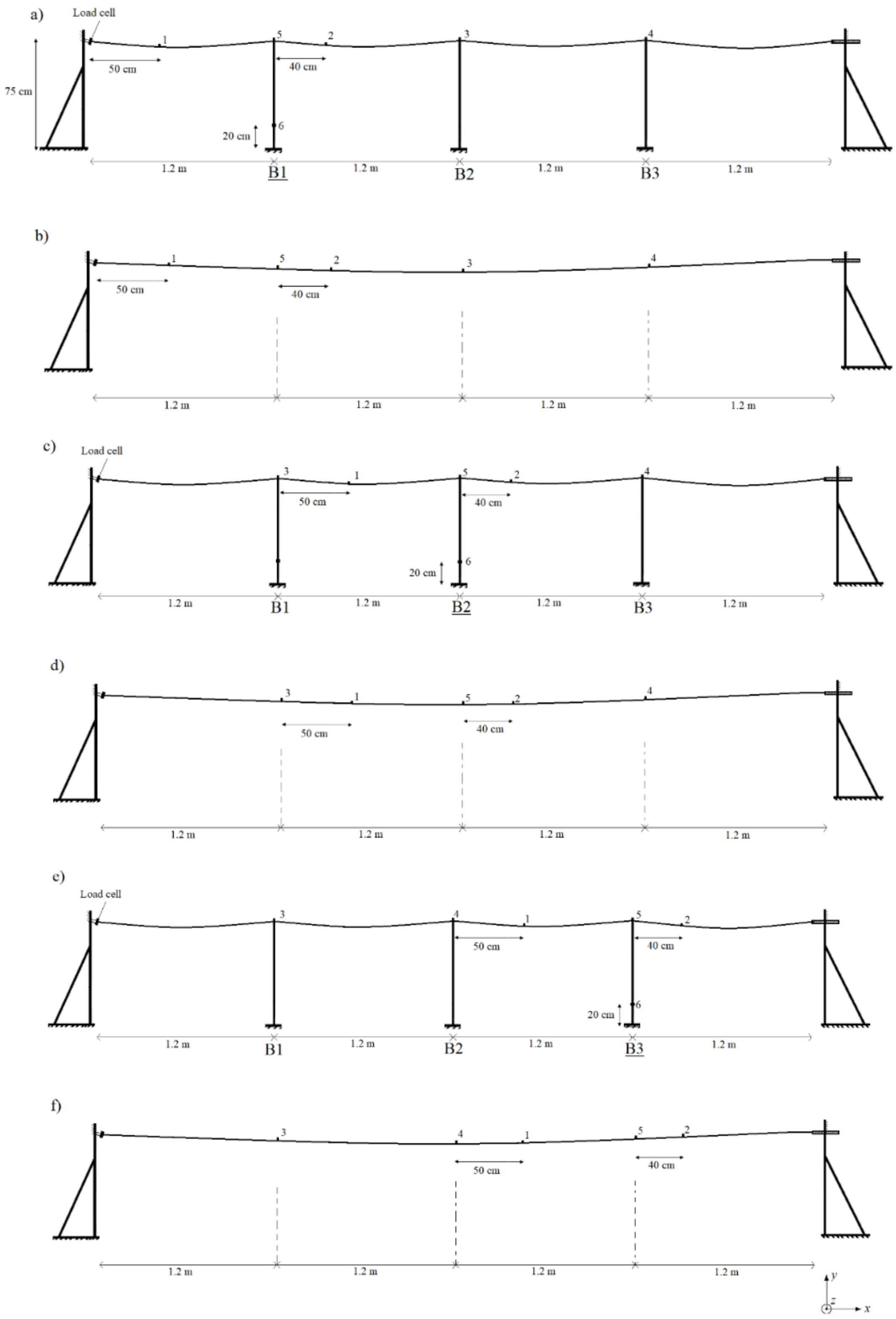

Figure 7.7: Schematic of multi-beam-cable system, cable and measurement points a-b) Beam B1 c-d) Beam B2 e-f) Beam B3

The overall system and cable-only setup, with measurement points, are shown in Figure 7.8.

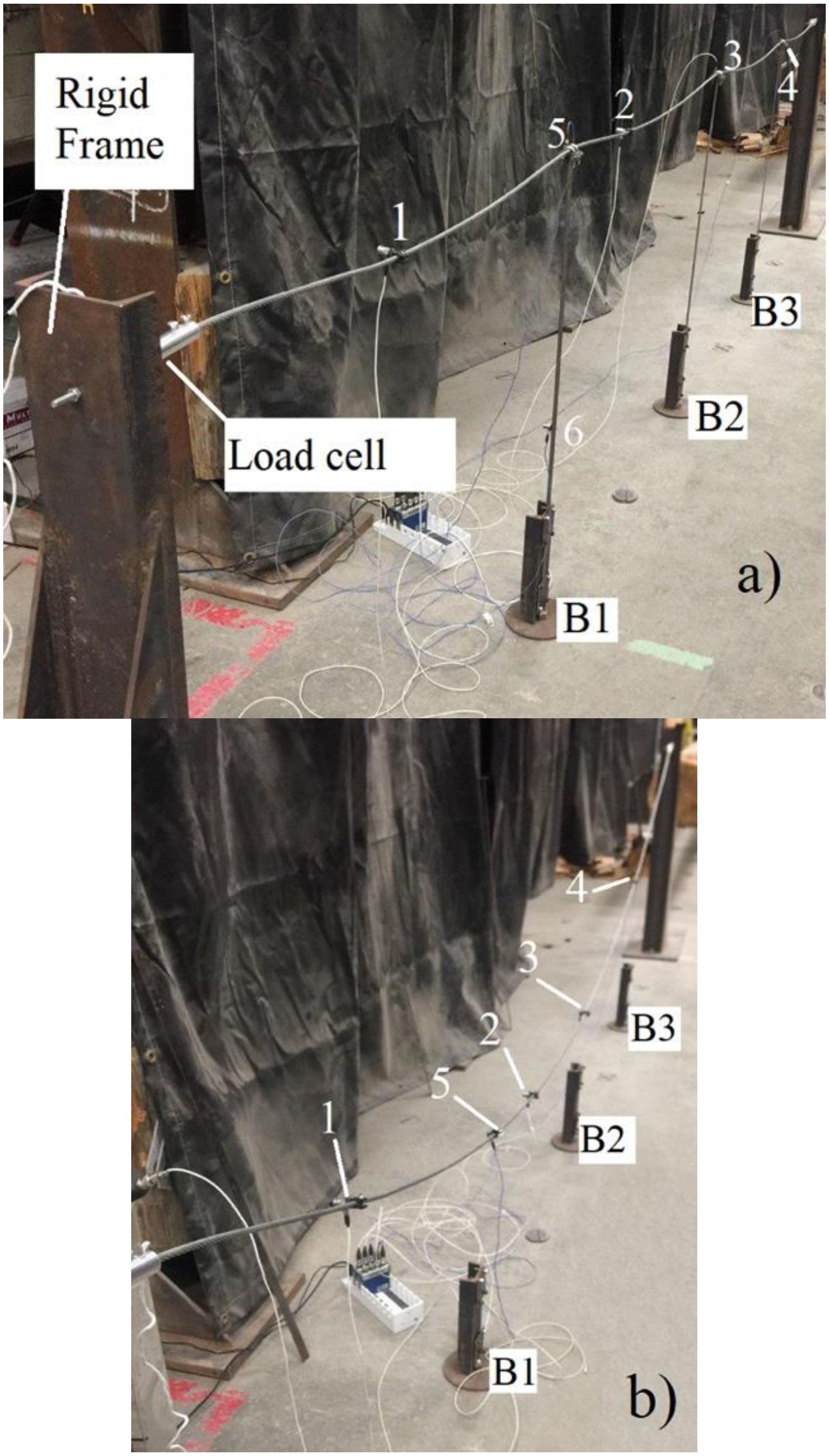

Figure 7.8: a) Multi-beam-cable system and measurement points b) Cable-only setup

Three beams used in the test have the same geometrical and mechanical properties but their measured FRFs are slightly different, likely due to manufacturing tolerances. Figure 7.9 compares the predicted and measured FRFs for 10 N and 100 N cable tensions.

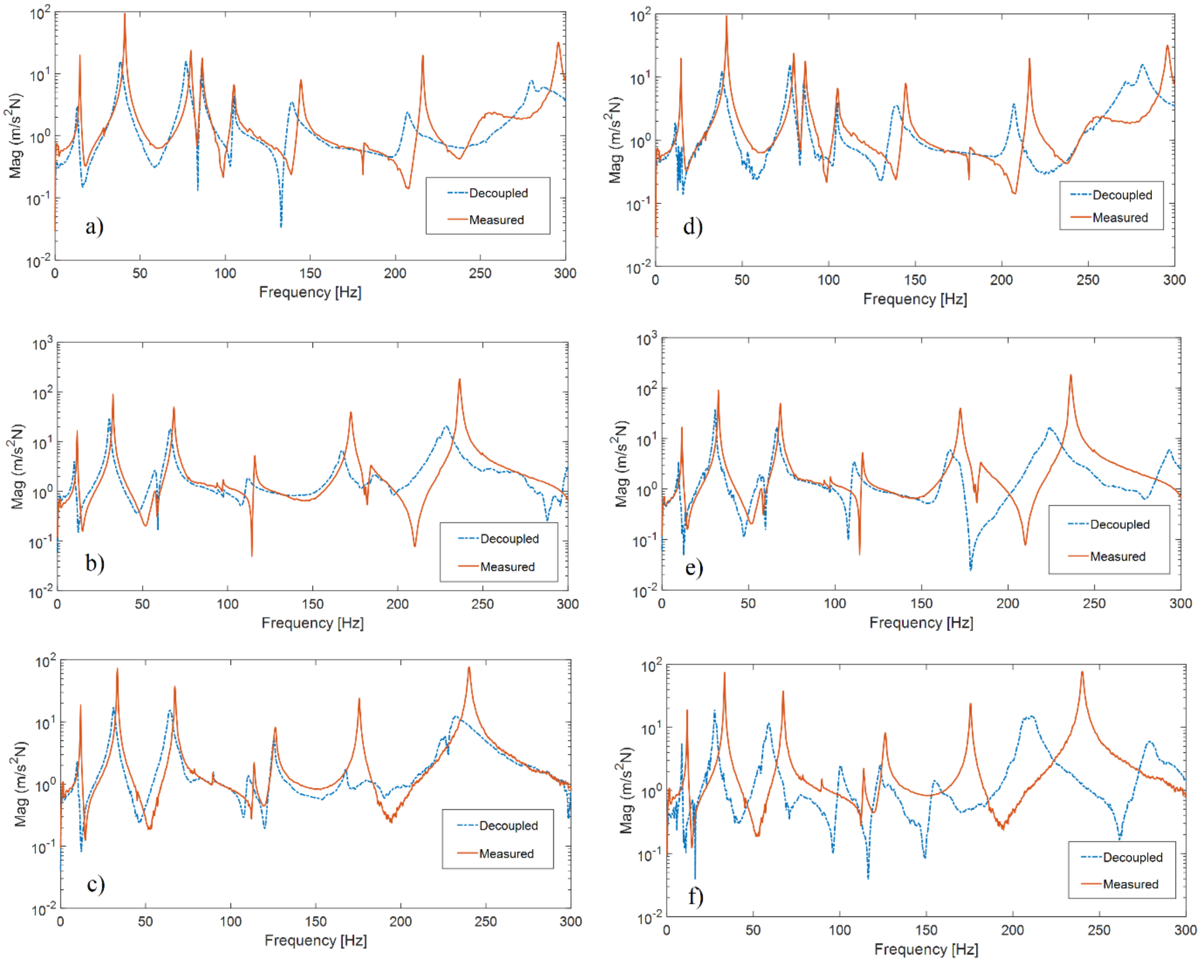

Figure 7.9: Comparison of predicted and measured FRF in a multi-beam-cable system with 10 N cable tension a) B1 b) B2 c) B3 and 100 N tension d) B1 e) B2 f) B3 and 100N tension d) B1 e) B2 f) B3

Natural frequencies and damping ratios of the beams extracted from the predicted FRFs and measured FRFs are compared in Table 7.2.

Table 7.2. Modal properties of beams: predicted using different tensions and measured in a multi-beam-cable system

Mode	**1**		**2**		**3**		**4**		**5**		**6**		**7**		**8**	
	Hz	%	Hz	%	Hz	%	Hz	%	Hz	%	Hz	%	Hz	%	Hz	%
B1																
Measured	2.0	1.5	14.6	0.27	41.0	0.18	79.8	0.26	86.4	0.19	105.2	0.23	144.4	0.28	180.0	0.67
Decoupled 10N	2.0	1.4	13.0	2.60	38.8	0.23	77	0.59	86	0.23	105.2	0.19	139.2	0.71	-	-
Decoupled 100N	-	-	11.2	0.22	38.4	0.90	77.6	0.56	85.6	0.33	105.0	0.19	139.2	0.60	-	-
B2																
Measured	1.6	1.5	11.6	0.40	32.6	0.2	58.0	1.1	68.6	0.33	115.8	0.37	172.4	0.33	183.8	1.37
Decoupled 10N	1.4	1.6	9.8	1.02	30.4	0.85	59.0	1.6	66.6	0.40	110.8	0.45	165.2	0.65	186.0	2.3
Decoupled 100N	1.4	-	9.6	0.80	30.8	0.51	58.4	0.96	66.4	0.62	111.2	0.40	166.4	0.7	-	-
B3																
Measured	1.4	-	11.74	0.92	33.3	0.342	67.12	0.743	89.6	0.23	113.8	0.318	126.2	0.73	175.6	0.17
Decoupled 10N	1.4	-	9.8	1.20	31.0	0.90	59.0	1.10	89.8	0.19	110.3	0.80	125.4	0.80	168	0.45
Decoupled 100N	1.4	-	8.6	0.89	27.6	0.56	58.4	0.90	-	-	100.0	0.75	123.2	0.82	154.2	0.32

The discrepancy between the predicted and measured modal properties is slightly higher than for the single-beam system. This is to be expected given that the number of measurement sites is the same but more structural elements are present. The authors believe the results show that the FRF prediction method is sound, considering the system complexity and limited number of sensors. Some measured FRF peaks were not sufficiently well defined to allow calculation of damping ratio, resulting in gaps in the table. In order to use the decoupling method in the field, some FRFs corresponding to inaccessible points should be generated by FE models. The theoretical foundation of FRF-based model updating was presented in section 7.3. The proposed procedure is applied to the cable-beam system and the results are presented in section 7.5.

7.5 Finite Element Model Updating

In order to use the decoupling method in the field, some FRFs corresponding to inaccessible points should be generated by FE models. The FRFs measured from the accessible points can be used to update the FE model, so that it can then accurately generate inaccessible-point FRFs. This is also a method for overcoming practical limitations in many structures on which mounting sensors at some points is impossible or unsafe.

Modeling of stranded cables has been studied with various levels of model complexity [90]. In this paper, bending stiffness of the cable (*EI*) is measured in different tensions using the procedure discussed in [15]. Figure 7.10 shows the FE model of the assembled system developed in Abaqus software with 320 nodes and 321 three-dimensional two-node linear beam elements (B31). The measured bending stiffness is 0.525 Nm^2 for 150 N tension. Only the system with 150 N tension is used here for modeling. In both the cable-beam assembled system model (Figure 7.10) and the cable-only system model (Figure 7.12), we adjust the diameter and density of our equivalent solid-section using the following equations:

$$\begin{aligned} E_c I_c = a \Rightarrow E_c \frac{\pi {d_c}^4}{64} = a \\ \rho_c A_c = b \Rightarrow \rho_c \frac{\pi {d_c}^2}{4} = b \end{aligned} \tag{7.27}$$

The quantities a and b are the measured bending stiffness and the catalogue value of linear density, respectively. Eq. (7.27) is solved for the equivalent diameter d_c and density ρ_c and the calculated values are used in the cable modeling. Three measurement/calculation points only are used here

(Figure 7.10) since it was shown in section 7.4.1.1 that these three points (points 4, 5, 6 in Figure 7.2) can lead to sufficiently accurate results.

The points 2 and 3 are accessible points in the field, but point 1 (the connection point of power line to pole) is not. Therefore, the FRFs ${H_{11}}^{CB}$, ${H_{12}}^{CB}$, ${H_{13}}^{CB}$(and their symmetric arrays) in the assembled system and ${H_{11}}^{C}$ of the cable substructure are not measurable in the field. Finite element model updating is used here. The FRF ${H_{22}}^{CB}$ is the comparison baseline for updating. The FE model of the assembled system is developed using Abaqus software and updating is performed with the use of Abaqus2Matlab software [125] and MATLAB's *fmincon* nonlinear constrained optimization routine. A convergence study was performed and the results did not change with a finer mesh. The beam and cable Young's modulus and density are the updating parameters. Multiple initial points were chosen to increase the possibility of finding a global optimum.

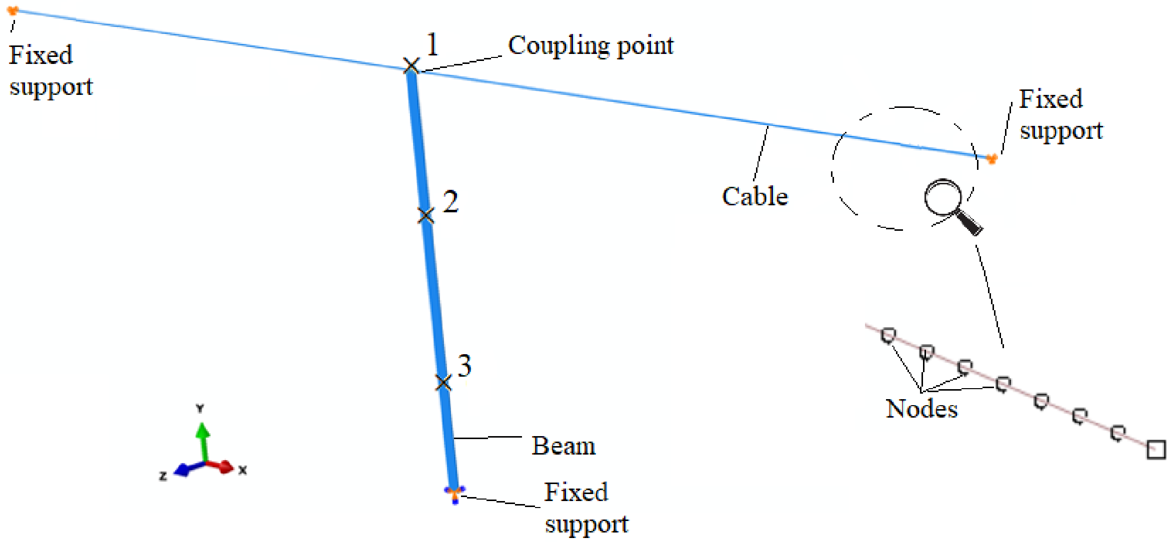

Figure 7.10: FE model of single-beam-cable system and the decoupling points

Figure 7.11 shows the updated and initial ${H_{22}}^{CB}$, compared to that obtained from experiment. There is an improvement from the initial to the updated FRF and this improvement is more significant in the 0-50 Hz frequency range. There are still some discrepancies which could be due to the low sensitivity of the FRF to some design variables in some frequency ranges, and to the cable model fidelity (equivalent solid section as opposed to stranded). The FRFs ${H_{11}}^{CB}$, ${H_{12}}^{CB}$ and ${H_{13}}^{CB}$ are then generated using the updated FE model and are used for the decoupling analysis.

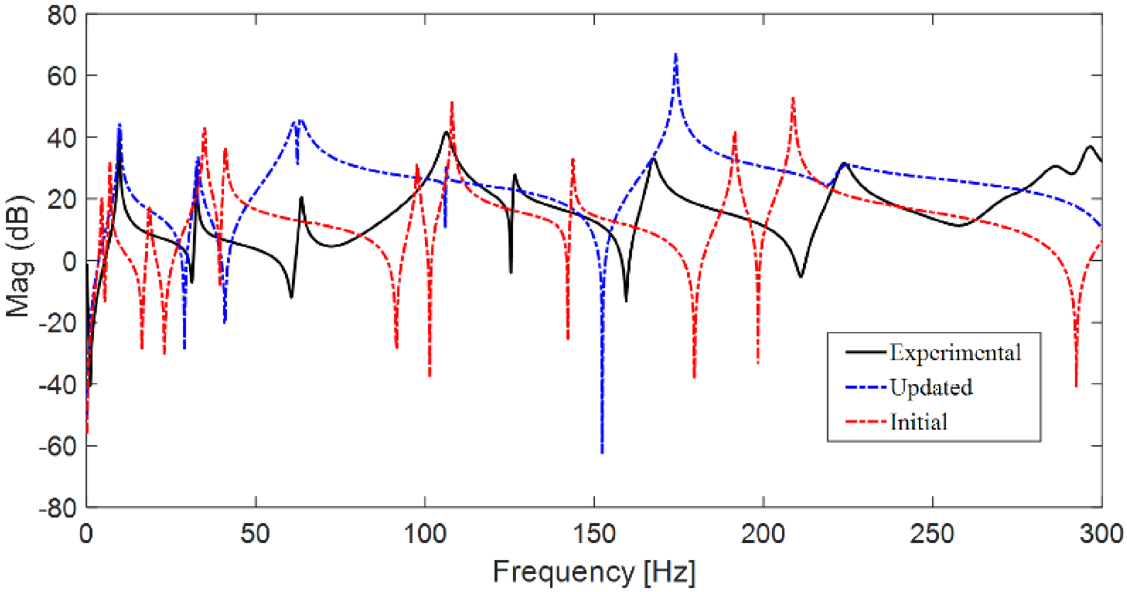

Figure 7.11: Comparison of experimental, updated and initial FRF H_{22}^{CB} in single-beam-cable system

In order to obtain the FRF of the isolated cable, ${H_{11}}^{C}$ (the only array in $\boldsymbol{H}^{C}$), the values of density and diameter calculated from Eq. (7.27) are used to model the cable with beam elements. Since the cable-only system is a smaller system than the cable-beam system, a better model updating performance can be achieved by having more optimization variables. It is possible to have large stiffness and mass matrices in the optimization process and update the matrix elements in each iteration. Figure 7.12 shows the schematic of the cable model with 100 beam elements and pinned at both ends. A MATLAB FE code was used instead of Abaqus to facilitate variable updating and interfacing with the optimizer. All the stiffness and mass elements are directly modified using the multipliers p in Eq. (7.23). Therefore, there are 100 multipliers for the stiffness matrices and 100 multipliers for the mass matrices that need to be updated in each iteration, a process that is impossible or extremely difficult in Abaqus. The process of updating the modifiers is done using *fmincon* algorithm in MATLAB. The lower and upper bounds for all the variables are considered to be 0.5 and 1.5, respectively.

There have been many studies for modeling stranded cables considering analytical/torsional and bending behavior and considering nonlinearity [126], [98], [127], [90], [17] but the purpose of cable modeling here is to demonstrate FE updating to improve the FRF obtained from the initial model. A more detailed model could be used but could cause the FE updating process to become too computationally expensive.

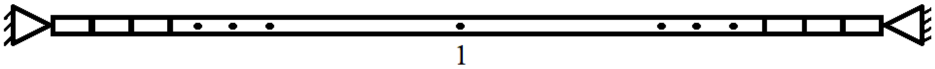

Figure 7.12: Cable FE model

Figure 7.13 shows the updated and initial FRF ${H_{11}}^{C}$compared to the FRF obtained from experiment. The magnitude of the updated FRF matches more with the experimental one and the sharpness of the peaks is closer to the experimental FRF. There are still some discrepancies but after using the generated FRFs in Eq. (7.20) for decoupling analysis, the result in section 7.6.1 shows that this discrepancy does not cause any unacceptable error between the final decoupled FRFs and the measured ones.

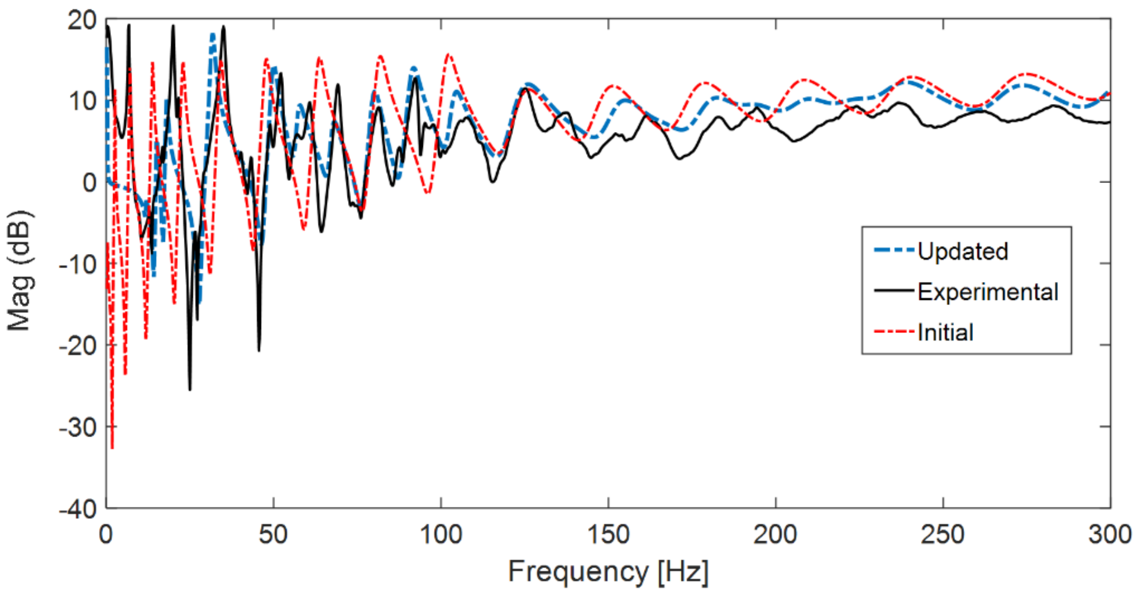

Figure 7.13: Comparison of updated and initial cable FRF with experimental FRF

7.6

7.6.1 Experimental-Numerical Decoupling Results

The FRFs obtained in the FE updating are used here beside the experimentally obtained FRFs to predict the beam FRF in the single-beam-cable system. Figure 7.14 shows the *CB* and *C* matrices and illustrates the numerical and experimental FRFs used in the decoupling analysis.

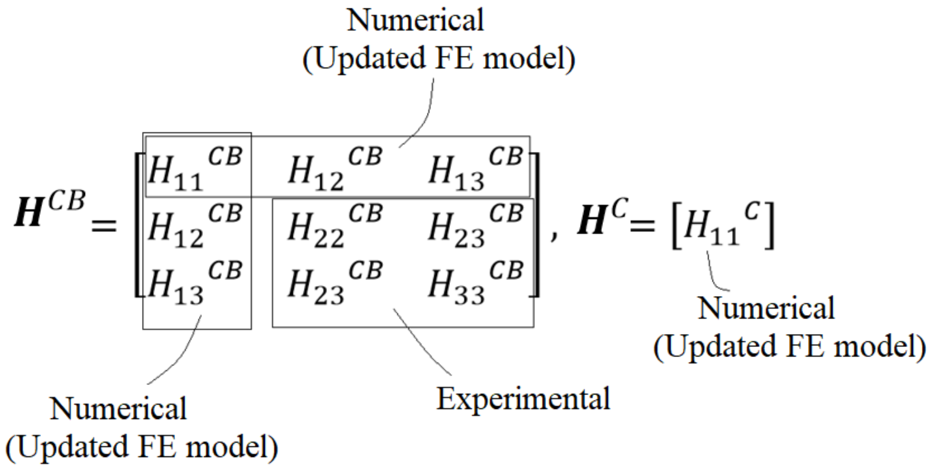

$$\boldsymbol{H}^{CB} = \begin{bmatrix} {H_{11}}^{CB} & {H_{12}}^{CB} & {H_{13}}^{CB} \\ {H_{12}}^{CB} & {H_{22}}^{CB} & {H_{23}}^{CB} \\ {H_{13}}^{CB} & {H_{23}}^{CB} & {H_{33}}^{CB} \end{bmatrix}, \ \boldsymbol{H}^{C} = \left[{H_{11}}^{C} \right]$$

Figure 7.14: Combination of experimental and numerical FRFs used in decoupling analysis

Figure 7.15 shows the predicted and measured ${H_{23}}^{B}$. Decoupled FRF show a good agreement with the measured FRF, demonstrating that using the FRFs obtained from the updated FE model beside the experimentally obtained FRFs can predict the beam FRFs with good accuracy.

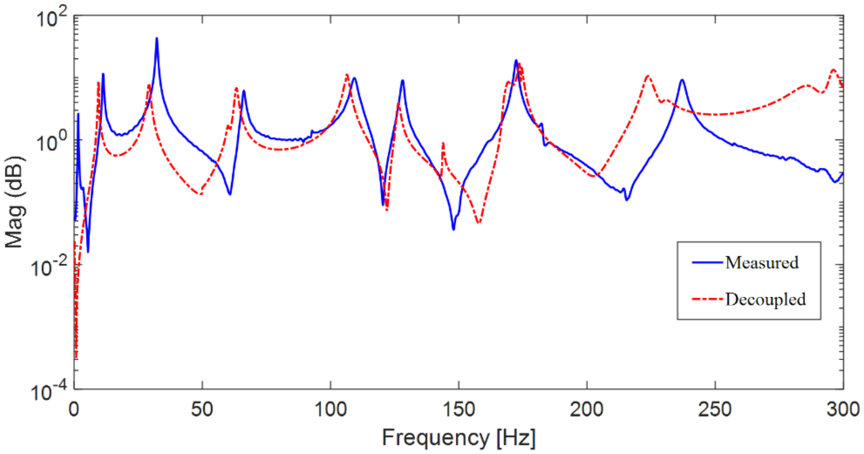

Figure 7.15: Comparison of decoupled and measured FRF H_{23}^{B} using numerical-experimental FRFs

7.7 Conclusion

This paper developed a frequency-based decoupling approach to extract the dynamic properties of individual structural elements in a cable-beam system. A single-beam-cable system was subjected to FRF-based experimental decoupling and the bean FRF was predicted. It was shown that frequency-based decoupling can be applied in cabled structures to extract the dynamics of the structure with the effects of the cables filtered out. Extension to a multi-beam-cable system showed that the decoupling analysis can extract the properties of one of multiple elements, even when they interact with other structural elements through the cables. Various amounts of cable sag were considered for the analyses and the decoupling analysis had a good result with low cable sag, which is significant given that cable sag at low tensions strongly influences dynamic response. The limitations of this method are that the FRFs corresponding to the coupling point(s) between the substructures must be measured, and finding the optimum number and location of sensors to achieve the best decoupling results is difficult. FRF-based finite element model updating was then used to overcome the problem of measuring FRFs corresponding to inaccessible points. The finite element model was updated based on measured FRFs of accessible points, after which FRFs corresponding to inaccessible points were generated using the updated model. FRF matrices consisting of a combination of experimental and numerically-obtained FRFs were then used in a decoupling analysis to predict a structural element FRF with good accuracy. In the future work, substructure decoupling will be used for a real utility pole-conductor system and the proposed FE updating method will be used to overcome the practical limitation of accessing some points of the real-world system for mounting sensors. Future work will also investigate an optimal number of sensors, and optimum sensor locations, to manage the tradeoff between accuracy and measurement cost.

Conflict of interests

The authors declare no conflict of interest in preparing this article.

Funding

The authors would like to thank Newfoundland and Labrador Hydro for their financial and in-kind support, and the

Natural Sciences and Engineering Research Council of Canada (NSERC) for their support under the Collaborative Research and Development (CRD) program.

Chapter 8

8 Prediction of Beam Dynamics in Cable-Beam Systems Through Experimental-Numerical Decoupling

[a*]Mohammad Hadi Jalali, [a] Geoff Rideout

[a] Faculty of Engineering and Applied Science, Memorial University, St. John’s, Canada

This chapter was presented as a conference paper in EURODYN2020 in Athens, Greece. In this chapter, FRF of the cable is obtained from finite element method and FRFs of the assembled cable-beam system are obtained experimentally. The combination of numerical and experimental FRFs are used in the decoupling analysis to obtain the FRF of the beam as an independent substructure. The co-authorship statement for this chapter follows:

The declaration applies to the following article	
Title of Chapter	Chapter 8: Prediction of Beam Dynamics in Cable-Beam Systems Through Experimental-Numerical Decoupling
Article status: Published	
The PhD student analyzed the literature, performed the experiments, collected the data, developed the codes and prepared the manuscript. The experimental setup was designed by the co-op student. The supervisor edited, helped organize the manuscript, and contributed to the choice of case studies.	

Abstract

Interactions between cable and structure affect the modal properties of cabled structures such as overhead electricity transmission and distribution line systems. Modal properties of an in-service pole, without the effects of conductors, are potentially useful for condition monitoring, but are difficult to determine. This paper presents a frequency-based decoupling method to extract modal properties of a beam with the effects of cable filtered out. A scalable experimental lab-scale pole-line for a cable-beam system consisting of a cantilever beam and stranded cable is used to validate the method. A finite element model for the stranded cable is developed and optimized using FRF-based nonlinear optimization based on experimentally obtained FRF and the FRFs of the assembled system are measured. The (unknown) FRF of the cantilever beam is predicted by substructural decoupling of the numerical cable dynamic model (known FRF matrix) from the measured assembled cable-beam dynamic model (known FRF matrix). Comparison of the estimated and directly measured beam FRF's show good agreement, demonstrating that the method can be used to filter out the effects of cable on the modal properties of the structure in cabled structures.

Keywords: Cable-Beam System, FRF-b.ased Decoupling, Finite Element Model Updating.

8.1 Introduction

Dynamic interaction between cables and the main structure in cabled structures such as cable-stayed bridges, guyed towers, cable-stayed wind turbines, and power transmission lines has been a topic of interest of researchers for many years. The focus of this study is power transmission lines and dynamic interaction between the conductor (cable) and the pole. The authors are developing a global NDT (Non-destructive Testing) method to detect damage at any location, based on vibration response from modal impact testing at a single arbitrary location [7,15–17,56]. Since power lines (conductors) are attached to the poles, vibrations of the conductors affect the modal properties of the pole. Removing the effect of the conductors to reveal pole properties requires a structural dynamic method to decouple the cable dynamic model from the assembled cable-pole dynamic model.

There are many studies in the literature about the interaction between cables and structures as a coupled system. Gattulli et. al. [77] investigated linear coupled vibration of two masonry walls connected by a cable. The system was modeled as two cantilever beams connected by a cable and the effect of different parameters on coupled vibration behavior was investigated. Potenza et. al. [128] and Gattulli et. al. [117] studied the same system using nonlinear analysis. Jalali et. al. [15] developed an analytical model to study the effect of cable sag and bending stiffness on coupled vibration behavior of a cable-beam system. Cable bending stiffness and sag had significant effects. The analytical results were verified by experiments on a lab-scale cable-beam system. Li et. al. [55] presented a simplified computational model for a high-voltage transmission tower-line system to study the coupling behavior of adjacent tower spans and cables due to seismic excitations. Reviewing the literature in cable-beam system dynamic analysis reveals that all the published papers studied the dynamic interaction of cable and beam in linear or nonlinear analysis and there is no research dealing with extraction of dynamic properties of the beam as an independent substructure.

Dynamic substructuring methods and the reverse problem (inverse dynamic substructuring) are well established [14,69,129–131]. Inverse dynamic substructuring or decoupling is a relevant issue for subsystems that cannot be measured separately, since they are coupled to their neighboring substructure(s) in operational conditions [13]. In this paper, a frequency-based or FRF-based decoupling technique is used to extract beam dynamics in a cable-beam system with the effects of connected cable filtered out. An experimental reduced-scale cable-beam set up of a cantilever beam connected to a stranded cable was built to measure the assembled system FRFs and a finite element model for the cable was developed and optimized using FRF-based optimization. The cable numerical model was then decoupled from the assembled (measured) system through experimental-numerical FRF-based decoupling.

The paper is outlined as follows. A summary of theory behind FRF-based decoupling is presented in Section 8.2 and FRF-based finite element model updating is described briefly in Section 8.3.

Section 8.4 describes the cable-beam system and finite element model updating of the cable. Decoupling results and discussion are presented in Section 8.5 and conclusion and future work are presented in Section 8.6.

8.2 Substructure decoupling

In a cable-beam system (Figure 8.1), the cable and the beam are “substructures” of the assembled system and the purpose of substructure decoupling is to find the dynamics of beam subsystem (*B*) as a “standalone” component that is completely decoupled from subsystem cable (*C*).

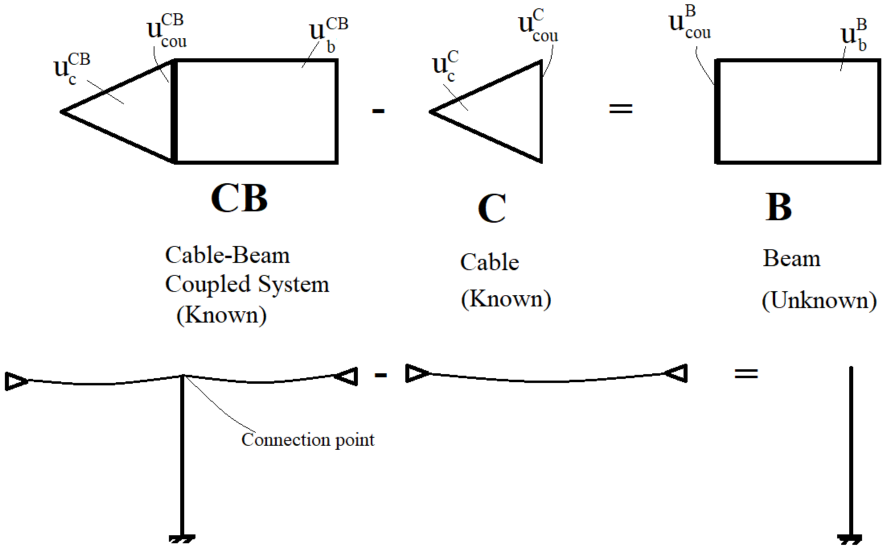

Figure 8.1: Substructure decoupling schematic

Assuming the dynamics of system *CB* and *C* are known, a dynamic stiffness representation of the assembled system *CB* in compact form is [13]:

$$\boldsymbol{Z}^{CB}\boldsymbol{u}^{CB} = \boldsymbol{f}^{CB} + \boldsymbol{g}^{CB}$$

$$\begin{bmatrix} \boldsymbol{Z}_{cc}^{CB} & \boldsymbol{Z}_{ccou}^{CB} & \boldsymbol{0} \\ \boldsymbol{Z}_{couc}^{CB} & \boldsymbol{Z}_{coucou}^{CB} & \boldsymbol{Z}_{coub}^{CB} \\ \boldsymbol{0} & \boldsymbol{Z}_{bcou}^{CB} & \boldsymbol{Z}_{bb}^{CB} \end{bmatrix} \begin{bmatrix} \boldsymbol{u}_c \\ \boldsymbol{u}_{cou} \\ \boldsymbol{u}_b \end{bmatrix} = \begin{bmatrix} \boldsymbol{f}_c \\ \boldsymbol{f}_{cou} \\ \boldsymbol{f}_b \end{bmatrix} + \begin{bmatrix} \boldsymbol{0} \\ \boldsymbol{g}_{cou} \\ \boldsymbol{0} \end{bmatrix} \tag{8.1}$$

And subsystem *C*:

$$\boldsymbol{Z}^C\boldsymbol{u}^C = \boldsymbol{f}^C - \boldsymbol{g}^C$$

$$\begin{bmatrix} \boldsymbol{Z}^C_{cc} & \boldsymbol{Z}^C_{ccou} \\ \boldsymbol{Z}^C_{couc} & \boldsymbol{Z}^C_{coucou} \end{bmatrix} \begin{bmatrix} \boldsymbol{u}^C_c \\ \boldsymbol{u}^C_{cou} \end{bmatrix} = \begin{bmatrix} \boldsymbol{f}_c \\ \boldsymbol{f}_{cou} \end{bmatrix} - \begin{bmatrix} \boldsymbol{0} \\ \boldsymbol{g}^C_{cou} \end{bmatrix} \tag{8.2}$$

where $\boldsymbol{u}^{CB} = \begin{bmatrix} \boldsymbol{u}_c \\ \boldsymbol{u}_{cou} \\ \boldsymbol{u}_b \end{bmatrix}$ is the vector of DOF of system *CB* (Figure 8.1) (the superscripts are omitted for brevity), $\boldsymbol{u}^C = \begin{bmatrix} \boldsymbol{u}^C_c \\ \boldsymbol{u}^C_{cou} \end{bmatrix}$ is the vector of DOF of substructure *C*, $\boldsymbol{Z}^{CB}$ and $\boldsymbol{Z}^C$ are the stiffness matrices of system *CB* and *C*, respectively (stiffness matrix is the inverse of FRF matrix ($\boldsymbol{Z} = \boldsymbol{H}^{-\boldsymbol{1}}$)). Vectors $\boldsymbol{f}^*$ are the external force vectors and vectors $\boldsymbol{g}^*$ represent the additional disconnection forces (with non-zero entries only at the interface DOF) felt from the decoupling of the neighboring components [13]. When two substructures are in contact and (de)coupling is carried out, compatibility and equilibrium conditions at the connected interface DOFs must always be satisfied. The compatibility condition ($\boldsymbol{u}^C_{cou} = \boldsymbol{u}_{cou}$) states that the displacements of connected interface DOF must be compatible and the equilibrium condition ($\boldsymbol{g}_{cou} + \boldsymbol{g}^C_{cou} = \boldsymbol{0}$) states that the connection forces between the substructures should be in equilibrium. A more systematic description of the problem can be written by introducing the Boolean matrices $\boldsymbol{B}$ and $\boldsymbol{L}$ and writing the compatibility and equilibrium in a compact from: [13]

$$\boldsymbol{B}\boldsymbol{u} = [\boldsymbol{B}^{CB} \quad \boldsymbol{B}^C] \begin{bmatrix} \boldsymbol{u}^{CB} \\ \boldsymbol{u}^C \end{bmatrix} = \boldsymbol{u}^C_{cou} - \boldsymbol{u}_{cou} = \boldsymbol{0} \tag{8.3}$$

$$\boldsymbol{L}^{\boldsymbol{T}}\boldsymbol{g} = [\boldsymbol{L}^{CB^T} \quad \boldsymbol{L}^{C^T}] \begin{bmatrix} \boldsymbol{g}^{CB} \\ \boldsymbol{g}^C \end{bmatrix} = \begin{bmatrix} \boldsymbol{0} \\ \boldsymbol{0} \\ \boldsymbol{0} \\ \boldsymbol{g}_{cou} + \boldsymbol{g}^C_{cou} \end{bmatrix} = \boldsymbol{0} \tag{8.4}$$

Eq. (8.3) presents the compatibility equation and Eq. (8.4) presents the equilibrium equation. Therefore, the decoupling problem can be described in the following equations:

$$\begin{gathered}
\begin{bmatrix} \boldsymbol{Z}^{CB} & \boldsymbol{0} \\ \boldsymbol{0} & \boldsymbol{Z}^{C} \end{bmatrix} \begin{bmatrix} \boldsymbol{u}^{CB} \\ \boldsymbol{u}^{C} \end{bmatrix} = \begin{bmatrix} \boldsymbol{f}^{CB} \\ \boldsymbol{f}^{C} \end{bmatrix} + \begin{bmatrix} \boldsymbol{g}^{CB} \\ -\boldsymbol{g}^{C} \end{bmatrix} \\
\begin{bmatrix} \boldsymbol{B}^{CB} & \boldsymbol{B}^{C} \end{bmatrix} \begin{bmatrix} \boldsymbol{u}^{CB} \\ \boldsymbol{u}^{C} \end{bmatrix} = \boldsymbol{0} \\
\begin{bmatrix} \boldsymbol{L}^{CB^T} & \boldsymbol{L}^{C^T} \end{bmatrix} \begin{bmatrix} \boldsymbol{g}^{CB} \\ \boldsymbol{g}^{C} \end{bmatrix} = \boldsymbol{0}
\end{gathered} \tag{8.5}$$

Employing the dual formulation for decoupling [60], the interface forces are satisfied a priori by choosing interface forces of the form of:

$$\boldsymbol{g} = -\boldsymbol{B}^{T}\boldsymbol{\lambda} \tag{8.6}$$

where $\boldsymbol{\lambda}$ are Lagrange multipliers, corresponding physically to the interface force intensities. The equilibrium condition in Eq. (8.4) thus becomes:

$$\boldsymbol{L}^{\boldsymbol{T}}\boldsymbol{g} = -\boldsymbol{L}^{\boldsymbol{T}}\boldsymbol{B}^{\boldsymbol{T}}\boldsymbol{\lambda} = \boldsymbol{0} \tag{8.7}$$

But by considering the fact that $\boldsymbol{L}^{\boldsymbol{T}}$ is the null space of $\boldsymbol{B}^{\boldsymbol{T}}$ [14], this condition is always satisfied. The decoupling methods can be categorized as collocated methods when both the compatibility and equilibrium are imposed at the same sets of DOFs ($\boldsymbol{C}^{*} = \boldsymbol{E}^{*}$) or non-collocated methods when different sets of DOFs ($\boldsymbol{C}^{*} \neq \boldsymbol{E}^{*}$) are used for imposing the compatibility and equilibrium conditions. The decoupling problem can therefore be formulated in a dual way as [13]:

$$\begin{bmatrix} \boldsymbol{Z}^{CB} & \boldsymbol{0} & \boldsymbol{E}^{CB^T} \\ \boldsymbol{0} & -\boldsymbol{Z}^{C} & \boldsymbol{E}^{C^T} \\ \boldsymbol{C}^{CB} & \boldsymbol{C}^{C} & \boldsymbol{0} \end{bmatrix} \begin{bmatrix} \boldsymbol{u}^{CB} \\ \boldsymbol{u}^{C} \\ \boldsymbol{\lambda} \end{bmatrix} = \begin{bmatrix} \boldsymbol{f}^{CB} \\ \boldsymbol{0} \\ \boldsymbol{0} \end{bmatrix} \tag{8.8}$$

By eliminating Lagrange multipliers $\boldsymbol{\lambda}$ in Eq. (8.8) and solving for decoupled DOF:

$$\begin{bmatrix} \boldsymbol{u}^{CB} \\ \boldsymbol{u}^{C} \end{bmatrix} = \left(\begin{bmatrix} \boldsymbol{H}^{CB} & \boldsymbol{0} \\ \boldsymbol{0} & -\boldsymbol{H}^{C} \end{bmatrix} - \begin{bmatrix} \boldsymbol{H}^{CB} & \boldsymbol{0} \\ \boldsymbol{0} & -\boldsymbol{H}^{C} \end{bmatrix} \begin{bmatrix} \boldsymbol{E}^{CB^{T}} \\ \boldsymbol{E}^{C^{T}} \end{bmatrix} \left([\boldsymbol{C}^{CB} \quad \boldsymbol{C}^{C}] \begin{bmatrix} \boldsymbol{H}^{CB} & \boldsymbol{0} \\ \boldsymbol{0} & -\boldsymbol{H}^{C} \end{bmatrix} \begin{bmatrix} \boldsymbol{E}^{CB^{T}} \\ \boldsymbol{E}^{C^{T}} \end{bmatrix} \right)^{+} [\boldsymbol{C}^{CB} \quad \boldsymbol{C}^{C}] \begin{bmatrix} \boldsymbol{H}^{CB} & \boldsymbol{0} \\ \boldsymbol{0} & -\boldsymbol{H}^{C} \end{bmatrix} \right) \boldsymbol{f} \tag{8.9}$$

which is the form of $\boldsymbol{u} = \boldsymbol{H}\boldsymbol{f}$, so that the decoupled FRF of substructure B in a general form can be found:

$$\boldsymbol{H}^{B} = \begin{bmatrix} \boldsymbol{H}^{CB} & \boldsymbol{0} \\ \boldsymbol{0} & -\boldsymbol{H}^{C} \end{bmatrix} - \begin{bmatrix} \boldsymbol{H}^{CB} & \boldsymbol{0} \\ \boldsymbol{0} & -\boldsymbol{H}^{C} \end{bmatrix} \begin{bmatrix} \boldsymbol{E}^{CB^{T}} \\ \boldsymbol{E}^{C^{T}} \end{bmatrix} \left([\boldsymbol{C}^{CB} \quad \boldsymbol{C}^{C}] \begin{bmatrix} \boldsymbol{H}^{CB} & \boldsymbol{0} \\ \boldsymbol{0} & -\boldsymbol{H}^{C} \end{bmatrix} \begin{bmatrix} \boldsymbol{E}^{CB^{T}} \\ \boldsymbol{E}^{C^{T}} \end{bmatrix} \right)^{+} [\boldsymbol{C}^{CB} \quad \boldsymbol{C}^{C}] \begin{bmatrix} \boldsymbol{H}^{CB} & \boldsymbol{0} \\ \boldsymbol{0} & -\boldsymbol{H}^{C} \end{bmatrix} \tag{8.10}$$

where + denotes the (Moore–Penrose) pseudo-inverse, since the matrix in parentheses is not necessarily a square matrix. Eq. (8.10) is used throughout the paper for decoupling analysis.

8.3 FRF-based Finite Element Model Updating

The form of the frequency response function (FRF) used in this study is accelerance which means acceleration response over force in the frequency domain. Accelerance FRF, $H_{a,b}(\omega)$, is the acceleration response at node *a*, $A_a(\omega)$, divided by the force at node *b*, $F_b(\omega)$, both in the frequency domain [122]:

$$H_{a,b}(\omega) = \frac{A_a(\omega)}{F_b(\omega)} \cong \sum_{i=1}^{m} \frac{-\omega^2 \hat{\phi}_{ai} \hat{\phi}_{bi}}{-\omega^2 + 2i\omega\Omega_i\xi_i + \Omega^2{}_i} \tag{8.11}$$

where m is the number of modes, ω is frequency, Ω_i is *i*th natural frequency of the system, ξ_i is *i*th damping ratio corresponding to *i*th mode and $\hat{\phi}_{ai}$ and $\hat{\phi}_{bi}$ are the scalar values of mode shape *i* at response node *a* and excitation node *b*, respectively. The maximum number of modes, m, that can be used to construct the response is equal to the total number of degrees of freedom of the system. However, it is not feasible to measure all degrees of freedom and the entire range of natural frequencies during structural testing. Therefore, a reduced number of mode shapes can be used.

Special care must be taken to include enough mode shapes in the formulation, typically more than measured [18]-[19]. For a rule of thumb, at least double the number of modes that are measured should be used for analytical FRF calculation [122].

From of FRF used for model updating is as follows and the values of the FRF magnitude is in dB scale:

$$\overline{H}_{a,b}(\omega) = 20\log_{10}\left(\left|H_{a,b}(\omega)\right|\right) \tag{8.12}$$

The goal of the FE model updating is to change the properties of a FEM such that the analytical response of the model matches that of measured data. The goal is to obtain an analytical FRF as close as possible to the experimental FRF in a desired frequency range. After developing the FE model, Eq. (8.12) and Eq. (8.11) are used to obtain the FRF at the response and excitation nodes corresponding to the response and excitation locations considered in the experiment. The problem then is a least squares problem where the difference between analytical and measured FRFs, the error or residual, is found and a scalar objective error function value is calculated [123]. With the scalar objective error function value, numerical optimization techniques are used to minimize the difference between the analytical and measured FRFs by modifying the parameters of the FEM such that the analytical FRF best matches the measured FRF [123].

Since all of the structural properties in the finite element can be modified, any combination of stiffness, mass, and damping updating may be performed. Stiffness, mass and damping parameter updating can also occur simultaneously. Substituting Eq. (8.11) into Eq. (8.12) and using modal responses as functions of the unknown updating parameters p results in Eq. (8.13) [123]:

$$\overline{H}_{a,b}(\omega,p) = 20\log_{10}\left(\left|\sum_{i=1}^{m}\frac{-\omega^2\widehat{\phi}_{ai}(p)\widehat{\phi}_{bi}(p)}{-\omega^2+2i\omega\Omega_i(p)\xi_i(p)+\Omega^2{}_i(p)}\right|\right) \tag{8.13}$$

The error function, or residual e, is defined as:

$$e(\omega, p) = \bar{H}^{a}{}_{a,b}(\omega, p) - \bar{H}^{m}{}_{a,b}(\omega, p) \tag{8.14}$$

where $\bar{H}^{a}{}_{a,b}(\omega, p)$ and $\bar{H}^{m}{}_{a,b}(\omega, p)$ are analytical and measured FRF, respectively. Then, a scalar objective error function J is created and is the quantity that is minimized through bounded numerical optimization:

$$J(p) = e^{T}(\omega, p) e(\omega, p) \tag{8.15}$$

The purpose of optimization is to minimize $J(p)$ by considering the upper and lower bounds for p [123]. The scalar objective error function is normalized by the initial value of the scalar objective error function $J(p)_1$ so that the optimization starts at a value of 1 and the perfect match would be a value of 0.

$$J(p)_i = \frac{J(p)_i}{J(p)_1} \tag{8.16}$$

The parameter p is a unitless modifier that modifies any structural parameter.

8.4 Cable-Beam system

The schematic of assembled cable-beam system (*CB*) and the cable substructure (*C*) is shown in Figure 8.2. The geometry of the (sub) structures is illustrated. The cantilever is a steel rectangular beam with cross section area of 46.67 mm^2 and the cable is a 7×19 steel stranded cable with a nominal diameter of 1/4 inch and linear density of 0.16667 kg/m. Three measurement points are considered for decoupling. In Figure 8.2-a, point 1 is a coupling DOF ($\boldsymbol{u}_{cou}^{CB}$in Figure 8.1) and points 2 and 3 are the beam internal DOFs ($\boldsymbol{u}_{b}^{CB}$in Figure 8.1) within the assembled system. There is no cable internal DOF ($\boldsymbol{u}_{a}^{CB}$in Figure 8.1) since it was intended to need the least number of DOF from the numerical cable model. In Figure 8.2-b, the coupling point 1 ($\boldsymbol{u}_{cou}^{C}$ in Figure 8.1) is shown. All the degrees of freedom are along the *z* direction. The cable tension is 150 N when the cable is connected to the beam (in system *CB*) and when the cable-only system is considered.

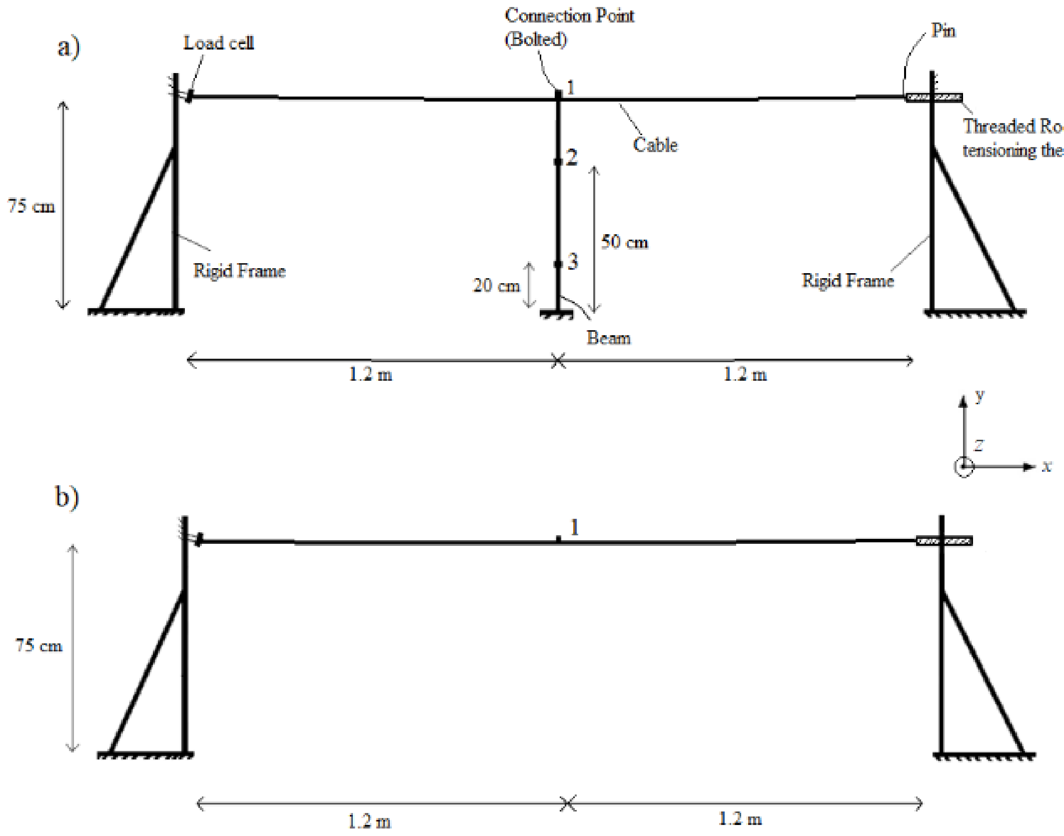

Figure 8.2: Schematic of a) Assembled cable-beam system (*CB*) b) Cable substructure (*C*)

FRFs of the assembled system ($\boldsymbol{H}^{CB}$ in Eq. (8.10)) are measured using modal testing and FRF of the cable at the coupling point ($\boldsymbol{H}^{C}$ in Eq. (8.10)) is obtained using a finite element model. Eq. (8.10) is then used to obtain the decoupled beam FRF, $\boldsymbol{H}^{B}$. The assembled system set up (*CB*) is shown in Figure 8.3. Two rigid frames were secured to the floor on the right and left sides. The natural frequencies of the frames were verified to be far away from the natural frequencies of the system. The right end of the cable was attached to a threaded rod to adjust the tension of the cable and an in-line load cell at the left end of the cable measured the longitudinal tension of the cable. Two U-bolts were used in the connection point of the cable and beam. Both ends of the cable are pinned and the beam is cantilevered. More details of the set up can be found in [15].

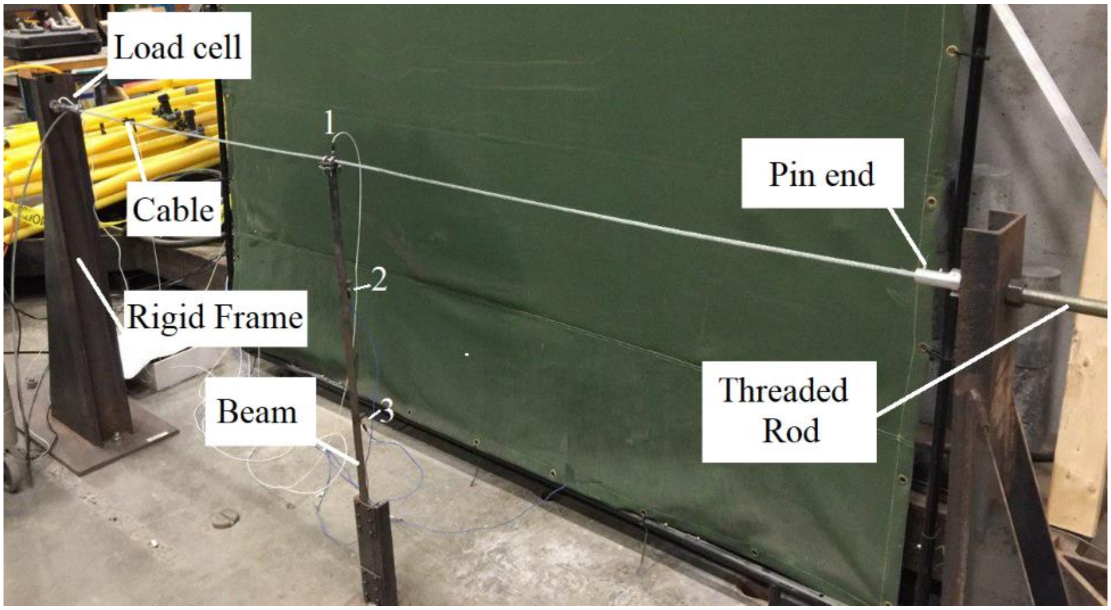

Figure 8.3: Experimental set up for cable-beam system

FRFs were obtained using a B&K 8205-002 impact hammer, a NI c-DAQ 9172 chassis and the software ModalView [95] was used to analyze the data.

8.5 Finite element model updating of the cable

In order to obtain the substructure C FRF matrix, $\boldsymbol{H}^C$ in Eq. (8.10), a finite element model for the cable is developed. The cable is modeled as pinned-pinned Euler beam with 100 finite elements. The bending stiffness (EI) of the cable was measured in the previous work of the authors [15] in different tensions and the measured value of 0.525 $Nm^2$is used in the FE model. The beam cross section area is 31.66 mm^2 and the linear density is 0.16667 kg/m.

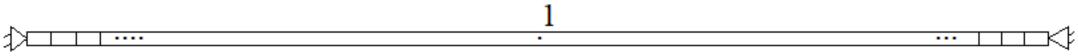

Figure 8.4. Finite element model of the cable

The FRF matrix $\boldsymbol{H}^C$ has only one array, ${H_{11}}^C$, since point 1 in Figure 8.2 is the only DOF on the cable substructure (C) that is being considered in the analysis. Therefore, in the FE model updating process, direct FRF of point 1 (excitation and response at the same place), ${H_{11}}^{C}$, that is obtained using Eq. (8.13) is updated based on the measured FRF. In the updating process, all the stiffness and mass elements are directly modified using the multipliers p in Eq. (8.13). Therefore, there are 100 multipliers (number of finite elements is 100) for the stiffness matrices and 100 multipliers for the mass matrices that need to be updated in each iteration. The nonlinear constrained optimization technique in MATLAB software is used. The lower and upper bounds for all the variables are considered to be 0.5 and 1.5, respectively. Figure 8.5 shows the updated and initial FRF compared to the FRF obtained from experiment. The magnitude of the updated FRF matches more with the experimental one and the sharpness of the peaks is closer to the experimental FRF in the updated FRF. There is still a slight discrepancy between the updated and experiment FRFs but the decoupling result in Section 8.6 shows that this discrepancy does not cause any unacceptable error in the final decoupling results.

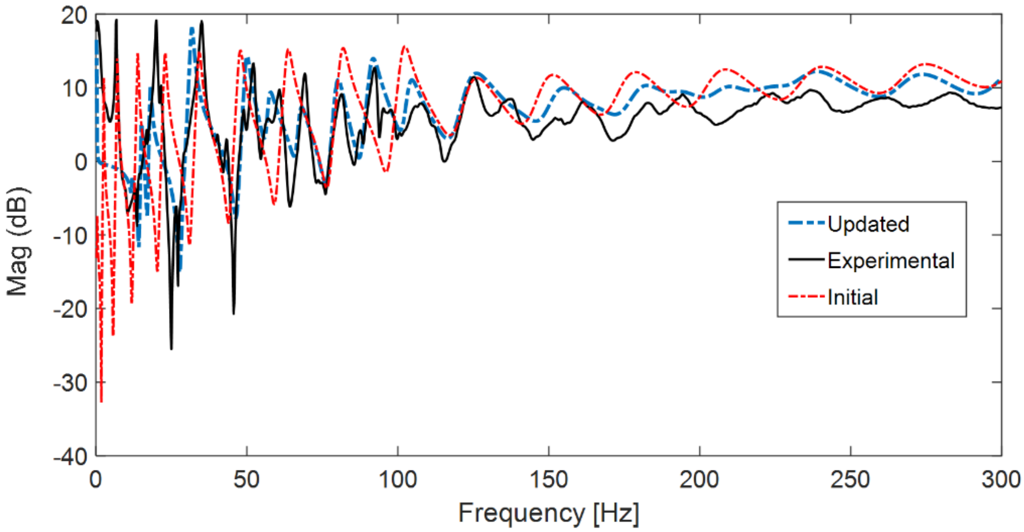

Figure 8.5: Comparison of updated and initial cable FRF with experimental FRF

8.6 Decoupling Results

The measured FRFs from the assembled system and the calculated FRF from the finite element model are used in Eq. (8.10) to predict the decoupled beam FRF. Figure 8.6 shows the predicted FRF $H_{33}{}^{B}$ and $H_{23}{}^{B}$ compared to the directly measured FRF. Decoupled FRFs show a good agreement with the measured FRFs. There is a spurious peak around 140 Hz which is probably due to numerical singularity that is common in dynamic substructuring [124]. A non-collocated approach [13] is used to obtain the results which means all the internal DOFs of the beam substructure were used for equilibrium condition.

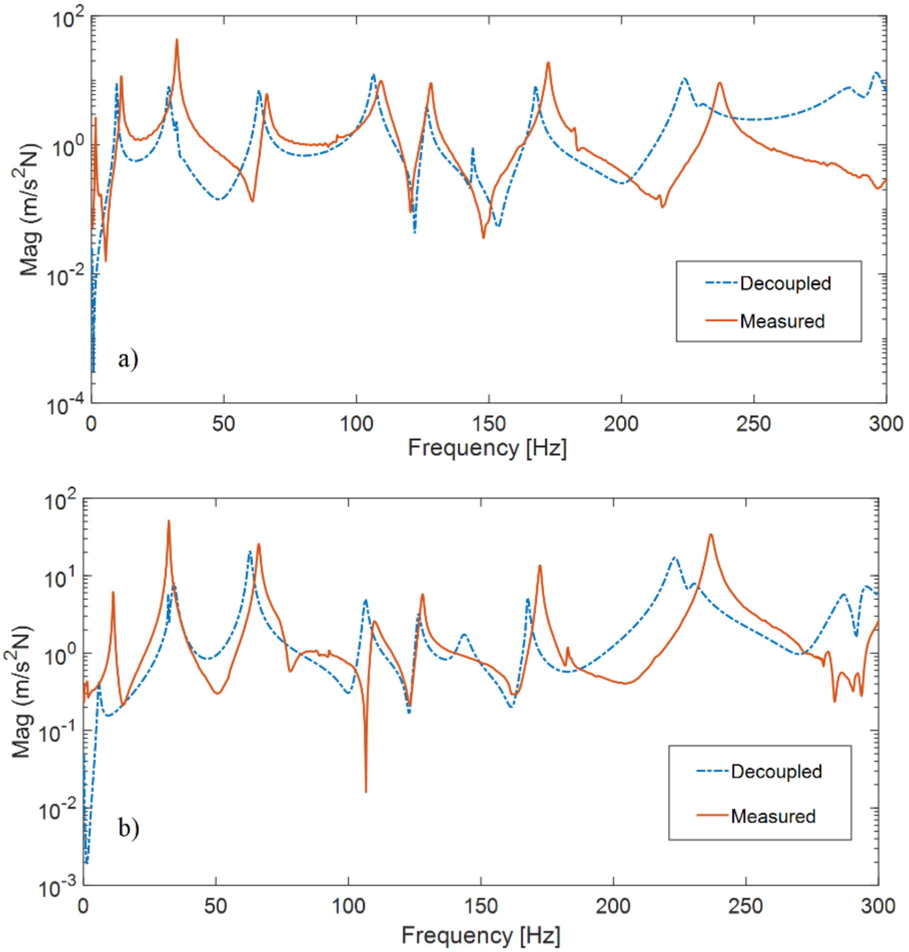

Figure 8.6: Comparison of decoupled beam FRF with measured FRF a) $H_{23}{}^{B}$ b) $H_{33}{}^{B}$

From the obtained FRFs, the modal properties of the beam can be extracted. Natural frequencies and damping ratios of the beam extracted from the predicted FRFs and measured FRFs are compared in Table 8.1. The 3 dB method [94] was used to extract the damping ratios from the FRF peaks. There is an acceptable agreement between the modal properties of the beam extracted from measured FRF and predicted FRF which shows that frequency based decoupling can be used to extract the modal properties of the beam in a cable-beam system with the cable effects filtered out. In some modes, the predicted and measured damping ratios differ which could be attributed to measurement error and difficulty in exciting the coupling point in the assembled and substructure at the same location. Damping ratio of the first mode was predicated with high error and it is not presented in the table. The reason for this error could be noise in low-frequency and as a result the peak is not clear enough to extract to damping ratio.

Table 8.1. Natural frequencies (Hz) and damping ratios (%) of beam: predicted (decoupled) and measured

Mode	1		2		3		4		5		6		7		8	
	Hz	%	Hz	%	Hz	%	Hz	%	Hz	%	Hz	%	Hz	%	Hz	%
Measured	1.6	2.03	11.2	1.42	32.2	0.52	66.2	0.52	92.8	0.19	109.4	0.68	128	0.35	172.4	0.23
Decoupled	1.4	-	9.6	1.37	32	0.37	63.2	0.59	--	--	106.2	0.57	126.4	0.31	167.6	0.21

8.7 Conclusions

In this study, a cable-beam system was studied through the application of experimental-numerical FRF-based decoupling and the beam FRF was predicted. A finite element model for the cable was developed and updated using FRF-based nonlinear optimization and then was decoupled from the measured assembled system. It was shown that frequency-based decoupling can be applied in cable structures to extract the dynamics of a structure with the effects of cable filtered out. In the field, some parts of the system such as connection point of the conductors and electricity pole are inaccessible. In future, reliable simulation models should be developed for the assembled system so that FRFs of such inaccessible points be replaced by simulation results.

Chapter 9

9 Substructural Damage Detection Using Frequency Response Function Based Inverse Dynamic Substructuring

[a*] Mohammad Hadi Jalali, [a] Geoff Rideout

[a] Faculty of Engineering and Applied Science, Memorial University, St. John’s, Canada

This chapter is a full manuscript that is under review in Mechanical Systems and Signal Processing Journal. In this chapter, a substructural damage detection method is developed for systems in which only one of the substructures, the main substructure or the target substructure, is susceptible to damage. The residual subsystem is considered unchanged and the target substructure frequency response functions (FRFs) are first obtained using the substructure decoupling method. Then, FRF-based finite element model updating is used for damage localization and quantification of the target substructure using a model of the target substructure. The co-authorship statement for this chapter follows:

The declaration applies to the following article	
Title of Chapter	Chapter 9: Substructural Damage Detection Using Frequency Response Function Based Inverse Dynamic Substructuring
Article status: Under Review	
The PhD student analyzed the literature, performed the experiments, collected the data, developed the codes and prepared the manuscript. The supervisor edited and helped organize the manuscript.	

Abstract

In this paper, a substructural damage detection approach is presented using FRF-based inverse dynamic substructuring and FRF-based model updating. In practice, often only one subsystem of the global structure is critical and susceptible to damage and therefore needs monitoring. In the proposed method, one subsystem is the “main” subsystem and is susceptible to damage and the “residual” subsystem(s) are considered undamaged and the damage identification is only applied to the main subsystem. The FRF matrix of the main subsystem is obtained as a “standalone” component that is completely decoupled from the residual subsystem(s) without the need of interface virtual support or identifying interface forces. The FRF measurement is performed on the global damaged structure but the FRFs of the main substructure (damaged) is obtained by “decoupling” the known FRF(s) of the residual subsystem from the global system FRFs and the damage detection is performed only on the main substructure. An FRF-based model updating method using numerical sensitivities is then used for damage identification of the main subsystem using only one frequency response function. The frequency response function obtained from the finite element model of the main substructure is updated using the frequency response function of the damaged main substructure (obtained from decoupling) and the location and quantity of the damage is identified. Numerical and experimental examples are presented to illustrate the damage detection procedure and the damage in the main substructure is detected, located and quantified with good accuracy.

Keywords: Structural Health monitoring, Substructural Damage detection, Inverse dynamic substructuring, Frequency-based decoupling, Finite element model updating.

9.1 Introduction

Structural health monitoring mainly aims at evaluating the symptoms of deterioration or damage that may affect the operation of the structure. Vibration-based methods are popularly used for the non-destructive damage identification of large-scale structures. The fundamental idea for the vibration-based damage identification is that the damage-induced changes in the physical properties (mass, damping, and stiffness) will cause detectable changes in modal information such as natural frequencies, modal damping, mode shapes and frequency response function (FRF). The substructural system identification approach is receiving increasing attention due to the advantage of a reduction in the number of unknown parameters to be identified, and a reduction in the system DOFs involved in the computation, with improvement in the convergence and computational efficiency [132].

In substructural damage identification methods, the global structure is usually divided into substructures and damage identification is applied locally only on the desired substructure rather than on the global structure [133]. This reduces the computational time and increases the accuracy since the modal parameters of the global structure have small sensitivity to the local damage. Zhang et.al [134] proposed a substructure identification procedure for large shear structures. In their method, an inductive identification procedure is proposed to estimate the structural story parameters from top to bottom recursively. A numerical example of a five-story structure was presented to illustrate the efficacy of the proposed substructure identification method. Zhang et. al. [135] proposed a substructure damage identification method for shear structures utilizing the dynamic equilibrium of a one-floor substructure and using the cross-power spectral densities between structural floor accelerations and a reference response. A ten-story shear structure was used to illustrate the effectiveness of the proposed substructure method. Xing et. al. [136] developed a substructual damage identification method by adopting the well-known ARMAX model to extract the modal information of each substructure in shear structures. The extent of damage was measured by using the squared original frequency and the squared damaged frequency. Many other studies have been performed on substructural damage identification for shear structures using different damage indices and different substructure identification [137–139]. Hou et. al. [140] proposed a substructure isolation approach for local health monitoring. Their proposed approach was based on the virtual distortion method (VDM) and used force distortions to model fixed supports in the boundary nodes to isolate the considered substructure from influences of the rest of the structure. The isolation method was based on applying virtual numerical fixed support on all the boundary DOFs of the target substructure. In another study, Hou et. al. [141] extended the substructure isolation method by proposing a free virtual support and investigated the method experimentally. Model updating based on natural frequencies was then used for damage identification of the isolated substructure. Hou et. al. [142] applied the substructure isolation method in the frequency domain and concluded that the frequency-domain method is computationally faster than the time-domain approach. Law et. al. [143] proposed a substructure damage detection method based on identification of interface and external forces acting on the target substructure and using time domain information. There has been also some studies on using substructural flexibility matrix or eigen solutions of the substructures to detect damage in the substructure [144–146]. In these studies, the global structure is divided into many manageable substructures and changes in eigen solution or flexibility matrix of the target substructure are used for damage identification.

Reviewing the literature reveals that there have been many studies published in development of substructural damage identification methods specifically for shear structures such as multi-story buildings and multi-story frames. These methods are restricted to shear structures and mostly use time response of different stories in the damage detection procedure. In the other published papers in substructure-based damage identification, either interface forces between the substructures are needed to be obtained or a numerical virtual support is needed to be placed in the target substructure boundary to isolate the target substructure from the rest of the structure. In this paper, an inverse substructuring method in dual form [13,14,147] is used to decouple the target substructure from the assembled structure using FRFs of the assembled structure and FRFs of the residual subsystem. The proposed method can be used for any civil or mechanical structure. In the proposed method, one subsystem is considered the “main” subsystem and is susceptible to damage and the “residual” subsystem(s) are considered unchanged and the damage identification is only applied to the main subsystem. The residual substructure(s) are considered unchanged which could be due to the fact that the residual substructure(s) are either not operating or their material or loading is such that they are not susceptible to dynamical change. The FRF matrix of the “main” subsystem is obtained as a “standalone” component that is completely decoupled from the residual subsystem(s) without the need of interface virtual support or identifying interface forces. Then an FRF-based finite element model updating is used to detect, localize and quantify the damage in the main substructure. This FRF-based model updating differs from the usual model updating methods by using numerical sensitivities to solve the inverse problem instead of analytical sensitivities [123]. In analytical sensitivity-based methods, direct access to mass and/or stiffness matrices is required, and a sensitivity matrix should be obtained [148][149]. In this paper, magnitudes of experimental and numerical FRFs are directly used for model updating with no need for a sensitivity matrix. The FRF-based model updating is used since the substructure decoupling technique is based on FRF measurement and calculation. Also, FRF-based model updating reveals more information than model updating methods based on modal characteristic properties [150]. In addition, curve fitting on the measured data is needed for extracting the modal properties, causing errors in the estimation of modal parameters, whereas FRF data do not require curve fitting and hence will not be contaminated with numerical errors and loss of information [151]. The FRF matrix of the residual substructure and the FRF matrix of the damaged global system are experimentally obtained and the main substructure’s FRFs (damaged) are obtained in the decoupling process.

Then the FE model of the main substructure is only needed for model updating and the damage is detected by iteratively comparing the numerically obtained FRF with the decoupled experimental

FRF of the main substructure. The damage is simulated with a stiffness reduction in the main subsystem. The FE model of the main subsystem is divided to different sections. In each iteration, a stiffness reduction is tried in each section and the FRF is obtained. Finally, the damage location is the section for which stiffness reduction leads to the damaged FRF. The quantity of the damage is also detected using the value of the stiffness reduction. In order to reduce the computation time in the model updating of the damaged structure and as a verification for decoupling analysis of the structure under study, decoupling can be first performed on the undamaged structure (before assembly of the substructures) and the undamaged main substructure FRF can be obtained. The accuracy of decoupling in different frequency ranges can be verified by comparing the decoupled FRF of the main substructure and the directly measured one. The accuracy of decoupling in different frequency ranges in undamaged condition would likely be the same in the damaged condition as well. Therefore, we will disregard the frequency ranges for which decoupling has significant error, if those regions of the FRF are not near peaks. We must consider the frequency ranges in the neighborhood of the peaks since damage (stiffness reduction) would likely shift the peak(s) location.

Two numerical examples and an experimental example are presented in order to illustrate the procedure. Section 9.2 describes the substructure decoupling method and Section 9.3 describes the substructural damage identification procedure. Numerical and experimental examples are presented in Section 9.4 and 9.5, respectively.

9.2 Substructure Decoupling

The purpose of substructure decoupling is to find the dynamics of subsystem *A* as a “standalone” component that is completely decoupled from the rest of the structure (*AB* and *B*). Without limitation, only two subsystems are considered here to illustrate the procedure but the method works for any number of subsystems. The FRF matrix of the assembled structure *AB* and the residual substructure *B* are known and the FRF matrix of Substructure *A* is to be obtained.

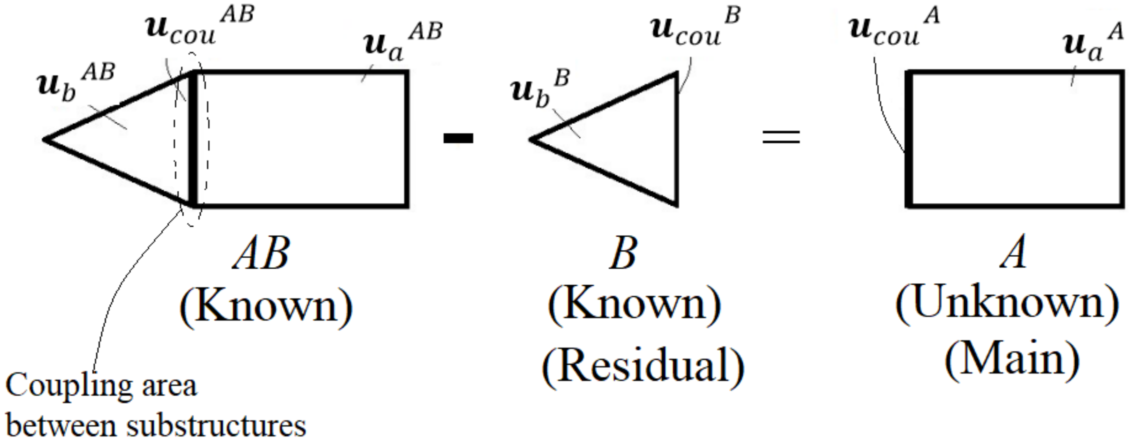

Figure 9.1: Substructure decoupling schematic

In Figure 9.1, system *AB* consists of degrees of freedom "internal to substructure *B*", $\boldsymbol{u}_b{}^{AB}$, "internal to substructure *A*", $\boldsymbol{u}_a{}^{AB}$ and the coupling DOF, $\boldsymbol{u}_{cou}{}^{AB}$. The subsystems *A* and *B* also have their internal DOFs, $\boldsymbol{u}_a{}^{A}$and $\boldsymbol{u}_b{}^{B}$, respectively and the coupling DOFs, $\boldsymbol{u}_{cou}{}^{A}$and $\boldsymbol{u}_{cou}{}^{B}$, respectively. Assuming the dynamics of system *AB* and *B* are known (measured), the following is a dynamic stiffness representation of the assembled system *AB* in compact form [13]:

$$\boldsymbol{Z}^{AB}\boldsymbol{u}^{AB} = \boldsymbol{f}^{AB} + \boldsymbol{g}^{AB}$$

$$\begin{bmatrix} \boldsymbol{Z}_{bb}^{AB} & \boldsymbol{Z}_{bcou}^{AB} & \boldsymbol{0} \\ \boldsymbol{Z}_{coub}^{AB} & \boldsymbol{Z}_{coucou}^{AB} & \boldsymbol{Z}_{coua}^{AB} \\ \boldsymbol{0} & \boldsymbol{Z}_{acou}^{AB} & \boldsymbol{Z}_{aa}^{AB} \end{bmatrix} \begin{bmatrix} \boldsymbol{u}_b \\ \boldsymbol{u}_{cou} \\ \boldsymbol{u}_a \end{bmatrix} = \begin{bmatrix} \boldsymbol{f}_b \\ \boldsymbol{f}_{cou} \\ \boldsymbol{f}_a \end{bmatrix} + \begin{bmatrix} \boldsymbol{0} \\ \boldsymbol{g}_{cou} \\ \boldsymbol{0} \end{bmatrix} \tag{9.1}$$

And subsystem *B*:

$$\boldsymbol{Z}^{B}\boldsymbol{u}^{B} = \boldsymbol{f}^{B} - \boldsymbol{g}^{B} \tag{9.2}$$

$$\begin{bmatrix} \boldsymbol{Z}_{bb}^{B} & \boldsymbol{Z}_{bcou}^{B} \\ \boldsymbol{Z}_{coub}^{B} & \boldsymbol{Z}_{coucou}^{B} \end{bmatrix} \begin{bmatrix} \boldsymbol{u}_b^{B} \\ \boldsymbol{u}_{cou}^{B} \end{bmatrix} = \begin{bmatrix} \boldsymbol{f}_b \\ \boldsymbol{f}_{cou} \end{bmatrix} - \begin{bmatrix} \boldsymbol{0} \\ \boldsymbol{g}_{cou}^{B} \end{bmatrix}$$

where $\boldsymbol{u}^{AB} = \begin{bmatrix} \boldsymbol{u}_b \\ \boldsymbol{u}_{cou} \\ \boldsymbol{u}_a \end{bmatrix}$ is the vector of DOF of system *AB* (Figure 9.1) (the superscripts *AB* are omitted for brevity), $\boldsymbol{u}^B = \begin{bmatrix} \boldsymbol{u}_b^B \\ \boldsymbol{u}_{cou}^B \end{bmatrix}$ is the vector of DOF of substructure *B*, $\boldsymbol{Z}^{AB}$ and $\boldsymbol{Z}^B$ are the stiffness matrices of system *AB* and *B*, respectively, vectors $\boldsymbol{f}^*$ are the external force vectors and vectors $\boldsymbol{g}^*$ represent the additional disconnection forces (with non-zero entries only at the interface DOF) felt from the decoupling of the neighboring components [13].

The displacement compatibility condition, Eq. (9.3) and force equilibrium condition, Eq. (9.4) between the two (sub)structures are as follow, respectively:

$$\boldsymbol{u}_{cou}^B = \boldsymbol{u}_{cou} \tag{9.3}$$

$$\boldsymbol{g}_{cou} + \boldsymbol{g}_{cou}^B = \boldsymbol{0} \tag{9.4}$$

A more systematic description of the problem can be written by introducing the Boolean matrices $\boldsymbol{B}$ and $\boldsymbol{L}$:

$$\boldsymbol{B}\boldsymbol{u} = [\boldsymbol{B}^{AB} \quad \boldsymbol{B}^B] \begin{bmatrix} \boldsymbol{u}^{AB} \\ \boldsymbol{u}^B \end{bmatrix} = \boldsymbol{u}_{cou}^B - \boldsymbol{u}_{cou} = \boldsymbol{0} \tag{9.5}$$

$$\boldsymbol{L}^{\boldsymbol{T}}\boldsymbol{g} = [\boldsymbol{L}^{AB^T} \quad \boldsymbol{L}^{B^T}] \begin{bmatrix} \boldsymbol{g}^{AB} \\ \boldsymbol{g}^B \end{bmatrix} = \begin{bmatrix} \boldsymbol{0} \\ \boldsymbol{0} \\ \boldsymbol{0} \\ \boldsymbol{g}_{cou} + \boldsymbol{g}_{cou}^B \end{bmatrix} = \boldsymbol{0} \tag{9.6}$$

Eq. (9.5) presents the compatibility equation and Eq. (9.6) presents the equilibrium equation and matrices $\boldsymbol{B}$ and $\boldsymbol{L}$ are:

$$\boldsymbol{B} = [\boldsymbol{B}^{AB} \quad \boldsymbol{B}^B] = [\boldsymbol{0} \quad \boldsymbol{I} \quad \boldsymbol{0} \ \| \ \boldsymbol{0} \quad -\boldsymbol{I}] \tag{9.7}$$

$$\boldsymbol{L}^{\boldsymbol{T}} = [\boldsymbol{L}^{AB^T} \quad \boldsymbol{L}^{B^T}] = \begin{bmatrix} \boldsymbol{I} & \boldsymbol{0} & \boldsymbol{0} & & \boldsymbol{0} & \boldsymbol{0} \\ \boldsymbol{0} & \boldsymbol{0} & \boldsymbol{I} & \| & \boldsymbol{0} & \boldsymbol{0} \\ \boldsymbol{0} & \boldsymbol{0} & \boldsymbol{0} & & \boldsymbol{I} & \boldsymbol{0} \\ \boldsymbol{0} & \boldsymbol{I} & \boldsymbol{0} & & \boldsymbol{0} & \boldsymbol{I} \end{bmatrix} \tag{9.8}$$

Therefore, the decoupling problem can be described in the following equations:

$$\begin{bmatrix} \boldsymbol{Z}^{AB} & \boldsymbol{0} \\ \boldsymbol{0} & \boldsymbol{Z}^{B} \end{bmatrix} \begin{bmatrix} \boldsymbol{u}^{AB} \\ \boldsymbol{u}^{B} \end{bmatrix} = \begin{bmatrix} \boldsymbol{f}^{AB} \\ \boldsymbol{f}^{B} \end{bmatrix} + \begin{bmatrix} \boldsymbol{g}^{AB} \\ -\boldsymbol{g}^{B} \end{bmatrix}$$

$$\begin{bmatrix} \boldsymbol{B}^{AB} & \boldsymbol{B}^{B} \end{bmatrix} \begin{bmatrix} \boldsymbol{u}^{AB} \\ \boldsymbol{u}^{B} \end{bmatrix} = \boldsymbol{0} \tag{9.9}$$

$$\begin{bmatrix} \boldsymbol{L}^{AB^T} & \boldsymbol{L}^{B^T} \end{bmatrix} \begin{bmatrix} \boldsymbol{g}^{AB} \\ \boldsymbol{g}^{B} \end{bmatrix} = \boldsymbol{0}$$

Employing the dual formulation for decoupling [60], the interface forces are satisfied a priori by choosing interface forces of the form of:

$$\boldsymbol{g} = -\boldsymbol{B}^{T}\boldsymbol{\lambda} \tag{9.10}$$

where $\boldsymbol{\lambda}$ are Lagrange multipliers, corresponding physically to the interface force intensities. The equilibrium condition in Eq. (7.6) thus becomes:

$$\boldsymbol{L}^{\boldsymbol{T}}\boldsymbol{g} = -\boldsymbol{L}^{\boldsymbol{T}}\boldsymbol{B}^{\boldsymbol{T}}\boldsymbol{\lambda} = \boldsymbol{0} \tag{9.11}$$

But this condition is always satisfied [14]. The decoupling problem can therefore be formulated in a dual way as:

$$\begin{bmatrix} \boldsymbol{Z}^{AB} & \boldsymbol{0} & \boldsymbol{B}^{AB^T} \\ \boldsymbol{0} & -\boldsymbol{Z}^{B} & \boldsymbol{B}^{B^T} \\ \boldsymbol{B}^{AB} & \boldsymbol{B}^{B} & \boldsymbol{0} \end{bmatrix} \begin{bmatrix} \boldsymbol{u}^{AB} \\ \boldsymbol{u}^{B} \\ \boldsymbol{\lambda} \end{bmatrix} = \begin{bmatrix} \boldsymbol{f}^{AB} \\ \boldsymbol{0} \\ \boldsymbol{0} \end{bmatrix} \tag{9.12}$$

In a more general form, different Boolean matrices for the compatibility and equilibrium conditions can be taken [13]:

$$\begin{bmatrix} \boldsymbol{Z}^{AB} & \boldsymbol{0} & \boldsymbol{E}^{AB^T} \\ \boldsymbol{0} & -\boldsymbol{Z}^{B} & \boldsymbol{E}^{B^T} \\ \boldsymbol{C}^{AB} & \boldsymbol{C}^{B} & \boldsymbol{0} \end{bmatrix} \begin{bmatrix} \boldsymbol{u}^{AB} \\ \boldsymbol{u}^{B} \\ \boldsymbol{\lambda} \end{bmatrix} = \begin{bmatrix} \boldsymbol{f}^{AB} \\ \boldsymbol{0} \\ \boldsymbol{0} \end{bmatrix} \tag{9.13}$$

where $\boldsymbol{E}^{*}$ are the Boolean matrices defining the location of the uncoupling forces while $\boldsymbol{C}^{*}$ are the matrices enforcing compatibility. In order to eliminate Lagrange multipliers $\boldsymbol{\lambda}$, Eq. (9.13) can be written:

$$\begin{bmatrix} \boldsymbol{Z} & \boldsymbol{E}^T \\ \boldsymbol{C} & \boldsymbol{0} \end{bmatrix} \begin{Bmatrix} \boldsymbol{u} \\ \boldsymbol{\lambda} \end{Bmatrix} = \begin{Bmatrix} \boldsymbol{f} \\ \boldsymbol{0} \end{Bmatrix} \tag{9.14}$$

where $\boldsymbol{Z} = \begin{bmatrix} \boldsymbol{Z}^{AB} & \boldsymbol{0} \\ \boldsymbol{0} & -\boldsymbol{Z}^{B} \end{bmatrix}$ $\boldsymbol{u} = \begin{bmatrix} \boldsymbol{u}^{AB} \\ \boldsymbol{u}^{B} \end{bmatrix}$, $\boldsymbol{f} = \begin{bmatrix} \boldsymbol{f}^{AB} \\ \boldsymbol{0} \end{bmatrix}$, $\boldsymbol{E}^T = \begin{bmatrix} \boldsymbol{E}^{AB^T} \\ \boldsymbol{E}^{B^T} \end{bmatrix}$ and $\boldsymbol{C} = [\boldsymbol{C}^{AB} \quad \boldsymbol{C}^{B}]$. Therefore, the system of equations is:

$$\begin{aligned} &\boldsymbol{Zu} + \boldsymbol{E}^T\boldsymbol{\lambda} = \boldsymbol{f} \\ &\boldsymbol{Cu} = \boldsymbol{0} \end{aligned} \tag{9.15}$$

From the first equation in Eqs.(9.15), it can be written:

$$\boldsymbol{u} = \boldsymbol{Z}^{-1}\boldsymbol{f} - \boldsymbol{Z}^{-1}\boldsymbol{E}^T\boldsymbol{\lambda} \tag{9.16}$$

By substituting Eq. (9.16) in the second equation in Eq. (9.15):

$$\boldsymbol{CZ}^{-1}\boldsymbol{f} - \boldsymbol{CZ}^{-1}\boldsymbol{E}^T\boldsymbol{\lambda} = \boldsymbol{0} \;\Rightarrow\; \boldsymbol{\lambda} = (\boldsymbol{CZ}^{-1}\boldsymbol{E}^T)^{+}\boldsymbol{CZ}^{-1}\boldsymbol{f} \tag{9.17}$$

where $^{+}$ denotes the (Moore–Penrose) pseudo-inverse since the matrix in the parenthesis is not necessarily an square matrix. By back-substitution of $\boldsymbol{\lambda}$ in the first equation in Eqs. (7.15) and considering $= \boldsymbol{Z}^{-1}$:

$$\boldsymbol{Zu} + \boldsymbol{E}^T[(\boldsymbol{CZ}^{-1}\boldsymbol{E}^T)^{+}\boldsymbol{CZ}^{-1}\boldsymbol{f}] = \boldsymbol{f} \;\Rightarrow\; \boldsymbol{u} = [\boldsymbol{H} - \boldsymbol{HE}^T(\boldsymbol{CHE}^T)^{+}\boldsymbol{CH}]\boldsymbol{f} \tag{9.18}$$

Eq. (9.18) can be expanded and written:

$$\begin{aligned} \begin{bmatrix} \boldsymbol{u}^{AB} \\ \boldsymbol{u}^{B} \end{bmatrix} = \Bigg(&\begin{bmatrix} \boldsymbol{H}^{AB} & \boldsymbol{0} \\ \boldsymbol{0} & -\boldsymbol{H}^{B} \end{bmatrix} - \\ &\begin{bmatrix} \boldsymbol{H}^{AB} & \boldsymbol{0} \\ \boldsymbol{0} & -\boldsymbol{H}^{B} \end{bmatrix} \begin{bmatrix} \boldsymbol{E}^{AB^T} \\ \boldsymbol{E}^{B^T} \end{bmatrix} \left([\boldsymbol{C}^{AB} \quad \boldsymbol{C}^{B}] \begin{bmatrix} \boldsymbol{H}^{AB} & \boldsymbol{0} \\ \boldsymbol{0} & -\boldsymbol{H}^{B} \end{bmatrix} \begin{bmatrix} \boldsymbol{E}^{AB^T} \\ \boldsymbol{E}^{B^T} \end{bmatrix} \right)^{+} [\boldsymbol{C}^{AB} \quad \boldsymbol{C}^{B}] \begin{bmatrix} \boldsymbol{H}^{AB} & \boldsymbol{0} \\ \boldsymbol{0} & -\boldsymbol{H}^{B} \end{bmatrix} \Bigg) \boldsymbol{f} \end{aligned} \tag{9.19}$$

Eq. (9.19) is the form of $\boldsymbol{u} = \boldsymbol{Hf}$. Therefore, the decoupled FRF matrix in a general form can be found:

$$\boldsymbol{H}^{A} = \begin{bmatrix} \boldsymbol{H}^{AB} & \boldsymbol{0} \\ \boldsymbol{0} & -\boldsymbol{H}^{B} \end{bmatrix} - \begin{bmatrix} \boldsymbol{H}^{AB} & \boldsymbol{0} \\ \boldsymbol{0} & -\boldsymbol{H}^{B} \end{bmatrix} \begin{bmatrix} \boldsymbol{E}^{AB^{T}} \\ \boldsymbol{E}^{B^{T}} \end{bmatrix} \left(\begin{bmatrix} \boldsymbol{C}^{AB} & \boldsymbol{C}^{B} \end{bmatrix} \begin{bmatrix} \boldsymbol{H}^{AB} & \boldsymbol{0} \\ \boldsymbol{0} & -\boldsymbol{H}^{B} \end{bmatrix} \begin{bmatrix} \boldsymbol{E}^{AB^{\boldsymbol{T}}} \\ \boldsymbol{E}^{B^{\boldsymbol{T}}} \end{bmatrix} \right)^{+} \begin{bmatrix} \boldsymbol{C}^{AB} & \boldsymbol{C}^{\boldsymbol{B}} \end{bmatrix} \begin{bmatrix} \boldsymbol{H}^{AB} & \boldsymbol{0} \\ \boldsymbol{0} & -\boldsymbol{H}^{B} \end{bmatrix} \tag{9.20}$$

Matrix $\boldsymbol{H}^{A}$ in Eq. (9.20) is called the decoupled FRF matrix of substructure A but also contains extra rows and columns corresponding to subsystem *B*. Also, those rows and the columns of $\boldsymbol{H}^{A}$ corresponding to compatibility and equilibrium DoFs appear twice, both in the rows and columns in $-\boldsymbol{H}^{B}$ and $\boldsymbol{H}^{AB}$ [121]. Therefore, only the rows and columns corresponding to the subsystem *A* are extracted from matrix $\boldsymbol{H}^{A}$ and are considered decoupled FRFs of subsystem *A*. Based on choosing different DoFs for compatibility ($\boldsymbol{C}$) and equilibrium ($\boldsymbol{E}$), various collocated and non-collocated decoupling approaches can be used.

9.3 Substructural Damage Identification Procedure

In the proposed damage identification procedure, the FRF measurement is performed on the global damaged structure and on the residual substructure (before assembly) and the damaged main substructure's FRFs are obtained using Eq. (9.20). Then the decoupled FRF (of the damaged main substructure) is used for FRF-based model updating and damage detection. Figure 9.2 depicts the schematic diagram of the damage identification procedure.

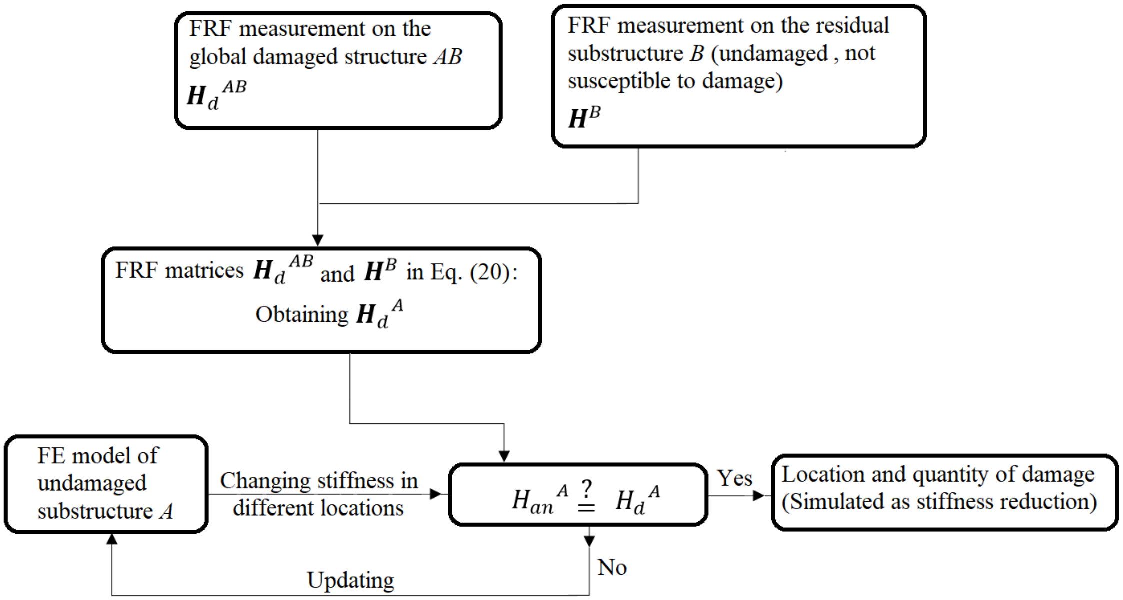

Figure 9.2: Substructural damage identification procedure diagram

where $\boldsymbol{H}_d{}^{A}$ is the FRF matrix of the damaged substructure A obtained from decoupling, $H_{an}{}^{A}$ is analytical FRF obtained from the FE model of substructure A and $H_d{}^{A}$ is one (or a few) FRF in the FRF matrix $\boldsymbol{H}_d{}^{A}$to be used for model updating. The damage is simulated with the decrease in the stiffness at some locations in the main substructure. In each iteration of model updating, the stiffness in different locations in the substructure A FE model is changed and the FRF obtained from the FE model is compared to the decoupled experimental FRF $H_d{}^{A}$ in the frequency range of interest. This process continues until the analytical and decoupled FRF are matched with the desired accuracy. The FRF-based model updating procedure is presented in the following section.

9.3.1 FRF-based Model Updating

The accelerance FRF $H_{a,b}(\omega)$ is the acceleration response at node a, $A_a(\omega)$, divided by the force at node b, $F_b(\omega)$, both in the frequency domain:

$$H_{a,b}(\omega) = \frac{A_a(\omega)}{F_b(\omega)} \cong \sum_{i=1}^{m} \frac{-\omega^2 \widehat{\Phi}_{ai} \widehat{\Phi}_{bi}}{-\omega^2 + 2i\omega\Omega_i\xi_i + \Omega^2{}_i} \tag{9.21}$$

where m is the number of modes used for constructing the FRF, ω is frequency, Ω_i is i^{th} natural frequency of the system, ξ_i is i^{th} damping ratio corresponding to i^{th} mode and $\hat{\phi}_{ai}$ and $\hat{\phi}_{bi}$ are the scalar values of mode shape i at response node a and excitation node b, respectively. The form of FRF used for model updating is as follows, with the values of the FRF magnitude in dB:

$$\bar{H}_{a,b}(\omega) = 20\log_{10}\left(\left|H_{a,b}(\omega)\right|\right) \tag{9.22}$$

The goal of the FE model updating is to change the properties of a FEM such that the analytical response of the model matches that of measured data. After developing the FE model, Eq. (9.21) and Eq. (9.22) are used to obtain the FRF at the response and excitation nodes corresponding to the response and excitation locations considered in the experiment (decoupled FRF). Then the difference between analytical and measured FRFs, the error or residual, is found and a scalar objective error function value is calculated [123]. With the scalar objective error function value, numerical optimization techniques are used to minimize the difference between the analytical and measured FRFs by modifying the parameters of the FEM [123]. Substituting Eq. (9.21) and Eq. (9.22) and using modal responses as functions of the unknown updating parameters p results in Eq. (9.23) [123]:

$$\bar{H}_{a,b}(\omega, p) = 20\log_{10}\left(\left|\sum_{i=1}^{m}\frac{-\omega^2\hat{\phi}_{ai}(p)\hat{\phi}_{bi}(p)}{-\omega^2+2i\omega\Omega_i(p)\xi_i(p)+\Omega^2{}_i(p)}\right|\right) \tag{9.23}$$

The error function, or residual e, is defined as:

$$e(\omega, p) = \bar{H}^a{}_{a,b}(\omega, p) - \bar{H}^m{}_{a,b}(\omega, p) \tag{9.24}$$

where $\bar{H}^a{}_{a,b}(\omega, p)$ and $\bar{H}^m{}_{a,b}(\omega, p)$ are analytical and measured FRFs (decoupled), respectively. Then, a scalar objective error function J is created and minimized through bounded numerical optimization:

$$J(p) = e^T(\omega, p)e(\omega, p) \tag{9.25}$$

The purpose of optimization is to minimize $J(\omega, p)$ by considering the upper and lower bounds for p [123]. The scalar objective error function is normalized by the initial value of the scalar objective error function $J(p)_1$ so that the optimization starts at a value of 1 and the perfect match would be a value of 0.

$$J(p)_i = \frac{J(p)_i}{J(p)_1} \tag{9.26}$$

The parameter p is a unitless modifier that modifies stiffness parameter.

9.4 Numerical Examples

In this section, two numerical examples are presented to illustrate the substructural damage identification procedure. The first example is a simple lumped parameter system and the second example is a simplified model of a utility pole-conductor system.

9.4.1 Numerical Case Study 1

The simple problem used here is shown in Figure 9.3 and consists of two lightly damped mass-spring-damper systems. Subsystem A has 5 degrees of freedom and is the main subsystem under damage, subsystem B possesses 3 DoF and it is not susceptible to damage. The two subsystems are coupled at a 2 DoF interface (m_{A4}, m_{B1} and m_{A5}, m_{B2}). The system properties are given in Table 9.1. Two damage scenarios are considered. The first scenario D1 is a single-damage scenario and the damage in subsystem *A* is simulated by 20% reduction in the value of stiffness parameter k_{A2} and the second scenario D2 is a multi-damage case and the damage is simulated by 10 % stiffness reduction in k_{A3} and 5 % reduction in k_{A5}. The first step in the procedure is obtaining the decoupled FRFs of subsystem *A* from the assembled structure.

Table 9.1. Lumped parameter system parameters

Subsystem A	Subsystem B
$\mathrm{m}_{A1} = 4\,,\mathrm{m}_{A2} = 3, \mathrm{m}_{A3} = 3, \mathrm{m}_{A4} = 6, \mathrm{m}_{A5} = 2\ kg$ $\mathrm{k}_{A1} = 500\,,\mathrm{k}_{A2} = 2000\,,\mathrm{k}_{A3} = 2000\,,\mathrm{k}_{A4} = 1000\,,\mathrm{k}_{A5} = 500\ \frac{N}{m}$ $\mathrm{c}_{A1} = 0.2, \mathrm{c}_{A2} = 0.5, \mathrm{c}_{A3} = 0.1, \mathrm{c}_{A4} = 0.1, \mathrm{c}_{A5} = 0.1\ \ \frac{N}{ms^2}$	$\mathrm{m}_{B1} = 2\,,\mathrm{m}_{B2} = 4, \mathrm{m}_{B3} = 8\ \ kg$ $\mathrm{k}_{B1} = 1000\,,\mathrm{k}_{B2} = 1000\,,\mathrm{k}_{B3} = 2000\ \ \frac{N}{m}$ $\mathrm{c}_{B1} = 0.4, \mathrm{c}_{B2} = 0.1, \mathrm{c}_{B3} = 0.3\ \ \frac{Ns}{m}$

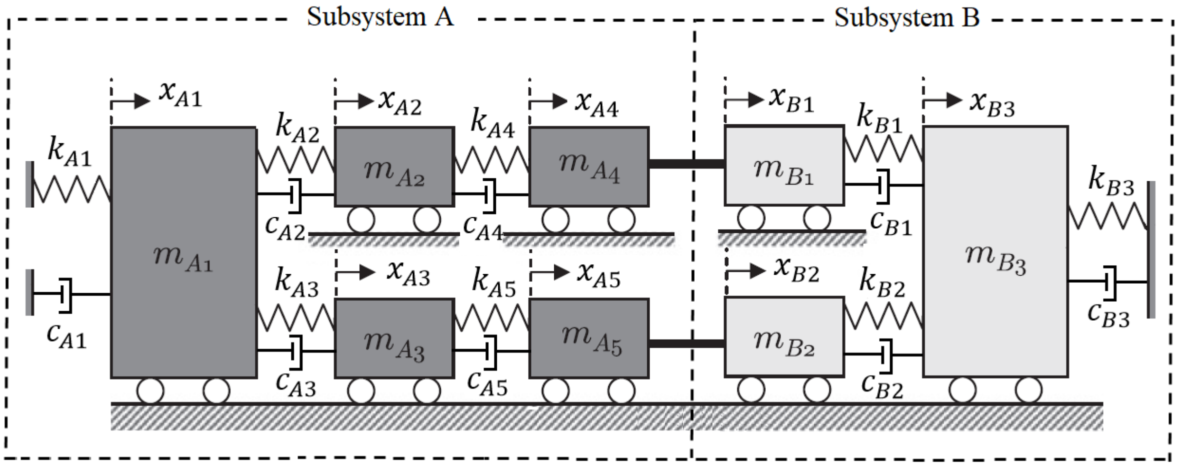

Figure 9.3: Lumped parameter system: Case study 1

Figure 9.4 shows the FRF $H_{34}{}^{\mathrm{A}}$, one of the FRFs in subsystem A, and the similar FRF obtained from decoupling in the undamaged and D1 damaged conditions. As can be seen, the FRFs completely match in both the conditions. This result is a motivation to use the decoupling method to obtain the main subsystem FRF when the global system is under operation and it is impossible to separate the subsystems. After obtaining the main subsystem FRF, the FRF-based model updating is used only on the main subsystem to detect the damage.

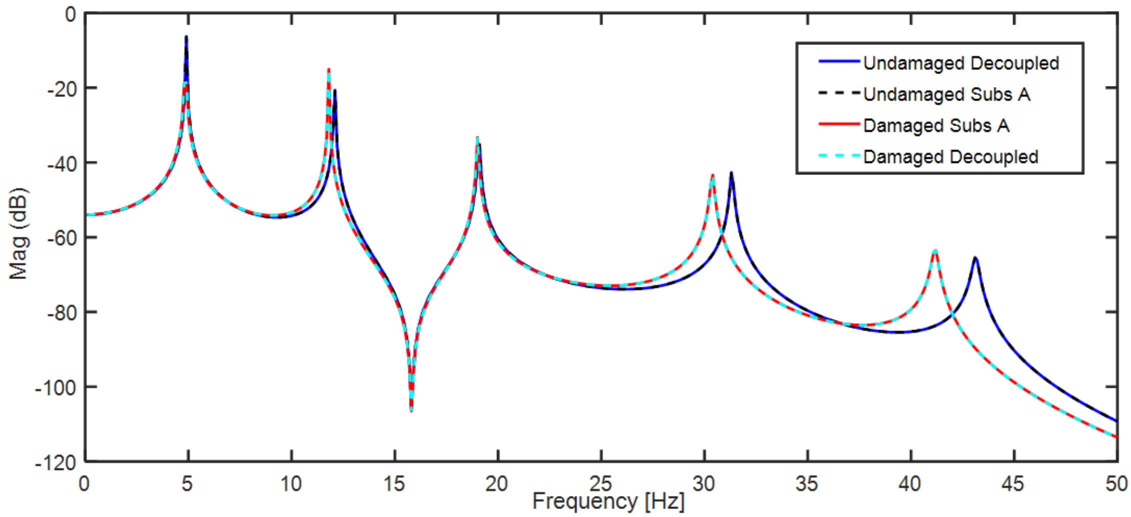

Figure 9.4: Subsystem A FRF ${H_{34}}^{A}$ and the decoupled FRF obtained from decoupling in damaged D1 and undamaged conditions

The decoupled FRF in the damaged condition in Figure 9.4 is used in the FE model updating using the subsystem A model to detect the location and quantity of stiffness reduction. Figure 9.5 shows the undamaged and damaged FRF (obtained from decoupling) and the updated FRF after model updating. The initial guess in the updating process is the undamaged FRF and the final result is the updated FRF. The optimization variables are the five stiffness parameter modifiers between 0 and 1 that is multiplied to each stiffness parameter $k_{A1}, k_{A2}, k_{A3}, k_{A4}, k_{A5}$. In each iteration, these five parameters are changed and the obtained FRF is compared to the damaged one until the two FRFs match with the desired accuracy. Figure 9.6 shows the stiffness parameter multiplier values after the updating process. The second stiffness parameter k_{A2} has 20 % reduction and it is detected in the updating process. Stiffness parameters 1-5 are corresponding to $k_{A1}, k_{A2}, k_{A3}, k_{A4}, k_{A5}$, respectively.

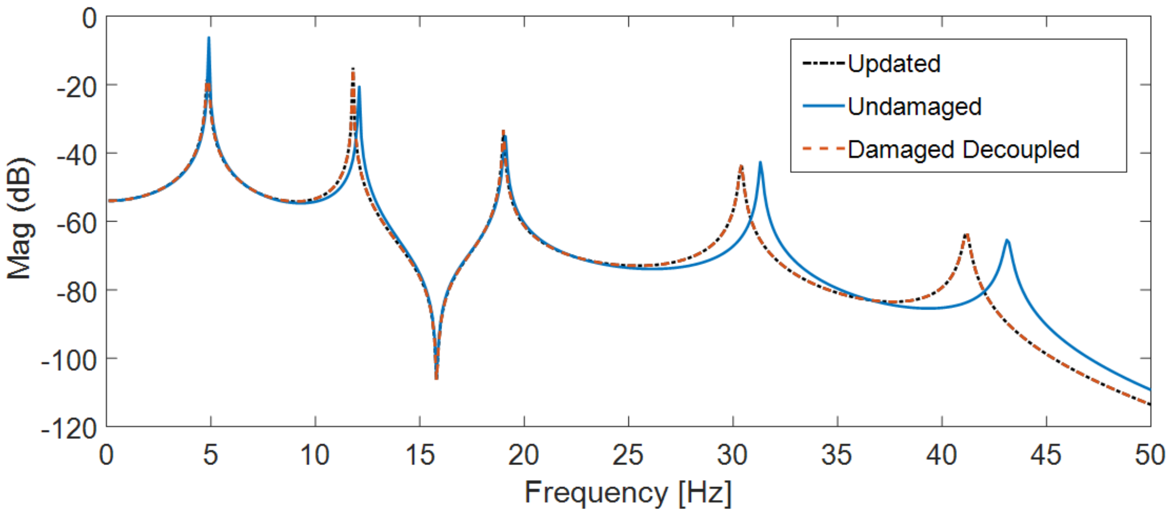

Figure 9.5: Subsystem A FRF ${H_{34}}^{A}$ in model updating—D1 scenario

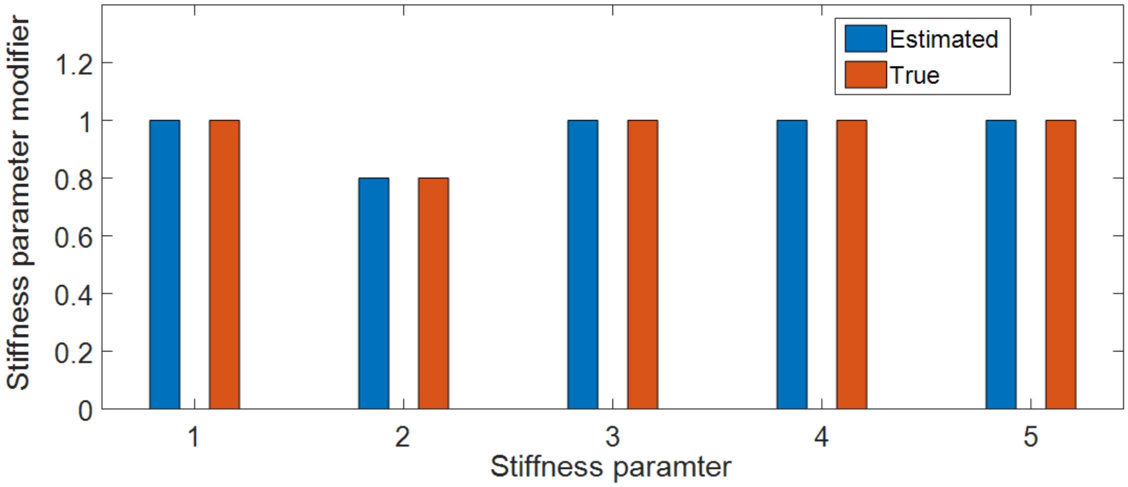

Figure 9.6: Stiffness parameter modifiers in subsystem A -- D1 scenario

Figure 9.7-a shows the FRF ${H_{34}}^{A}$ in D2 scenario and the similar decoupled FRF. The decoupled FRF matches the true one in the multi-damage case as well. Figure 9.7-b shows the updated FRF after updating process similar to D1 case. The stiffness parameter modifiers in D2 scenario are shown in Figure 9.8. The location and quantity of stiffness reduction is detected accurately.

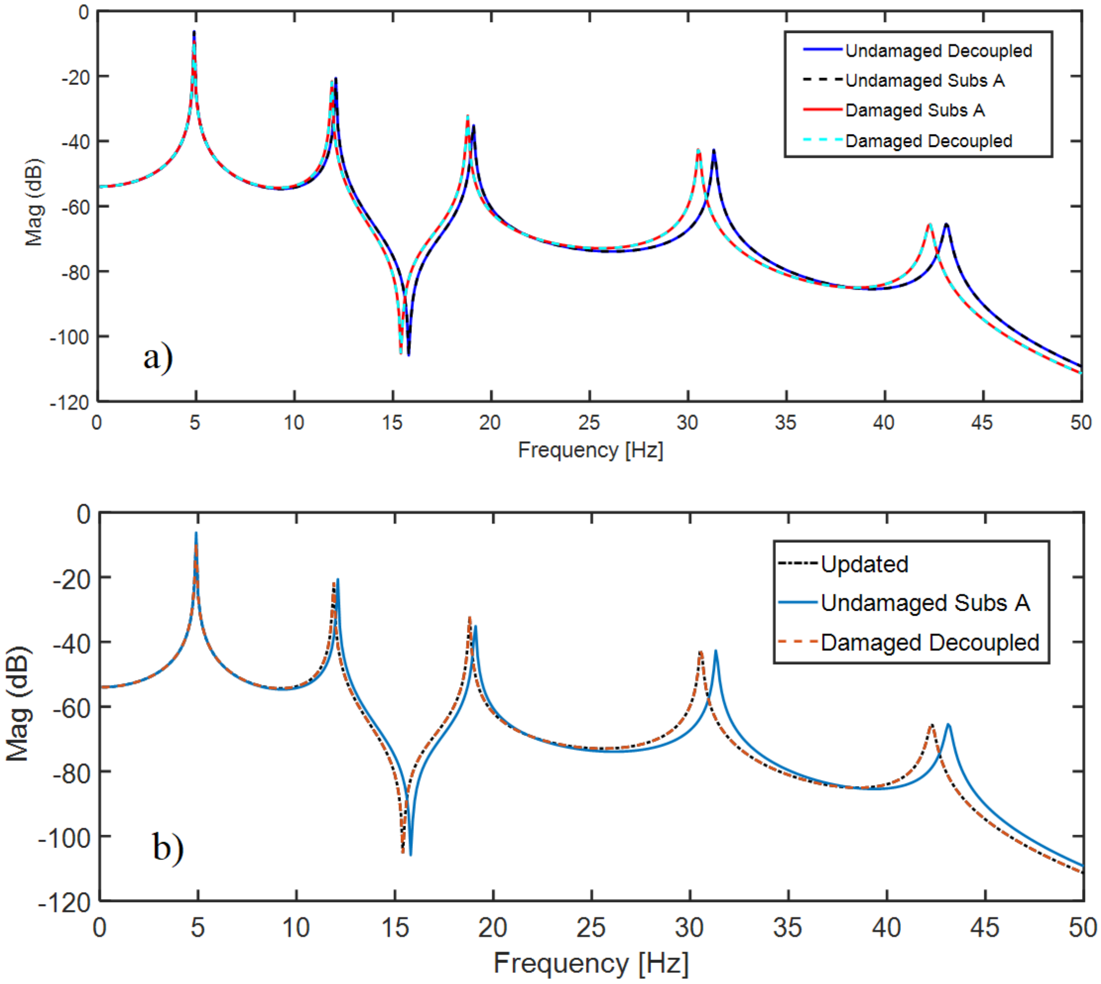

Figure 9.7: Subsystem A FRF $H_{34}{}^{A}$ and the decoupled FRF obtained from decoupling in damaged D2 and undamaged conditions

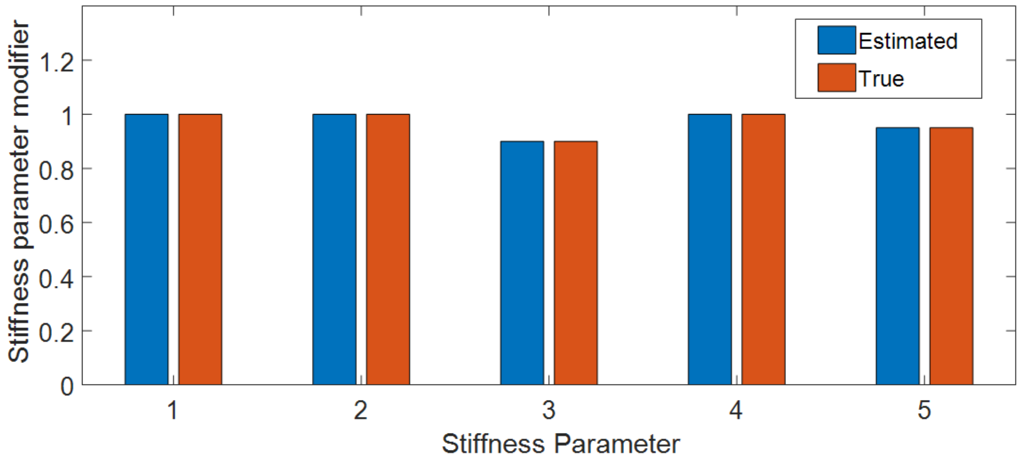

Figure 9.8: Stiffness parameter modifiers in subsystem A – D2 scenario

9.4.2 Numerical Case study 2

The global system in this numerical example is shown in Figure 9.9 and it consists of 34 nodes and 33 three-dimensional beam elements. The main subsystem (A) and the residual subsystem (B) are shown. The material for the main subsystem has Young's modulus of $E = 90\ GPa$ and the density of 500 kg/m^3 and the residual subsystem has Young's modulus of $E = 220\ GPa$ and density of 3000 kg/m^3. Three points P1, P2 and P3 are used for obtaining the FRFs of the assembled system (in X direction) and the residual subsystem and the FRFs of the main subsystem are obtained through the decoupling process. Damage detection is performed for the five sections shown in the figure. Each section is 1 m length in the model. Two damage scenarios D1 and D2 are considered. In the first scenario D1, the damage is simulated by 20 % reduction in the Young's modulus value in section 3 and scenario D2 is a multi-damage scenario and is simulated by 20 % reduction in Young's modulus of section 2, 20 % reduction in section 4 and 10 % reduction in section 5. The FE model is developed using Abaqus software and FE updating is performed with the use of Abaqus2Matlab software [125] and MATLAB's *fmincon* nonlinear constrained optimization routine. The optimization variables are five stiffness parameter modifiers between 0 and 1 that are multiplied to the young modulus of sections 1-5 in the pole model.

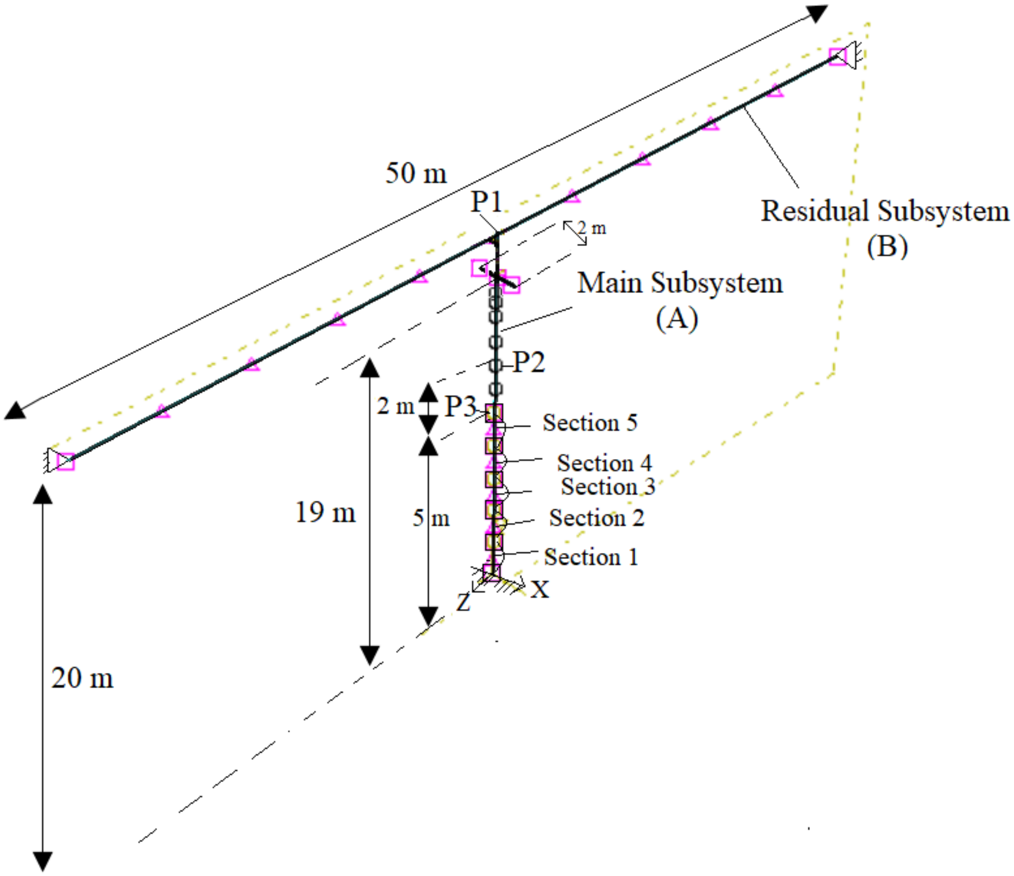

Figure 9.9: Numerical case study 2 FE model

FRFs corresponding to points P1, P2 and P3 in the assembled structure are obtained by applying a unit 1N load at each of the points and obtaining the acceleration at the other points in the frequency domain. Then the FRF matrix $\boldsymbol{H}^{AB}$ is obtained by inserting all the FRFs in a matrix. The symmetric arrays are obtained only once since they are equal. The FRF matrix of the residual subsystem contains only one FRF ${H_{11}}^{B}$ since only one point P1 is needed in the decoupling process. The FRF matrices are then inserted in Eq. (9.20) to obtain the decoupled FRFs of the main (pole) subsystem. Figure 9.10-a shows the FRF corresponding to point P3 in subsystem A, ${\mathrm{H}_{33}}^{A}$, in the undamaged and damaged D1 condition and the similar FRF obtained from decoupling (Eq.(9.20)). The FRF obtained from the pole-only model (Damaged Main Subs) and the one obtained from decoupling (Damaged Main Subs – Decoupled) match very well. There is a slight difference around the first mode which could be due to numerical singularity in the decoupling. Figure 9.10-b shows the damaged and the updated FRF of the main subsystem obtained from model updating. Figure 9.11 shows the stiffness parameter modifiers of sections 1-5 obtained after model updating in D1 scenario. The location of the damage (stiffness reduction) is detected very well but the quantity of it (20 %) has an slight error.

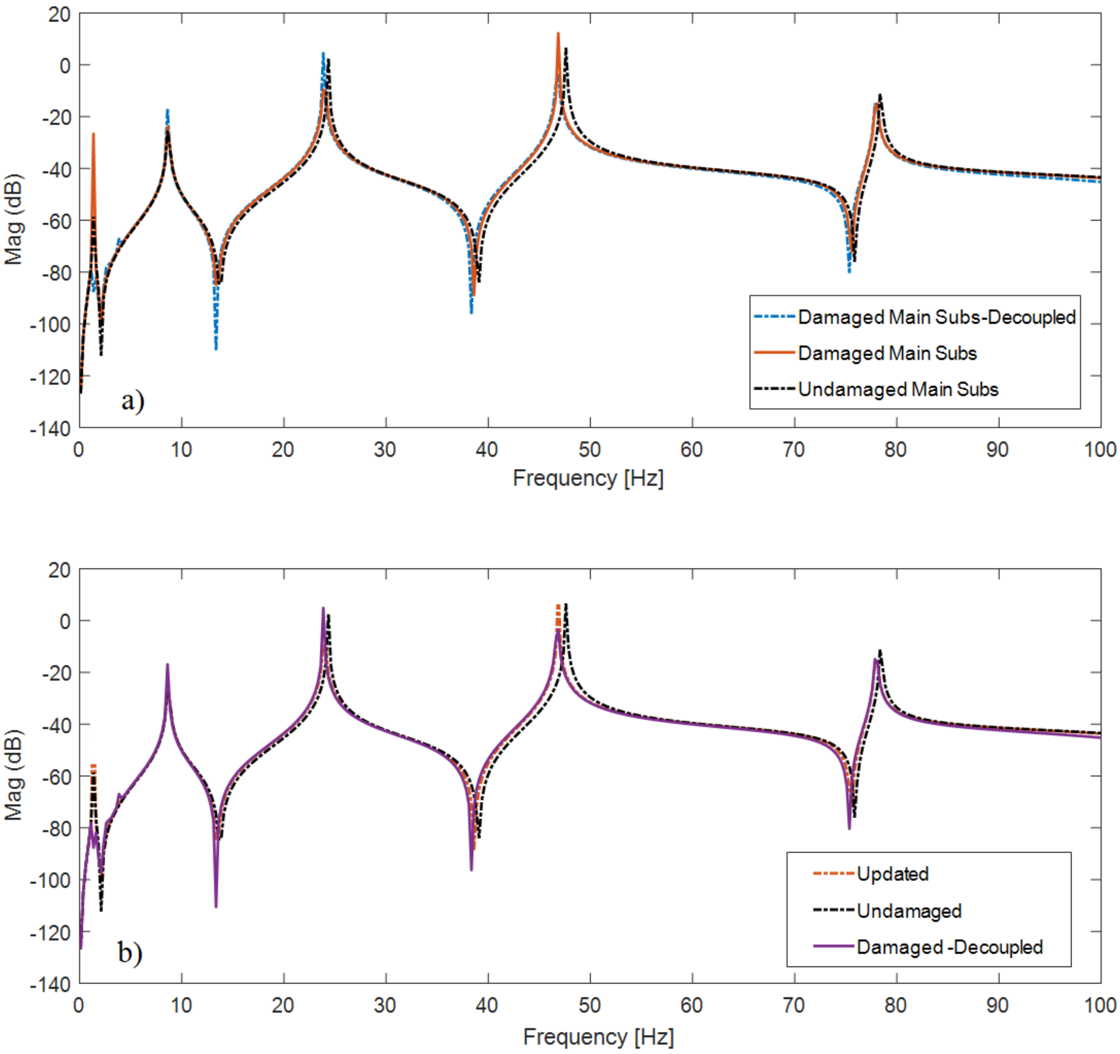

Figure 9.10: a) FRF $H_{33}{}^{A}$ of the main subsystem and the decoupled FRF $H_{33}{}^{A}$ in damaged D1 and undamaged conditions b) Damaged, undamaged and updated FRF in D1 scenario

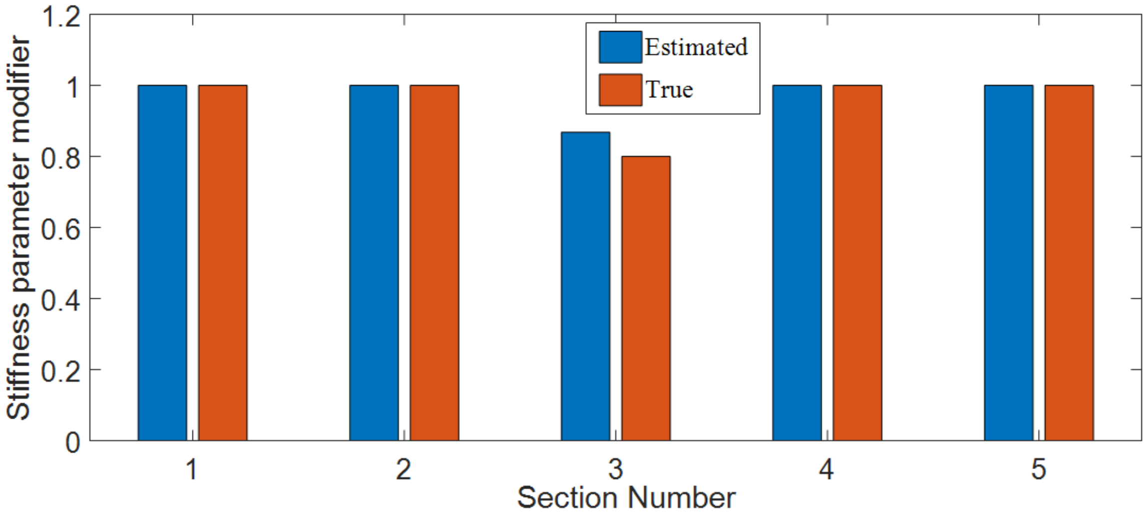

Figure 9.11: Stiffness parameter modifiers in D1 scenario

Figure 9.12 and Figure 9.13 show the same result as Figure 9.10 and Figure 9.11, respectively for the scenario D2. The locations of the damage is detected again but the quantity has a small error (Figure 9.13).

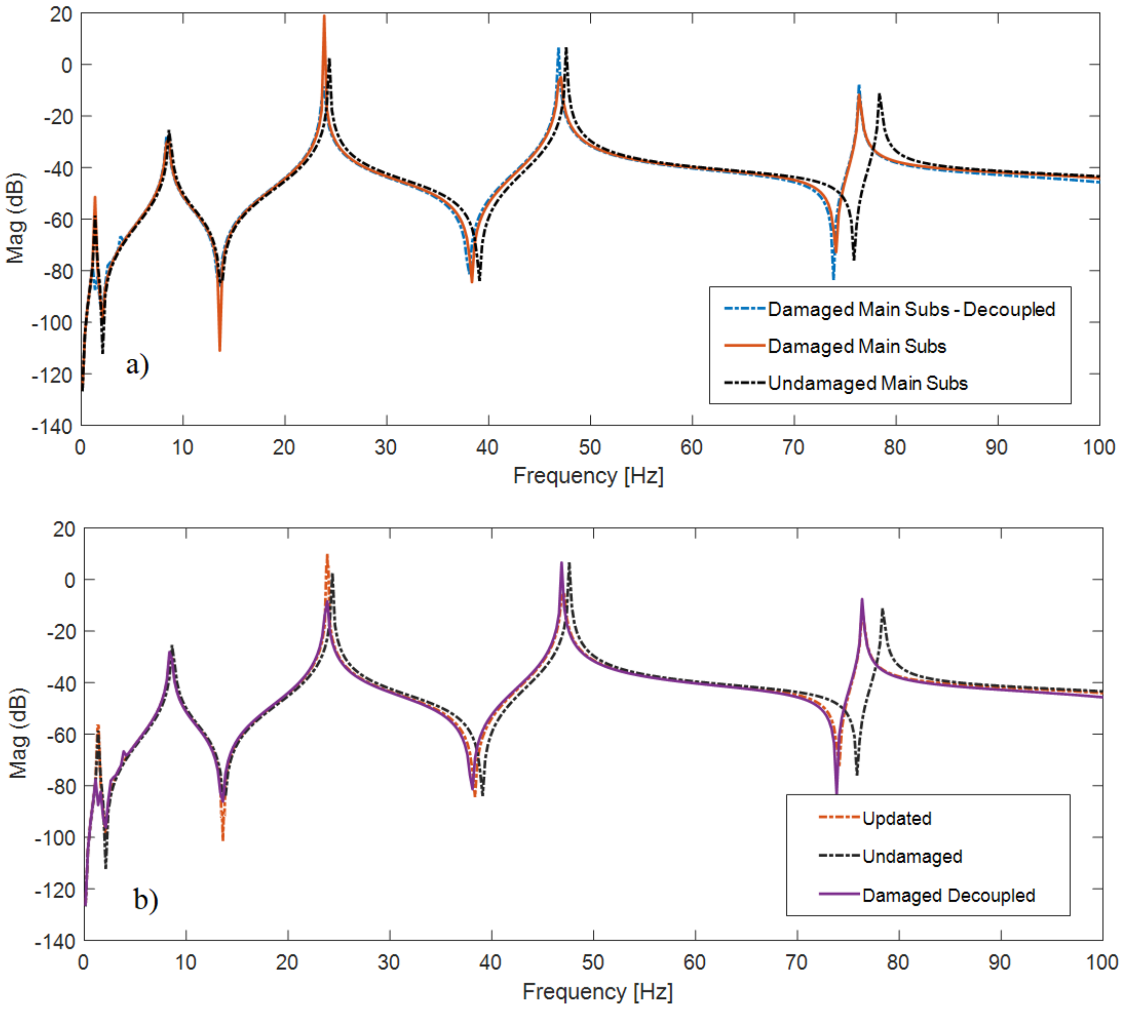

Figure 9.12: a) FRF ${H_{33}}^{A}$ of the main subsystem and the decoupled FRF ${H_{33}}^{A}$ in damaged D2 and undamaged conditions b) Damaged, undamaged and updated FRF in D2 scenario

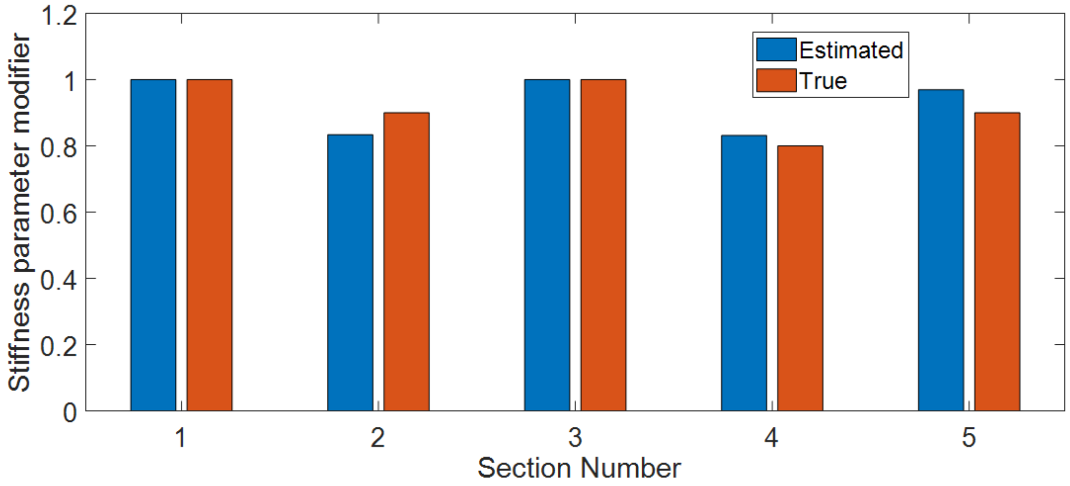

Figure 9.13: Stiffness parameter modifiers in D2 scenario

9.5 Experimental Case Study

The experimental example is a simple structure consisting of two subsystems that are bolted together. The structure is shown in Figure 9.14 with the dimensions shown. Two aluminum beams are bolted together at point P1 (Coupling point) and the main (A) and residual (B) substructures are shown in Figure 9.14. The cross section of the beams are $20 \times 2\ \text{mm}^2$ with a Young's modulus of $E = 70\ GPa$ and density of 2700 $\frac{kg}{m^3}$. The structure was first tested in the undamaged state. Afterwards, one cut with the dimensions displaced in Figure 9.14-b was introduced in the main substructure. The width of the cut is 4 mm on each side with 8 cm length, therefore the width of the beam in the cut section is 12 mm, simulating damage as 40% stiffness reduction in that section. Five sections, sections 1-5 as shown in Figure 9.14-b, are used in the model updating of the main subsystem and the location of the damage (section 1) is identified in the damage detection. Each section is 8 cm length, the same length as the cut. Before model updating, experimental vibration measurement was performed on the global structure and the residual subsystem. The FRFs of the global structure in both the undamaged and damaged states were obtained at points P1 and P2 and the FRF of the residual substructure was obtained at P1. The residual subsystem was the same before and after introducing the damage since we consider this subsystem not susceptible to damage. Figure 9.15 shows the damaged assembled structure, the cut in the main subsystem, the residual subsystem modal test setup and mounting the sensor on the coupling point. The residual subsystem was tested in free-free condition and two thin elastic bands were used to simulate the free-free boundary condition. Two B&K 4507-B-004 accelerometers were used at the two locations P1 and P2 to obtain the FRFs of the assembled structure and one accelerometer is used at point P1 to measure the FRF of the residual subsystem. FRFs were obtained using a B&K 8205-002 impact hammer, a National Instruments c-DAQ 9172 chassis and the software ModalView [95] was used to analyze the data. In each measurement, the structure was impacted five times to average the signals. A 2×2 matrix $\boldsymbol{H}^{AB}$ and a 1×1 matrix $\boldsymbol{H}^{B}$ were measured and the measured FRFs are used in Eq. (9.20) to predict the FRF of the main subsystem, decoupled from the rest of the structure.

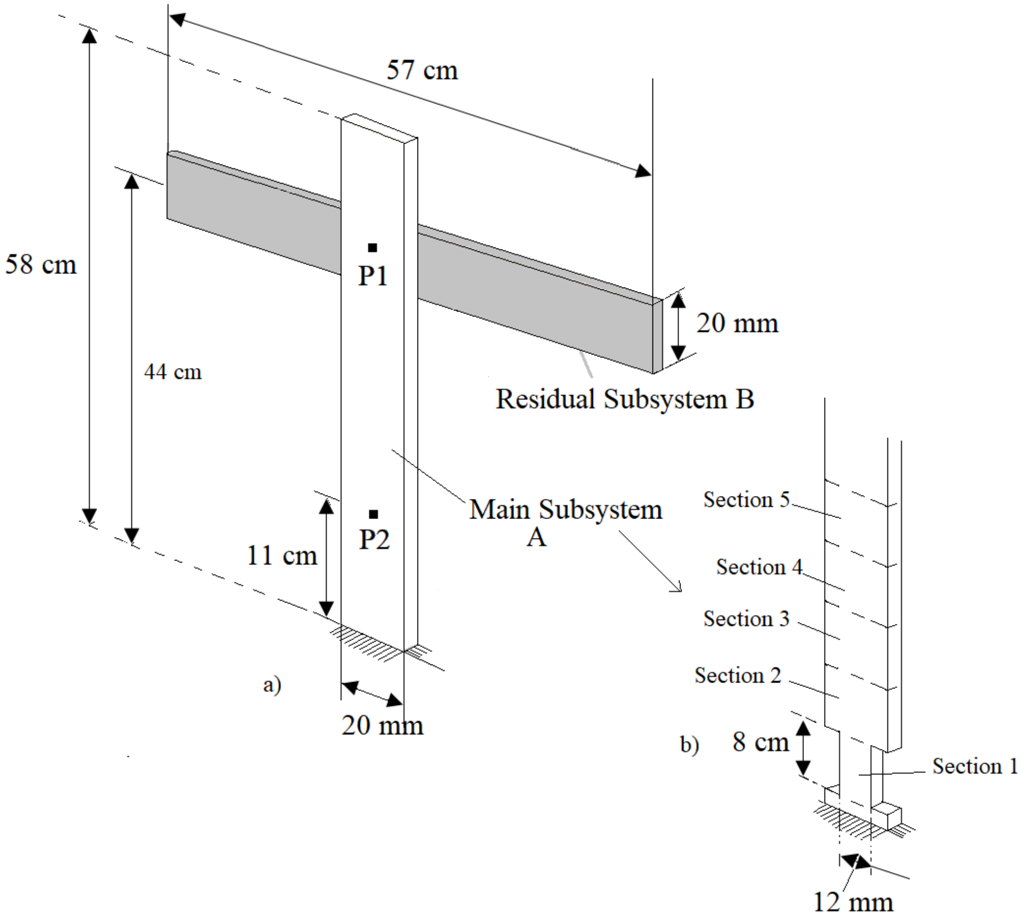

Figure 9.14: a) Schematic of the experimental case study b) The cut in the main subsystem to introduce damage

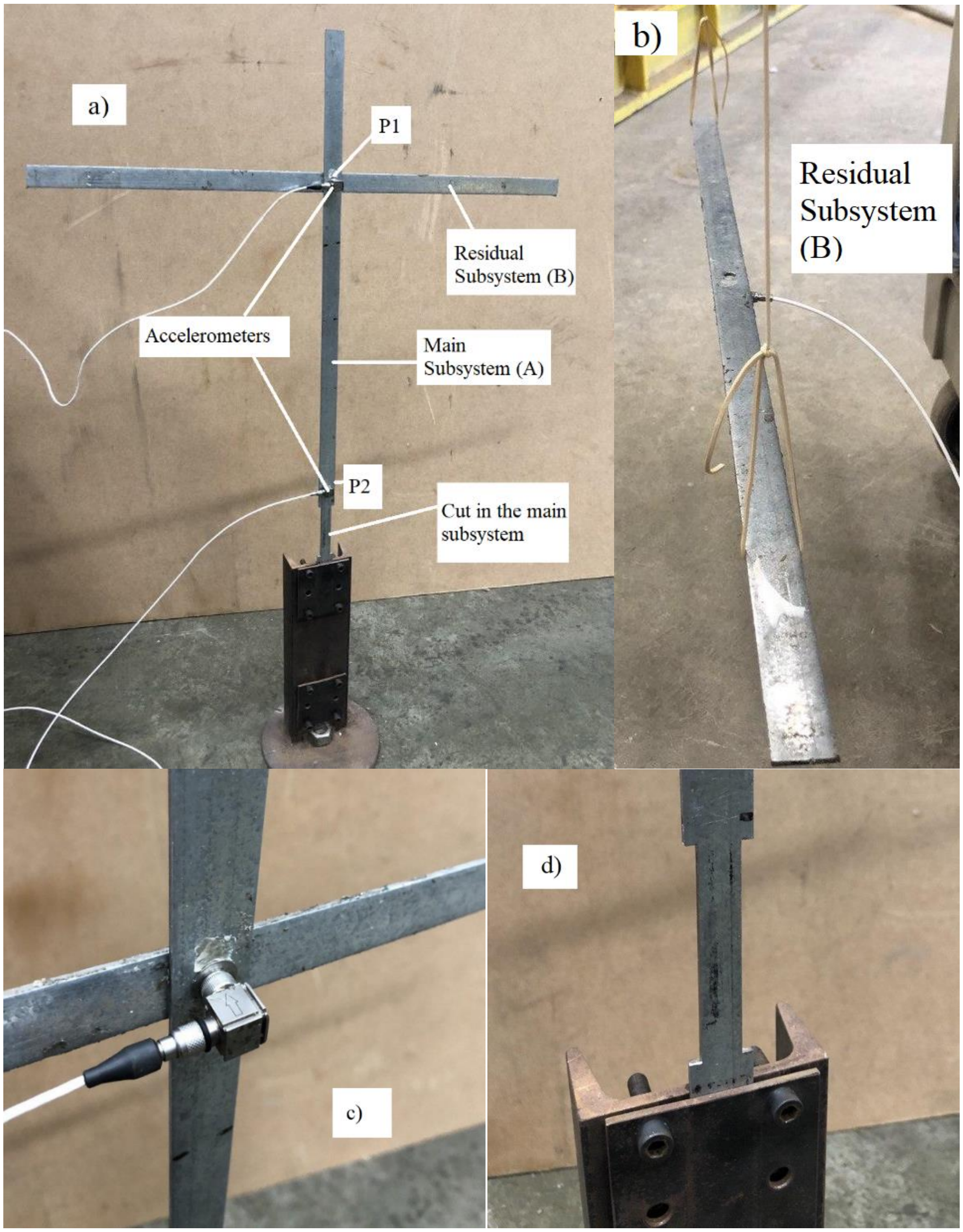

Figure 9.15: Experimental case study a) Damaged global structure b) The residual subsystem (Free-free boundary conditions) c) Coupling point accelerometer d) The cut in the main substructure

Figure 9.16 shows the FRF ${H_{11}}^A$ obtained from subsystem A and obtained from decoupling in the undamaged state. The FRFs match well in most of the frequency ranges and the error could be due to measurement error and the error in simulating the free-free condition of the residual subsystem. A frequency range of 30-60 Hz is used for model updating of the damaged state since there is a good match between FRFs in the undamaged state.

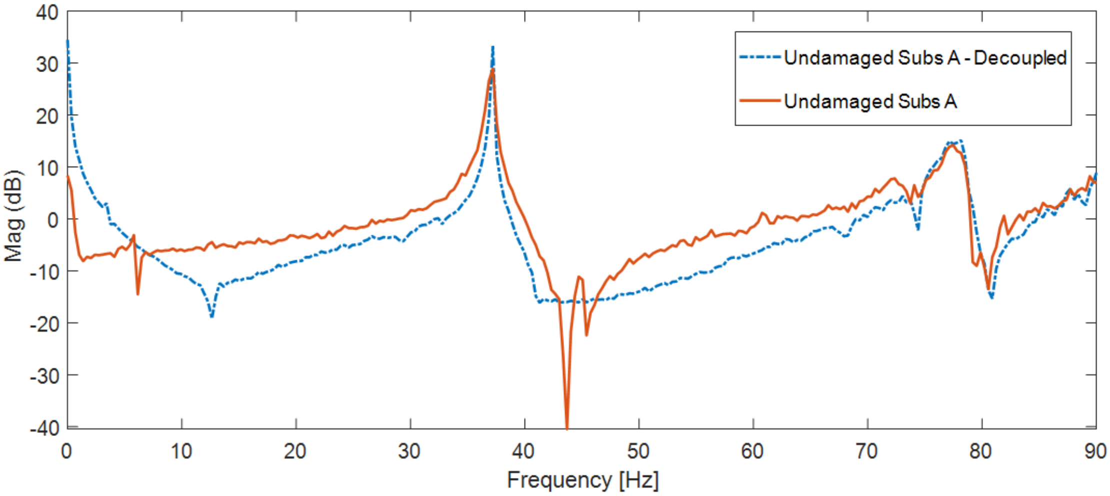

Figure 9.16: FRF of the main subsystem and the FRF obtained from decoupling in undamaged state

The FE model of the subsystem A (a cantilever beam) is developed using Abaqus software and FE updating is performed with the use of Abaqus2Matlab software [125] and MATLAB's *fmincon* nonlinear constrained optimization routine. Five sections 1-5 are defined (Figure 9.14) in the FE model and five modifiers between 0-1 are used to multiply to the cross-section width of the sections in each iteration. The initial FRF obtained from the model was significantly different from the experimental FRF. The thickness of the beam was changed to 3.5 mm in the FE model (instead of 2 mm) and the FRF result improved significantly. This thickness change in the model does not affect the damage detection results since we need the stiffness reduction percentage (percentage of width reduction) and more importantly where the stiffness reduction exists in the structure. Figure 9.17 shows the FRF ${H_{12}}^A$, obtained from the FE model before and after updating, the experimentally obtained FRF in the undamaged state and the FRF obtained from decoupling of the damaged main subsystem. The "initial" FRF in this figure is the FRF obtained after modification of the model (the thickness change to 3.5 mm). The damaged FRF shows a shift to the left which is a sign of stiffness reduction compared to the undamaged FRF and the updated FRF match with the damaged FRF. The stiffness modifiers are shown in Figure 9.18. The location of the damage is detected (section 1) and there is a slight error in detecting the damage quantity.

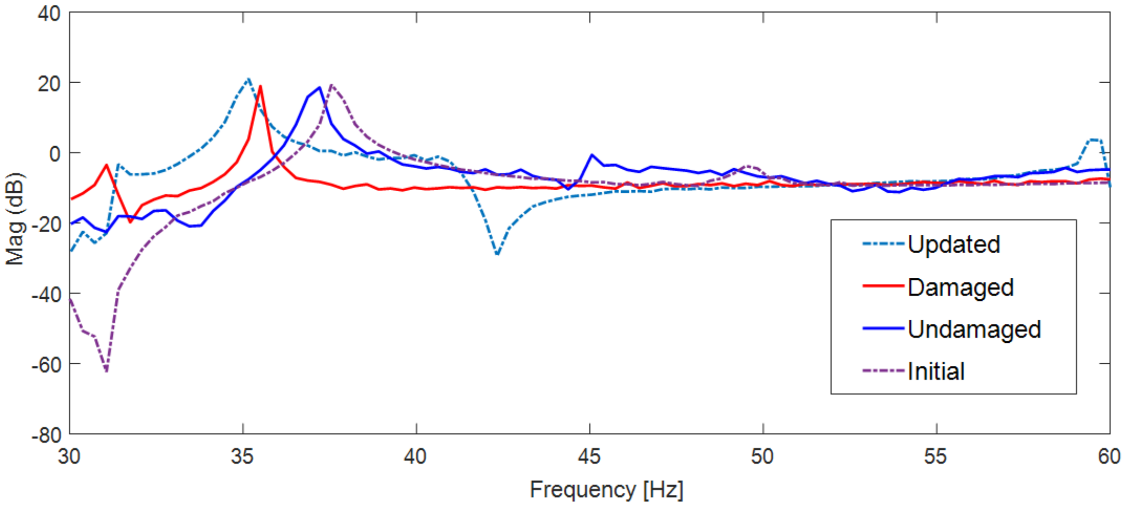

Figure 9.17: FRF updating of the main subsystem

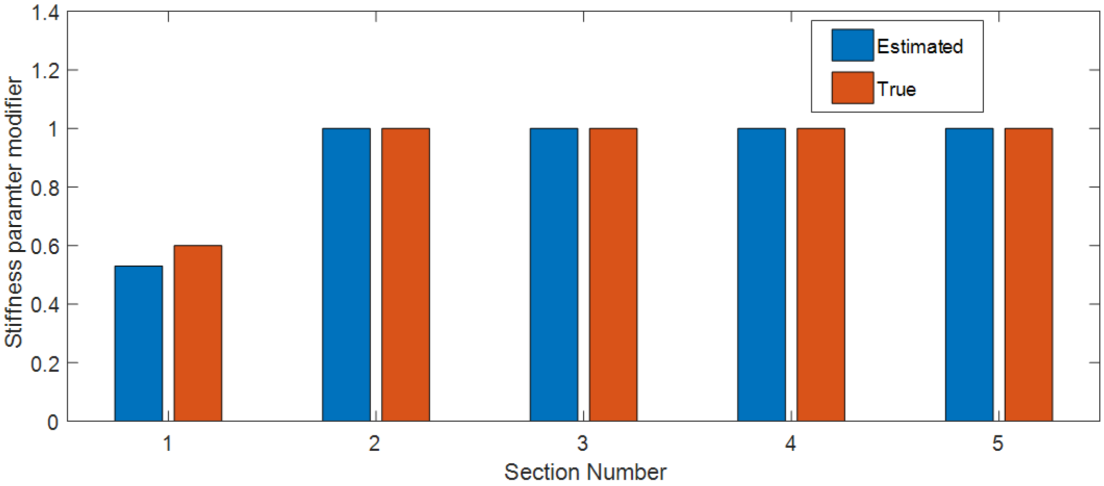

Figure 9.18: Stiffness parameter modifiers in experimental case study

9.6 Conclusion

This paper proposes a substructural damage detection method using frequency response functions. In the proposed method, one substructure is considered the main substructure and under damage and the rest of the substructure(s) are considered undamaged or not susceptible to damage, a situation which often happens in practice. The residual substructure(s) are considered undamaged which could be due the fact that the residual substructure(s) are either not under operation (the main substructure is only under operation) or their material and loading are such that they are not susceptible to damage. In the proposed method, unlike other substructural damage detection methods, there is no need for placing a numerical virtual support in the target substructure boundary or obtaining the interface forces. The frequency response functions of the assembled damaged structure and the frequency response function(s) of the residual substructure(s) are needed to obtain the FRFs of the main substructure, completely decoupled from the rest of the structure. An FRF-based model updating is then performed using only the FE model of the main substructure to detect, localize and quantify the damage in the main substructure. In order to reduce the computation time in the model updating of the damaged structure, a smaller frequency range in the FRF can be chosen based on the accuracy of decoupling result in the undamaged structure. Two numerical examples and an experimental case study are presented to illustrate the procedure. The damage in the main substructure is detected and quantified with a good accuracy in the numerical and experimental case studies. More studies can be done in future to apply the method on a real engineering application. The limitation of this method is the need to have the residual subsystem dynamics, but the advantage is that we do not need any interface force identification or virtual support between the subsystems.

Chapter 10

10 Conclusions and Future work

This thesis was a continuation of a project to develop a vibration-based non-destructive testing method for wooden utility poles. The aim of this thesis was to study the effects of conductors on the vibration response of in-service utility poles and to achieve this aim, the thesis was done in three different parts. The first part was analytical modeling of cable-beam systems to understand the coupled vibration and to understand the effects of cable on the vibration of coupled system. The results of the first part are summarized in section 10.1. The second part of this thesis was application of substructure decoupling method to decouple the beam dynamics from the assembled cable-beam system dynamics. The results of this part are summarized in section 10.2. The third part of this thesis was performing modal tests in the lab and in the field and destructive tests on the full-scale utility poles. The results of this part are presented in Appendices and are summarized in section 10.3. Future work that is recommended to continue this thesis is presented in section 10.5.

10.1 Analytical modeling

Analytical and mathematical modeling of cable-beam systems was studied in this thesis:

√ In Chapter 3, the cable sag and bending stiffness was considered in the modeling for the first time in the literature. The bending stiffness of the cable was measured in different tensions using a specially designed apparatus. The natural frequencies, mode shapes and frequency response function were obtained from the analytical model and the results were verified with the experimental results obtained from modal testing of the lab-scale pole-line system. It is concluded that cable bending stiffness and sag have significant effect on the natural frequencies and frequency response of the cable-beam systems and should be considered in analytical modeling. It is also concluded that by adding the cable to the beam, three different type of vibration modes occur: cable dominated, beam dominated, and hybrid (coupled) These can be identified upon visual inspection of the mode shapes of the system.

√ In Chapter 4 and Chapter 5, two-dimensional and three-dimensional bond graph models were developed for the stranded cables, respectively. These models studied the vibration behavior of the cable-only system and investigated the effects of different properties such as bending stiffness and sag and tension on the response of the cable. In-plane and out-of-plane natural frequencies and free and forced vibration response were obtained from the models and they were verified with the modal test results on the cable. An experimental bending stiffness parametrization was also performed to measure the bending stiffness. It is concluded that the bond graph method can be used for simulation of stranded cable vibration in spite of the complicated mechanical behavior of these cables. A more comprehensive study can be done to study the interaction between the layers in the stranded cables and model this interaction in bond graph.

√ In Chapter 6, a three-dimensional bond graph model was developed for a cable-beam system considering bending stiffness and sag. A complete experimental cable parametrization was also performed for the bending and axial stiffness of the stranded cable to obtain axial and bending stiffness. Free and forced vibration response of the coupled system in in-plane and out-of-plane were compared to the experimental results and the model was verified. This model allows prediction of out-of-plane vibration which is usually not studied in the literature. This model can be easily extended to simulate the real utility pole-conductor system and to study the effects of cables in the full-scale system.

10.2 Substructure Decoupling

Substructure decoupling or inverse dynamic substructuring method was proposed in this thesis to filter out the effects of cable in utility pole-power line system.

√ In Chapter 7, a single-beam-cable system and a multi-beam-cable system were used in the lab to investigate the method experimentally. Experimental modal tests were performed on two cable-beam systems in the lab and FRF matrices were used in the decoupling formulation. The first cable-beam system consisted of one cantilever beam and a cable and the second system was a multi-beam-cable system consisted of three cantilever beams that are connected together with a cable. The FRFs of the beams were obtained after decoupling analysis and were then compared to the directly measured FRF from the beam subsystem. Natural frequencies and damping ratios obtained from the two FRFs (directly measured and decoupled) were compared and good agreement was achieved. It is concluded that the inverse substructuring method is a reliable method to obtain the frequency response of the beam as an independent substructure with the effect of the cable filtered out. It is also concluded that the beam FRF can be achieved with good accuracy regardless of the amount of cable sag and tension as long as cable dynamics are also available. FRF-based finite element model updating was also proposed to overcome the practical limitation of accessing some points to measure the FRFs. A finite element model of the cable-beam system was developed and FRF of the coupling point was obtained from the FE model. Then FE updating was used to improve the numerically obtained FRF. A combination of numerical and experimental FRFs were used in the decoupling formulation and the beam FRF was obtained. It is concluded that FRF-based FE updating can be used to improve the FRFs obtained from FE model, therefore, the FRFs that are impossible to be measured in the field can be obtained numerically and then be used in the decoupling formulation.

- √ In Chapter 8, experimental-numerical decoupling was applied to the single-beam-cable system. The cable FRFs were obtained from the finite element model and the assembled system's FRFs were measured. The beam FRF was decoupled and compared to the directly measured beam FRF. It is concluded that finite element can be used to provide the FRFs of a subsystem when they cannot be measured, and good accuracy can be obtained from experimental-numerical decoupling.
- √ In Chapter 9, a substructural damage detection was also developed using the substructure decoupling method and FE updating. The FRF of the target substructure was first obtained using the substructure decoupling approach and then FRF-based model updating was used for the purpose of damage detection, localization and quantification. The developed method can be used for damage detection of the structures that consist of multiple substructures, only one of which is susceptible to damage. Unlike the other substructural damage detection methods in the literature, dynamics of the main subsystem can be obtained without the need for numerical virtual support at the interface or identifying interface forces.

10.3 Experimental Tests on Full-Scale Utility Poles

In order to expand our database of strength prediction of utility poles, destructive tests were performed in this thesis on 20 full-scale poles that were transferred from the field to the lab in memorial university. Destructive tests are based on the ASTMD1036 standard and a summary of the test details is included in Appendix A. Modal tests were also performed on 30 utility poles in two batch of poles (first batch 10 poles and the second batch 20 poles). In order to study the effects of conductors on FRF of in-situ poles, the first batch of poles (in Goose bay, Labrador) were modally tested with and without the connected cables and the test results are summarized in Appendix B. The FRFs of the poles with cables showed a shift toward left which could be due to the added cable mass but also showed more damping in high frequency range which is due to high cable damping. The second batch (in Paradise, Newfoundland) was tested only without the connected cables. This batch was then transmitted to the lab and was modally tested in the lab. The results of this batch of poles are also presented in Appendix B. The FRFs of the “in-lab” poles showed higher stiffness (shift toward right) and also higher damping (less sharp peaks) in high frequency range.

10.4 Contribution list

The following items are the main research contributions of this thesis:

1. Substructure decoupling method is used to decouple cable dynamics from the assembled cable-beam system dynamics. It is concluded that this method is a reliable and effective method to be used in cable structures.
2. State of the art of the cable-beam system modeling was improved by considering cable bending stiffness and sag in modeling.
3. A substructural damage detection method was developed for systems in which the main subsystem is susceptible to damage and the residual subsystems are undamaged and dynamically unchanged.

10.5 Future work

In this thesis, analytical and mathematical modeling of cable-beam systems were studied. The decoupling method was also proposed to decouple the pole dynamics from the assembled system. The following suggestions are presented for future work:

- Substructure decoupling method should be applied to the full-scale utility pole system alongside the FE updating to decouple the conductors FRF from the assembled system. The FRFs of the pole without and with the conductors are available from one of the field tests in this thesis. The measured FRFs can be used as a basis for updating the FE model of the real utility pole and the combination of numerical and experimental FRFs can be used in the decoupling formulation to obtain the FRF of the pole with the effects of conductors filtered out. The directly measured FRF of the pole without conductors can then be used for verification.

- In the analytical modeling of the cable-beam systems, this thesis assumed system linearity in modeling. A better and maybe more accurate modeling can be done considering cable nonlinearity and internal resonances in the system. Nonlinear modeling of cable-beam systems considering cable bending stiffness and sag is a study that has never been done in the literature.
- A more comprehensive study can be done to study the interaction between the layers in stranded cables during bending and vibration in the cable-beam system. The cable layers interaction has been studied extensively in the literature but the effects of these interactions on the vibration of a coupled cable-beam system is an interesting topic that can be done as future work.
- Newer damage detection methods such as machine learning-based and deep learning-based can be investigated for damage detection of utility poles. There have been many studies using these methods for damage detection but there is no study on the specific application of utility poles.
- Foundation effects on the FRF of the poles can be investigated as future work. Investigation of what effects different foundations can have on the FRF of the in-situ poles.
- Operation modal analysis (OMA) or ambient vibration measurement alongside the substructure decoupling can be studied in future. Investigation of whether it is possible to filter out the effects of cables from the ambient vibration response of the poles would be an interesting topic to be studied.

References

[1] A. Haldar, Wood Pole Line Management Using RCM Principles, Rep. Prep. TRO Div. Newfoundl. Labrador Hydro. (2004).

[2] J.J. Morrell, Estimated service life of wood poles, Tech. Bull. North Am. Wood Pole Counc. (2008).

[3] F.H. Schweingruber, Wood structure and environment, Springer Science & Business Media, 2007.

[4] www.ndt.net, (n.d.).

[5] M. Nguyen, G. Foliente, X.M. Wang, State-of-the-practice & challenges in non-destructive evaluation of utility poles in service, in: Key Eng. Mater., Trans Tech Publ, 2004: pp. 1521–1528.

[6] S. Hiller, No Title, (2016). https://nlhydro.com/hydro-invest-271-4-million-capital-projects-2017-strengthen-aging-grid/.

[7] D. Rideout, O.F. Whelan, Modeling of tapered cantilever beams for simulation of utility pole vibration, in: Proc. Int. Conf. Bond Graph Model. Simulation, Monterey, USA, 2014: pp. 6–10.

[8] L.M. Downer, Detecting damage in beams and structures through modal analysis, (2010).

[9] https://edmlink.com/, (n.d.).

[10] M. Brown, Report on Wood Pole Testing. 2008: Memorial University Faculty of Engineering and Applied Science Industrial Outreach Group Project ID-009-01-05 NL Hydro., 2008.

[11] G. Whelan, O F, Rideout, Improved Damage Detection and Strength Prediction for Wooden Transmission Line Poles, Phase II Progress Report, 2013.

[12] P.F. Pinto, Experimental and numerical investigation of the influence of cables on utility

pole modal property extraction, (2017).

[13] S.N. Voormeeren, D.J. Rixen, A family of substructure decoupling techniques based on a dual assembly approach, Mech. Syst. Signal Process. 27 (2012) 379–396.

[14] D. de Klerk, D.J. Rixen, S.N. Voormeeren, General framework for dynamic substructuring: history, review and classification of techniques, AIAA J. 46 (2008) 1169–1181.

[15] M.H. Jalali, G. Rideout, Analytical and experimental investigation of cable–beam system dynamics, J. Vib. Control. 25 (2019) 2678–2691.

[16] M.H. Jalali, G. Rideout, Development and Validation of a Numerical Model for Vibration of Power Lines, in: CSME Int. Congr. Toronto, 2018, CSME-SCGM, Toronto, 2018.

[17] M.H. Jalali, R. McKercher, G. Rideout, Three dimensional dynamic model development and validation for stranded cables, in: ASME 2019 Int. Mech. Eng. Congr. Expo., Salt Lake, Utah, US, 2019.

[18] M.H. Jalali, G. Rideout, Three-Dimensional Dynamic Modelling and Validation for Vibration of a Beam-Cable System, Math. Comput. Model. Dyn. Syst. 27 (2021) 87–116.

[19] M.H. Jalali, D.G. Rideout, Frequency-based decoupling and finite element model updating in vibration of cable–beam systems, J. Vib. Control. (2021) 1077546321996936.

[20] M.H. Jalali, G. Rideout, Prediction of beam dynamics in cable-beam systems through experimental-numerical decoupling, in: XI Int. Conf. Struct. Dyn. EURODYN2020, 2020.

[21] S. Baraneedaran, E.F. Gad, I. Flatley, A. Kamiran, J.L. Wilson, Review of in-service assessment of timber poles, Proc. Aust. Earthq. Eng. Soc. Newcastle. (2009).

[22] M. Luminari, System for detecting and correcting defects in articles being processed, in particular wood panels with splits, knot-holes, etc., (1991).

[23] M.M. Hosseini, A. Umunnakwe, M. Parvania, T. Tasdizen, Intelligent damage classification and estimation in power distribution poles using unmanned aerial vehicles and

convolutional neural networks, IEEE Trans. Smart Grid. 11 (2020) 3325–3333.

[24] N. Kerle, F. Nex, M. Gerke, D. Duarte, A. Vetrivel, UAV-based structural damage mapping: A review, ISPRS Int. J. Geo-Information. 9 (2020) 14.

[25] J. Kim, Y. Ham, Vision-Based Analysis of Utility Poles Using Drones and Digital Twin Modeling in the Context of Power Distribution Infrastructure Systems, in: Constr. Res. Congr. 2020 Comput. Appl., American Society of Civil Engineers Reston, VA, 2020: pp. 954–963.

[26] T. Tannert, R.W. Anthony, B. Kasal, M. Kloiber, M. Piazza, M. Riggio, F. Rinn, R. Widmann, N. Yamaguchi, In situ assessment of structural timber using semi-destructive techniques, Mater. Struct. 47 (2014) 767–785.

[27] F. Rinn, Basics of typical resistance-drilling profiles, West. Arborist. 17 (2012) 30–36.

[28] L.R. Costello, S.L. Quarles, Detection of wood decay in blue gum and elm: an evaluation of the Resistograph [R] and the portable drill, J. Arboric. 25 (1999) 311–318.

[29] T.P. Nowak, J. Jasieńko, K. Hamrol-Bielecka, In situ assessment of structural timber using the resistance drilling method–Evaluation of usefulness, Constr. Build. Mater. 102 (2016) 403–415.

[30] B. Kasal, M. Kloiber, M. Drdacky, Field investigation of the 14th century Castle Pernstejn before and after fire damage, in: Build. Integr. Solut., 2006: pp. 1–8.

[31] K. Schabowicz, Non-destructive testing of materials in civil engineering, (2019).

[32] E. Ezer, Measurement of wood pole strength-Polux/sup (R)/a new nondestructive inspection method, in: 2001 Rural Electr. Power Conf. Pap. Present. 45th Annu. Conf. (Cat. No. 01CH37214), IEEE, 2001: pp. C6-1.

[33] A.J. Stamm, The Electrical Resistance of Wood as AMeasure of Its Moisture Content, Ind. Eng. Chem. 19 (1927) 1021–1025.

[34] M. Riggio, R.W. Anthony, F. Augelli, B. Kasal, T. Lechner, W. Muller, T. Tannert, In situ assessment of structural timber using non-destructive techniques, Mater. Struct. 47 (2014) 749–766.

[35] W.M. Bulleit, R.H. Falk, Modeling stress wave passage times in wood utility poles, Wood Sci. Technol. 19 (1985) 183–191.

[36] F.C. Beall, Overview of the use of ultrasonic technologies in research on wood properties, Wood Sci. Technol. 36 (2002) 197–212.

[37] F. Tallavo, G. Cascante, M.D. Pandey, A novel methodology for condition assessment of wood poles using ultrasonic testing, Ndt E Int. 52 (2012) 149–156.

[38] M. Krause, U. Dackermann, J. Li, Elastic wave modes for the assessment of structural timber: ultrasonic echo for building elements and guided waves for pole and pile structures, J. Civ. Struct. Heal. Monit. 5 (2015) 221–249.

[39] K. Shen, H. Zhao, X. Ding, M. Li, Application of acoustic emission in wood processing., World For. Res. 28 (2015) 56–60.

[40] F. Lamy, M. Takarli, N. Angellier, F. Dubois, O. Pop, Acoustic emission technique for fracture analysis in wood materials, Int. J. Fract. 192 (2015) 57–70.

[41] M. Kloiber, L. Reinprecht, J. Hrivnák, J. Tippner, Comparative evaluation of acoustic techniques for detection of damages in historical wood, J. Cult. Herit. 20 (2016) 622–631.

[42] H.D. Thomas, Non-destructive evaluation of wood utility poles using computed axial tomography imaging, (2006).

[43] P. Wells, J.R. Davis, M.J. Morgan, S.S. Som, J. Grant, N. Benci, D.S. Skerrett, Industrial non-destructive testing and evaluation using X-ray and gamma-ray computed tomography, in: 9th Pacific Basin Nucl. Conf. Nucl. Energy, Sci. Technol. Pacific Partnership; Proc., Institution of Engineers, Australia, 1994: p. 399.

[44] R.J. Ross, Nondestructive testing for assessing wood members in structures: A review, US Department of Agriculture, Forest Service, Forest Products Laboratory, 1994.

[45] A. Alvandi, C. Cremona, Assessment of vibration-based damage identification techniques, J. Sound Vib. 292 (2006) 179–202.

[46] Y.J. Yan, L. Cheng, Z.Y. Wu, L.H. Yam, Development in vibration-based structural damage detection technique, Mech. Syst. Signal Process. 21 (2007) 2198–2211.

[47] M.H. Jalali, B. Shahriari, M. Ghayour, S. Ziaei-Rad, S. Yousefi, Evaluation of Dynamic Behavior of a Rotor-Bearing System in Operating Conditions, in: WASET, Dubai, 2014, n.d.

[48] B. Shahriari, M. Jalali, M.R. Karamooz Ravari, Vibration analysis of a rotating variable thickness bladed disk for aircraft gas turbine engine using generalized differential quadrature method, Proc. Inst. Mech. Eng. Part G J. Aerosp. Eng. 231 (2017) 2739–2749.

[49] D. ASTM, 1036, Standard Test Methods for Static Tests of Wood Poles, ASTM Int. West Conshohocken. PA. (2012).

[50] K.O. Papailiou, On the bending stiffness of transmission line conductors, IEEE Trans. Power Deliv. 12 (1997) 1576–1588.

[51] G. Ricciardi, F. Saitta, A continuous vibration analysis model for cables with sag and bending stiffness, Eng. Struct. 30 (2008) 1459–1472.

[52] H.J. Kang, Y.Y. Zhao, H.P. Zhu, Linear and nonlinear dynamics of suspended cable considering bending stiffness, J. Vib. Control. 21 (2015) 1487–1505.

[53] R.A. Sousa, R.M. Souza, F.P. Figueiredo, I.F.M. Menezes, The influence of bending and shear stiffness and rotational inertia in vibrations of cables: An analytical approach, Eng. Struct. 33 (2011) 689–695.

[54] V. Gattulli, M. Morandini, A. Paolone, A parametric analytical model for non-linear

dynamics in cable-stayed beam, Earthq. Eng. Struct. Dyn. 31 (2002) 1281–1300.

[55] H.-N. Li, W.-L. Shi, G.-X. Wang, L.-G. Jia, Simplified models and experimental verification for coupled transmission tower–line system to seismic excitations, J. Sound Vib. 286 (2005) 569–585.

[56] P. Ferreira Pinto, G. Rideout, Development and validation of an in-situ utility pole simulation model for virtual modal testing, in: ASME 2016 Int. Mech. Eng. Congr. Expo., American Society of Mechanical Engineers Digital Collection, 2016.

[57] S. Voormeeren, D.J. Rixen, Substructure decoupling techniques–a review and uncertainty propagation analysis, in: Proc. Twenty-Seventh Int. Modal Anal. Conf. Orlando, Florida, 2009.

[58] J.R. Crowley, A. Klosterman, G.T. Rocklin, H. Vold, Direct structural modification using frequency response functions, in: Proc. Second Int. Modal Anal. Conf. Orlando, FL, Society for Experimental Mechanics Bethel, CT, 1984: pp. 58–65.

[59] B. Jetmundsen, R.L. Bielawa, W.G. Flannelly, Generalized frequency domain substructure synthesis, J. Am. Helicopter Soc. 33 (1988) 55–64.

[60] D. de Klerk, D.J. Rixen, J. de Jong, The frequency based substructuring (FBS) method reformulated according to the dual domain decomposition method, in: 24th Int. Modal Anal. Conf. St. Louis, MO, 2006.

[61] W. D'Ambrogio, A. Fregolent, Promises and pitfalls of decoupling procedures, Proceeding 26th IMAC. Orlando. (2008).

[62] P. Peeters, S. Manzato, T. Tamarozzi, W. Desmet, Reducing the impact of measurement errors in FRF-based substructure decoupling using a modal model, Mech. Syst. Signal Process. 99 (2018) 384–402.

[63] D. de Klerk, D. Rixen, S.N. Voormeeren, F. Pasteuning, Solving the RDoF problem in

experimental dynamic substructuring, in: Proc. Twentysixth Int. Modal Anal. Conf. Orlando, FL, 2008.

[64] D. De Klerk, S. Voormeeren, Uncertainty propagation in experimental dynamic substructuring, in: Proc. Twenty Sixth Int. Modal Anal. Conf. Orlando, FL, Society for Experimental Mechanics Bethel, CT, 2008.

[65] M. Law, H. Rentzsch, S. Ihlenfeldt, Predicting mobile machine tool dynamics by experimental dynamic substructuring, Int. J. Mach. Tools Manuf. 108 (2016) 127–134.

[66] Ş. Tol, Dynamic characterization of bolted joints using FRF decoupling and optimization, Mech. Syst. Signal Process. 54 (2015) 124–138.

[67] M. V Van der Seijs, Experimental dynamic substructuring: analysis and design strategies for vehicle development, (2016).

[68] M. Mehrpouya, E. Graham, S.S. Park, FRF based joint dynamics modeling and identification, Mech. Syst. Signal Process. 39 (2013) 265–279.

[69] W. D'Ambrogio, A. Fregolent, Use of experimental dynamic substructuring to predict the low frequency structural dynamics under different boundary conditions, Math. Mech. Solids. 23 (2018) 1444–1455.

[70] B.B. Eliasdottir, M. Karamooz Mahdiabadi, A. Bartl, D.J. Rixen, An experimental-numerical substructuring approach in dual form, in: Proc. 27th ISMA, A Conf. Noise Vib. Eng., 2016.

[71] D. Giagopulos, S. Natsiavas, Hybrid (numerical-experimental) modeling of complex structures with linear and nonlinear components, Nonlinear Dyn. 47 (2007) 193–217.

[72] R.L. Mayes, D.P. Rohe, Coupling Experimental and Analytical Substructures with a Continuous Connection Using the Transmission Simulator Method BT - Topics in Experimental Dynamic Substructuring, Volume 2, in: R. Mayes, D. Rixen, M. Allen (Eds.),

Springer New York, New York, NY, 2014: pp. 123–135.

[73] R.L. Mayes, Tutorial on experimental dynamic substructuring using the transmission simulator method, in: Top. Exp. Dyn. Substruct. Wind Turbine Dyn. Vol. 2, Springer, 2012: pp. 1–9.

[74] M.S. Allen, R.L. Mayes, E.J. Bergman, Experimental modal substructuring to couple and uncouple substructures with flexible fixtures and multi-point connections, J. Sound Vib. 329 (2010) 4891–4906.

[75] O. Barry, J.W. Zu, D.C.D. Oguamanam, Analytical and experimental investigation of overhead transmission line vibration, J. Vib. Control. 21 (2015) 2825–2837.

[76] Y.Q. Ni, J.M. Ko, G. Zheng, Dynamic analysis of large-diameter sagged cables taking into account flexural rigidity, J. Sound Vib. 257 (2002) 301–319.

[77] V. Gattulli, M. Lepidi, F. Potenza, U. Di Sabatino, Dynamics of masonry walls connected by a vibrating cable in a historic structure, Meccanica. 51 (2016) 2813–2826.

[78] M.Y. Park, S. Kim, I. Paek, C. Cui, Frequency analysis of a tower-cable coupled system, J. Mech. Sci. Technol. 27 (2013) 1731–1737.

[79] V. Gattulli, M. Lepidi, J.H.G. Macdonald, C.A. Taylor, One-to-two global-local interaction in a cable-stayed beam observed through analytical, finite element and experimental models, Int. J. Non. Linear. Mech. 40 (2005) 571–588.

[80] Z. Wang, Z. Yi, Y. Luo, Energy-based formulation for nonlinear normal modes in cable-stayed beam, Appl. Math. Comput. 265 (2015) 176–186.

[81] Z. Wang, C. Sun, Y. Zhao, Z. Yi, Modeling and nonlinear modal characteristics of the cable-stayed beam, Eur. J. Mech. 47 (2014) 58–69.

[82] H.M. Irvine, Cable Structures The MIT Press, Cambridge, MA. (1981) 15–24.

[83] A. Luongo, G. Rega, F. Vestroni, Planar non-linear free vibrations of an elastic cable, Int.

J. Non. Linear. Mech. 19 (1984) 39–52.

[84] S. Zhou, F. Li, C. Zhang, Vibration characteristics analysis of disordered two-span beams with numerical and experimental methods, J. Vib. Control. 24 (2018) 3641–3657.

[85] S. Sorrentino, A. Fasana, S. Marchesiello, Frequency domain analysis of continuous systems with viscous generalized damping, Shock Vib. 11 (2004) 243–259.

[86] K.G. McConnell, W.P. Zemke, The measurement of flexural stiffness of multistranded electrical conductors while under tension, Exp. Mech. 20 (1980) 198–204.

[87] A. Filiatrault, C. Stearns, Flexural properties of flexible conductors interconnecting electrical substation equipment, J. Struct. Eng. 131 (2005) 151–159.

[88] N. Barbieri, O.H. de Souza Junior, R. Barbieri, Dynamical analysis of transmission line cables. Part 2—damping estimation, Mech. Syst. Signal Process. 18 (2004) 671–681.

[89] M.L.Q. Wang, H.N. Li, Aseismic calculation of transmission tower–conductor system, Earthq. Eng. Eng. Vib. 9 (1989) 73–87.

[90] K. Spak, G. Agnes, D. Inman, Cable modeling and internal damping developments, Appl. Mech. Rev. 65 (2013).

[91] K.S. Spak, G.S. Agnes, D.J. Inman, Modeling vibration response and damping of cables and cabled structures, J. Sound Vib. 336 (2015) 240–256.

[92] K.S. Spak, G.S. Agnes, D. Inman, Towards modeling of cable-harnessed structures: cable damping experiments, in: 54th AIAA/ASME/ASCE/AHS/ASC Struct. Struct. Dyn. Mater. Conf., 2013: p. 1889.

[93] D.C. Karnopp, D.L. Margolis, R.C. Rosenberg, System dynamics: modeling, simulation, and control of mechatronic systems, John Wiley & Sons, 2012.

[94] L. Meirovitch, Fundamentals of vibrations, Waveland Press, 2010.

[95] ABSignal, Getting started with ModalView, (2012).

[96] N. Uddin, J.T. Gravdahl, Bond graph modeling of centrifugal compression systems, Simulation. 91 (2015) 998–1013.

[97] I. Kraincanic, R.E. Hobbs, Axial stiffness and torsional effects in a 76 mm wire rope: Experimental data and theoretical predictions, J. Strain Anal. Eng. Des. 34 (1999) 39–51.

[98] R. Judge, Z. Yang, S.W. Jones, G. Beattie, Full 3D finite element modelling of spiral strand cables, Constr. Build. Mater. 35 (2012) 452–459.

[99] L. Xiang, H.Y. Wang, Y. Chen, Y.J. Guan, Y.L. Wang, L.H. Dai, Modeling of multi-strand wire ropes subjected to axial tension and torsion loads, Int. J. Solids Struct. 58 (2015) 233–246.

[100] K. Spak, G. Agnes, D. Inman, Parameters for modeling stranded cables as structural beams, Exp. Mech. 54 (2014) 1613–1626.

[101] B. Chen, W. Guo, P. Li, W. Xie, Dynamic responses and vibration control of the transmission tower-line system: a state-of-the-art review, Sci. World J. 2014 (2014).

[102] G. McClure, M. Lapointe, Modeling the structural dynamic response of overhead transmission lines, Comput. Struct. 81 (2003) 825–834.

[103] P.C. Breedveld, Multibond graph elements in physical systems theory, J. Franklin Inst. 319 (1985) 1–36.

[104] M. Sarker, D.G. Rideout, S.D. Butt, Dynamic model for 3D motions of a horizontal oilwell BHA with wellbore stick-slip whirl interaction, J. Pet. Sci. Eng. 157 (2017) 482–506.

[105] M. Kebdani, G. Dauphin-Tanguy, A. Dazin, R. Albach, P. Dupont, Two-phase reservoir: development of a transient thermo-hydraulic model based on bond graph approach with experimental validation, Math. Comput. Model. Dyn. Syst. 23 (2017) 476–503.

[106] D.G. Rideout, A. Ghasemloonia, F. Arvani, S.D. Butt, An intuitive and efficient approach to integrated modelling and control of three-dimensional vibration in long shafts, Int. J.

Simul. Process Model. 10 (2015) 163–178.

[107] M. Sarker, D.G. Rideout, S.D. Butt, Dynamic model for longitudinal and torsional motions of a horizontal oilwell drillstring with wellbore stick-slip friction, J. Pet. Sci. Eng. 150 (2017) 272–287.

[108] D.G. Rideout, J.L. Stein, L.S. Louca, Systematic assessment of rigid internal combustion engine dynamic coupling, J. Eng. Gas Turbines Power. 130 (2008).

[109] L. Xiang, H.Y. Wang, Y. Chen, Y.J. Guan, L.H. Dai, Elastic-plastic modeling of metallic strands and wire ropes under axial tension and torsion loads, Int. J. Solids Struct. 129 (2017) 103–118.

[110] B.J. Buckham, Dynamics modelling of low-tension tethers for submerged remotely operated vehicles, 2003.

[111] S. Lalonde, R. Guilbault, F. Légeron, Modeling multilayered wire strands, a strategy based on 3D finite element beam-to-beam contacts-Part I: Model formulation and validation, Int. J. Mech. Sci. 126 (2017) 281–296.

[112] Y. Yu, Z. Chen, H. Liu, X. Wang, Finite element study of behavior and interface force conditions of seven-wire strand under axial and lateral loading, Constr. Build. Mater. 66 (2014) 10–18.

[113] J.M. Hamilton, Vibration-based techniques for measuring the elastic properties of ropes and the added mass of submerged objects, J. Atmos. Ocean. Technol. 17 (2000) 688–697.

[114] P.N. Brown, G.D. Byrne, A.C. Hindmarsh, VODE: A variable-coefficient ODE solver, SIAM J. Sci. Stat. Comput. 10 (1989) 1038–1051.

[115] X. Su, H. Kang, T. Guo, Y. Cong, Dynamic analysis of the in-plane free vibration of a multi-cable-stayed beam with transfer matrix method, Arch. Appl. Mech. 89 (2019) 2431–2448.

[116] K. Yerrapragada, A. Salehian, Coupled Dynamics of Cable-Harnessed Structures:

Experimental Validation, J. Vib. Acoust. 141 (2019).

[117] V. Gattulli, M. Lepidi, F. Potenza, U. Di Sabatino, Modal interactions in the nonlinear dynamics of a beam–cable–beam, Nonlinear Dyn. 96 (2019) 2547–2566.

[118] M. Lepidi, V. Gattulli, A parametric multi-body section model for modal interactions of cable-supported bridges, J. Sound Vib. 333 (2014) 4579–4596.

[119] S.N. Voormeeren, Dynamic substructuring methodologies for integrated dynamic analysis of wind turbines, (2012).

[120] J. Wang, Z. Wang, L. Lu, Step-by-step decoupling method for inverse substructuring analysis of a three-component coupled packaging system, J. Vib. Control. 21 (2015) 676–683.

[121] W. D'Ambrogio, A. Fregolent, Substructure decoupling as the identification of a set of disconnection forces, Meccanica. 52 (2017) 3117–3129.

[122] D.J. Ewins, Modal testing: theory and practice, Research studies press Letchworth, 1984.

[123] J.D. Sipple, M. Sanayei, Finite element model updating using frequency response functions and numerical sensitivities, Struct. Control Heal. Monit. 21 (2014) 784–802.

[124] W. D'Ambrogio, A. Fregolent, The role of interface DoFs in decoupling of substructures based on the dual domain decomposition, Mech. Syst. Signal Process. 24 (2010) 2035–2048.

[125] G. Papazafeiropoulos, M. Muñiz-Calvente, E. Martínez-Pañeda, Abaqus2Matlab: a suitable tool for finite element post-processing, Adv. Eng. Softw. 105 (2017) 9–16.

[126] V. Gattulli, L. Martinelli, F. Perotti, F.V.-C.M. in Applied, U. 2004, Nonlinear oscillations of cables under harmonic loading using analytical and finite element models, Comput. Methods Appl. Mech. Eng. 193 (2004).

[127] L. Faravelli, F. Ubertini, Nonlinear state observation for cable dynamics, J. Vib. Control.

15 (2009) 1049–1077.

[128] F. Potenza, M. Lepidi, U. Di Sabatino, V. Gattulli, Nonlinear dynamics of a parametric analytical model for beam-cable-beam structures, Procedia Eng. 199 (2017) 796–801.

[129] M. Law, H. Rentzsch, S. Ihlenfeldt, M. Putz, Application of substructure decoupling techniques to predict mobile machine tool dynamics: numerical investigations, Procedia CIRP. 46 (2016) 537–540.

[130] S. Rahimi, D. de Klerk, D.J. Rixen, The Ampair 600 wind turbine benchmark: results from the frequency based substructuring applied to the rotor assembly, in: Top. Exp. Dyn. Substruct. Vol. 2, Springer, 2014: pp. 179–192.

[131] A.W. Otto, D.O. Elias, R.L. Hatton, Modeling transverse vibration in spider webs using frequency-based dynamic substructuring, in: Dyn. Coupled Struct. Vol. 4, Springer, 2018: pp. 143–155.

[132] J. Li, S.S. Law, Y. Ding, Substructure damage identification based on response reconstruction in frequency domain and model updating, Eng. Struct. 41 (2012) 270–284.

[133] S. Weng, H. Zhu, Y. Xia, J. Li, W. Tian, A review on dynamic substructuring methods for model updating and damage detection of large-scale structures, Adv. Struct. Eng. 23 (2020) 584–600.

[134] D. Zhang, E.A. Johnson, Substructure identification for shear structures I: Substructure identification method, Struct. Control Heal. Monit. 20 (2013) 804–820.

[135] D. Zhang, E.A. Johnson, Substructure identification for shear structures: cross-power spectral density method, Smart Mater. Struct. 21 (2012) 55006.

[136] Z. Xing, A. Mita, A substructure approach to local damage detection of shear structure, Struct. Control Heal. Monit. 19 (2012) 309–318.

[137] D. Zhang, S. Li, H. Li, Adaptive substructure identification for shear structures with virtual

control system, Mech. Syst. Signal Process. 121 (2019) 426–440.

[138] C. DeVore, Z. Jiang, R.E. Christenson, G. Stromquist-LeVoir, E.A. Johnson, Experimental verification of substructure identification for damage detection in shear buildings, J. Eng. Mech. 142 (2016) 4015060.

[139] L. Mei, H. Li, Y. Zhou, W. Wang, F. Xing, Substructural damage detection in shear structures via ARMAX model and optimal subpattern assignment distance, Eng. Struct. 191 (2019) 625–639.

[140] J. Hou, Ł. Jankowski, J. Ou, A substructure isolation method for local structural health monitoring, Struct. Control Heal. Monit. 18 (2011) 601–618.

[141] J. Hou, Ł. Jankowski, J. Ou, Experimental study of the substructure isolation method for local health monitoring, Struct. Control Heal. Monit. 19 (2012) 491–510.

[142] J. Hou, Ł. Jankowski, J. Ou, Frequency-domain substructure isolation for local damage identification, Adv. Struct. Eng. 18 (2015) 137–153.

[143] S.S. Law, D. Yong, Substructure methods for structural condition assessment, J. Sound Vib. 330 (2011) 3606–3619.

[144] S. Weng, Y. Xia, Y.-L. Xu, H.-P. Zhu, An iterative substructuring approach to the calculation of eigensolution and eigensensitivity, J. Sound Vib. 330 (2011) 3368–3380.

[145] S. Weng, H.-P. Zhu, Y. Xia, L. Mao, Damage detection using the eigenparameter decomposition of substructural flexibility matrix, Mech. Syst. Signal Process. 34 (2013) 19–38.

[146] S. Weng, H.-P. Zhu, P.-H. Li, Y. Xia, L. Ye, Construction of orthogonal projector for the damage identification by measured substructural flexibility, Measurement. 88 (2016) 441–455.

[147] S.N. Voormeeren, D.J. Rixen, A dual approach to substructure decoupling techniques, in:

Struct. Dyn. Vol. 3, Springer, 2011: pp. 601–616.

[148] J.E. Mottershead, M. Link, M.I. Friswell, The sensitivity method in finite element model updating: A tutorial, Mech. Syst. Signal Process. 25 (2011) 2275–2296.

[149] C.-D. Zhang, Y.-L. Xu, Multi-level damage identification with response reconstruction, Mech. Syst. Signal Process. 95 (2017) 42–57.

[150] Z. Niu, Two-step structural damage detection method for shear frame structures using FRF and Neumann series expansion, Mech. Syst. Signal Process. 149 (2021) 107185.

[151] A. Esfandiari, M. Nabiyan, F.R. Rofooei, Structural damage detection using principal component analysis of frequency response function data, Struct. Control Heal. Monit. (2020) e2550.

Appendix A

A. Destructive tests on the full-scale utility poles

Destructive test of the full-scale utility poles was performed in this thesis based on ASTMD2016 standard [49]. Each destructive test was performed by first weighing the specimen using a load cell attached to the laboratory overhead crane so that density could later be determined. The specimen was then clamped at an appropriate ground line position near the butt end. The location of ground line for each specimen was measured from the butt end as ten percent of the specimen overall length plus two feet. This is typical of in-service pole. The clamp was secured to the lab's concrete floor. Geometry such as length and circumferences (taken at five feet intervals) were also measured and recorded.

The static test was performed by applying a vertical load until failure occurred (Figure A.1). The load was applied at a position of two feet from each pole's tip using a hydraulic winch mounted above the point of load. Figure A.2 shows the hydraulic winch. A load cell, which is shown in Figure A.3, was attached in-line with the winch and measured the applied load. The hydraulic winch was positioned on a carriage which was he1d in place using the laboratory's overhead crane. The winch was mounted on a trolley and was free to move in the longitudinal direction (along the poles length) as the pole deflected. This longitudinal displacement was measured during each test and was taken into account for stress calculations.

Figure A.1: Destructive test of full-scale pole

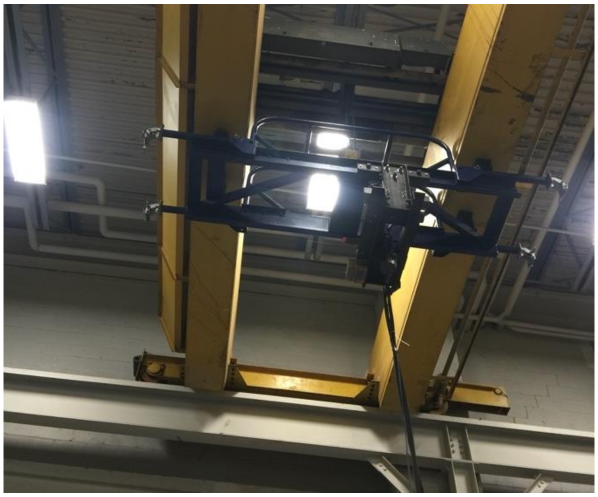

Figure A.2: Hydraulic winch for destructive test

Figure A.3: Load cell used to measure the applied load

Controlled flow in the winch's hydraulic lines ensured that a proper strain rates was maintained during tests. Vertical deflection of the pole was also measured at four locations during the test (at the point of load as well as twelve, twenty-four and thirty-six feet from the ground line) and are shown in . LVDTs were positioned on either side of the clamp and measured the angle of flexure in the clamp. This fixture was also taken into consideration when performing calculations. Appropriate calculations were later performed for each pole in order to determine elastic modulus, density, maximin stress at the break location, maximum stress at the ground line, yield stress at the break location and yield stress at the ground line.

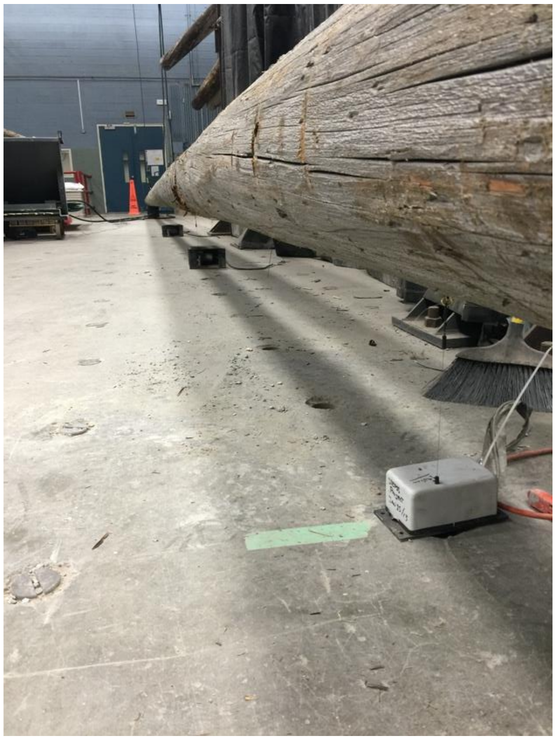

Figure A.4: Measurement of displacement in four different positions along the pole

A spreadsheet with all the calculations in detail was created for each pole. The spreadsheet report for two of the poles follow as a sample:

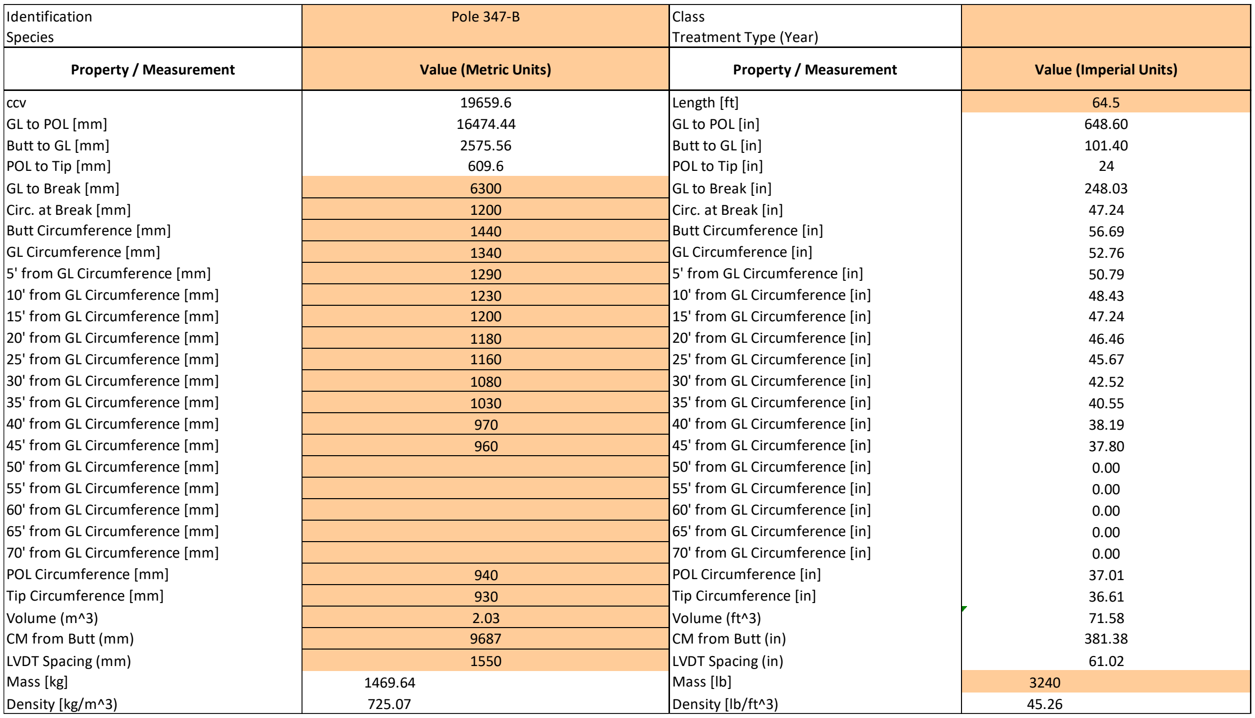

Identification Species	Pole 347-B	Class Treatment Type (Year)	
Property / Measurement	**Value (Metric Units)**	**Property / Measurement**	**Value (Imperial Units)**
ccv	19659.6	Length [ft]	64.5
GL to POL [mm]	16474.44	GL to POL [in]	648.60
Butt to GL [mm]	2575.56	Butt to GL [in]	101.40
POL to Tip [mm]	609.6	POL to Tip [in]	24
GL to Break [mm]	6300	GL to Break [in]	248.03
Circ. at Break [mm]	1200	Circ. at Break [in]	47.24
Butt Circumference [mm]	1440	Butt Circumference [in]	56.69
GL Circumference [mm]	1340	GL Circumference [in]	52.76
5' from GL Circumference [mm]	1290	5' from GL Circumference [in]	50.79
10' from GL Circumference [mm]	1230	10' from GL Circumference [in]	48.43
15' from GL Circumference [mm]	1200	15' from GL Circumference [in]	47.24
20' from GL Circumference [mm]	1180	20' from GL Circumference [in]	46.46
25' from GL Circumference [mm]	1160	25' from GL Circumference [in]	45.67
30' from GL Circumference [mm]	1080	30' from GL Circumference [in]	42.52
35' from GL Circumference [mm]	1030	35' from GL Circumference [in]	40.55
40' from GL Circumference [mm]	970	40' from GL Circumference [in]	38.19
45' from GL Circumference [mm]	960	45' from GL Circumference [in]	37.80
50' from GL Circumference [mm]		50' from GL Circumference [in]	0.00
55' from GL Circumference [mm]		55' from GL Circumference [in]	0.00
60' from GL Circumference [mm]		60' from GL Circumference [in]	0.00
65' from GL Circumference [mm]		65' from GL Circumference [in]	0.00
70' from GL Circumference [mm]		70' from GL Circumference [in]	0.00
POL Circumference [mm]	940	POL Circumference [in]	37.01
Tip Circumference [mm]	930	Tip Circumference [in]	36.61
Volume (m^3)	2.03	Volume (ft^3)	71.58
CM from Butt (mm)	9687	CM from Butt (in)	381.38
LVDT Spacing (mm)	1550	LVDT Spacing (in)	61.02
Mass [kg]	1469.64	Mass [lb]	3240
Density [kg/m^3)	725.07	Density [lb/ft^3)	45.26

Figure A.5: Pole 347B geometrical properties table

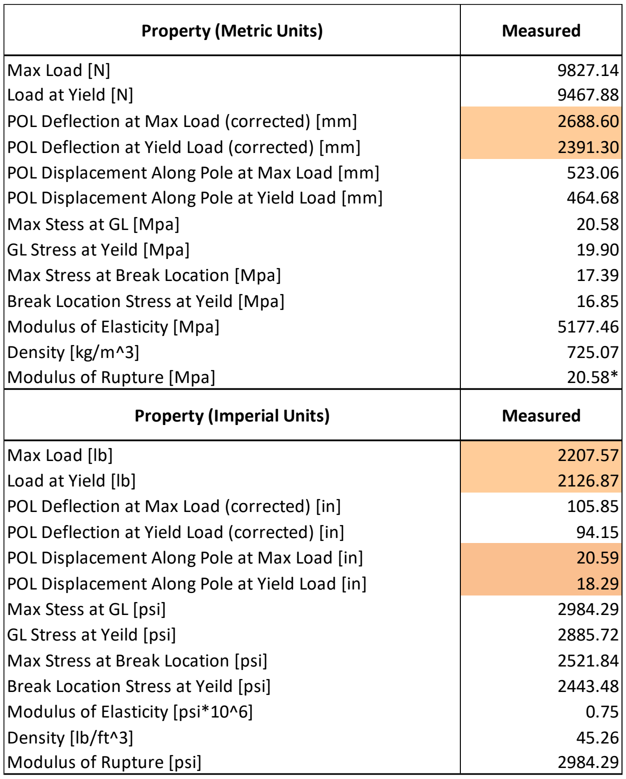

Property (Metric Units)	Measured
Max Load [N]	9827.14
Load at Yield [N]	9467.88
POL Deflection at Max Load (corrected) [mm]	2688.60
POL Deflection at Yield Load (corrected) [mm]	2391.30
POL Displacement Along Pole at Max Load [mm]	523.06
POL Displacement Along Pole at Yield Load [mm]	464.68
Max Stess at GL [Mpa]	20.58
GL Stress at Yeild [Mpa]	19.90
Max Stress at Break Location [Mpa]	17.39
Break Location Stress at Yeild [Mpa]	16.85
Modulus of Elasticity [Mpa]	5177.46
Density [kg/m^3]	725.07
Modulus of Rupture [Mpa]	20.58*
Property (Imperial Units)	**Measured**
Max Load [lb]	2207.57
Load at Yield [lb]	2126.87
POL Deflection at Max Load (corrected) [in]	105.85
POL Deflection at Yield Load (corrected) [in]	94.15
POL Displacement Along Pole at Max Load [in]	20.59
POL Displacement Along Pole at Yield Load [in]	18.29
Max Stess at GL [psi]	2984.29
GL Stress at Yeild [psi]	2885.72
Max Stress at Break Location [psi]	2521.84
Break Location Stress at Yeild [psi]	2443.48
Modulus of Elasticity [psi*10^6]	0.75
Density [lb/ft^3]	45.26
Modulus of Rupture [psi]	2984.29

Figure A.6: Pole 347B stress results table

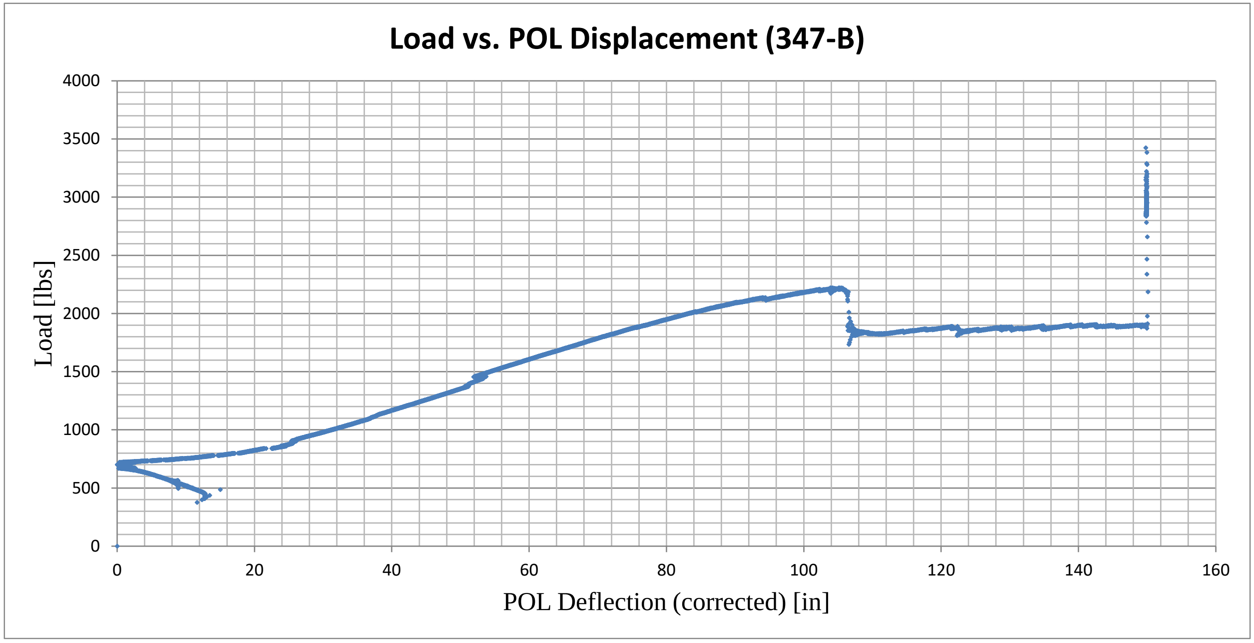

Figure A.7: Pole 347B load diagram from destructive test

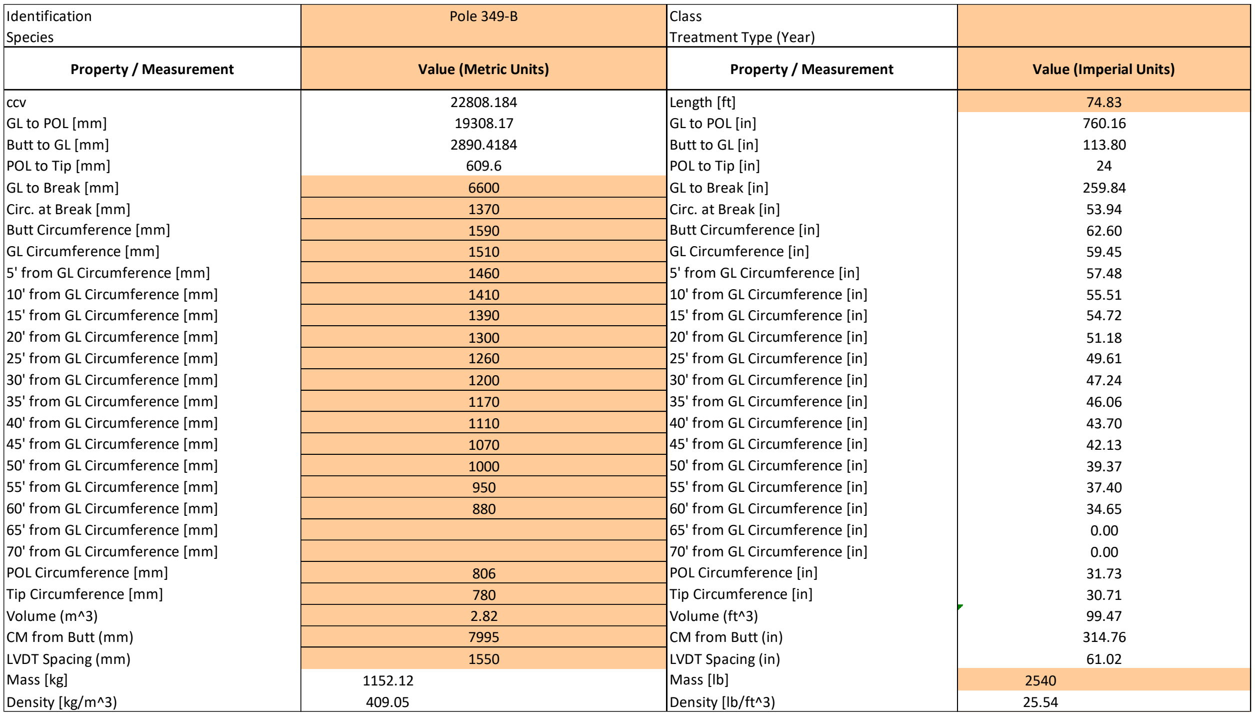

Identification Species	Pole 349-B	Class Treatment Type (Year)	
Property / Measurement	**Value (Metric Units)**	**Property / Measurement**	**Value (Imperial Units)**
ccv	22808.184	Length [ft]	74.83
GL to POL [mm]	19308.17	GL to POL [in]	760.16
Butt to GL [mm]	2890.4184	Butt to GL [in]	113.80
POL to Tip [mm]	609.6	POL to Tip [in]	24
GL to Break [mm]	6600	GL to Break [in]	259.84
Circ. at Break [mm]	1370	Circ. at Break [in]	53.94
Butt Circumference [mm]	1590	Butt Circumference [in]	62.60
GL Circumference [mm]	1510	GL Circumference [in]	59.45
5' from GL Circumference [mm]	1460	5' from GL Circumference [in]	57.48
10' from GL Circumference [mm]	1410	10' from GL Circumference [in]	55.51
15' from GL Circumference [mm]	1390	15' from GL Circumference [in]	54.72
20' from GL Circumference [mm]	1300	20' from GL Circumference [in]	51.18
25' from GL Circumference [mm]	1260	25' from GL Circumference [in]	49.61
30' from GL Circumference [mm]	1200	30' from GL Circumference [in]	47.24
35' from GL Circumference [mm]	1170	35' from GL Circumference [in]	46.06
40' from GL Circumference [mm]	1110	40' from GL Circumference [in]	43.70
45' from GL Circumference [mm]	1070	45' from GL Circumference [in]	42.13
50' from GL Circumference [mm]	1000	50' from GL Circumference [in]	39.37
55' from GL Circumference [mm]	950	55' from GL Circumference [in]	37.40
60' from GL Circumference [mm]	880	60' from GL Circumference [in]	34.65
65' from GL Circumference [mm]		65' from GL Circumference [in]	0.00
70' from GL Circumference [mm]		70' from GL Circumference [in]	0.00
POL Circumference [mm]	806	POL Circumference [in]	31.73
Tip Circumference [mm]	780	Tip Circumference [in]	30.71
Volume (m^3)	2.82	Volume (ft^3)	99.47
CM from Butt (mm)	7995	CM from Butt (in)	314.76
LVDT Spacing (mm)	1550	LVDT Spacing (in)	61.02
Mass [kg]	1152.12	Mass [lb]	2540
Density [kg/m^3)	409.05	Density [lb/ft^3)	25.54

Figure A.8: Pole 349B geometrical properties table

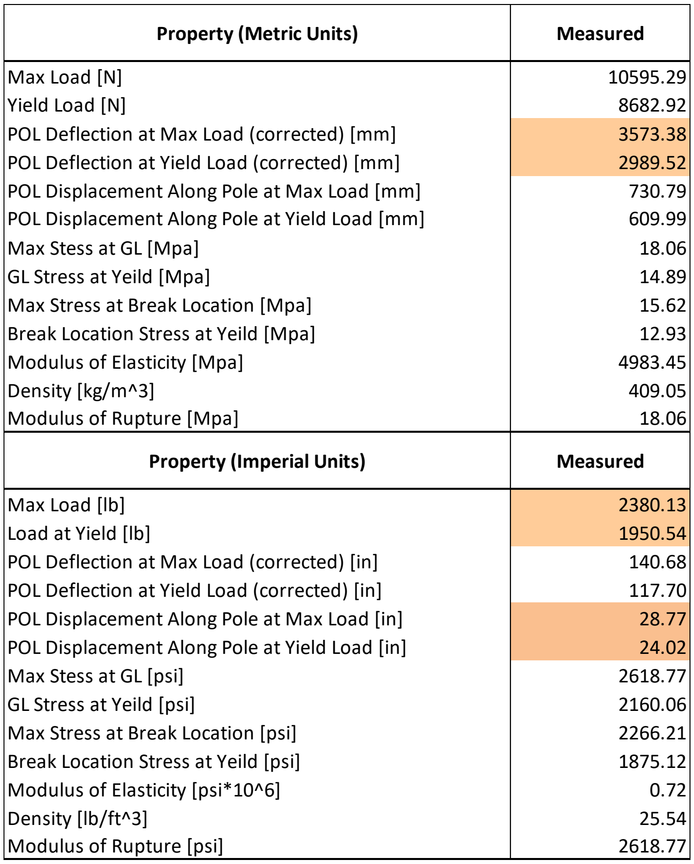

Property (Metric Units)	**Measured**
Max Load [N]	10595.29
Yield Load [N]	8682.92
POL Deflection at Max Load (corrected) [mm]	3573.38
POL Deflection at Yield Load (corrected) [mm]	2989.52
POL Displacement Along Pole at Max Load [mm]	730.79
POL Displacement Along Pole at Yield Load [mm]	609.99
Max Stess at GL [Mpa]	18.06
GL Stress at Yeild [Mpa]	14.89
Max Stress at Break Location [Mpa]	15.62
Break Location Stress at Yeild [Mpa]	12.93
Modulus of Elasticity [Mpa]	4983.45
Density [kg/m^3]	409.05
Modulus of Rupture [Mpa]	18.06
Property (Imperial Units)	**Measured**
Max Load [lb]	2380.13
Load at Yield [lb]	1950.54
POL Deflection at Max Load (corrected) [in]	140.68
POL Deflection at Yield Load (corrected) [in]	117.70
POL Displacement Along Pole at Max Load [in]	28.77
POL Displacement Along Pole at Yield Load [in]	24.02
Max Stess at GL [psi]	2618.77
GL Stress at Yeild [psi]	2160.06
Max Stress at Break Location [psi]	2266.21
Break Location Stress at Yeild [psi]	1875.12
Modulus of Elasticity [psi*10^6]	0.72
Density [lb/ft^3]	25.54
Modulus of Rupture [psi]	2618.77

Figure A.9: Pole 349B stress results table

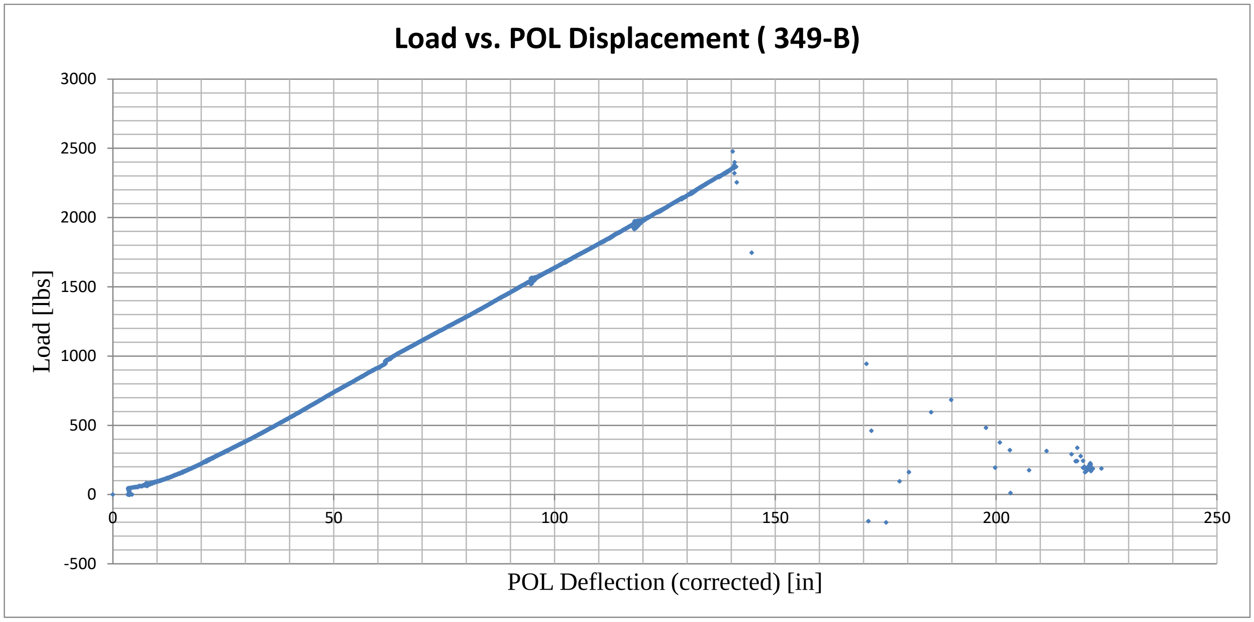

Figure A.10: Pole 349B load diagram from destructive test

Appendix B

B. Modal Testing of Full-Scale Utility Poles

Modal test of the full-scale utility poles was performed in this thesis in the lab and in the field. The modal test was carried out on 30 utility poles in the field in two separate test batches. The first batch of poles (10 poles in Goose bay, Labrador) were modally tested in two different conditions of with and without the connected cables and the purpose of this test was to study the effects of cables on the FRFs of the pole in the field. The second batch (20 poles in Paradise, Newfoundland) was tested only without the connected cables. This batch was then transmitted to the lab and was modally tested. The purpose of test of the second batch was to compare the FRFs obtained from the in-ground poles and in the lab-fixture poles. Therefore, 30 poles were modally tested in the field and 20 poles were modally tested in the lab. The details of modal tests are presented as follows:

10.6 B.1 Field Modal tests

In all the in-field tests, the poles were "in-ground" with the ground foundation. The first batch of poles were chosen from a distribution line in Good bay, Labrador by NL Hydro company. The modal tests were first performed in one day when the conductors were connected to the poles and then the next day, the conductors were disconnected from the poles and another modal test with the same procedure was performed on the same poles. The modal tests were performed using a modal hammer and two accelerometers. Two accelerometers were positioned 1.5 m and 2 m from the ground line and the hammer hit was at 2.2 m form the ground line. The accelerometers and the hammer hit were close to the ground to perform a modal test that is feasible in the field. Tests were performed with a Bruel & Kjaer 8205-002 impact hammer, 4507 B 004 70-g accelerometers, and a National Instruments NI USB-4432 power supply and signal conditioner. The software

ModalView [95] was used to analyze the data. Figure B.1 shows the pole modal test setup in the field. Each test was done five times and the average was considered for the final result. A rubber piece (Figure B.2) was bolted to the pole and the accelerometers were placed in the rubber piece since the accelerometer wax did not hold the accelerometers on the pole. The second batch of poles (20 poles) was in Paradise, Newfoundland and they were all without the cables. The same procedure for modal test was used in the second batch.

Figure B.1: Field modal test a) Modal hammer b) Accelerometers c) Test setup

Figure B.2: Mounting accelerometer a) accelerometer in the rubber piece b) bolting the piece to the wooden pole

Figure B.3 shows the FRFs of the two poles with and without the cables. As can be seen, when the cable disconnected, there is a shift toward right and the peaks are more sharped. This could be due to the mass and damping of the cables that are not in the system anymore. Decreased mass could cause a shift to the right in the frequency response and less damping could make the peaks less sharp.

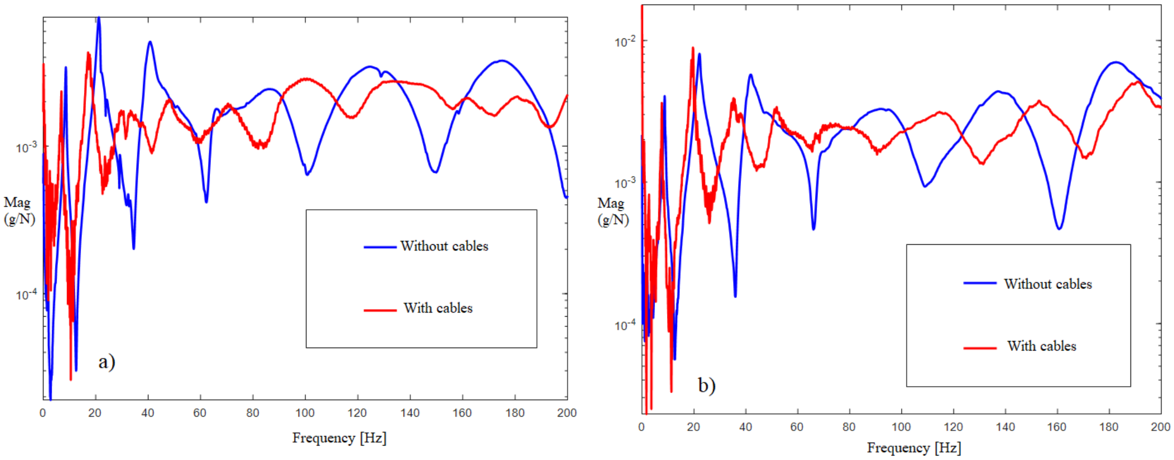

Figure B.3 : FRF of two different utility poles with and without cable –Field Modal test

10.7 B.2 Lab Modal Tests

The same procedure and equipment that was used in field modal testing was used in the lab. The second batch of poles were transmitted from the field to the lab and modal tests were performed. The poles were clamped using the fixture shown in Figure B.5 and two accelerometers were mounted in 1.5 m and 2 m form the ground line and hammer hit was 2.2 m from the ground line. Figure B.5 shows a full-scale pole in the lab. The location of ground line for each specimen was measured from the butt end as ten percent of the specimen overall length plus two feet. Figure B.6 shows the mounted accelerometers on the pole.

Figure B.4: Clamp fixture in the lab

Figure B.5: Full-scale pole in the clamp

Figure B.6: Accelerometers mounted on the pole in the lab

All the poles were marked in the field so that each pole was recognizable in the lab and the same pole's FRF were compared with each other. The FRFs obtained from the "in-fixture" test and "in-ground" tests for two of the poles are shown in Figure B.7.

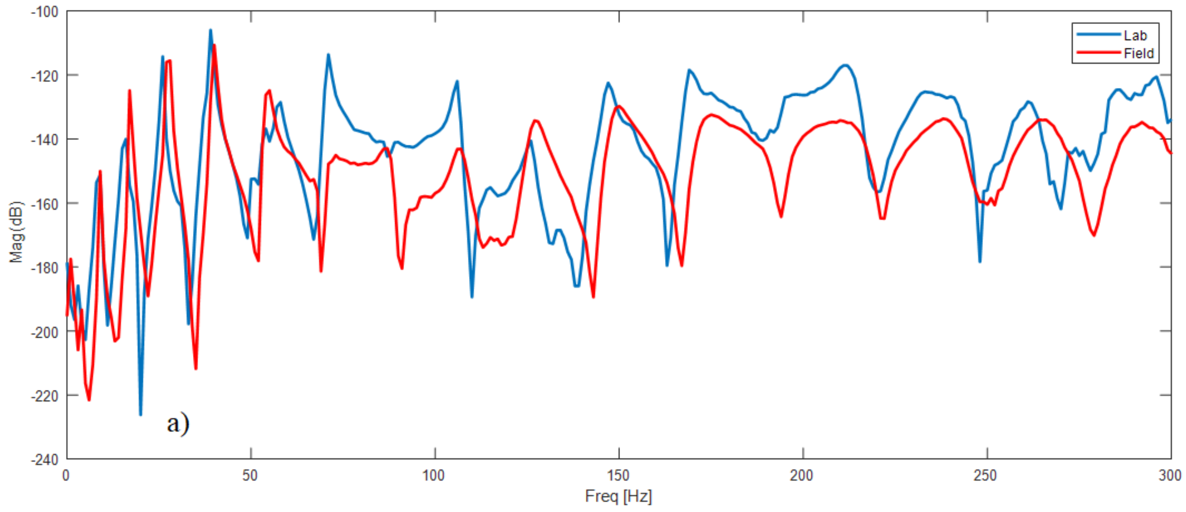
Mag(dB)
-100
-120
-140
-160
-180
-200
-220
-240
0
50
100
150
200
250
300
Freq [Hz]
Lab
Field
a)

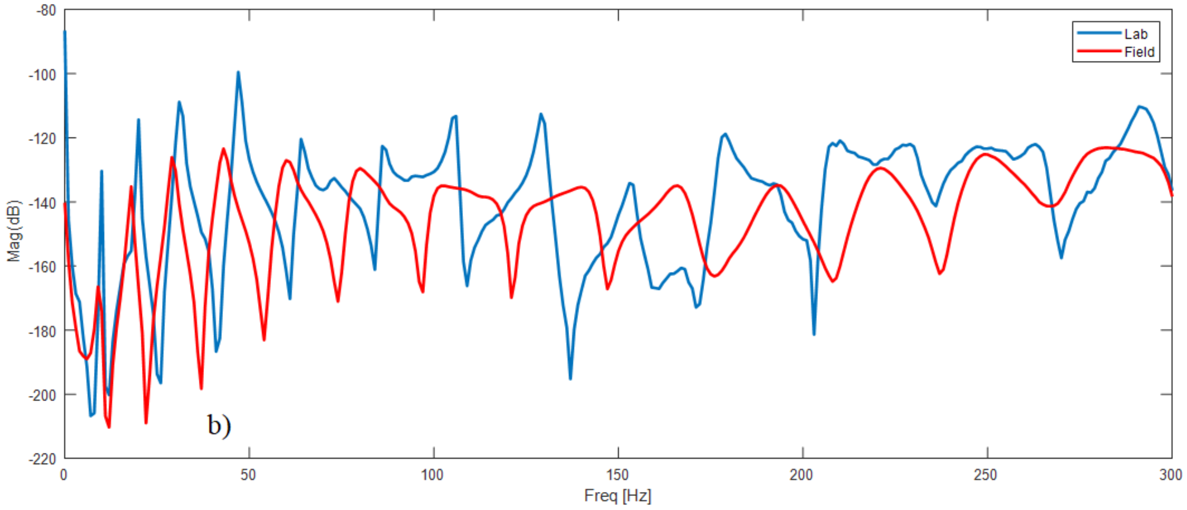
Mag(dB)
-80
-100
-120
-140
-160
-180
-200
-220
0
50
100
150
200
250
300
Freq [Hz]
Lab
Field
b)

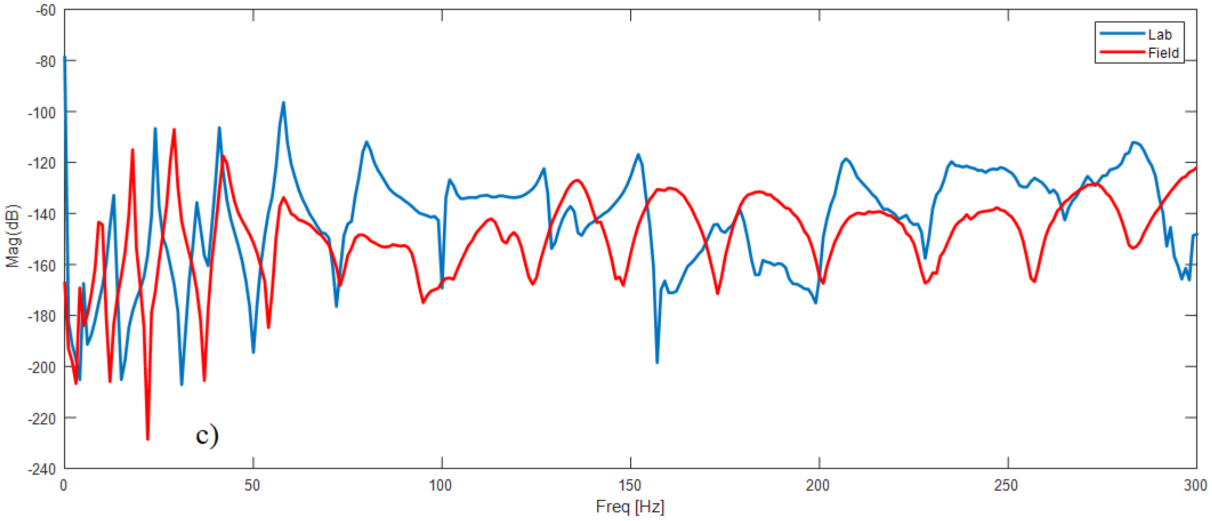
Mag(dB)
-60
-80
-100
-120
-140
-160
-180
-200
-220
-240
0
50
100
150
200
250
300
Freq [Hz]
Lab
Field
c)

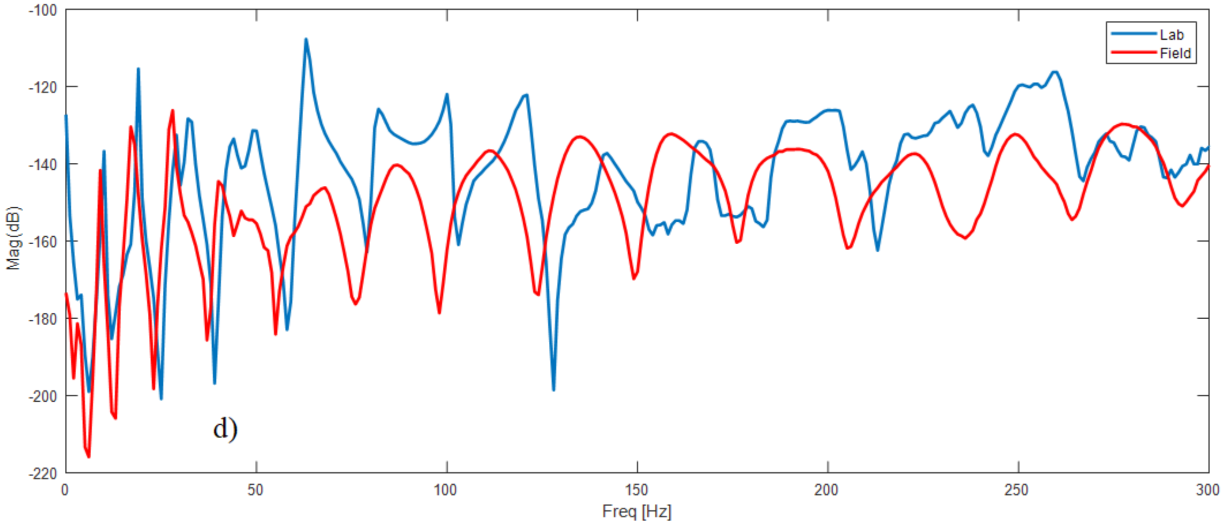

Figure B.7: FRFs of four different poles in the lab fixture and in-ground